



Edited by
Ning Xi
King Wai Chiu Lai

NANO-OPTOELECTRONIC SENSORS AND DEVICES

Nanophotonics from Design to Manufacturing

Micro & Nano Technologies Series

Nano-Optoelectronic Sensors and Devices

Nanophotonics from Design to Manufacturing

Edited by

Ning Xi

Michigan State University

King Wai Chiu Lai

Michigan State University



Amsterdam • Boston • Heidelberg • London • New York • Oxford
Paris • San Diego • San Francisco • Singapore • Sydney • Tokyo

William Andrew is an imprint of Elsevier



William Andrew is an imprint of Elsevier
225 Wyman Street, Waltham, 02451, USA
The Boulevard, Langford Lane, Kidlington, Oxford OX5 1GB, UK

First edition 2012

Copyright © 2012 Elsevier Inc. All rights reserved.

No part of this publication may be reproduced or transmitted in any form or by any means, electronic or mechanical, including photocopying, recording, or any information storage and retrieval system, without permission in writing from the publisher. Details on how to seek permission, further information about the Publisher's permissions policies and arrangements with organizations, such as the Copyright Clearance Center and the Copyright Licensing Agency, can be found at our website: www.elsevier.com/permissions.

This book and the individual contributions contained in it are protected under copyright by the Publisher (other than as may be noted herein).

Notice

Knowledge and best practice in this field are constantly changing. As new research and experience broaden our understanding, changes in research methods, professional practices, or medical treatment may become necessary.

Practitioners and researchers must always rely on their own experience and knowledge in evaluating and using any information, methods, compounds, or experiments described herein. In using such information or methods they should be mindful of their own safety and the safety of others, including parties for whom they have a professional responsibility.

To the fullest extent of the law, neither the Publisher nor the authors, contributors, or editors, assume any liability for any injury and/or damage to persons or property as a matter of products liability, negligence or otherwise, or from any use operation of any methods, products, instructions, or ideas contained in the material herein.

Library of Congress Cataloging-in-Publication Data

A catalog record for this book is available from the Library of Congress.

British Library Cataloguing in Publication Data

A catalogue record for this book is available from the British Library.

ISBN: 978-1-4377-3471-3

For information on all Elsevier publications
visit our web site at www.elsevierdirect.com

Printed and bound in Great Britain
12 13 10 9 8 7 6 5 4 3 2 1

Working together to grow
libraries in developing countries

www.elsevier.com | www.bookaid.org | www.sabre.org

ELSEVIER

BOOK AID
International

Sabre Foundation

Preface

This book presents a comprehensive report on the research on nanosensors and -devices conducted by the researchers in the Robotics and Automation Laboratory at Michigan State University and our collaborators. The Robotics and Automation Laboratory was established after I joined the faculty of Michigan State University in 1997. For the last decade, the research directions of the laboratory have been expanded from traditional industrial robots to nanorobots. After we successfully tested our nanorobotic system for nano manipulations and assembly, we were looking for opportunities to develop nanodevices to demonstrate the capability of our newly developed nanorobotic system. In 2004, I met Dr Harold Szu, US Army Night Vision and Electronic Sensors Directorate (formerly with Office of Naval Research), in a conference. We had a very interesting discussion on nanomanufacturing and nanosensors. He inspired me to consider using nanorobots to manufacture nanowire-based infrared detectors. This has led to many interesting projects. Over the years, Harold has provided us with much valuable advice. I wish to express my deep appreciation for his inspiration and assistance.

Dr King Wai Chiu Lai was my first research associate working on the nanodevices. He played important roles in many of the research efforts reported in the book. King, as my coeditor, has put a lot of effort into this book. The completion of this book would have not been possible without his tireless and careful work. In addition, all of the contributors of this book are my former or current PhD students, postdoctoral research associates, and collaborators. I wish to thank all of them for their contributions to this book.

Last but not least, I express my sincere thanks to Office of Naval Research, in particular Drs James Buss, Keith Krapels, James Waterman, and Michael Duncan, and the National Science Foundation for providing financial support for the research efforts reported in this book.

Ning Xi

Contents

Preface	xi
Acknowledgments	xiii
About the Editors	xv
List of Contributors	xvii
CHAPTER 1 Introduction	1
1.1 Overview	1
1.2 Impact of Nanomaterials	2
1.3 Challenges and Difficulties in Manufacturing Nanomaterials-Based Devices....	4
1.3.1 Role of Microfluidics	5
1.3.2 Role of Robotic Nanoassembly	6
1.4 Summary	6
References.....	7
CHAPTER 2 Nanomaterials Processing for Device Manufacturing.....	11
2.1 Introduction	11
2.2 Characteristics of Carbon Nanotubes	13
2.3 Classification of Carbon Nanotubes using Microfluidics	14
2.3.1 Dielectrophoretic Phenomenon on CNTs	16
2.3.2 Experimental Results: Separation of Semiconducting CNTs	19
2.4 Deposition of CNTs by Microrobotic Workstation.....	21
2.5 Summary	24
References.....	25
CHAPTER 3 Design and Generation of Dielectrophoretic Forces for Manipulating Carbon Nanotubes.....	29
3.1 Overview	29
3.2 Dielectrophoretic Force Modeling	30
3.2.1 Modeling of Electrorotation for Nanomanipulation.....	34
3.2.2 Dynamic Modeling of Rotational Motion of Carbon Nanotubes for Intelligent Manufacturing of CNT-Based Devices.....	35
3.2.3 Dynamic Effect of Fluid Medium on Nano Particles by Dielectrophoresis	36
3.3 Theory for Microelectrode and Electric Field Design for Carbon Nanotube Applications	37
3.3.1 Microelectrode Design	37
3.3.2 Theory for Microelectrode Design	38

3.4	Electric Field Design	39
3.5	Carbon Nanotubes Application-Simulation Results	40
3.5.1	Dielectrophoretic Force: Simulation Results	40
3.5.2	Electrorotation (Torque): Simulation Results	45
3.5.3	Rotational Motion of Carbon Nanotubes: Simulation Results	45
3.6	Summary	49
	References.....	49
CHAPTER 4	Atomic Force Microscope-Based Nanorobotic System for Nanoassembly	51
4.1	Introduction to AFM and Nanomanipulation.....	51
4.1.1	AFM's Basic Principle	52
4.1.2	Imaging Mode of AFM.....	53
4.1.3	AFM-Based Nanomanipulation	55
4.2	AFM-Based Augmented Reality System	56
4.2.1	Principle for 3D Nanoforce Feedback	56
4.2.2	Principle for Real-Time Visual Feedback Generation	59
4.2.3	Experimental Testing and Discussion.....	59
4.3	Augmented Reality System Enhanced by Local Scan	62
4.3.1	Local Scan Mechanism for Nanoparticle	62
4.3.2	Local Scan Mechanism for Nanorod.....	64
4.3.3	Nanomanipulation with Local Enhanced Augmented Reality System.....	66
4.4	CAD-Guided Automated Nanoassembly	71
4.5	Modeling of Nanoenvironments	72
4.6	Automated Manipulation of CNT.....	74
4.7	Summary	78
	References.....	78
CHAPTER 5	On-Chip Band Gap Engineering of Carbon Nanotubes	81
5.1	Introduction	81
5.2	Quantum Electron Transport Model	82
5.2.1	Nonequilibrium Green's Functions	82
5.2.2	Poisson's Equation and Self-Consistent Algorithm	84
5.3	Electrical Breakdown Controller of a CNT	85
5.3.1	Extended Kalman Filter for Fault Detection.....	85
5.4	Effects of CNT Breakdown	87
5.4.1	Current-Voltage Characteristics	87
5.4.2	Infrared Responses.....	89
5.5	Summary	91
	References.....	91

CHAPTER 6	Packaging Processes for Carbon Nanotube-Based Devices	93
6.1	Introduction	93
6.2	Thermal Annealing of Carbon Nanotubes	94
6.3	Electrical and Optical Responses of Carbon Nanotubes After Thermal Annealing	96
6.4	Parylene Thin Film Packaging	100
6.5	Electrical and Optical Stability of the CNT-Based Devices After Packaging	101
6.6	Summary	103
	References	104
CHAPTER 7	Carbon Nanotube Schottky Photodiodes	107
7.1	Introduction	107
7.2	Review of CNT Photodiodes	108
7.3	Design of CNT Schottky Photodiodes	111
7.4	Symmetric Schottky Photodiodes	112
7.5	Asymmetric Schottky Photodiodes	117
7.6	Summary	121
	References	121
CHAPTER 8	Carbon Nanotube Field-Effect Transistor-Based Photodetectors	125
8.1	Introduction	125
8.2	Back-Gate Au–CNT–Au Transistors	127
8.3	Back-Gate Ag–CNT–Ag Transistors	130
8.4	Back-Gate Au–CNT–Ag Transistors	132
8.5	Middle-Gate Transistors	136
8.6	Multigate Transistors	139
8.7	Detector Array Using CNT-Based Transistors	146
8.8	Summary	147
	References	148
CHAPTER 9	Nanoantennas on Nanowire-Based Optical Sensors	151
9.1	Introduction	151
9.2	Nanoantenna Design Consideration for IR Sensors	152
9.2.1	Optical Nanoantennas Combined with CNT-Based IR Sensors	152
9.3	Theoretical Analysis: Nanoantenna Near-Field Effect	153
9.4	Fabrication of Nano Sensor Combined with Nanoantenna	154
9.5	Photocurrent Measurement on Nano Sensor Combined with Nanoantenna	157
9.6	Summary	158
	References	160

CHAPTER 10	Design of Photonic Crystal Waveguides	163
10.1	Introduction	163
10.2	Review of the Photonic Crystal	164
10.3	Principle for Photonic Crystal	165
10.4	Photonic Band Gap of Photonic Crystal	166
10.4.1	Effect from Dielectric Constants	167
10.4.2	Effect from Different Structures	168
10.5	Photonic Crystal Cavity	173
10.5.1	Basic Design of Photonic Crystal Defect	173
10.5.2	Defect from Dielectric Constants	174
10.5.3	Defect from Dielectric Size	176
10.5.4	Effect from Lattice Number	177
10.6	Design and Experimental Results of Photonic Crystal Cavity	178
10.6.1	Design	178
10.6.2	Photoresponses of CNT-Based IR Sensors with Photonic Crystal Cavities	179
10.6.3	Photocurrent Mapping of the CNT-Based IR Sensors with Photonic Crystal Cavities	180
10.7	Summary	181
	References	182
CHAPTER 11	Organic Solar Cells Enhanced by Carbon Nanotubes	183
11.1	Introduction	183
11.2	Application of Carbon Nanotubes in Organic Solar Cells	184
11.3	Fabrication of Carbon Nanotube-Enhanced Organic Solar Cells	185
11.4	Performance Analysis of OSCs Enhanced by CNTs	185
11.4.1	J-V of SWCNTs-Enhanced OSCs Under Illumination	186
11.4.2	J-V of SWCNTs-Enhanced OSCs in Dark	190
11.5	Electrical Role of SWCNTs in OSCs	193
11.6	Summary	197
	References	197
CHAPTER 12	Development of Optical Sensors Using Graphene	199
12.1	Introduction	199
12.2	Fabrication of Graphene-Based Devices	200
12.3	Dielectrophoretic Effect on Different Graphene Flakes	202
12.4	Electrical and Optical Behaviors of Various Graphene-Based Devices	203
12.5	Summary	206
	References	206

CHAPTER 13	Indium Antimonide (InSb) Nanowire-Based Photodetectors	209
13.1	Introduction	209
13.2	Growth of InSb Nanowires	214
13.3	Photodetectors Using Single InSb Nanowires	216
13.3.1	Symmetric InSb Nanowire Photodetectors	216
13.3.2	Asymmetric InSb Nanowire Photodetectors	218
13.4	Summary	223
	References	223
CHAPTER 14	Carbon Nanotube-Based Infrared Camera Using Compressive Sensing	225
14.1	Introduction	225
14.2	Theoretical Foundation of Compressive Sensing	228
14.2.1	General Idea	229
14.2.2	Sparsity	229
14.2.3	Restricted Isometry Property	230
14.2.4	Random Matrix	231
14.2.5	Compressive Sensing Applications	231
14.3	Compressive Sensing for Single-Pixel Photodetectors	231
14.3.1	System Architecture	231
14.3.2	Measurement Matrix	233
14.3.3	Data Sampling and Image Reconstruction Algorithm	234
14.4	Experimental Setup and Results	236
14.4.1	Static Measurement	236
14.4.2	Dynamic Observation	237
14.4.3	Performance Analysis	237
14.5	Summary and Perspectives	240
	References	241
Index		245

Introduction

1

King Wai Chiu Lai and Ning Xi

*Department of Electrical and Computer Engineering,
Michigan State University, Michigan*

CHAPTER OUTLINE

1.1 Overview	1
1.2 Impact of Nanomaterials	2
1.3 Challenges and Difficulties in Manufacturing Nanomaterials-Based Devices	4
1.3.1 Role of Microfluidics	5
1.3.2 Role of Robotic Nanoassembly	6
1.4 Summary	6
References	7

1.1 OVERVIEW

Nanomaterials can be used as novel sensing elements and they allow us to build devices much smaller than before. Research into nanomaterials and nanomanufacturing is tremendously important, because most nanoscale materials and systems are different from current macro- and micro systems. This book covers a range of matters regarding the development of nano-optoelectronic devices.

Optoelectronics plays a significant role in the semiconductor industry, and silicon-based optoelectronic devices are now so ubiquitous in modern society. The range of applications for optoelectronic devices like light-emitting diodes (LEDs), laser, optical sensors, and solar cells continues to grow, resulting in a new generation of electronics products such as computer displays, flat screen TVs, high-speed communication devices, etc. While silicon-based devices and electronics have been developed for 30 years, scaling down and further improving the performance of current silicon-based devices are still very challenging. Therefore, new technologies and materials have to be developed to meet these challenges. In 1971, the feature widths of semiconductor manufacturing processes were about 10 μm . Nowadays the smallest feature size of silicon-based devices is about 32 nm. Highly specialized techniques, facilities, and equipment are essential to further reduce the size of conventional optoelectronic devices. With the recent advance in nanotechnology, various kinds of novel nanomaterials have been introduced. These materials offer superior quantum optical, electrical, and mechanical effects due to their sizes (nanometer scale), which opens up the possibility to replace silicon for

high-performance optoelectronic devices. Since the nanomaterials exist usually in the form of powders or fluids, a systematic approach to make use of different nanomaterials for optoelectronic devices is necessary.

Nanomanufacturing refers to a series of fabrication processes to build nanoscale structures and devices using nanomaterials. It also refers to the development of some technologies or specialized equipment to handle or process nanomaterials. Since 2000, the term *nanomanufacturing* has been widely used in academic societies and worldwide government agencies, such as the Institute of Electrical and Electronics Engineers (IEEE), U.S. National Nanotechnology Initiative (NNI), and European Technology Platform: Micro- and NanoManufacturing (MINAM).

The contents of the book start with discussing the fundamental structure of nanodevices as well as the significance of nanomaterials and nanostructure to the photonic devices. Afterward, a series of processes for manufacturing nanodevices will be given, attempting to meet the challenges and difficulties of design and fabrication using nanomaterials. Classification of nanomaterials using micro fluidics and dielectrophoresis is described in Chapter 2, following by a detailed discussion in Chapter 3. Chapter 4 introduces nanorobotic manipulation and assembly methods. A precise nanoassembly can be achieved by an atomic force microscopy-based nanorobotic system, which are capable of manipulating nanomaterial efficiently. Because band gap of semiconducting material is an important property for many optoelectronic applications, such as optical detectors and solar cells, band gap engineering of nanomaterials is given in Chapter 5. The nanomanufacturing processes culminates in Chapter 6 with the development of thermal annealing process and packaging process to maintain the stability and reliability of the nanodevices.

Development of specific nanodevices is discussed in the next six chapters (see Figure 1.1). In Chapter 7, design and performance of carbon nanotube-based Schottky photodiodes is presented. Chapter 8 describes improvement of the photodiodes using field effect transistors. Field enhancement and confinement of nanoantennas and photonic crystal are reported in Chapters 9 and 10, respectively. Apart from carbon nanotube-based photodiode, more other optoelectronic devices are discussed as the following: solar cells (Chapter 11), graphene-based optical sensors (Chapter 12), and nanowire-based infrared detectors (Chapter 13). Finally, the development of infrared imaging using carbon nanotubes is given in Chapter 14.

1.2 IMPACT OF NANOMATERIALS

Nanomaterials are likely candidates to create breakthroughs in the field of nano-optoelectronics. When the size of a material reduces to the nanometer range, quantum effects become very pronounced, which cannot be found at macroscopic and microscopic level. As a result, the behavior of these nanomaterials is very different from other conventional materials. Over the last 20 years, a variety of nanomaterials have been found and developed, including carbon nanotubes (CNTs), graphene, quantum dots, and quantum wells and many different kinds of metal nanowires.

The CNT is one of the most well-known nanomaterials, which has been studied extensively in the last couple of decades after its discovery in early 1990s [1]. CNT is a hollow cylindrical structure that has unique and attractive one-dimensional (1D) properties. The diameter of a single CNT is in the range of nanometers, and CNTs can range in length from a typical 10 μm to as long as 18 cm [2].

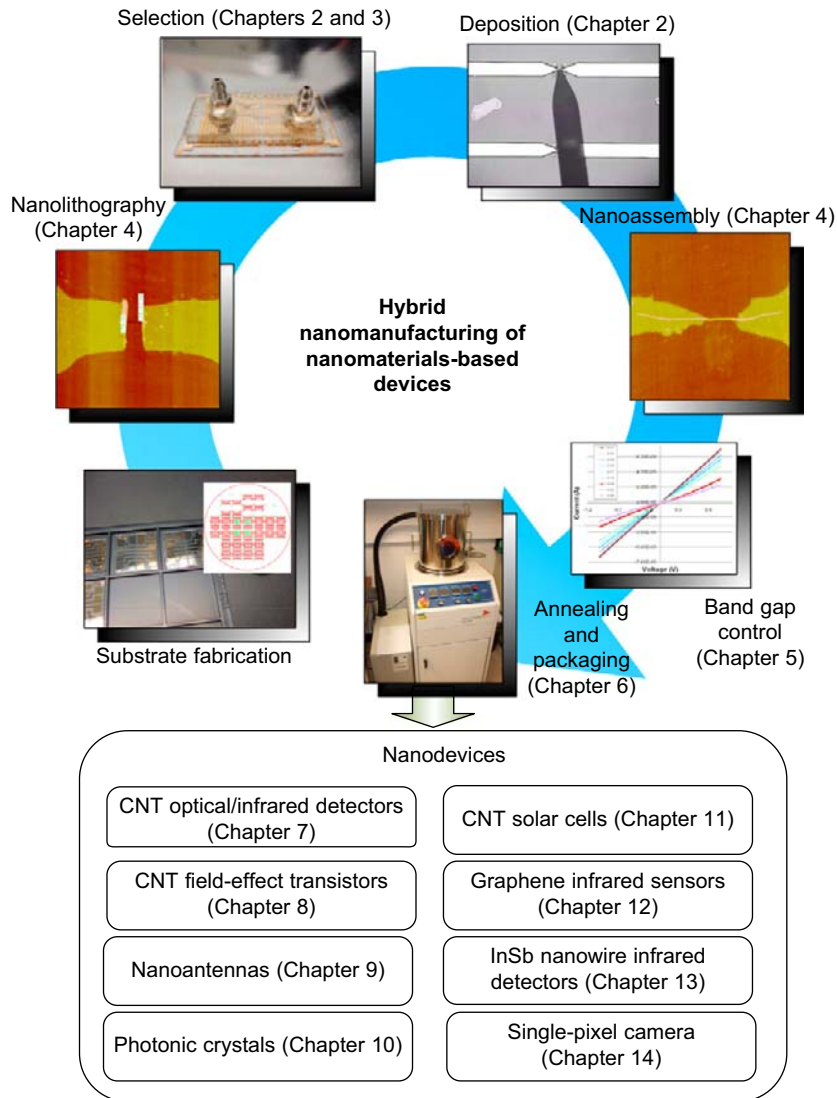
**FIGURE 1.1**

Illustration of the nanomanufacturing process for CNT-based devices.

CNTs have been shown to exhibit remarkable electronic properties such as adjustable bandgap [3] and ballistic transport [4]. Additionally, this extremely strong material also has good thermal conductivity. Therefore, CNTs have been investigated as one of the most promising candidates for a wide variety of optical [5], electrical [6], and mechanical [7] applications. For example, CNTs can work as fundamental

building blocks of various nanoelectronic devices. Many scientists and engineers are looking into the possibility to use CNTs as fundamental building blocks in real nanodevices such as in nanoelectronics [8, 9], optoelectronics [10–12], transistors [4, 13], and nanomechanical devices [14–16]. As we all know, different carbon nanotubes have different properties. For example, electrical and optical properties of nanotubes are dependent on their diameters and chiralities [17]. However, current fabrication processes of nanotubes still have limited capability to control such properties, so it is very important to develop methods to control the properties of the nanotube in order to use it as a functional device.

1.3 CHALLENGES AND DIFFICULTIES IN MANUFACTURING NANOMATERIALS-BASED DEVICES

In the conventional semiconductor industry, the fabrication process of optoelectronic devices can be divided into four areas as shown in Table 1.1. First, *deposition* involves single or multiple processes to add or place materials on a substrate. Second, *patterning* is done by photolithography that usually employs a mask to generate structure and pattern on materials. Third, *properties control* usually involves several processes to adjust the electrical properties of materials. Fourth, *etching* includes both dry etching and wet etching to remove specific material during fabrication. Some of them can still be used for the manufacturing of nanodevices. However, conventional photolithographic processes cannot be used on the ultrasmall nanomaterials. Therefore, new fabrication technologies have to be developed for the manufacture of nanodevices.

In general, the technique to manufacture nanodevices can be classified into bottom-up and top-down approaches. Connecting a single CNT or a CNT thin film to a pair of metal electrodes can form a typical nanodevice. As shown in Fig. 1.2, the nanomanufacturing processes of CNT-based devices can be divided into CNT synthesis, direct growth, self-assembly, purification, selection, deposition, nanoassembly, device annealing, and packaging. Synthesis, direct growth, and self-assembly can be considered as bottom-up methods, whereas top-down methods include the processes of selection, deposition, and nanoassembly.

Table 1.1 Four Major Areas of General Conventional Microfabrication Processes

Deposition	Patterning	Properties Control	Etching
Chemical vapor deposition (CVD)	Photolithography	Electrical doping	Chemical wet etching
Plasma-enhanced CVD	Electron beam lithography, etc.	Ion implantation	Plasma dry etching
Electrochemical deposition		Thermal annealing	Reactive-ion etching
Molecular beam epitaxy, etc.		UV processing, etc.	Mechanical planarization, etc.

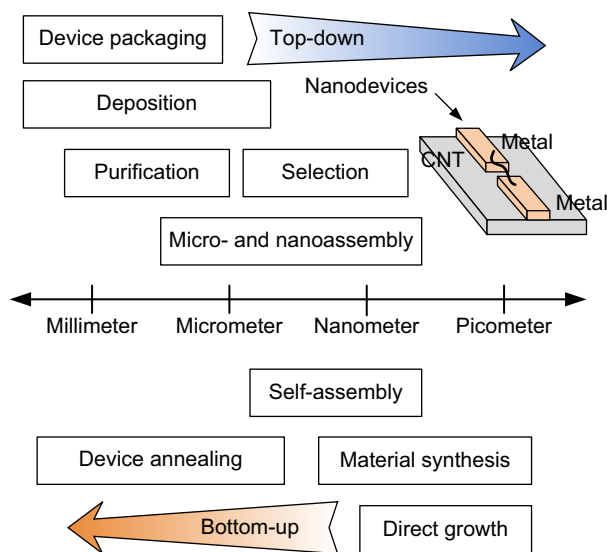
**FIGURE 1.2**

Illustration of various fabrication processes involved in manufacturing of nanodevices.

1.3.1 Role of Microfluidics

CNTs are mixed together after synthesis; the CNT aggregates comprising both metallic and semi-conducting CNTs. This results in a large variation of the physical and electronic properties of CNTs. Thus, many researchers have been working on controlling the properties of these nanotubes. Although a number of techniques such as chemical vapor deposition (CVD), high-pressure carbon monoxide (HiPco), arch discharge, and laser ablation have been developed to produce CNTs, the electronic properties of nanotubes are still difficult to control. For example, Li et al. reported a plasma-enhanced chemical vapor deposition method to grow high concentrations of semiconducting CNTs [18], but the band gap cannot easily be controlled. HiPco synthesis process has been demonstrated to grow a narrow distribution of CNTs at high pressure and high temperature [19, 20]. However, the band gap of the CNT produced by this process was limited by its small diameter (<1.5 nm). Therefore, additional processes of CNT mixture such as purification and classification are needed to overcome current limitations. In [Chapter 2](#), we will discuss how this problem can be solved by using a microfluidic system.

Micro- or nanomanipulation is a process to handle different objects with sizes in the range of micrometers, submicrometers, and even a few nanometers. As the reducing of physical scale of different targets, microscopic and nanoscopic systems are needed to deal with the objects at the same scale. Micro- or nanofluidics is one of the most promising manipulation methods and has been drawing increasing attention in MEMS and nanotechnology research. It consists of a sequence of operations for moving fluid containing specific micro- or nanoparticles such as CNTs, nanowire, cells, proteins, etc. By designing a microfluidic system, extremely small amounts of fluid down to nanoliter or picoliter range can be manipulated effectively. Such a system could be one of the most significant approaches

for studying different nanomaterials and biological processes as it provides a platform for transporting, separating, and sorting different nanomaterials and biological samples. In recent years, automated micro- or nanomanipulation has become a new and emerging area and offers many crucial applications in the areas of semiconductor technology, material research, nanotechnology, and biotechnology.

1.3.2 Role of Robotic Nanoassembly

One of the bottom-up approaches, direct growth of CNTs across microelectrodes, has been suggested as a means to fabricate CNT-based devices [21, 22]. However, these methods have limitations and uncertainties in terms of repeatability and mass production. It is difficult to grow a single CNT between the microelectrodes while CNT bundles and impurities are mostly formed between the electrodes. It further affects the electronic properties of the final device, resulting in inconsistent and unstable performance of a CNT-based device.

Therefore, deposition and nanoassembly of CNTs still plays an important role in fabricating CNT-based devices. Dielectrophoresis (DEP) has been employed to put as-grown CNTs on metal electrodes [23–25]. A number of CNTs can be attracted to the electrodes by controlling the AC voltage and the concentration of the CNT solution. However, it is still difficult to deposit a single CNT by using this method. Another approach for CNT-based device assembly is to fabricate metal electrodes on top of as-deposited CNTs by electron beam lithography (EBL) [26, 27] or shadow masks [28]. The EBL fabrication method provides a good contact condition between CNTs and microelectrodes. However, this method is very inefficient for batch manufacturing due to the low efficiency of the EBL fabrication process. More importantly, the CNTs are randomly distributed on the substrate after EBL, and it is impractical to form a regular CNT array with the desired pattern. Hence, the EBL fabrication method is mostly used for prototyping an individual device.

Nanoassembly of CNT-based devices can be considered as a process to mechanically manipulate CNTs to bridge the microelectrodes. CNT has been manipulated three-dimensionally in a scanning electron microscopy (SEM) [29, 30], but the process needs to operate in a vacuum environment. Atomic force microscopy (AFM) provides a new way for precise nanomanipulation and overcomes the limitations of SEM. AFM was invented by Binnig, Quate and Gerber in 1986 [31] and employs a tiny probe to move over the surface of a substrate. The AFM probe is a tiny tip mounted at the end of a cantilever that bends in response to the force between the tip and the sample at the molecular level. The surface topography is acquired by recording the bending of the cantilever at each sampling point. Preliminary AFM-based nanoassembly has been demonstrated by using an AFM probe as a robotic end effector [32, 33]. Our research group has spent over five years developing an AFM-based nanorobotic system for precision manipulation of nano-objects [34–36].

1.4 SUMMARY

In this book, we will focus on the development of nanomanufacturing, designs, and applications of nanomaterials-based devices. The process starts from the microfluidic-based delivery and separation of nanomaterials [37]. Precise assembly can be achieved by the AFM-based nanorobotic system. It is capable of manipulating a nanomaterial at the desired position efficiently [36]. Since the band gap of

a semiconducting material is an important consideration for many optical applications, such as optical detectors and solar cells, we have developed an electrical breakdown control method to adjust the band structure of a CNT [38]. This process has provided a steady and high-yield on-chip band gap engineering approach in batch electronics fabrication. Therefore, the spectral response of the devices can be adjusted. Finally, thermal annealing process and packaging process have been developed to maintain stability and reliability of nanodevices [39]. Additionally, the development of nanoantennas [40] and photonic crystal cavities [41] will be discussed, which introduce field enhancement for nano-optoelectronic devices. The integration of the above technologies has provided an effective and efficient nanomanufacturing process for fabrication of next generation of nano-optical sensors and electronic devices [42, 43].

The materials contained herein provide senior undergraduate students and graduate students appropriate background knowledge to pursue the research in the area of nano-optoelectronic devices, nanomanipulation and nanoassembly. Furthermore, the book will also allow engineers to find a way to turn nanomaterials into realistic devices. It is our aim to provide a comprehensive book on nanomanufacturing for various nanomaterial-based devices. The university faculties, students, researchers, and engineers will be able to learn the recent advances in the area of nanotechnology, optical sensors, and nanomaterials.

References

- [1] S. Iijima. Helical microtubules of graphitic carbon. *Nature*, 354:56–58, 1991.
- [2] X. Wang, Q. Li, J. Xie, Z. Jin, J. Wang, Y. Li, K. Jiang, and S. Fan. Fabrication of ultralong and electrically uniform single-walled carbon nanotubes on clean substrates. *Nano Lett.*, 9(9):3137–3141, 2009. PMID: 19650638.
- [3] K. W. C. Lai, N. Xi, C. K. M. Fung, H. Chen, and T.-J. Tarn. Engineering the band gap of carbon nanotube for infrared sensors. *Appl. Phys. Lett.*, 95:221107, 2009.
- [4] A. Javey, J. Guo, Q. Wang, M. Lundstrom, and H. Dai. Ballistic carbon nanotube field-effect transistors. *Nature*, 424:654–657, 2003.
- [5] W. Fa, X. Yang, J. Chen, and J. Dong. Optical properties of the semiconductor carbon nanotube intramolecular junctions. *Phys. Lett. A*, 323:122–131, 2004.
- [6] P. Avouris. Carbon nanotube electronics. *Chem. Phys.*, 281:429–445, 2002.
- [7] M. F. Yu. Fundamental mechanical properties of carbon nanotubes: current understanding and the related experimental studies. *J. Eng. Mater. Technol.*, 126(3):271–278, 2004.
- [8] A. Bachtold, P. Hadley, T. Nakanishi, and C. Dekker. Logic circuits with carbon nanotube transistors. *Science*, 294:1317–1320, 2001.
- [9] V. Derycke, R. Martel, J. Appenzeller, and P. Avouris. Carbon nanotube inter- and intramolecular logic gates. *Nano. Lett.*, 1:453–456, 2001.
- [10] I. A. Levitsky and W. B. Euler. Photoconductivity of single-wall carbon nanotubes under CWHIR illumination. *Appl. Phys. Lett.*, 83:1857–1859, 2003.
- [11] A. Fujiwara, Y. Matsuoka, H. Suematsu, N. Ogawa, K. Miyano, H. Kataura, Y. Maniwa, S. Suzuki, and Y. Achiba. Photoconductivity in semiconducting single-walled carbon nanotubes. *Jpn. J. Appl. Phys.*, 40:1229–1231, 2001.
- [12] S. Lu and B. Panchapakesan. Photoconductivity in single wall carbon nanotube sheets. *Nanotechnology*, 17:1843–1850, 2006.

- [13] Z. Chen, J. Appenzeller, Y.-M. Lin, J. Sippel-Oakley, A. G. Rinzler, J. Tang, S. J. Wind, P. M. Solomon, and P. Avouris. An integrated logic circuit assembled on a single carbon nanotube. *Science*, 311:1735, 2006.
- [14] D. Qian, G. J. Wagner, W. K. Liu, M.-F. Yu, and R. S. Ruoff. Mechanics of carbon nanotubes. *Appl. Mech. Rev.*, 55:495–533, 2002.
- [15] S. Lu and B. Panchapakesan. Nanotube micro-optomechanical actuators. *Appl. Phys. Lett.*, 88(25):253107, 2006.
- [16] S. Lu, S. V. Ahir, E. M. Terentjev, and B. Panchapakesan. Alignment dependent mechanical responses of carbon nanotubes to light. *Appl. Phys. Lett.*, 91(10):103106, 2007.
- [17] J. W. G. Wilder, L. C. Venema, A. G. Rinzler, R. E. Smalley, and C. Dekker. Electronic structure of atomically resolved carbon nanotubes. *Nature*, 391:59–62, 1998.
- [18] Y. Li, D. Mann, M. Rolandi, W. Kim, A. Ural, S. Hung, A. Javey, J. Cao, D. Wang, E. Yenilmez, Q. Wang, J. F. Gibbons, Y. Nishi, and H. Dai. Preferential growth of semiconducting single-walled carbon nanotubes by a plasma enhanced cvd method. *Nano Lett.*, 4(2):317–321, 2004.
- [19] S. M. Bachilo, M. S. Strano, C. Kittrell, R. H. Hauge, R. E. Smalley, and R. B. Weisman. Structure-assigned optical spectra of single-walled carbon nanotubes. *Science*, 298(5602):2361–2366, 2002.
- [20] M. J. O’Connell, S. M. Bachilo, C. B. Huffman, V. C. Moore, M. S. Strano, E. H. Haroz, K. L. Rialon, P. J. Boul, W. H. Noon, C. Kittrell, J. Ma, R. H. Hauge, R. B. Weisman, and R. E. Smalley. Band gap fluorescence from individual single-walled carbon nanotubes. *Science*, 297(5581):593–596, 2002.
- [21] P. Qi, O. Vermesh, M. Grecu, A. Javey, Q. Wang, H. Dai, S. Peng, and K. J. Cho. Toward large arrays of multiplex functionalized carbon nanotube sensors for highly sensitive and selective molecular detection. *Nano Lett.*, 3:347–351, 2003.
- [22] A. Nojeh, A. Ural, R. F. Pease, and H. Dai. Electric-field-directed growth of carbon nanotubes in two dimensions. *J. Vac. Sci. Technol. B*, 22:3421–3425, 2004.
- [23] J. Li, Q. Zhang, D. Yang, and J. Tian. Fabrication of carbon nanotube field effect transistors by AC dielectrophoresis method. *Carbon*, 42:2263–2267, 2004.
- [24] S. Taeger, D. Sickert, P. Atanasov, G. Eckstein, and M. Mertig. Self-assembly of carbon nanotube field-effect transistors by AC-dielectrophoresis. *Phys. Stat. Sol. (b)*, 243:3355–3358, 2006.
- [25] P. Makaram, S. Selvarasah, X. Xiong, C.-L. Chen, A. Busnaina, N. Khanduja, and M. R. Dokmeci. Three-dimensional assembly of single-walled carbon nanotube interconnects using dielectrophoresis. *Nanotechnology*, 18:395204, 2007.
- [26] C. Lu, L. An, Q. Fu, J. Liu, H. Zhang, and J. Murduck. Schottky diodes from asymmetric metal-nanotube contacts. *Appl. Phys. Lett.*, 88:133501, 2006.
- [27] Z. Chen, J. Appenzeller, J. Knoch, Y. Lin, and P. Avouris. The role of metal-nanotube contact in the performance of carbon nanotube field-effect transistors. *Nano Lett.*, 5:1497–1502, 2005.
- [28] M. M. Deshmukh, D. C. Ralph, M. Thomas, and J. Silcox. Nanofabrication using a stencil mask. *Appl. Phys. Lett.*, 75:1631–1633, 1999.
- [29] M. Yu, M. J. Dyer, G. D. Skidmore, H. W. Rohrs, X. Lu, K. D. Ausman, J. R. Von Ehr, and R. S. Ruoff. Three-dimensional manipulation of carbon nanotubes under a scanning electron microscope. *Nanotechnology*, 10:244–252, 1999.
- [30] T. Fukuda, F. Arai, and L. Dong. Assembly of nanodevices with carbon nanotubes through nanorobotic manipulations. *Proc. IEEE*, 91:1803–1818, 2003.
- [31] G. Binnig, C. F. Quate, and C. Gerber. Atomic force microscope. *Phys. Rev. Lett.*, 56(9):930–933, 1986.
- [32] T. Hertel, R. Martel, and P. Avouris. Manipulation of individual carbon nanotubes and their interaction with surfaces. *J. Phys. Chem. B*, 102:910–915, 1998.
- [33] H. W. C. Postma, A. Sellmeijer, and C. Dekker. Manipulation and imaging of individual single-walled carbon nanotubes with an atomic force microscope. *Adv. Mater.*, 12:1299–1302, 2000.

- [34] H. Chen, N. Xi, and G. Li. Cad-guided automated nanoassembly using atomic force microscopy-based nonrobotics. *IEEE Trans. Autom. Sci. and Eng.*, 3:208–217, 2006.
- [35] G. Li, N. Xi, and M. Yu. Development of augmented reality system for AFM based nanomanipulation. *IEEE/ASME Trans. Mechatron.*, 9:358–365, 2004.
- [36] G. Li, N. Xi, H. Chen, C. Pomeroy, and M. Prokos. Videolized atomic force microscopy for interactive nanomanipulation and nanoassembly. *IEEE Trans. Nanotechnol.*, 4:605–615, 2005.
- [37] K. W. C. Lai, N. Xi, C. K. M. Fung, J. Zhang, H. Chen, Y. Luo, and U. C. Wejinya. Automated nanomanufacturing system to assemble carbon nanotube based devices. *Int. J. Rob. Res.*, 28(4):523–536, 2009.
- [38] K. W. C. Lai, N. Xi, C. K. M. Fung, H. Chen, and T.-J. Tarn. Engineering the band gap of carbon nanotube for infrared sensors. *Appl. Phys. Lett.*, 95(22):221107, 2009.
- [39] K. W. C. Lai, N. Xi, J. Zhang, G. Li, and H. Chen. Packaging carbon nanotube based infrared detector. In *Proc. 7th IEEE Conf. Nanotechnology IEEE-NANO 2007*, pages 778–781, 2007.
- [40] C. K. M. Fung, N. Xi, B. Shanker, and K. W. C. Lai. Nanoresonant signal boosters for carbon nanotube based infrared detectors. *Nanotechnology*, 20(18):185201, 2009.
- [41] C. K. M. Fung, N. Xi, J. Lou, K. W. C. Lai, and H. Chen. Photonic crystal wave guide for non-cryogenic cooled carbon nanotube based middle wave infrared sensors. In *Proc. SPIE 7834*, page 78340L, 2010.
- [42] H. Chen, N. Xi, K. W. C. Lai, C. K. M. Fung, and R. Yang. Development of infrared detectors using single carbon-nanotube-based field-effect transistors. *IEEE Trans. Nanotechnol.*, 9(5):582–589, 2010.
- [43] J. Zhang, N. Xi, H. Chen, K. Lai, G. Li, and U. C. Wejinya. Design, manufacturing, and testing of single-carbon-nanotube-based infrared sensors. *IEEE Trans. Nanotechnol.*, 8(2):245–251, 2009.

Nanomaterials Processing for Device Manufacturing

2

King Wai Chiu Lai*, Ning Xi*, Carmen Kar Man Fung†, and Hongzhi Chen*

*Department of Electrical and Computer Engineering, Michigan State University, Michigan

†Hong Kong Productivity Council, Hong Kong

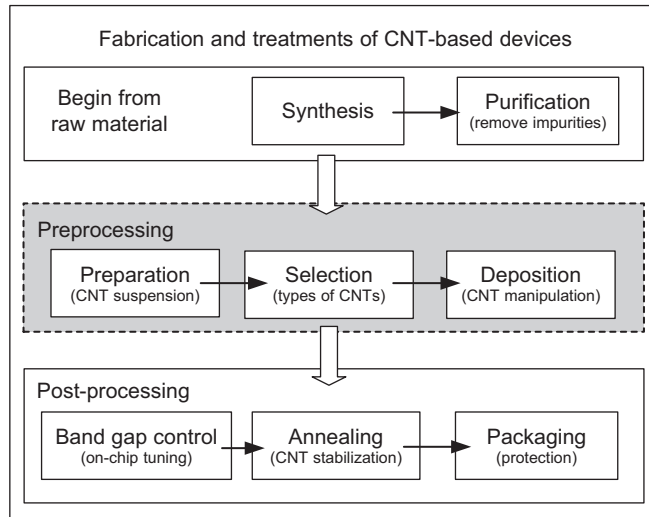
CHAPTER OUTLINE

2.1 Introduction	11
2.2 Characteristics of Carbon Nanotubes	13
2.3 Classification of Carbon Nanotubes using Microfluidics	14
2.3.1 Dielectrophoretic Phenomenon on CNTs	16
2.3.2 Experimental Results: Separation of Semiconducting CNTs	19
2.4 Deposition of CNTs by Microrobotic Workstation	21
2.5 Summary	24
References	25

2.1 INTRODUCTION

As mentioned earlier, carbon nanotubes (CNTs) have been studied as one of the most promising nanomaterials for a wide variety of applications. The optical [1], electrical [2], and mechanical [3] properties of CNTs have been characterized extensively, and the remarkable properties of CNTs such as ballistic transport [4–6] make them a potential candidate for use as high-speed circuit and optical sensors. Also, electronic properties of nanotubes depend on their diameter and chirality. CNTs consist of both metallic and semiconducting types, which can be used for different applications such as in nanotransistors [4, 7, 8], logic devices [9–11], optical sensors [12–14], light-emitting devices [15, 16], chemical sensors [17–19], etc. Most of these CNT-based devices consist of a single nanotube or multiple nanotubes connecting between a pair of metal electrodes. In order to make use of nanotubes for optoelectronic devices such as infrared sensors or solar cells, two major issues have to be considered. First, how to obtain homogeneous electronic properties of CNTs and narrow the electronic distribution of CNTs during the manufacturing process? Second, a single nanotube is highly desirable when making CNT-based nanodevices because it has superb properties that cannot be seen with CNT bundles. Therefore, having a method to control the manufacture of a single CNT and deposit it on a metal electrode is essential.

The general fabrication and treatment of CNTs can be divided into CNT synthesis, purification, selection, deposition, annealing, and packaging, as shown in Fig. 2.1. Various techniques have been

**FIGURE 2.1**

Flow chart of fabrication and treatments of CNT-based devices.

developed to synthesize nanotubes, which includes high pressure carbon monoxide (HiPco) [20, 21], arc discharge [22], chemical vapor deposition (CVD) [23], and laser ablation [24]. The details of CNT synthesis and purification have been discussed in many other papers [25–27]. Our focus here is different and we aim at establishing a novel method for selection and deposition of a single CNT with the desired electronic properties.

In this chapter, we will focus on the discussion about the possibilities to use a microfluidic system to narrow the electronic properties of CNTs. Electrokinetic force is employed to separate heterogeneous nanotubes. Several major issues have been considered for developing such a system. For example, the yield in obtaining homogeneous CNTs is very important because it affects the success rate to fabricate nano-optoelectronic devices with consistent properties and repeatable response. The separation method is designed to be compatible with different CNT synthesis methods. The development of a novel separation system to classify the electronic types of CNTs will be described, which involves the fabrication of a microfluidic chamber and preparation of CNT suspensions. The separation result for various CNTs will also be presented. We have experimentally shown that the yield in forming semiconducting CNTs could be increased by using the system, which provides an important reference to manufacture uniform CNT-based devices.

Moreover, electrokinetic force can be employed to deposit a single CNT or multiple CNTs across two prefabricated electrodes. A CNT deposition workstation was created by integrating electrokinetic force with a microrobotic manipulation system. The CNT deposition workstation was also integrated with other components such as computer-controllable micromanipulators and a microactive nozzle for mass-producing consistent nanodevices. Detailed experimental studies of the deposition processes have been performed, and preliminary results showed that CNTs could be manipulated to multiple pairs of microelectrodes repeatedly. Consistent CNT formations and I-V characteristics of the fabricated

devices were obtained. Therefore, CNT-based nano-optoelectronic devices with specific and consistent electronic properties can be manufactured effectively by using the microfluidic system and the deposition system.

2.2 CHARACTERISTICS OF CARBON NANOTUBES

In order to make use of carbon nanotubes for nanodevices effectively, some fundamental concepts of CNTs must be understood and these will now be introduced. The diameter of a single CNT is about few nanometers, and it can be as long as 18 cm [28]. CNT can be classified into two categories: single-walled carbon nanotube (SWCNT) and multiwalled carbon nanotube (MWCNT). A SWCNT can be considered as a sheet of graphene rolling into a cylinder along a lattice vector (m, n) in the graphene plane. The vector (m, n) determines the diameter and the particular roll orientation of a CNT, which is called a chiral vector (Fig. 2.2). The angle between the roll orientation and the axis of the nanotube is named the chiral angle. The chirality (or chiral vector) is very important because it determines the electronic properties of a CNT. CNTs can be classified into semiconducting and metallic depending on their chirality. Based on the specific roll orientation, there are three types of nanotube: armchair, zigzag, and chiral [29]. Armchair CNTs are formed when $m = n$ and the CNTs are metallic. The chiral angle of an armchair CNT is 30 degree. Zigzag CNTs are formed when either m or n equals zero, where the chiral angle is 0. All other lattice vectors result in chiral CNTs. Both zigzag and chiral CNTs are semiconducting. Furthermore, it is known that the vector (m, n) is related to the diameter of a SWCNT, which is determined with the equation [30]:

$$D_{\text{nanotube}} = \frac{L_{\text{chiral}}}{\pi} \quad (2.1)$$

where L_{chiral} is the length of the chiral vector (m, n) and given by

$$L_{\text{chiral}} = a\sqrt{3(m^2 + mn + n^2)} \quad (2.2)$$

where a is the length between consecutive carbon atoms (1.42 Å).

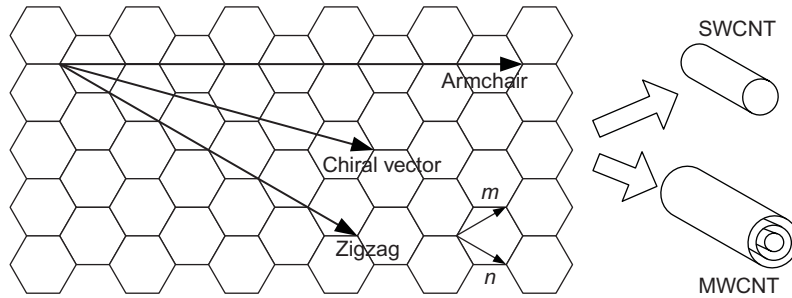


FIGURE 2.2

Illustration of a graphene indicating the chiral vector of a nanotube.

Both metallic and semiconducting CNTs have electronic properties superior to traditional materials. Semiconducting CNT has a higher mobility than many existing semiconductors, and it can be considered as the active material for many electronic devices. Metallic CNT has extremely high conductivity [31] and can be used as interconnection between nanodevices. The band gap is one of the important properties for quantum optoelectronic devices, and the energy of the band gap of a CNT can be calculated from the following equation [30]:

$$Energy_{\text{bandgap}} = \frac{4}{3} \frac{\hbar v_f}{D_{\text{nanotube}}} \quad (2.3)$$

where v_f is the fermi velocity, and \hbar is the Dirac constant. Based on the above equation, the band gap is inversely proportional to the diameter of a CNT.

A MWCNT consists of multiple concentrically rolled layers of graphene sheet, so the diameter of a MWCNT is larger than that of a SWCNT. As a result, the band gap of SWCNTs is usually larger than that of MWCNT. Unlike the SWCNT, the MWCNT is rolled in different orientations and so the electronic properties are more complex and difficult to predict.

2.3 CLASSIFICATION OF CARBON NANOTUBES USING MICROFLUIDICS

Since CNTs are easily bundled together after their synthesis, there is a large variation in their electronic properties. Many approaches to grow pure CNTs have been developed to overcome this problem. Li and his co-workers tried to grow high concentrations of semiconducting CNTs by the plasma-enhanced chemical vapor deposition method [27], but further improvement is still needed to control the band gap of CNTs. A narrow distribution of CNTs has been grown at high pressure and high temperature using the high-pressure carbon monoxide (HiPco) technique [20, 21]. However, the CNTs produced by this process are small in diameter (<1.5 nm), resulting in the nanotubes having a large energy band gap. Therefore, specialized processing such as separation and filtering, of the nanotube mixture is necessary. Since the diameter of a single CNT is in the range of nanometers, it is extremely difficult to perform large-scale separation using traditional robotic manipulation. Instead, microfluidics is a promising technique to manipulate these nanomaterials because most can be easily dissolved into a liquid medium. Basically, various methods have been developed to separate different electronic types of CNTs. Homogeneous CNTs can be classified by using surfactants or encapsulating agents [32], but it is hard to integrate with the microfluidic system. Dielectrophoresis (DEP) is another approach, and it has been used extensively for separating biological cells. Recently, dielectrophoresis has been demonstrated to enrich metallic CNT thin film [33, 34]. We foresee that the latter method might be further integratable with microfluidic systems for CNT classification. Therefore, we will further discuss studies in this area.

Typical microfluidic devices consist of microchambers and microchannels. More complicated devices, such as micromixers and microreactors, can be integrated together to form a state-of-the-art lab-on-a-chip device. Various fabrication processes and materials have been developed to fabricate these devices. For example, polymethylmethacrylate (PMMA) is used as a common material for microfluidic systems because of its low fabrication cost, biocompatibility, optical transparency and being electrically and thermally insulating. The fabrication process of a typical microchannel is shown in Fig. 2.3. PMMA substrate can be patterned with microchannels by the hot embossing technique. This technique provides a low cost solution to replicate microchannel structures from a fabricated

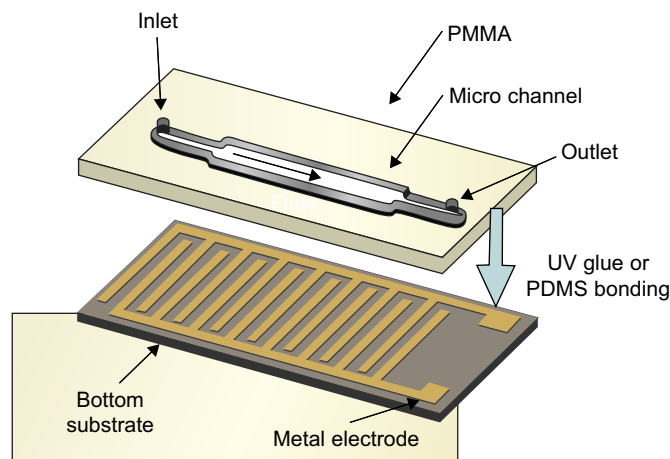
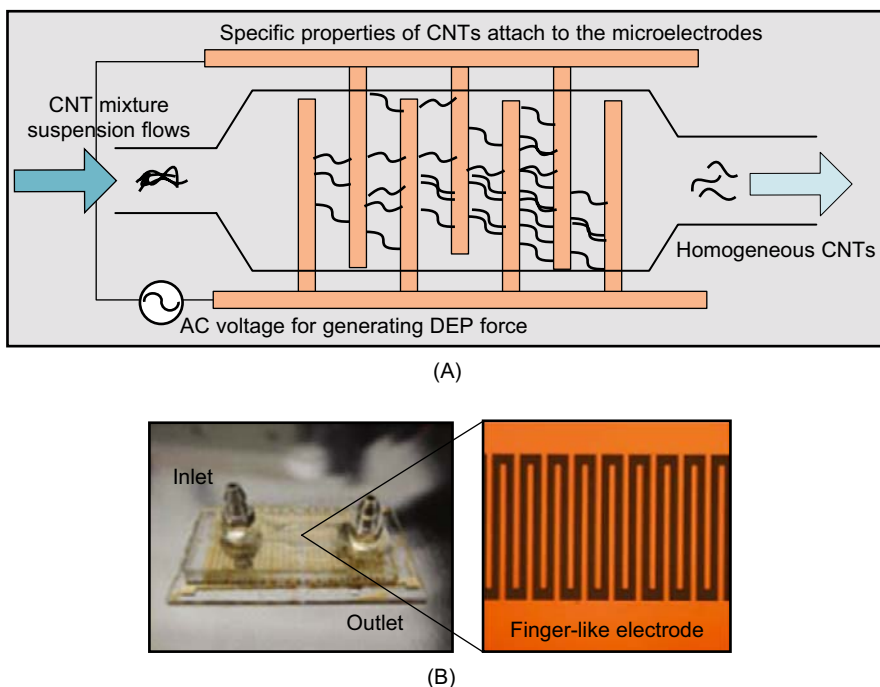
**FIGURE 2.3**

Illustration of the fabrication process of a PMMA-based microfluidic device.

metal mold. The PMMA substrate can then be bonded with another substrate to form an enclosed channel or chamber. The interior of the channels can also be coated with a polymer layer such as Parylene. Parylene is very popular in lab-on-a-chip because it is incompatible and insoluble with most organic solvents. It can also be used as a barrier for flexible electronic applications [35].

Sorting of nanotubes can be achieved by proper design of the microfluidic device with dielectrophoresis. Dielectrophoresis generates attractive forces or repulsive forces on micro- and nanomaterials under specific conditions. More information will be given in the next section. The device consists of chamber, microchannels, and microelectrodes as shown in Fig. 2.4B. An array of finger-like metal microelectrodes is fabricated inside the chamber. These microelectrodes can be fabricated by a standard photolithography process. Smaller features can also be patterned by e-beam lithography or focused ion beam etching. Performance of the sorting process is confined by the dimension of the microchamber and the design of the finger-like microelectrodes. A microelectrode structure with higher density induces stronger dielectrophoretic force such that more CNTs can be attracted to the microelectrodes. The spacing between these microelectrodes should be small enough to match the length scale of CNTs as shown in Fig. 2.4A. When CNT suspension flows into the chamber, a desired AC voltage can be applied to the finger-like microelectrodes. Since different properties of nanotubes are affected differently by the DEP force, CNTs of specific properties are attracted to the microelectrodes and retained in the chamber. Then, unaffected CNTs remain in the suspension and flow out from the outlet of the chamber. As a result, CNTs with desired electronic properties can be separated from the mixture of nanotube powder. The applications of the microfluidic devices are not limited to CNTs. They can also be used for different nanomaterials and biological samples.

We fabricated a simple microchamber for CNT classification. By using the hot embossing technique, the PMMA substrate was patterned with a microchannel ($5\text{ mm L} \times 1\text{ mm W} \times 500\text{ }\mu\text{m H}$) and a microchamber ($1\text{ cm L} \times 5\text{ mm W} \times 500\text{ }\mu\text{m H}$) by replicating from a fabricated metal mold. In order to protect the PMMA substrate from the CNTs-alcohol suspension, a Parylene C thin film layer was coated on the substrate as an insoluble chemical resistive layer. Alternatively, quartz was used as the

**FIGURE 2.4**

(A) Illustration of a microfluidic device to sort nanotubes. CNTs of desired properties are attracted to the microelectrodes. (B) Images of a fabricated device with an array of finger-like microelectrodes.

bottom substrate and arrays of the gold microelectrodes were fabricated on the substrate by using a standard photolithography process. The gap distance between the finger-like microelectrodes was 5–10 μm as shown in Fig. 2.4B. Finally, PMMA and quartz substrate were bonded together by UV glue to form a closed chamber. The fittings were connected at the ends of the channel to form an inlet and an outlet for the microseparation chamber. As a result, the CNT suspension can pass through the microchamber.

2.3.1 Dielectrophoretic Phenomenon on CNTs

Due to the low efficiency of using conventional hydrodynamic force for manipulation in a microfluidic system, the electric field-assisted method is commonly used in micro- or nanofluidic manipulation. Micro- or nanofluidic handling using electrokinetic (EK) forces, has been developed in the past decades. EK forces, such as dielectrophoretic (DEP) force and electroosmotic (EO) forces, have been widely employed in many microfluidic devices. Proper understanding of these EK forces enable us to design a microfluidic system to move micro- and nanomolecules effectively. For example, DEP force was demonstrated to manipulate bundled CNTs [36, 37].

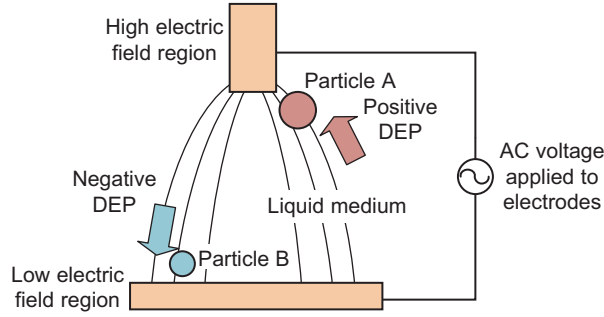
**FIGURE 2.5**

Illustration of dielectrophoretic phenomena.

DEP manipulation induces movement of micro- or nanoparticles under nonuniform electric fields, as shown in Fig. 2.5. An effective dipole moment is present in the particle under nonuniform electric fields and results in the movement of the particle [38, 39]. The particle is polarized when it is subjected to an electric field. The movement of the particle depends on its polarizability with respect to the surrounding medium. To study the phenomenon of DEP manipulation on a CNT, the CNT is considered as an object and dispersed in a liquid medium. When the CNT is more polarizable than the medium, a net dipole is induced parallel to the electric field in the CNT, and therefore the CNT is attracted to the high electric field region. On the contrary, an opposite net dipole is induced when the CNT is less polarizable than the medium, and the CNT is repelled by the high electric field region.

Mathematically, the direction of DEP force on the object is given by the Clausius–Mossotti factor (CM factor, K). When $\text{Re}[K] > 0$, the DEP force is positive, and therefore the object is moved toward the microelectrodes. When $\text{Re}[K] < 0$, the DEP force is negative, and the object is repelled away from the microelectrode. The CM factor is defined as a complex factor, describing a relaxation in the effective permittivity of the particle with a relaxation time described by [39, 40]:

$$K(\varepsilon_p^*, \varepsilon_m^*) = \frac{\varepsilon_p^* - \varepsilon_m^*}{\varepsilon_p^* + 2\varepsilon_m^*} \quad (2.4)$$

Complex permittivities of the object (ε_p^*) and medium (ε_m^*) are defined and given by [39, 40]:

$$\varepsilon_p^* = \varepsilon_p - i \frac{\sigma_p}{\omega} \quad (2.5)$$

$$\varepsilon_m^* = \varepsilon_m - i \frac{\sigma_m}{\omega} \quad (2.6)$$

where ε_p and ε_m are the real permittivities of the object and the medium, respectively; σ_p and σ_m are the conductivities of the object and the medium, respectively; ω is the angular frequency of the applied electric field; hence, the CM factor is frequency dependent.

The time-averaged DEP force acting on the particle is given by [39, 40]:

$$F_{\text{DEP}} = \frac{1}{2} V \varepsilon_m \text{Re}(K) \nabla |E|^2 \quad (2.7)$$

where V is the volume of the particle and $\nabla |E|^2$ is the root mean square of the applied electric field. A theoretical analysis of the DEP manipulation on a CNT was performed. CM factors were calculated for a metallic SWCNT (m-SWCNT) and a semiconducting MWCNT (s-SWCNT). In the analysis, semiconducting and metallic CNT mixtures are dispersed in the alcohol medium. Different parameters could be obtained from various literary articles, for example the following:

$\varepsilon_{s-SWCNT}$ is the permittivity of a s-SWCNT: $5\varepsilon_0$ [33]

$\varepsilon_{m-SWCNT}$ is the permittivity of a m-SWCNT: $10^4\varepsilon_0$ [36]

ε_m is the permittivity of alcohol: $20\varepsilon_0$

ε_0 is the permittivity of free space: 8.854188×10^{-12}

$\sigma_{s-SWCNT}$ is the conductivity of a s-SWCNT: 10^5 S/m [36]

$\sigma_{m-SWCNT}$ is the conductivity of a m-SWCNT: 10^8 S/m [36]

σ_m is the conductivity of alcohol: $0.13 \mu\text{S/m}$

Based on these parameters and Eq. (2.4), plots of $\text{Re}[K]$ for different CNTs are obtained (shown in Fig. 2.6). The result indicated that s-SWCNTs undergo a positive DEP force at low frequencies ($<1 \text{ MHz}$) while the DEP force is negative when the applied frequency is larger than 10 MHz . However, m-SWCNTs always undergo the positive DEP force at the applied frequency from 10 to 10^9 Hz . The result also matched the experimental result from [34], which showed that the positive DEP effect on SWCNTs reduced as the frequency of applied electric field increased. In addition, the theoretical result provides a better understanding of the DEP manipulation on different types of CNTs. DEP force can be used to separate and identify different electronic types of CNTs (metallic and semiconducting). Therefore, it is possible to make use of the dielectrophoretic phenomenon to

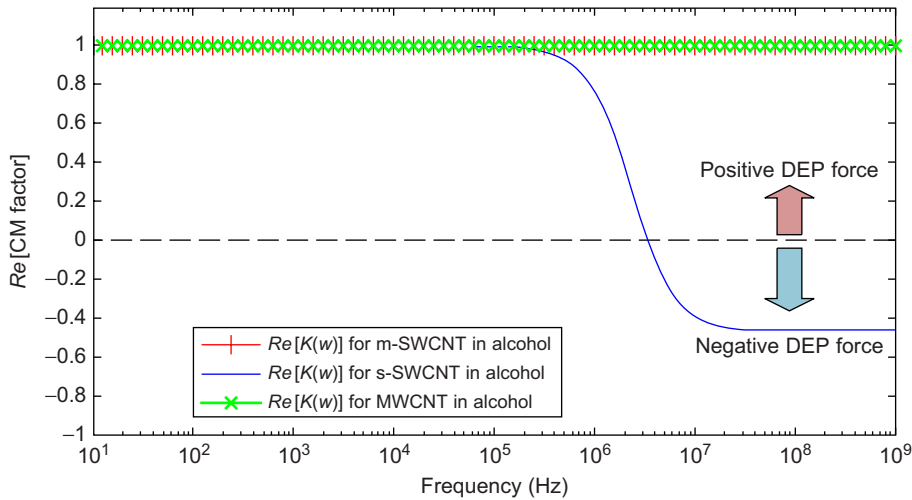


FIGURE 2.6

Plots of the CM factor with different properties of nanotubes. Positive and negative DEP forces induced at different frequencies.

classify CNTs in microfluidic devices by optimizing the design of the microchannels, microchambers, microelectrodes, etc.

2.3.2 Experimental Results: Separation of Semiconducting CNTs

In order to validate the separation performance of different CNTs by use of the microseparation chamber, experiments for both raw CNT suspension (before passing through the microseparation chamber) and filtered CNT suspension were conducted. SWCNT powder (BU-203, Bucky USA, Nanotex Corp.) was dispersed in an alcohol liquid medium, and the CNT suspension was put in the ultrasonicator for 15 minutes. A small amount of the suspension was extracted and diluted into alcohol again. The length of the SWCNT is 0.5–4 μm . The process is shown in Fig. 2.7A, and the concentration of the final raw SWCNT was about 1.1 $\mu\text{g/mL}$. Afterwards, the separation process was performed on the raw SWCNT suspension as illustrated in Fig. 2.7B. The raw SWCNT suspension was pumped to the DEP chamber through a micropump. The flow rate was about 0.03 L/min. A high frequency AC voltage (1.5 Vpp, 40 MHz) was applied to the microelectrodes in the separation chamber, and a positive DEP force was induced on metallic SWCNTs in the suspension, whereas a negative DEP force was induced on semiconducting SWCNTs. Since the metallic SWCNTs were attracted to the microelectrodes and stayed in the microseparation chamber, it is predicted that only semiconducting SWCNTs remained in the filtered SWCNT suspension. The filtered SWCNT suspension was then obtained at the outlet of the chamber for the later CNT deposition process. After preparing the raw and filtered SWCNT

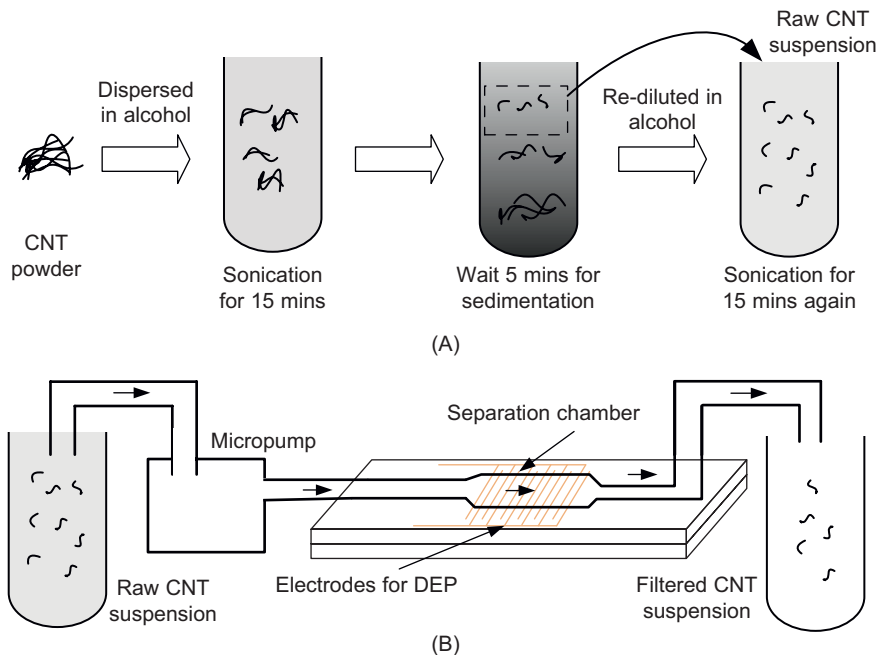


FIGURE 2.7

(A) Illustration of the preparation of the raw CNT suspension. (B) Illustration of the CNT separation process.

suspension, the deposition process was performed by using our CNT deposition workstation, which will be introduced in the next section. In the experiment, the raw SWCNT suspension and the filtered SWCNT suspension were deposited on the microchip 20 times. The electronic properties of CNTs in both suspensions were then studied by measuring the corresponding current-voltage (I-V) characteristics. Typical I-V curves of a metallic CNT and a semiconducting CNT are shown in Fig. 2.8, and the curves clearly indicate that different CNTs exhibited different electronic behaviors.

The yields of semiconducting CNTs from the raw CNT suspension and filtered CNT suspension were also compared statistically. Based on the data, the yield of deposited semiconducting SWCNTs (from the raw SWCNT suspension) was about 30% as shown in Fig. 2.9A; the yield of deposited semiconducting SWCNTs (from the filtered SWCNT suspension) was about 65% as shown in Fig. 2.9B. Similarly, we also tested the separation process on MWCNTs because it is also important to find semiconducting CNTs even if the MWCNTs only have very small band gap. Based on this observation, we obtained the yield of deposited MWCNTs with semiconducting properties. This changed from 35% to 60% after the separation process, as shown in Figs 2.9C and 2.9D. The result indicated that it is also possible to separate MWCNTs with different electronic properties by using the microseparation chamber.

The yield associated with forming semiconducting CNTs is very important because it affects the success rate for fabricating nanodevices. The results indicated that there was significant improvement in forming semiconducting CNTs on the microelectrodes by using our microfluidic device. The yield for forming semiconducting CNTs changed from 30% (before the filtering process) to 65% (after the filtering process). The yield should be improved by optimizing the concentration of CNT suspension, the strength of the DEP force, the flow rate of the suspension in the microfluidic chamber, the structure of the channel, and the microelectrodes of the chamber.

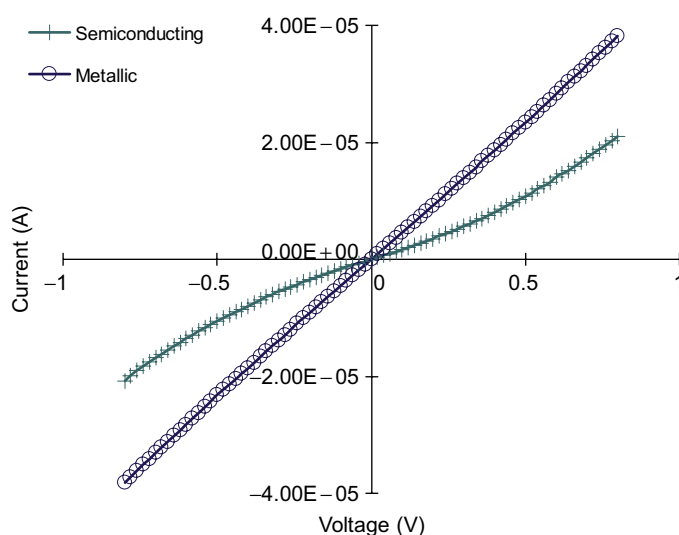
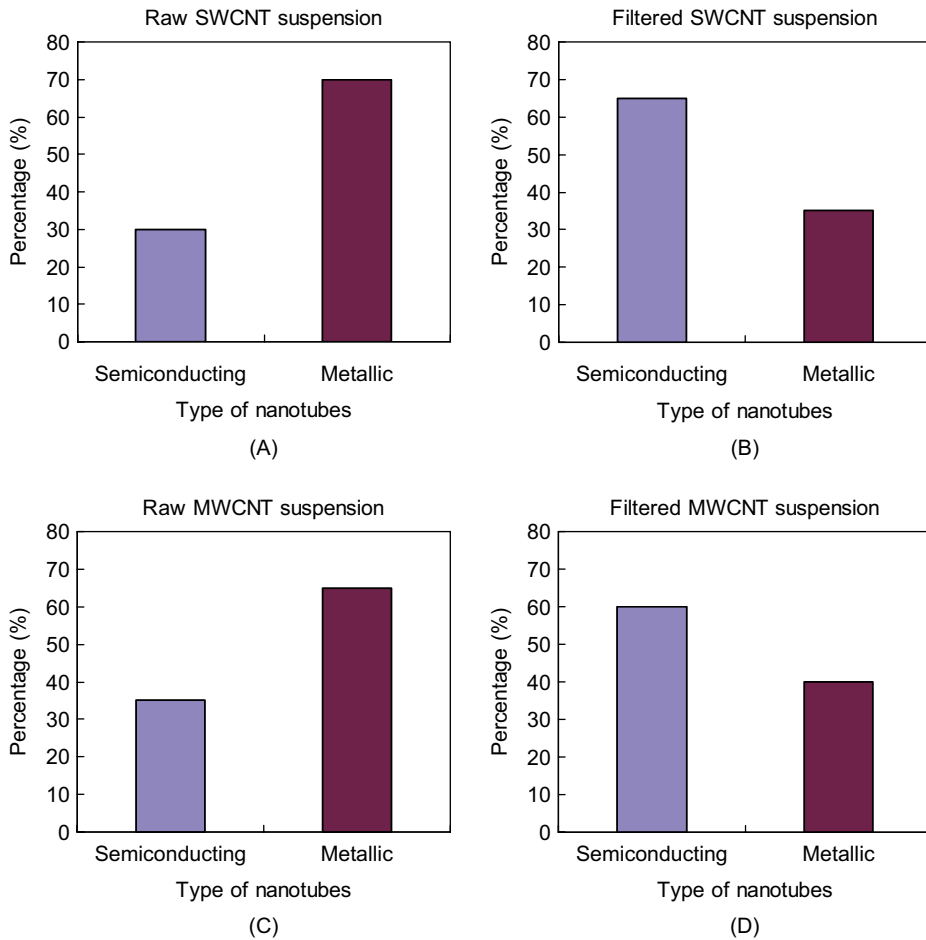


FIGURE 2.8

Typical I-V curves for a metallic CNT and a semiconducting CNT.

**FIGURE 2.9**

Histograms of CNTs found from four different suspensions: (A) raw SWCNT suspension; (B) filtered SWCNT suspension; (C) raw MWCNT suspension; and (D) filtered MWCNT suspension.

2.4 DEPOSITION OF CNTs BY MICROROBOTIC WORKSTATION

Now, we should consider how to deposit a single nanotube onto a pair of metal electrodes. With the help of a micro probe station, a CNT deposition workstation was designed as shown in Fig. 2.10. Several essential components were employed, which includes a microactive nozzle, the microseparation chamber, a DC microdiaphragm pump and three micromanipulators. By integrating these components into the deposition workstation, a specific type of CNT can be deposited onto the desired position of the microelectrodes precisely and automatically. The development of this system benefits the assembling and manufacturing of CNT-based devices.

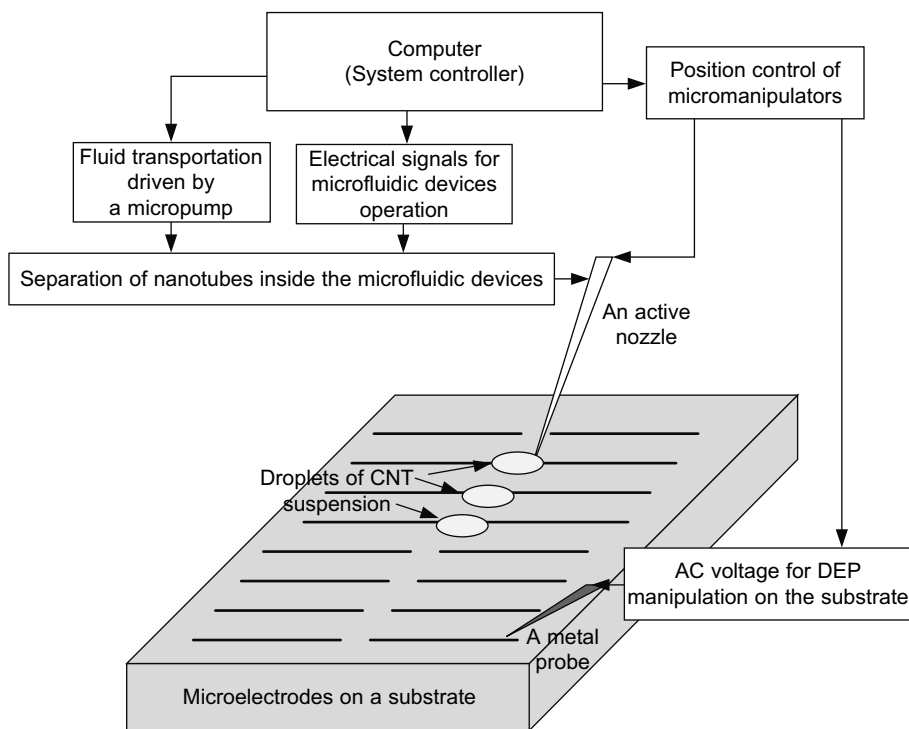
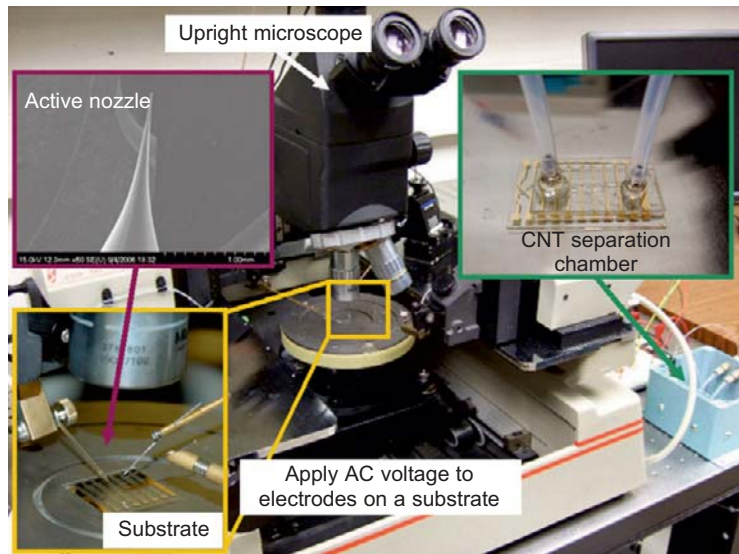
**FIGURE 2.10**

Illustration of the CNT deposition workstation.

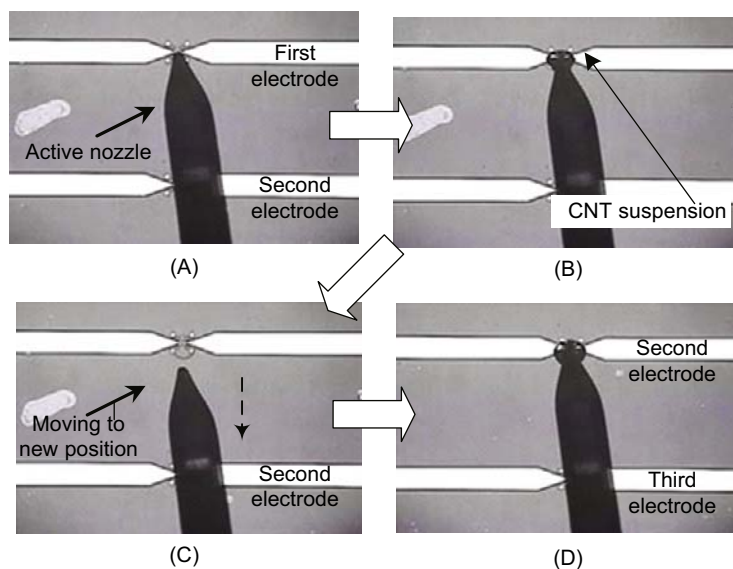
First, CNT suspension is prepared and pumped to the microseparation chamber through a DC microdiaphragm pump (NF10, KNF Neuberger, Inc.). After the separation process, the CNT suspension from the microseparation chamber is delivered to an active nozzle for CNT deposition. The system needs to control the droplet size because the volume of the droplet is critical because excessive CNT suspension causes the formation of multiple CNTs easily. In order to deposit a small droplet (about $400\text{ }\mu\text{m}$) of CNT suspension on the metal electrodes, a micron-sized active nozzle is needed, which can be made by mechanical pullers or chemical etching of glass capillary. Also, the active nozzle can move to the desired position of the microelectrodes by mounting the active nozzle on one of the computer-controllable micromanipulators (CAP945, Signatone Corp.). In order to generate the DEP force to attract nanotubes to microelectrodes on the substrate, an electric field is applied to the microelectrodes during the deposition process. This can be done by moving another pair of micromanipulators to apply AC voltage to the desired microelectrode location. The micromanipulators, DC microdiaphragm pump, and electrical circuit are controlled simultaneously by a computer during the entire deposition process. By controlling the position of the micromanipulators, the magnitude and frequency of the applied AC voltage, and the flow rate of the micropump, the CNT suspension can be handled automatically and deposited at the desired position.

**FIGURE 2.11**

Experimental setup of the CNT deposition workstation.

We experimentally demonstrated the possibility of the deposition process of CNTs. The experimental setup of the system is shown in Fig. 2.11. Before the deposition experiment, the suspension was dispersed in alcohol, as discussed previously. The concentration of the CNT suspension was about $1.1 \mu\text{g/mL}$. After preparing the CNT suspension, the fabricated microchip was put on the stage of the CNT deposition workstation and aligned with respect to the micromanipulator. During the deposition process, an AC voltage (1.5 Vpp, 1 kHz) was applied to microelectrodes on the microchip, and the CNT suspension was transferred to the microelectrodes by the active nozzle.

CNT deposition on multiple pairs of microelectrodes was implemented by controlling the movement of the micromanipulator, which was connected with the active nozzle. Since the position of each pair of the microelectrodes was known from the design CAD file, distances (along x and y axis) between each pair of the microelectrodes were then calculated and recorded in the deposition system. At the start, the active nozzle was aligned to the first pair of the microelectrodes as shown in Fig. 2.12A. The position of the active nozzle tip was 2 mm above the microchip. When the deposition process started, the active nozzle moved down 2 mm and a droplet of CNT suspension was deposited on the first pair of microelectrodes as shown in Fig. 2.12B. Afterwards, the active nozzle moved up 2 mm and traveled to the next pair of microelectrodes. The micromanipulator moved down again to deposit the CNT suspension on the second pair of microelectrodes as shown in Fig. 2.12D. This process repeated continuously until CNT suspension was deposited on each pair of microelectrodes on the microchip. By activating the AC voltage simultaneously, a CNT was attracted and connected between each pair of microelectrodes. The activation time was short (~ 2 s) to avoid the formation of bundled CNTs on the microelectrodes. In order to verify the linkage of the CNT between the microelectrodes, I-V characteristics and AFM images of multiple CNT-based devices were also obtained. Typical I-V curves

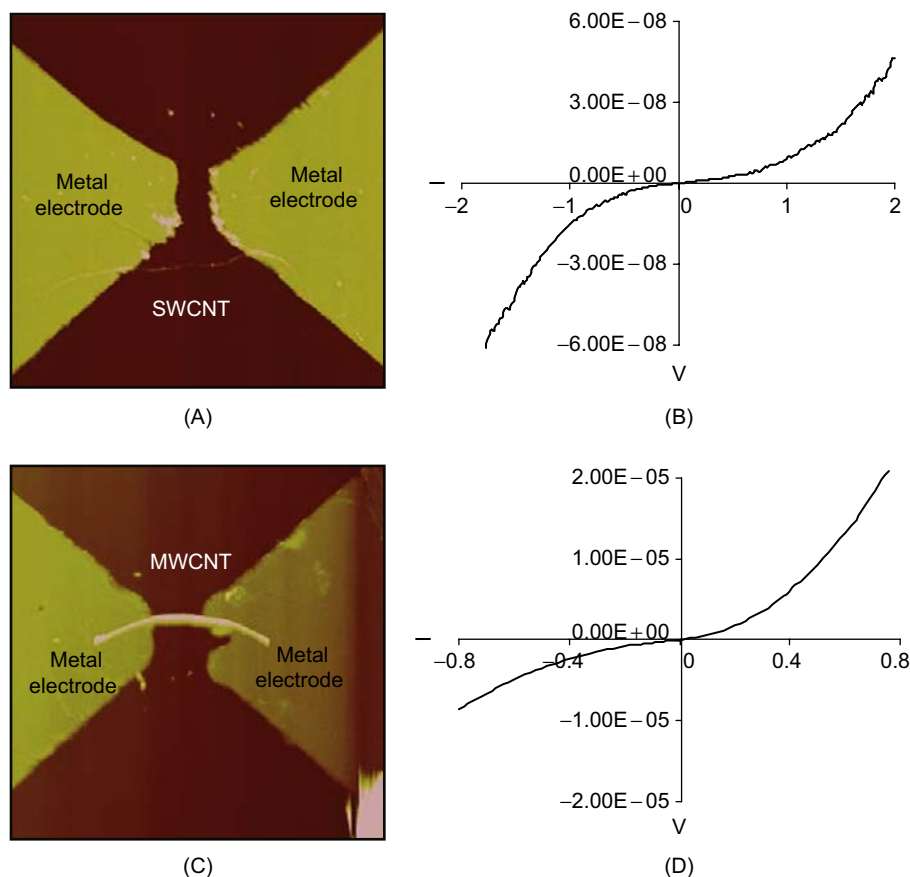
**FIGURE 2.12**

CNT deposition process observed under the optical microscope. (A) The active nozzle tip aligned to the initial electrodes, (B) CNT suspension deposited, (C) nozzle moving to following electrodes, (D) CNT suspension deposited on the second electrode.

and AFM image of SWCNTs and MWCNTs are shown in Fig. 2.13, and this indicates that repeatable CNT formations can be obtained in different pairs of microelectrodes by using the deposition system.

2.5 SUMMARY

CNTs are known to be a very unique material for various kinds of practical nanodevices. Due to large variations in electronic properties of CNTs and their extremely small size, a systemic approach for large-scale production of CNT-based nanodevices with consistent properties is still lacking. Manipulation and classification of CNTs is challenging and is not easily implemented by using the traditional robotic system. In this chapter, a new approach to classify and deposit nanotubes has been given that provides an effective and reliable means to manufacture CNT-based devices. Homogeneous nanotubes can be precisely selected by using a microfluidic system and applying electrokinetic force to grade the nanotubes based on their electronic properties. Results indicated that directions of dielectrophoretic forces on different types of CNTs can be controlled by varying the frequency of the applied electric field. Repeatable and consistent experimental results of multiple CNT-based devices have been obtained by using the separation and deposition processes. Hence, the system provides a batch manipulation of CNTs for device manufacturing. As a result,

**FIGURE 2.13**

(A) AFM image and (B) I-V curve of an individual SWCNT deposited on the microelectrodes. (C) AFM image and (d) I-V curve of an individual MWCNT deposited on the microelectrodes.

this enhances the manufacturing and assembly of CNT-based nanodevices, which is important for the development of future nano-optoelectronic sensors and devices. A more comprehensive analysis of the dielectrophoretic effect on CNTs will be given in [Chapter 3](#).

References

- [1] W. Fa, X. Yang, J. Chen, and J. Dong. Optical properties of the semiconductor carbon nanotube intramolecular junctions. *Phys. Lett. A*, 323:122–131, 2004.
- [2] P. Avouris. Carbon nanotube electronics. *Chem. Phys.*, 281:429–445, 2002.

- [3] M. F. Yu. Fundamental mechanical properties of carbon nanotubes: current understanding and the related experimental studies. *J. Eng. Mater. Technol.*, 126(3):271–278, 2004.
- [4] A. Javey, J. Guo, Q. Wang, M. Lundstrom, and H. Dai. Ballistic carbon nanotube field-effect transistors. *Nature*, 424:654–657, 2003.
- [5] P. Avouris, J. Appenzeller, R. Martel, and S. J. Wind. Carbon nanotube electronics. *Proc. IEEE*, 91:1772–1784, 2003.
- [6] A. Rahman, J. Guo, S. Datta, and M. S. Lundstrom. Theory of ballistic nanotransistors. *IEEE Trans. Electron Devices*, 50:1853–1864, 2003.
- [7] A. Javey, J. Guo, D. B. Farmer, Q. Wang, D. Wang, R. G. Gordon, M. Lundstrom, and H. Dai. Carbon nanotube field-effect transistors with integrated ohmic contacts and high-k gate dielectrics. *Nano Lett.*, 4(3):447–450, 2004.
- [8] H. J. Dai, A. Javey, E. Pop, D. Mann, and Y. R. Lu. Electrical transport properties and field effect transistors of carbon nanotubes. *Nano*, 1:1–13, 2006.
- [9] A. Javey, Q. Wang, A. Ural, Y. Li, and H. Dai. Carbon nanotube transistor arrays for multi-stage complementary logic and ring oscillators. *Nano Lett.*, 2:929–932, 2002.
- [10] A. Bachtold, P. Hadley, T. Nakanishi, and C. Dekker. Logic circuits with carbon nanotube transistors. *Science*, 294:1317–1320, 2001.
- [11] A. Bachtold, P. Hadley, T. Nakanishi, and C. Dekker. Logic circuits with carbon nanotube transistors. *Science*, 294:1317–1320, 2001.
- [12] I. A. Levitsky and W. B. Euler. Photoconductivity of single-wall carbon nanotubes under continuous-wave near-infrared illumination. *Appl. Phys. Lett.*, 83:1857–1859, 2003.
- [13] H. Chen, N. Xi, K. W. C. Lai, C. K. M. Fung, and R. Yang. Development of infrared detectors using single carbon-nanotube-based field-effect transistors. *IEEE Trans. Nanotechnol.*, 9:582–589, 2010.
- [14] L. Liu and Y. Zhang. Multi-wall carbon nanotube as a new infrared detected material. *Sens. Actuators A*, 116:394–397, 2004.
- [15] D. Liu, M. Fina, J. Guo, X. Chen, G. Liu, S. G. Johnson, and S. S. Mao. Organic light-emitting diodes with carbon nanotube cathode-organic interface layer. *Appl. Phys. Lett.*, 94:013110, 2009.
- [16] J. A. Misewich, R. Martel, P. Avouris, J. C. Sang, S. Heinze, and J. Tersoff. Electrically induced optical emission from a carbon nanotube fet. *Science*, 300:783–786, 2003.
- [17] A. Salehi-Khojin, C. R. Field, J. Yeom, and R. I. Masel. Sensitivity of nanotube chemical sensors at the onset of Poole–Frenkel conduction. *Appl. Phys. Lett.*, 96:163110, 2010.
- [18] L. Valentini, I. Armentano, J. M. Kenny, C. Cantanlini, L. Lozzi, and S. Santucci. Sensors for sub-ppm no₂ gas detection based on carbon nanotube thin films. *Appl. Phys. Lett.*, 82:4623–4625, 2003.
- [19] J. Kong, N. R. Franklin, C. Zhou, M. G. Chapline, S. Peng, K. Cho, and H. Dai. Nanotube molecular wires as chemical sensors. *Science*, 287:622–625, 2000.
- [20] S. M. Bachilo, M. S. Strano, C. Kittrell, R. H. Hauge, R. E. Smalley, and R. B. Weisman. Structure-assigned optical spectra of single-walled carbon nanotubes. *Science*, 298(5602):2361–2366, 2002.
- [21] M. J. O’Connell, S. M. Bachilo, C. B. Huffman, V. C. Moore, M. S. Strano, E. H. Haroz, K. L. Rialon, P. J. Boul, W. H. Noon, C. Kittrell, J. Ma, R. H. Hauge, R. B. Weisman, and R. E. Smalley. Band gap fluorescence from individual single-walled carbon nanotubes. *Science*, 297(5581):593–596, 2002.
- [22] T. W. Ebbesen and P. M. Ajayan. Large-scale synthesis of carbon nanotubes. *Nature*, 358:220–222, 1992.
- [23] M. Jose-Yacamán, M. Miki-Yoshida, L. Rendon, and J. G. Santiesteban. Catalytic growth of carbon microtubules with fullerene structure. *Appl. Phys. Lett.*, 62:657, 1993.
- [24] T. Guo, P. Nikolaev, A. Thess, D. T. Colbert, and R. E. Smalley. Catalytic growth of single-walled nanotubes by laser vaporization. *Chem. Phys. Lett.*, 243:49–54, 1995.
- [25] G. Cao, editor. *Nanostructures and Nanomaterials: Synthesis, Properties and Applications*. World Scientific, Singapore, 2004.

- [26] Z. L. Wang, editor. *Metal and Semiconductor Nanowires*. Springer, UK, 2005.
- [27] Y. Li, D. Mann, M. Rolandi, W. Kim, A. Ural, S. Hung, A. Javey, J. Cao, D. Wang, E. Yenilmez, Q. Wang, J. F. Gibbons, Y. Nishi, and H. Dai. Preferential growth of semiconducting single-walled carbon nanotubes by a plasma enhanced CVD method. *Nano Lett.*, 4(2):317–321, 2004.
- [28] X. Wang, Q. Li, J. Xie, Z. Jin, J. Wang, Y. Li, K. Jiang, and S. Fan. Fabrication of ultralong and electrically uniform single-walled carbon nanotubes on clean substrates. *Nano Lett.*, 9(9):3137–3141, 2009. PMID: 19650638.
- [29] H. Dai. Carbon nanotubes: synthesis, integration, and properties. *Acc. Chem. Res.*, 35:1035–1044, 2002.
- [30] M. Dresselhaus, G. Dresselhaus, and Phaedon Avouris, editors. *Carbon Nanotubes: Synthesis, Structure, Properties and Application*. Springer, UK, 2001.
- [31] P. L. McEuen, M. S. Fuhrer, and H. Park. Single-walled carbon nanotube electronics. *IEEE Trans. Nanotechnol.*, 1:78–85, 2002.
- [32] M. S. Arnold, A. A. Green, J. F. Hulvat, S. I. Stupp, and M. C. Hersam. Sorting carbon nanotubes by electronic structure using density differentiation. *Nat. Nanotechnol.*, 1:60–65, 2006.
- [33] R. Krupke, F. Hennrich, H. v. Lohneysen, and M. M. Kappes. Separation of metallic from semiconducting single-walled carbon nanotubes. *Science*, 301:344–347, 2003.
- [34] R. Krupke, F. Hennrich, H. v. Lohneysen, and M. M. Kappes. Thin films of metallic carbon nanotubes prepared by dielectrophoresis. *Adv. Mater.*, 18:1468–1470, 2006.
- [35] T.-N. Chen, D.-S. Wu, C.-C. Wu, C.-C. Chiang, Y.-P. Chen, and R.-H. Horng. Improvements of permeation barrier coatings using encapsulated parylene interlayers for flexible electronic applications. *Plasma Process. Polym.*, 4(2):180–185, 2007.
- [36] M. Dimaki and P. Boggild. Dielectrophoresis of carbon nanotubes using microelectrodes: a numerical study. *Nanotechnology*, 15:1095–1102, 2004.
- [37] J. Li, Q. Zhang, N. Peng, and Q. Zhu. Manipulation of carbon nanotubes using AC dielectrophoresis. *Appl. Phys. Lett.*, 86:153116–153118, 2005.
- [38] H.-C. Chang and L. Y. Yeo, editors. *Electrokinetically-Driven Microfluidics and Nanofluidics*. Cambridge University Press, UK, 2009.
- [39] H. Morgan and N. G. Green. *AC Electrokinetics: Colloids and Nanoparticles*. Research Studies Press Ltd, UK, 2003.
- [40] T. B. Jones. *Electromechanics of Particles*. Cambridge University Press, UK, 1995.

Design and Generation of Dielectrophoretic Forces for Manipulating Carbon Nanotubes

Uchechukwu C. Wejinya*, Ning Xi[†], and King Wai Chiu Lai[†]

*Department of Mechanical Engineering, University of Arkansas, Arkansas

[†]Department of Electrical and Computer Engineering, Michigan State University, Michigan

CHAPTER OUTLINE

3.1 Overview	29
3.2 Dielectrophoretic Force Modeling	30
3.2.1 Modeling of Electroration for Nanomanipulation	34
3.2.2 Dynamic Modeling of Rotational Motion of Carbon Nanotubes for Intelligent Manufacturing of CNT-Based Devices	35
3.2.3 Dynamic Effect of Fluid Medium on Nano Particles by Dielectrophoresis	36
3.3 Theory for Microelectrode and Electric Field Design for Carbon Nanotube Applications	37
3.3.1 Microelectrode Design	37
3.3.2 Theory for Microelectrode Design	38
3.4 Electric Field Design	39
3.5 Carbon Nanotubes Application-Simulation Results	40
3.5.1 Dielectrophoretic Force: Simulation Results	40
3.5.2 Electroration (Torque): Simulation Results	45
3.5.3 Rotational Motion of Carbon Nanotubes: Simulation Results	45
3.6 Summary	49
References	49

3.1 OVERVIEW

Dielectrophoresis is the motion of a particle produced by the interaction of nonuniform electric field with induced effective dipole moment \mathbf{p} of the particle [1, 2]. Figure 3.1 shows a schematic of dielectrophoresis. In Fig. 3.1, the direction of the arrows exemplifies the direction of the electric field and the length of the arrows represents the magnitude of the electric field.

If the electric field is uniform, the force on each of the two poles of the dipole is equal and opposite; therefore, the net force is zero and there is no movement. On the other hand, if the electric field

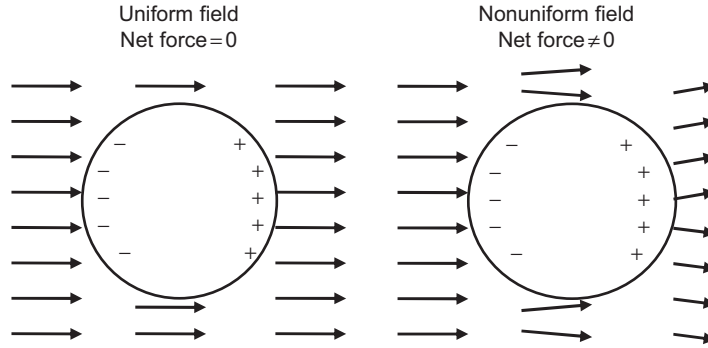
**FIGURE 3.1**

Illustration of dielectrophoresis.

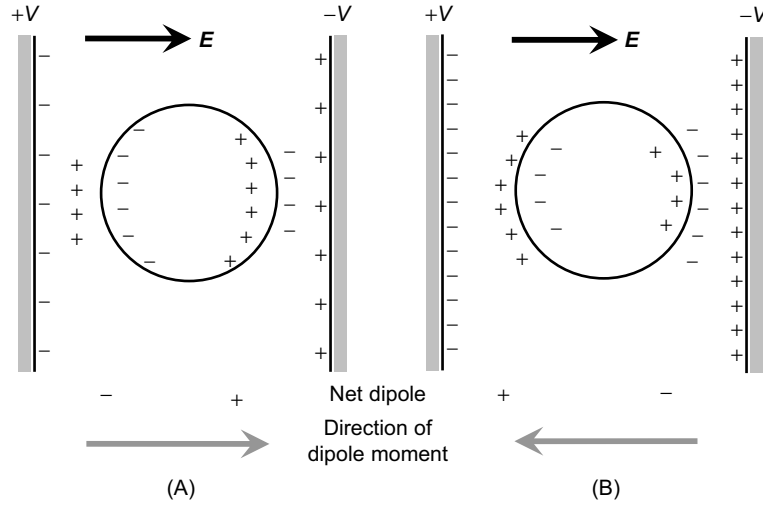
is nonuniform, the force on each of the two poles of the dipole is not equal; therefore, the net force is not equal to zero and there is movement of the particle. Furthermore, when a polarizable object is subjected to an electric field, a dipole moment is induced. If the electric field is inhomogeneous, the field strength and thus the force acting on each side of the particle will be different, causing the particle to move with respect to the medium. Depending on the polarizability of the particle compared with that of the medium, the force could push the particle toward high electric field regions or low electric field regions. Furthermore, if the particles have a higher polarizability (conductivity) than their immersion medium, they move toward regions of high electric field. Conversely, if the particles have lower conductivity than the medium, they move away from regions of high electric field and toward regions of low electric field. The movement of the particle toward a high electric field region is called positive dielectrophoresis (+DEP), and the movement of the particle toward a low electric field region is called negative dielectrophoresis (−DEP) [3–5]. In the case of an alternating electric field, the direction of the force and thus the direction of motion will remain the same even upon field reversal, because the dipole moment will be inverted as well. Furthermore, positive and negative dielectrophoresis can be achieved by choosing appropriate frequencies. The frequency at which there is no force acting on the particle or particles is known as the crossover frequency [6].

3.2 DIELECTROPHORETIC FORCE MODELING

Figure 3.2 illustrates how different dielectric particles polarize. Figure 3.2A shows a particle with a much higher polarizability than the suspending medium, and Fig. 3.2B shows a particle with a much lower polarizability than the suspending medium. If the polarizability is higher, more charge is produced on the inside of the particle/fluid interface and there is a net dipole across the particle that is parallel to the applied electric field. If the polarizability is lower, more charge is produced on the outside of the particle/fluid interface and the net dipole points in the opposite direction, against the field.

Hence, the force exerted by an electric field E on a dipole with dipole moment p [2, 7] is given by

$$F = (p \cdot \nabla)E \quad (3.1)$$


FIGURE 3.2

Polarizability of dielectric particles in medium.

where ∇ is the del operator. The effective dipole moment of a particle is given by

$$\mathbf{p} = v\tilde{\alpha}\mathbf{E} \quad (3.2)$$

where v is the volume of the particle, and $\tilde{\alpha}$ is the complex effective polarizability. The complex effective polarizability is defined as

$$\begin{aligned} \tilde{\alpha} &= 3\epsilon_m \underbrace{\left(\frac{\tilde{\epsilon}_p - \tilde{\epsilon}_m}{\tilde{\epsilon}_p + 2\tilde{\epsilon}_m} \right)}_{\tilde{f}_{CM}} \\ &= 3\epsilon_m \tilde{f}_{CM} \end{aligned} \quad (3.3)$$

where $\tilde{\epsilon}_p$ and $\tilde{\epsilon}_m$ refer to the complex permittivity of the particle and the medium, respectively, defined by

$$\tilde{\epsilon}_{m,p} = \epsilon - j\frac{\sigma}{\omega} \quad (3.4)$$

Here, σ is the conductivity, ϵ is the real permittivity of both the particle and the medium, respectively, and $\omega = 2\pi f$ is the angular frequency of the applied electric field.

The magnitude of the polarizability and the effective dipole moment of the particle is frequency dependent. This dependence is defined by \tilde{f}_{CM} in Eq. (3.3), and it is referred to as the *Clausius-Mossotti factor*. It is complex, describing a relaxation in the effective permittivity or polarizability of the particle with a relaxation time described in [2] as follows:

$$\tau_{MW} = \frac{\epsilon_p + 2\epsilon_m}{\sigma_p + 2\sigma_m} \quad (3.5)$$

Combining Eqs (3.1) and (3.2), the force exerted by an electric field \mathbf{E} on a dipole with dipole moment \mathbf{p} can be written as follows:

$$\mathbf{F} = (\nu \tilde{\alpha} \mathbf{E} \cdot \nabla) \mathbf{E} \quad (3.6)$$

On the basis of dielectrophoresis theory, to model the DEP force distribution for manipulating CNTs, we reasonably assumed that carbon nanotubes form a particle-by-particle line structure after undergoing AC electric field. Our derivation is based on this assumption and is as described in Fig. 3.3.

Following the geometry of Fig. 3.3, we write the volume of carbon nanotube particles as

$$v = \pi r^2 dL \quad (3.7)$$

where r is the radius of the carbon nanotube particles, and dL is the CNT change in length. By using the Pythagorean theorem, dL can be written as

$$dL = \sqrt{dx^2 + dy^2} \quad (3.8)$$

Hence Eq. (3.6) is written as

$$\begin{aligned} dF_{DEP} &= (\pi r^2 dL \tilde{\alpha} \mathbf{E} \cdot \nabla) \mathbf{E} \\ &= (\pi r^2 dL \tilde{\alpha}) (\mathbf{E} \cdot \nabla) \mathbf{E} \end{aligned} \quad (3.9)$$

By employing vector calculus and the fact that the electric field is irrotational, i.e., a vector field whose curl is zero ($\nabla \times \mathbf{E} = 0$), Eq. (3.9) becomes

$$dF_{DEP} = \frac{1}{2} \pi r^2 dL \operatorname{Re}\{\tilde{\alpha}\} \nabla |\mathbf{E}|^2 \quad (3.10)$$

where $\operatorname{Re}\{\tilde{\alpha}\}$ is the real part of the complex effective polarizability of both the CNT particle and the medium.

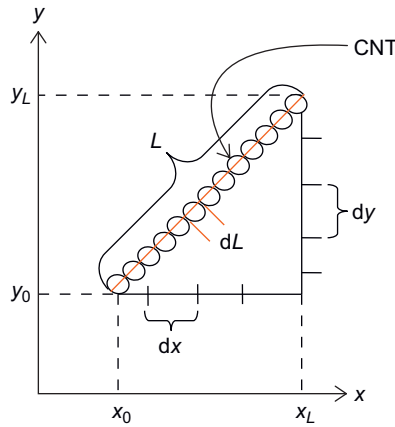


FIGURE 3.3

Illustration of a carbon nanotube (CNT) as a line.

Assuming that CNT is a 2D object and following the geometry of CNT in Fig. 3.3, we define the following:

$$L : y = f(x) \quad (3.11)$$

By differentiating Eq. (3.11), we get the following:

$$dy = f'(x)dx \quad (3.12)$$

Combining Eqs (3.8) and (3.12), dL becomes

$$dL = \sqrt{(f'(x)dx)^2 + dx^2} \quad (3.13)$$

Simplifying Eq. (3.13), we get the following equation:

$$dL = \sqrt{1 + (f'(x))^2} dx \quad (3.14)$$

Substituting Eq. (3.14) into Eq. (3.10), we obtain the following DEP equation:

$$dF_{DEP} = \frac{1}{2} \pi r^2 \sqrt{1 + (f'(x))^2} Re\{\tilde{\alpha}\} \nabla |E|^2 dx \quad (3.15)$$

Integrating both sides of Eq. (3.15), the dielectrophoretic force on a whole CNT particle structure under an AC electric field is as follows:

$$F_{DEP} = \int_{x_0}^{x_L} \frac{1}{2} \pi r^2 \sqrt{1 + (f'(x))^2} Re\{\tilde{\alpha}\} \nabla |E|^2 dx \quad (3.16)$$

It can be seen from Eq. (3.16), the electric field function now becomes a function of one variable x rather than two variables x and y .

Substituting Eq. (3.3) into Eq. (3.16) and simplifying, Eq. (3.16) becomes

$$F_{DEP} = \frac{3}{2} \pi r^2 \varepsilon_m Re\{\tilde{f}_{CM}\} \int_{x_0}^{x_L} \sqrt{1 + (f'(x))^2} \nabla |E|^2 dx \quad (3.17)$$

It can be seen from Eq. (3.17) that the derived dielectrophoretic force F_{DEP} model for carbon nanotubes depends on the real part of the Clausius-Mossotti \tilde{f}_{CM} factor, and therefore on the permittivity and conductivity of both the carbon nanotube particles and the suspending medium, as well as the frequency of the applied electric field.

Furthermore, the DEP force is proportional to the size of the particles. For small carbon nanotubes, the DEP force can be overpowered by thermal motion. To trap CNT particles, the DEP potential has to exceed thermal energy. This condition is expressed in [3] as

$$F_{DEP} \geq \frac{3}{2} kT \quad (3.18)$$

where k is the Boltzmann constant, and T is the temperature.

3.2.1 Modeling of Electrorotation for Nanomanipulation

The action of an externally applied electric field on a polarized particle results in the formation of an induced dipole moment [2]. When the dipole sits in a uniform electric field, each charge on the dipole experiences an equal and opposite force tending to align the dipole parallel to the electric field, i.e., it experiences a torque. There is usually a time delay that exists between the establishment of the electric field and the formation of the dipole. Consequently, if the field vector changes direction, the induced dipole moment vector must realign itself with the electric field vector, causing particle rotation.

Generally, the torque (electrorotation) experienced by the polarizable particle due to an applied electric field can be defined in [2] as

$$\mathbf{T} = \frac{1}{2} \text{Re}[\mathbf{p} \times \mathbf{E}] \quad (3.19)$$

where \mathbf{p} and \mathbf{E} are the effective dipole moment and electric field, respectively. Following the definition of the effective dipole moment given in Eq. (3.2), the torque can be written as

$$\begin{aligned} \mathbf{T} &= \frac{1}{2} v \text{Re}[\tilde{\alpha}(\mathbf{E} \times \mathbf{E})] \\ &= -v \text{Im}[\tilde{\alpha}](\text{Re}[\mathbf{E}] \times \text{Im}[\mathbf{E}]) \end{aligned} \quad (3.20)$$

As shown in Fig. 3.4, the torque is zero when the phase angle θ between the particle's polarization vector \mathbf{p} and the applied electric field \mathbf{E} is zero. On the other hand, the torque is maximum when the phase angle is $\pm 90^\circ$. If the induced dipole moment lags behind the electric field, then the direction of rotation is with the electric field and vice versa for the induced dipole moment that leads the electric field.

Then, the torque equation can be written as

$$\mathbf{T} = -v \text{Im}[\tilde{\alpha}] |\mathbf{E}|^2 \quad (3.21)$$

Following the derivation of dielectrophoretic force, we model the electrorotation (torque) of the CNT particles by making the the following assumptions:

1. We assume a carbon nanotube to be a particle line as illustrated in Fig. 3.3.
2. Torque on the carbon nanotube is the sum of the segmented (dL) torque as described in Fig. 3.3.

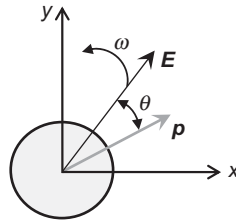


FIGURE 3.4

Schematic showing how induced dipole moment of a particle lags behind a rotating applied electric field.

Hence, by combining Eqs (3.3), (3.7), (3.8), and (3.11)–(3.14), Eq. (3.21) becomes

$$dT = -3\pi r^2 \varepsilon_m \text{Im}\{\tilde{f}_{CM}\} \sqrt{1 + (f'(x))^2} |E|^2 dx \quad (3.22)$$

Integrating both sides of Eq. (3.22), we obtain the electrorotation (torque) on the carbon nanotube under AC electric field as follows:

$$T = -3\pi r^2 \varepsilon_m \text{Im}\{\tilde{f}_{CM}\} \int_{x_0}^{x_L} \sqrt{1 + (f'(x))^2} |E|^2 dx \quad (3.23)$$

It can be seen from Eq. (3.23) that the derived electrorotation (torque), T , model for carbon nanotubes in an AC electric field depends on the imaginary part of the Clausius-Mossotti \tilde{f}_{CM} factor, and therefore on the permittivity and conductivity of both the carbon nanotube particles and the suspending medium, as well as the frequency of the applied electric field.

3.2.2 Dynamic Modeling of Rotational Motion of Carbon Nanotubes for Intelligent Manufacturing of CNT-Based Devices

When a particle rotates, it experiences a drag torque. This drag torque is characterized by a friction coefficient. The friction coefficient depends on the viscosity of the medium and the geometry of the surface properties of the particle, such as the length and the radius.

For carbon nanotube particles, which we will define as a long and very thin rod, we derive the torque due to rotation through the center of the carbon nanotube as follows:

$$I\ddot{\theta}(\omega) - \frac{L}{2}k\dot{\theta}(\omega) = T \quad (3.24)$$

In Eq. (3.24), I is the moment of inertia at the center of carbon nanotube particles assuming a line model described in Fig. 3.3, $\ddot{\theta}(\omega)$ is the angular acceleration of carbon nanotube particles, $\dot{\theta}(\omega)$ is the angular velocity of carbon nanotube particles, L is the length of carbon nanotube particles, k is the rotational friction coefficient of carbon nanotube structure, T is the torque due to electrorotation described in Eq. (3.23).

For CNT-like structures, the rotational friction coefficient k is given as follows [8–10].

$$k = \frac{\pi \eta L^3}{3 \ln(L/r)} \quad (3.25)$$

where η is the viscosity of the medium, L and r are the length and the radius of CNT, respectively.

Furthermore, in Eq. (3.24), the moment of inertia I is given as [11].

$$I = \frac{1}{12}mL^2 \quad (3.26)$$

where m is the mass of carbon nanotubes, and L is the length of CNT.

In Eq. (3.23), the electric field function depends on the electrode geometry as well as number of electrodes. For this derivation, we use two pairs of microelectrodes because applications involving intelligent sensor manufacturing using carbon nanotubes are conducted on two or more pairs of microelectrodes.

By defining the appropriate electric field function, Eq. (3.24) can be solved numerically to obtain the rotation angle and rotational velocity of carbon nanotubes in viscous medium for varying frequencies, consequently leading to an effective and efficient method of manufacturing carbon nanotube-based devices.

3.2.3 Dynamic Effect of Fluid Medium on Nano Particles by Dielectrophoresis

Because carbon nanotubes are dispersed in fluidic medium, it becomes very important that the dynamic effect of the fluidic medium on the CNT particles be analyzed.

When CNT particles move in a fluid, the viscous force that is proportional to their velocity retards the particles, and the particles are accelerated by a deterministic force. In this case, the deterministic force is the dielectrophoretic F_{DEP} force, and the particles experience an increasing drag force. For a constant applied force F_{DEP} , the particles reach a terminal velocity beyond which they do not accelerate. If the fluid medium is in motion itself, this terminal velocity also depends on the fluid's velocity. The dynamics of this system can be examined by employing Newton's second law of motion as follows:

$$m \frac{d\mathbf{v}}{dt} = F_{DEP} \quad (3.27)$$

where m is the mass of CNT particles, and \mathbf{v} is the velocity of the particles.

When DEP force is applied to the CNT particles where the fluid is moving with velocity \mathbf{u} , the drag force experienced by the particles is proportional to their velocity due to the fluid. The drag force is expressed in [2] as

$$F_\eta = f(\mathbf{u} - \mathbf{v}) \quad (3.28)$$

where f is referred to as the friction factor and depends on the range of particle parameters such as size, shape, and surface characteristics, and the viscosity of the fluid. For a prolate ellipsoid (an ellipsoid formed by the rotation of an ellipse about its major axis) such as CNT that moves in a random direction, the friction factor f is given in [2] as

$$f = \frac{6\pi\eta l}{\ln(2l/r)} \quad (3.29)$$

where η , l , and r are the viscosity of the fluid, the length of a CNT, and the radius of a CNT, respectively.

Continually, Eq. (3.27) becomes

$$m \frac{d\mathbf{v}}{dt} = F_{DEP} + f(\mathbf{u} - \mathbf{v}) \quad (3.30)$$

We write Eq. (3.30) as

$$\frac{d\mathbf{v}}{dt} + \frac{f}{m} \mathbf{v} = \frac{F_{DEP}}{m} + \frac{f}{m} \mathbf{u} \quad (3.31)$$

Recognizing that Eq. (3.31) is a first-order differential equation, and assuming that the CNT particles are initially at rest, i.e., $v(0) = 0$, the solution to Eq. (3.31) is

$$v(t) = \left(\frac{F_{DEP}}{f} + u \right) \left(1 - e^{-(f/m)t} \right), \quad t > 0 \quad (3.32)$$

The acceleration of the CNT particles is described by the exponential term of equation (3.32), and it has a characteristic time constant, $\tau = m/f$. With respect to a CNT in a viscous medium, the order of τ is much smaller than the timescale that we are considering, and a carbon nanotube particle reaches its terminal velocity as soon as it is exposed to an AC electric field. For times greater than τ , the particles move at terminal velocity given by

$$v_T = \frac{F_{DEP}}{f} + u \quad (3.33)$$

With no fluidic motion, CNT particles move with terminal velocity, given by

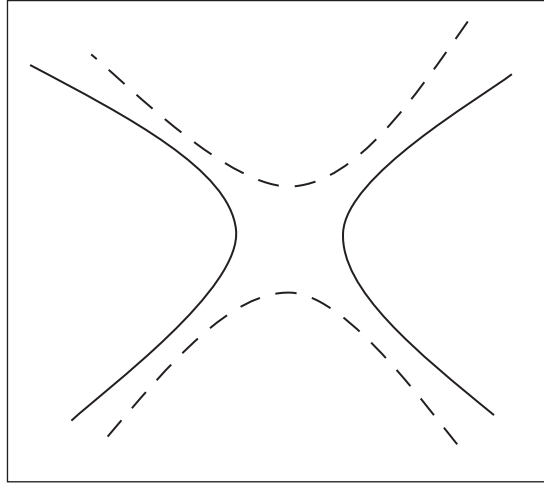
$$v_T = \frac{F_{DEP}}{f} \quad (3.34)$$

3.3 THEORY FOR MICROELECTRODE AND ELECTRIC FIELD DESIGN FOR CARBON NANOTUBE APPLICATIONS

3.3.1 Microelectrode Design

To effectively deposit, manipulate, and implement carbon nanotubes using dielectrophoresis on microelectrodes, it becomes necessary to mathematically describe the microelectrode geometry. The microelectrode design is based on the assumption that the electrical potential at any point (x , y , and z) created by a microelectrode of interest is defined by a polynomial that obeys Laplace's equation [12]. The solution to Laplace's equation is also known as potential theory. By substituting this polynomial into Laplace's equation, the corresponding equipotentials can therefore be determined, and these in turn can be used to define the required microelectrode boundaries for use in carbon nanotube deposition, manipulation, and implementation using dielectrophoresis. Furthermore, the microelectrode design method can readily be applied to three-dimensional microelectrode design, for the sake of simplicity and the fact that carbon nanotube deposition and manipulation is carried out on a two-dimensional microelectrode array, the theoretical development being restricted to two-dimensional microelectrode design.

Figure 3.5 shows the microelectrode design for carbon nanotube deposition, manipulation, and implementation using dielectrophoresis as described in Chapter 3. It is worth noting that the design is not restricted to that depicted in Fig. 3.5. Notice that in Fig. 3.5, the number of microelectrode pairs is two; hence, a second-order polynomial is employed to derive the necessary boundary conditions and applied potential between any pair of microelectrodes.

**FIGURE 3.5**

Microelectrode design for carbon nanotube implementation.

3.3.2 Theory for Microelectrode Design

In designing microelectrodes for deposition, manipulation, and implementation of carbon nanotubes using dielectrophoresis, an electric potential defined by a second-order Laplace's polynomial is considered. We defined this polynomial as follows:

$$f_2(x, y) = a_1x^2 + a_2xy + a_3y^2 \quad (3.35)$$

In Eq. (3.35), the subscript 2 in $f_2(x, y)$ indicates the order n of the polynomial. Because electrodes are in pairs, and we are defining a second-order polynomial for electrode geometry, there will be $2n$ electrodes. Here we'll have four electrodes or two pairs of electrodes as depicted in Fig. 3.5.

From Eq. (3.35), and in general, there will be a total number of C_{n+1}^n coefficients. In our case, there will be C_3^2 coefficients.

Following Laplace's equation, i.e.,

$$\frac{\partial^2 f_2(x, y)}{\partial x^2} + \frac{\partial^2 f_2(x, y)}{\partial y^2} = 0, \quad (3.36)$$

we get the following:

$$\frac{\partial^2 f_2(x, y)}{\partial x^2} = 2a_1 \quad (3.37)$$

and

$$\frac{\partial^2 f_2(x, y)}{\partial y^2} = 2a_3 \quad (3.38)$$

Substituting Eqs (3.37) and (3.38) into Laplace's equation, Eq. (3.36), we get the following:

$$2a_1 + 2a_3 = 0 \quad (3.39)$$

Simplifying Eq. (3.39), we get the following:

$$a_3 = -a_1 \quad (3.40)$$

Hence Eq. (3.35) can be expressed generally as

$$f_2(x, y) = a_1x^2 + a_2xy - a_1y^2 \quad (3.41)$$

where a_1 and a_2 are independent parameters, and $f_2(x, y)$ is the linear combination of the following two independent functions.

$$\begin{aligned} f_{2a} &= x^2 - y^2 \\ f_{2b} &= xy \end{aligned} \quad (3.42)$$

Furthermore, because the electric potential function based on f_{2a} is $f_2(x, y) = a_1(x^2 - y^2)$, it can be used to define the equipotentials in the electric field. For instance, equipotentials can be constructed using the following equations.

$$\begin{aligned} k &= x^2 - y^2 \\ -k &= x^2 - y^2 \end{aligned} \quad (3.43)$$

Equation (3.43) is clearly represented in Fig. 3.5 for both positive and negative polarities.

Furthermore, if the electrodes are shaped according to equipotential lines depicted in Fig. 3.5, and positive and negative potentials of $+v$ and $-v$ are applied, then the potential $f_2(x, y)$ at any point (x, y) in the interelectrode space is given by the following equation.

$$f_2(x, y) = \frac{v}{k} (x^2 - y^2) \quad (3.44)$$

It is important to note that the constant k in Eq. (3.43) used to determine equipotentials can be chosen arbitrarily and will not affect the final electric field pattern established by the electrode. On the other hand, its value does determine the size of the designed electrode.

3.4 ELECTRIC FIELD DESIGN

The use of dielectrophoresis defined by [1, 2] as the motion of a particle produced by the interaction of nonuniform electric field with induced effective dipole moment \mathbf{p} of the particle, to trap and manipulate carbon nanotubes on microelectrodes, was described earlier. However, for controlled and predictable applications of dielectrophoresis, a knowledge of the non-uniform electric field distribution established by the microelectrode geometry becomes absolutely critical and necessary. In Section 3.3.2, the theory for microelectrode design was developed in detail. This theory also governs electric potentials for the designed microelectrodes.

The mathematical model was derived for the application of dielectrophoresis on carbon nanotubes. The derived model takes into account the spatial variation of both the electric field and the gradient of

the electric field of microelectrodes. Therefore, the spatial variations of the electric field, $|E|$ and $\nabla|E|^2$, described in the dielectrophoretic force model (DEP) earlier is choosing for a second-order polynomial microelectrode geometry derived in Section 3.3.2.

In Eq. (3.35), the microelectrode structure is in two dimensions, i.e. (x, y) . Hence, the electric field would comprise two components, E_x and E_y . These field components are determined by taking the partial differential of the potential function $f_n(x, y)$. In this case, $n = 2$ as described in Eq. (3.35). It is important to note that for $n = 1$, the electric field is uniform; hence, $\nabla|E|^2 = 0$ and no DEP force is exerted on carbon nanotube particles located between the microelectrodes. For $n > 1$, then $\nabla|E|^2$ becomes a function of position (x, y) and n . Without the loss of generality, in [12], $\nabla|E|^2$ varies as $(x^2 + y^2)^{n-1.5}$. Hence, electric field function is indicated based on the aforementioned derivation and as a function of position (x, y) on the designed microelectrodes.

3.5 CARBON NANOTUBES APPLICATION-SIMULATION RESULTS

3.5.1 Dielectrophoretic Force: Simulation Results

To obtain simulation results for the developed DEP force model, the Clausius-Mossotti factor \tilde{f}_{CM} , was obtained from Eq. (3.3). From Eq. (3.3), \tilde{f}_{CM} depends on the conductivity and the real permittivity of both the CNT and the fluidic medium. It also depends on ω , the angular frequency of the applied electric field. In the simulation, metallic multiwalled CNTs are disbursed in liquid acetone, and the parameters are described as follows.

- σ_p : conductivity of metallic multiwall CNT (S/m)
- ε_p : permittivity (dielectric constant) of metallic multiwall CNT
- σ_m : conductivity of fluid medium, acetone (S/m)
- ε_m : permittivity (dielectric constant) of fluid medium, acetone.

The values of the parameters used in the simulation at room temperature are as follows:

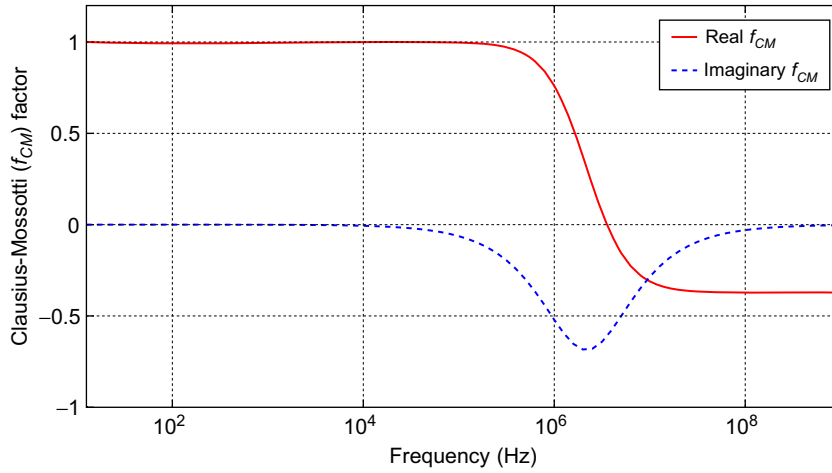
$$\sigma_p = 1 \times 10^8 \text{ S/m}, \varepsilon_p = 3.9, \sigma_m = 100 \times 10^{-12} \text{ S/m}, \text{ and } \varepsilon_m = 21.$$

Figure 3.6 shows the real and complex plot of the Clausius-Mossotti, \tilde{f}_{CM} factor for the given parameters of the medium acetone, and metallic MWCNT particles. Furthermore, because carbon nanotubes are also dispersed in other media such as ethanol, Fig. 3.7 shows the Clausius-Mossotti, \tilde{f}_{CM} factor for both acetone and ethanol. The real part of \tilde{f}_{CM} will be used to determine the DEP force, whereas its complex part will be used to determine the electrorotation (torque) on the CNT.

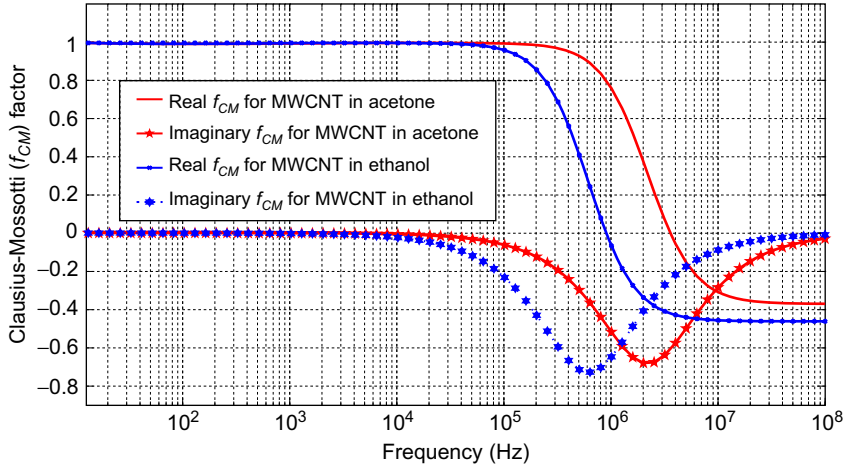
Because the DEP force highly depends on the applied electric field, it is paramount that the electric field function be chosen and investigated appropriately. First, in our simulation, electric field and the square of the electric field functions are chosen based on a second-order polynomial derived from Laplace's equations for defining electrode geometry as described in [12].

Figure 3.8 shows 3D simulation results of the chosen electric field function and its gradient. Figure 3.8A shows the 3D plot of the electric field as a function of the electrodes, while Fig. 3.8B shows the 3D plot of the gradient of the electric field as a function of the electrodes.

Consequently, Fig. 3.9 shows the relationship between the electric field function and the applied voltage. This relationship is also based on a second-order polynomial derived from Laplace's equations

**FIGURE 3.6**

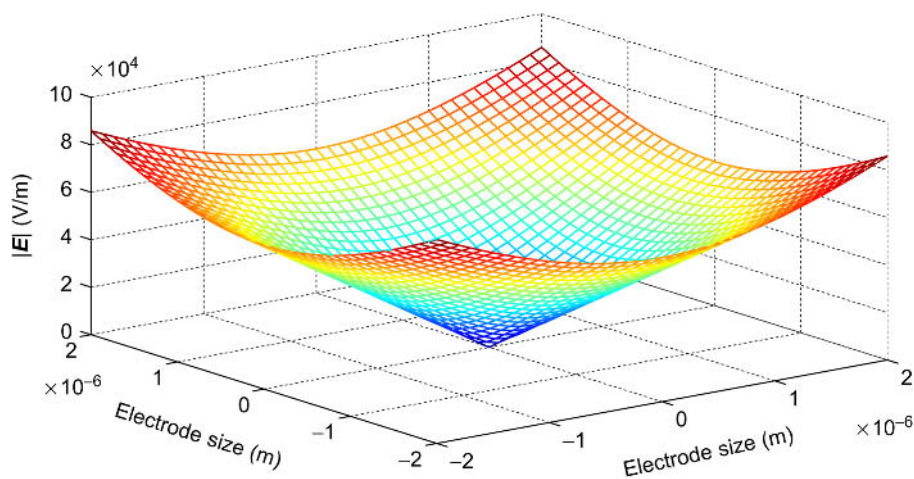
Clausius-Mossotti factor for DEP analysis (metallic MWCNT in acetone).

**FIGURE 3.7**

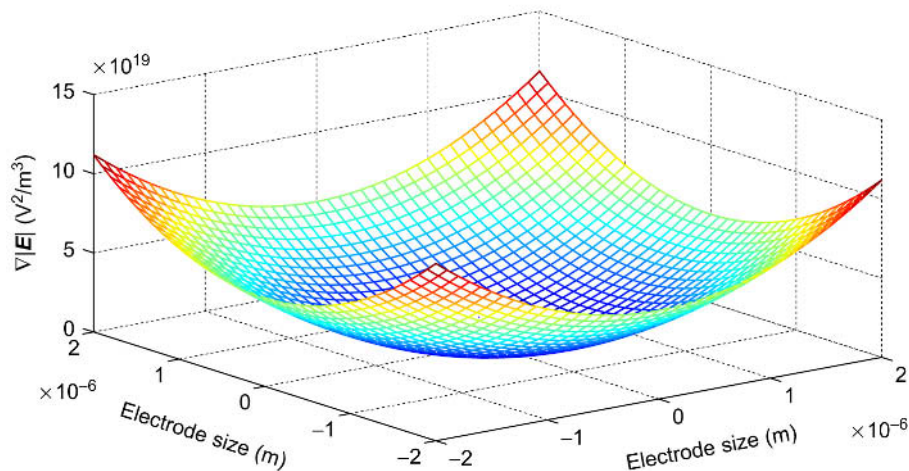
Clausius-Mossotti factor for DEP analysis (Metallic MWCNT in acetone and ethanol).

for defining electrode geometry as described in [12]. As the voltage increases, the electric field also increases as depicted in Fig. 3.9.

Figure 3.10 shows the relationship between the voltage and the gap between microelectrodes. In this figure, because carbon nanotubes will burn at voltage greater than 2V, it becomes absolutely critical that the gap between microelectrodes be less than or equal to $2\mu\text{m}$ for applied constant electric field.



(A) Electric field as a function of electrode size



(B) Gradient of the electric field as a function of electrode size

FIGURE 3.8

3D plots showing the relationship between electric field and its gradient as a function of electrode size.

In addition, because DEP force also depends on the frequency of the AC electric field, we examined the relationship between frequency and applied electric field. Figure 3.11 shows 3D plots describing the relationship between frequency, voltage, and the electric field function. Figure 3.11A shows the 3D plot of the electric field as a function of frequency and voltage, while Fig. 3.11B describes the relationship between the gradient of the electric field, frequency, and voltage.

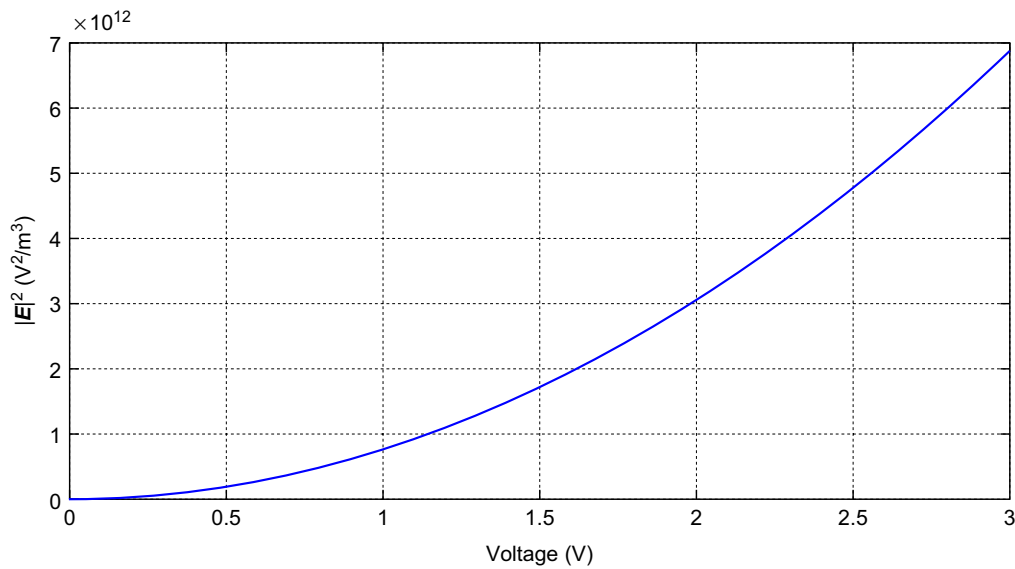


FIGURE 3.9
Electric field as a function of applied voltage.

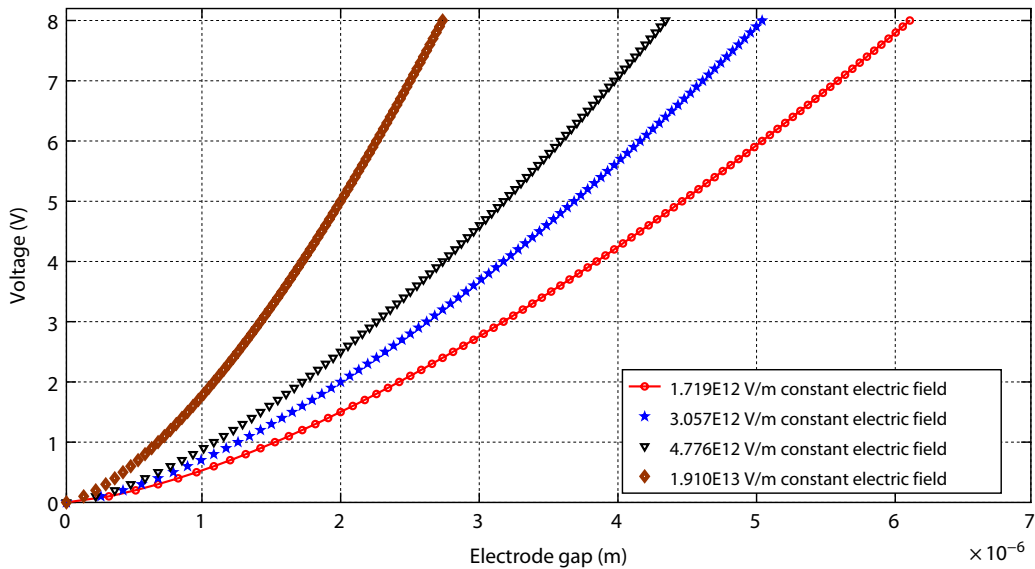
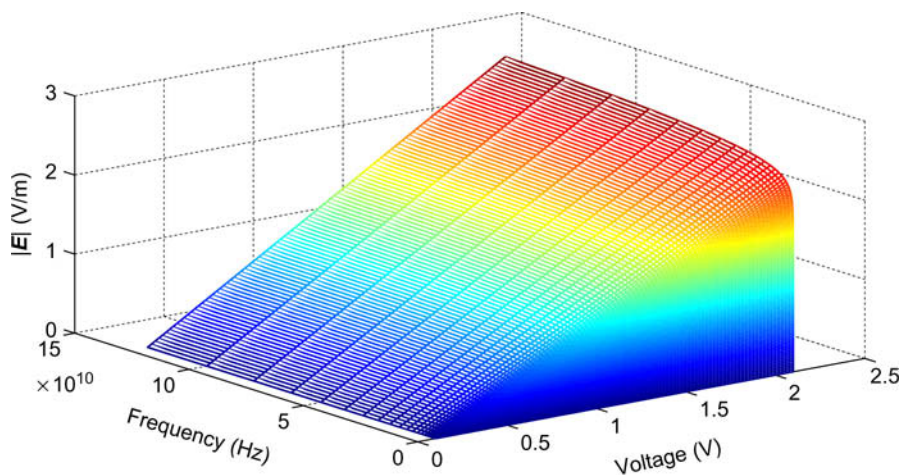
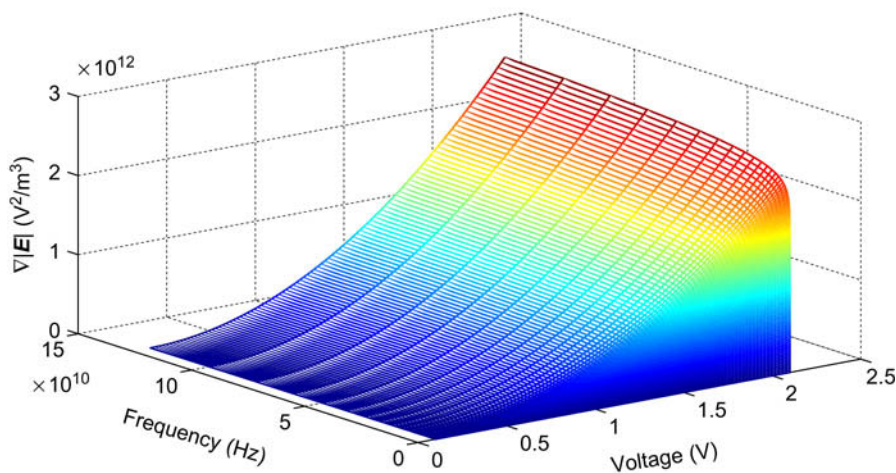


FIGURE 3.10
Relationship between voltage and microelectrode gap for constant electric field.



(A) Electric field as a function of frequency and voltage

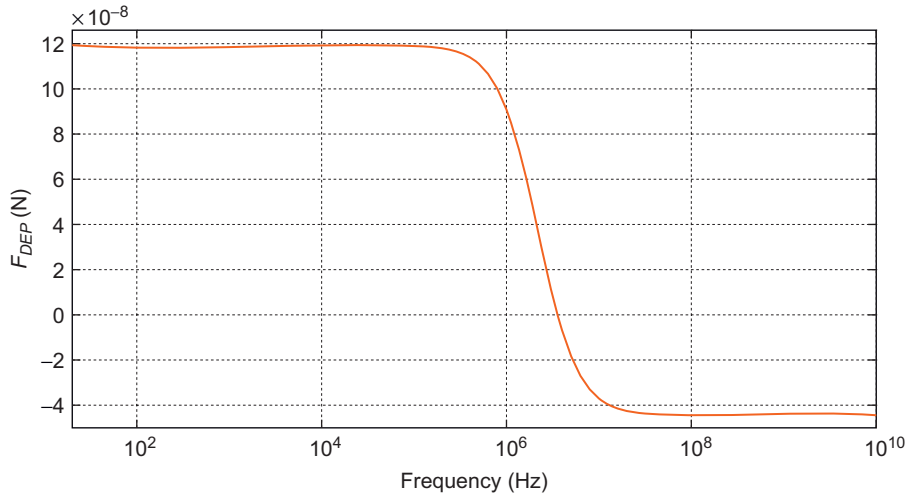


(B) Gradient of the electric field as a function of frequency and voltage

FIGURE 3.11

3D plots showing the relationship between electric field and its gradient as a function of frequency and voltage.

Figure 3.12 shows the total dielectrophoretic force on the CNT after undergoing an AC electric field. In this figure, it is clear that F_{DEP} is a positive constant for frequencies less than 8×10^4 Hz. The magnitude of dielectrophoretic force F_{DEP} reduces between 8×10^4 Hz and 3.5×10^6 Hz for the parameters used, and it is still positive. For frequencies between 3.5×10^6 Hz and 7×10^7 Hz, the dielectrophoretic force F_{DEP} is negative. Furthermore, for frequencies greater than 7×10^7 Hz, DEP

**FIGURE 3.12**

Dielectrophoretic force F_{DEP} on metallic MWCNT in acetone.

force becomes negative constant. This implies that for MWCNT, the metallic or more polarized CNTs will be attracted toward the electrode (high electric field region), while the semiconducting ones will be repelled from the electrode (low electric field region) and possibly move toward the middle of the electrode. The semiconducting CNTs now can be extracted and use for electronics design exploration.

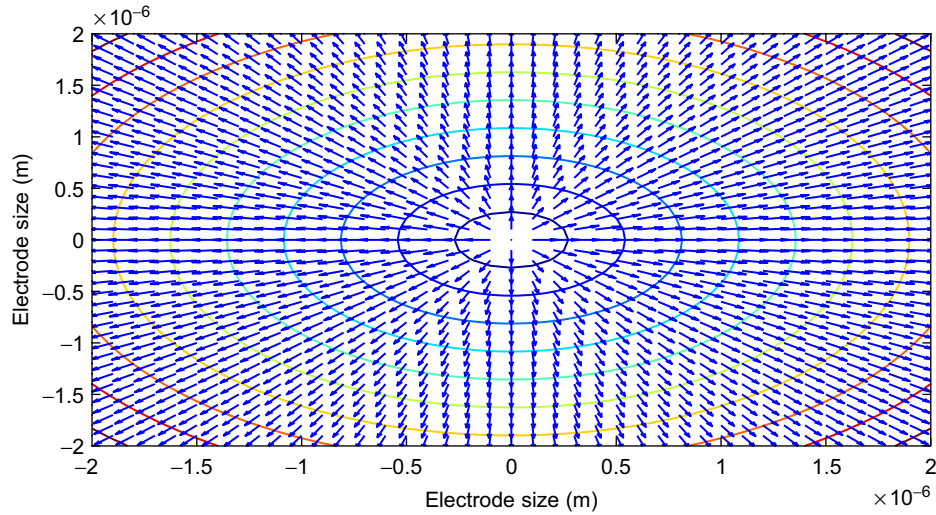
Furthermore, a simulation of the spatial variation of the electric field and its gradient was investigated. Figure 3.13 shows the electric field variation on the microelectrodes. Figure 3.13A shows the spacial variation of the electric field on microelectrodes, while Fig. 3.13B depicts the spatial variation of the gradient of the electric field on microelectrodes. This can be used to determine the direction of the moving CNTs as well as high electric field regions and low electric field regions.

3.5.2 Electroration (Torque): Simulation Results

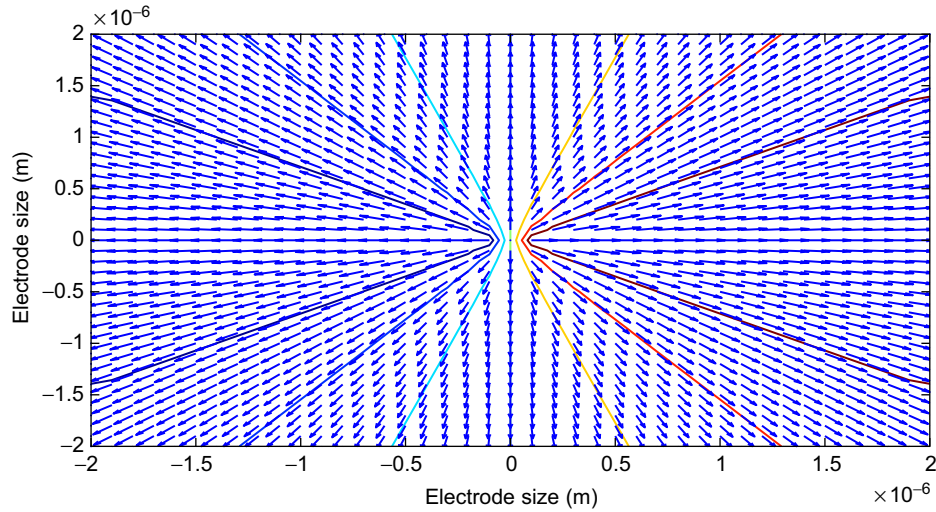
Figure 3.14 shows the electroration (torque) acting on CNT after undergoing an AC electric field. In this figure, the maximum electroration occurs when the frequency is 2.1×10^6 Hz, and decreases for frequencies greater than 2.1×10^6 Hz. The electroration (torque) is positive for all frequencies of the applied electric field.

3.5.3 Rotational Motion of Carbon Nanotubes: Simulation Results

The resulting rotational dynamics of carbon nanotubes in a viscous medium is given in Eq. (3.24). Following Eqs (3.25) and (3.26), and constructing the appropriate electric field function, the governing resulting equation of motion for CNT is obtained. To verify this derivation, simulation was done by choosing appropriate parameters.



(A) Spatial variation of the electric field on microelectrodes



(B) Spatial variation of the gradient of the electric field on microelectrodes

FIGURE 3.13

Spatial variation of the electric field and its gradient on microelectrodes for CNT manipulation and separation.

The values of some of the parameters used in the simulation at room temperature are as follows:

$$L = 2 \mu\text{m}, \eta = 300 \times 10^{-6} \text{ Ns/m}^2, m = 20 \times 10^{-9} \text{ kg}, \text{ and } r = 20 \text{ nm}.$$

Figures 3.15 and 3.16 show the simulation results of both CNT rotation angles and rotation velocities in viscous medium for different initial conditions. Figure 3.15 shows that the CNT model as a line particle

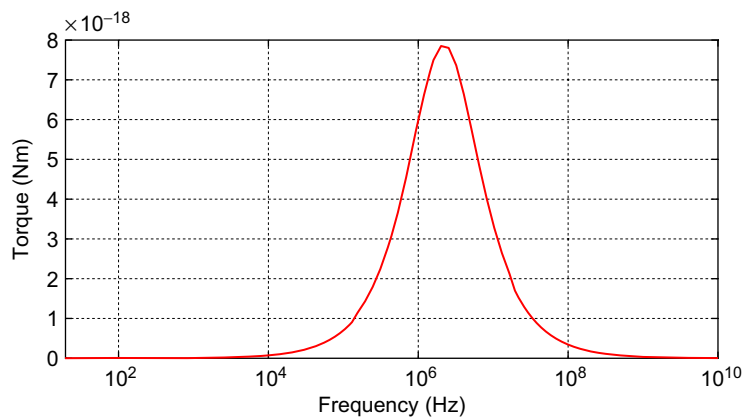


FIGURE 3.14
Electrorotation (torque) acting on metallic MWCNT in acetone.

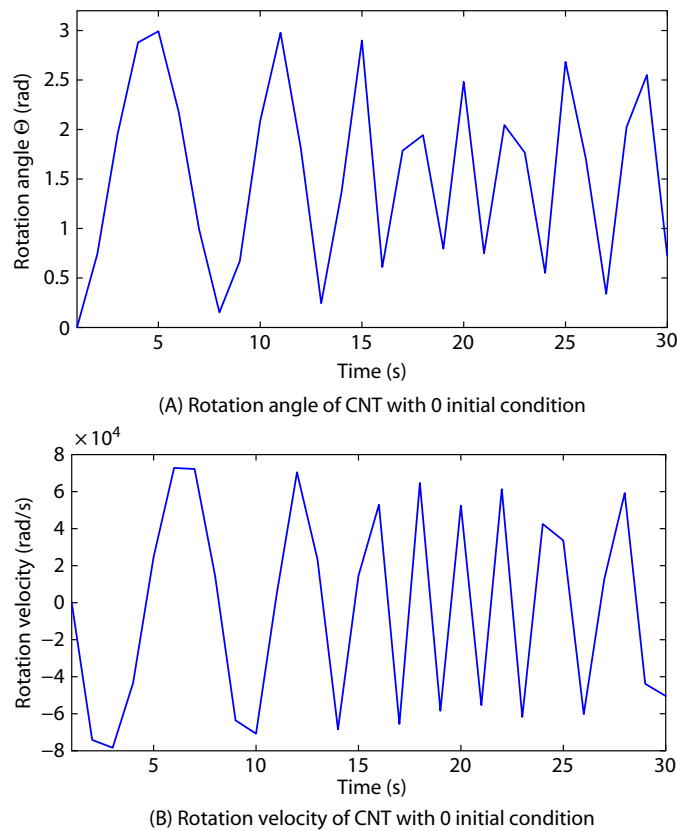
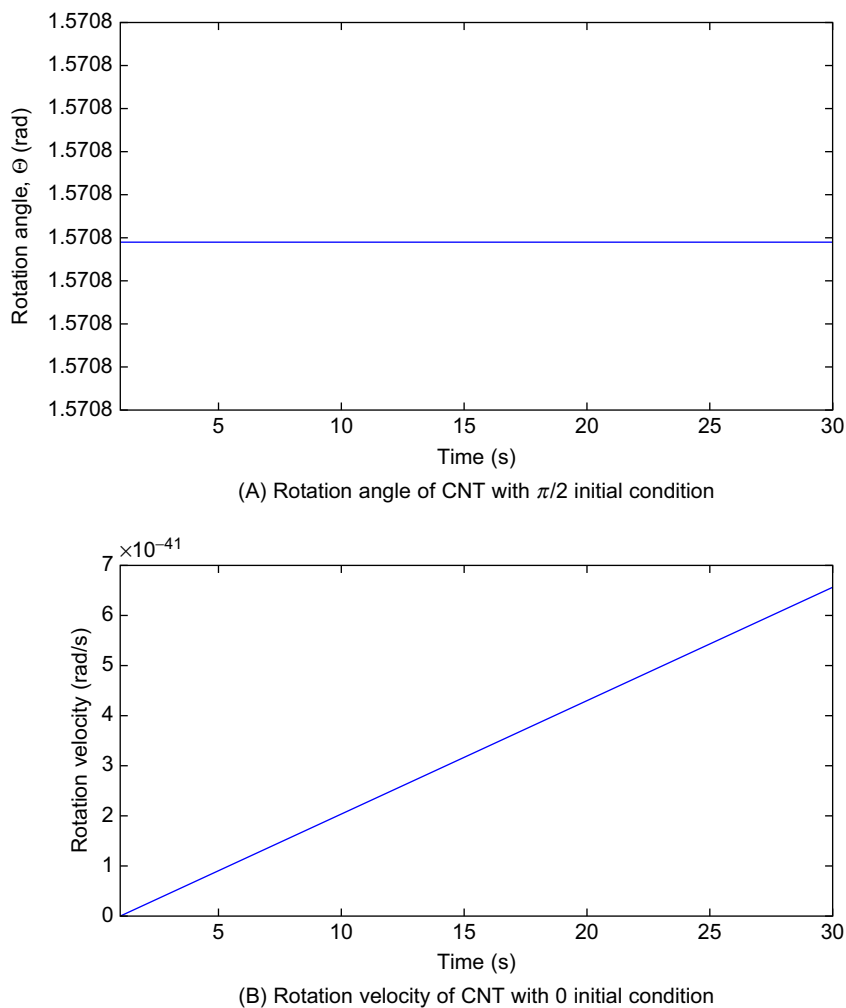


FIGURE 3.15
Rotation angle and velocity of CNT in acetone with initial condition (0, 0).

**FIGURE 3.16**

Rotation angle and velocity of CNT in acetone with initial condition $(\pi/2, 0)$.

will continue to rotate until an external force is applied to it. This external force will result from the applied electric field, termed dielectrophoresis force (DEP). On the other hand, Fig. 3.16 shows that CNT will stop rotating when it is perpendicular to the applied electric field. Hence, the rotation velocity becomes zero. Based on the simulation results, the model can be used to effectively control the orientation/rotation of carbon nanotubes for application in intelligent manufacturing of CNT-based optical sensors and other applications such as electrical circuits, fiber and film, computer circuits, etc.

3.6 SUMMARY

In this chapter, the modeling of dielectrophoretic force for manipulating carbon nanotubes was presented. The dielectrophoretic force model was derived assuming CNT to be a particle line structure after undergoing AC electric field. Simulation results were presented for the dielectrophoretic force model to verify the developed model. Furthermore, a model for controlling the rotation/orientation of carbon in nano assembly was derived and presented. This model precisely described the rotational motion of carbon nanotubes in viscous medium (acetone). The derivation of this model correctly assumed that carbon nanotubes form a line shape after undergoing AC electric field, compared to the existing model that assumes carbon nanotubes to be a spherical particle. Simulation results were presented for both rotational motion of carbon nanotubes in viscous mediums and the electrorotation (torque) model to verify the developed models.

References

- [1] H. A. Pohl. *Dielectrophoresis: The Behavior of Neutral Matter in Nonuniform Electric Fields*. Cambridge University Press, Cambridge, UK, 1978.
- [2] H. Morgan and N. G. Green. *AC Electrokinetics: Colloids and Nanoparticles*. Research Studies Press Ltd, Hertfordshire, England, 2003.
- [3] J.-E. Kim and C.-S. Han. Use of dielectrophoresis in the fabrication of an atomic force microscope tip with a carbon nanotube: a numerical analysis. *Nanotechnology*, 16(10):2245–2250, 2005.
- [4] A. Ramos, H. Morgan, N. G. Green, and A. Castellanos. AC electrokinetics: a review of forces in microelectrode structures. *J. Phys. D: Appl. Phys.*, 31:2338–2353, 1998.
- [5] H. Morgan, M. P. Hughes, and N. G. Green. Separation of submicron bioparticles by dielectrophoresis. *Biophys. J.*, 77(1):516–525, 1999.
- [6] S. B. Asokan, L. Jawerth, R. L. Carroll, R. E. Cheney, S. Washburn, and R. Superfine. Two-dimensional manipulation and orientation of actin-myosin systems with dielectrophoresis. *Nano. Lett.*, 3:431–437, 2003.
- [7] T. B. Jones. *Electromechanics of Particles*. Cambridge University Press, Cambridge, UK, 1995.
- [8] Y.-G. Tao, W. K. den Otter, J. K. G. Dhont, and W. J. Briels. Isotropic-nematic spinodals of rigid long thin rodlike colloids by event-driven Brownian dynamics simulations. *J. Chem. Phys.*, 124:1–10, 2006.
- [9] M. Doi and S. F. Edwards. *The Theory of Polymer Dynamics*. Clarendon Press, Oxford, UK, 1986.
- [10] J. K. G. Dhont. *An Introduction to Dynamics of Colloids*. Elsevier, Amsterdam, The Netherlands, 1996.
- [11] B. M. Das, A. Kassimali, and S. Sami. *Engineering Mechanics: Statics*. Richard D. Irwin, Inc., Boston, USA, 1994.
- [12] Y. Huang and R. Pethig. Electrode design for negative dielectrophoresis. *Meas. Sci. Technol.*, 2:1142–1146, 1991.

Atomic Force Microscope-Based Nanorobotic System for Nanoassembly

Lianqing Liu*, Ning Xi[†], Guangyong Li**, and Heping Chen[‡]

**State Key Lab of Robotics, P. R. China*

[†]Department of Electrical and Computer Engineering, Michigan State University, Michigan

***Department of Electrical and Computer Engineering, University of Pittsburgh, Pittsburgh, Pennsylvania*

[‡]Ingram School of Engineering, Texas State University, Texas

CHAPTER OUTLINE

4.1 Introduction to AFM and Nanomanipulation	51
4.1.1 AFM's Basic Principle	52
4.1.2 Imaging Mode of AFM	53
4.1.3 AFM-Based Nanomanipulation	55
4.2 AFM-Based Augmented Reality System	56
4.2.1 Principle for 3D Nanoforce Feedback	56
4.2.2 Principle for Real-Time Visual Feedback Generation	59
4.2.3 Experimental Testing and Discussion	59
4.3 Augmented Reality System Enhanced by Local Scan	62
4.3.1 Local Scan Mechanism for Nanoparticle	62
4.3.2 Local Scan Mechanism for Nanorod	64
4.3.3 Nanomanipulation with Local Enhanced Augmented Reality System	66
4.4 CAD-Guided Automated Nanoassembly	71
4.5 Modeling of Nanoenvironments	72
4.6 Automated Manipulation of CNT	74
4.7 Summary	78
References	78

4.1 INTRODUCTION TO AFM AND NANOMANIPULATION

Use of the atomic force microscope provides a very high-resolution type of scanning probe microscopy (SPM). It was invented by Binnig, Quate, and Gerber in 1986 to overcome the basic drawback with scanning tunneling microscopy (STM): it can only image conducting or semiconducting surfaces.

Atomic force microscopy (AFM), however, has the advantage of imaging almost any type of surface, including polymers, ceramics, composites, glass, and biological samples. Since its invention, the atomic force microscope has attracted tremendous interest from researchers all over the world in different fields, and has become one of the foremost microscopy technologies in use today. The resolution of AFM can be down to less than 1 nm both in lateral and vertical directions, which is more than 1000 times better than the optical diffraction limit. The images from AFM can determine roughness, grain size, and features of the sample on the nanoscale. It is being used to solve processing and materials problems in a wide range of technologies affecting the electronics, telecommunications, biological, chemical, automotive, aerospace, and energy industries. The materials being investigated include thin and thick film coatings, ceramics, composites, glasses, synthetic and biological membranes, metals, polymers, and semiconductors. AFM is being applied to studies on phenomena such as abrasion, adhesion, cleaning, corrosion, etching, friction, lubrication, plating, and polishing. The invention and wide application of AFM has generated a huge impact on all aspects of scientific research globally.

4.1.1 AFM's Basic Principle

The word “microscopy” in AFM may give the false impression that AFM operates on a principle similar to that of traditional optical microscopy technology. Actually, the AF microscope collects data by “feeling” rather than “looking.” A typical AF microscope consists of an extremely sharp tip mounted or integrated on the end of a tiny cantilever that is moved by the mechanical scanner over the sample surface to be observed. The variation of the surface will change the interaction force acting on the tip and therefore cause a deflection of the cantilever. Under Hook’s law, there should be a linear relationship between the topography change and the cantilever deflection. Therefore, surface topography information can be obtained through tracking the deflection of the cantilever. In the early days of AFM, the deflection of the cantilever was tracked through monitoring the tunneling current of a second tip positioned above the cantilever. Although the design of this prototype is hardly used in today’s AF microscope, it demonstrated the conceptual feasibility of the AFM. Taking advantage of the rapid progress in tip manufacture, most AF microscopes in use today employ an optical lever technique, which has a resolution comparative with STM-based detection and a lower cost. The basic idea is that the deflection of the cantilever will change the reflection angle of the laser beam that is shot on to the end of the cantilever. Due to the amplification effect of the optical cantilever, a relatively large displacement will be generated with the traveling of the reflected laser and detected by a split photodiode.

There are two basic types of scanning mechanism: Tip scanning and sample scanning AFM. For tip scanning AFM, the probe tip scans above a stationary sample, whereas with the sample scanning design, the sample is scanned below a fixed probe tip. In a sample scanning configuration, the sample is mounted on a piezoelectric tube, which can move the sample in the z direction for maintaining a constant force, and the x and y directions for scanning the sample. The resulting map of $M(x, y)$ represents the topography of the sample. In the configuration of a tip scanning AF microscope, the probe is mounted on a piezoelectric tube, which can move the tip in z direction for maintaining a constant force, and the x and y directions for scanning the sample. This kind of configuration brings the benefit of less disturbance to the scanner because the AFM probe is very small, while the sample may be very big. It also offers further benefit of observing the transparent sample through an inverted optical microscope. But the shortcoming is that the laser has to track the movement of the AFM tip,

which will bring extra noise to the system due to the tracking movement. Thus, the sample scanning AF microscope has a better performance than the tip scanning type.

4.1.2 Imaging Mode of AFM

Over the years, several imaging modes of AFM have been developed. The primary modes of imaging are contact mode, noncontact mode, and tapping mode. More advanced modes are adding to the AFM technology and some of them have developed into new categories of SPMs such as Lateral Force Microscopy, Electrical and Magnetic Force Microscopy, etc. Only the primary modes are going to be discussed here and the advanced modes are beyond the scope of this chapter. To give readers an in-depth understanding to these three primary imaging modes of AFM, we will first give an brief introduction to the force–distance curve of AFM. It is the basis for all of the imaging modes of AFM.

The force most commonly associated with atomic force microscopy is an interatomic force called van der Waals force. The force value is depended on the distance between the probe and the sample surface. As shown in Fig. 4.1, in noncontact regime A, the tip-sample distance is large, and the interaction force is nearly zero. As the tip moves toward the sample and enters the attractive regime B, there will be a small attractive force between tip and sample. The attractive force keeps increasing until the tip approaches point C. After this point, the atom of AFM tip and sample surface has been so close to each other, a repulsive force will be induced due to the repelled electron cloud between them, which weakens the attractive force. The force goes to zero when the distance between the atoms reaches a couple of angstroms, about the length of a chemical bond. When the total van der Waals force becomes positive (repulsive), the atoms are theoretically in contact. The slope of the van der Waals curve is very steep in the repulsive regime. As a result, the repulsive van der Waals force balances almost any force that attempts to push the atoms closer together. For AFM, this means that when the cantilever pushes the tip against the sample, the cantilever bends rather than forcing the tip atoms to come closer

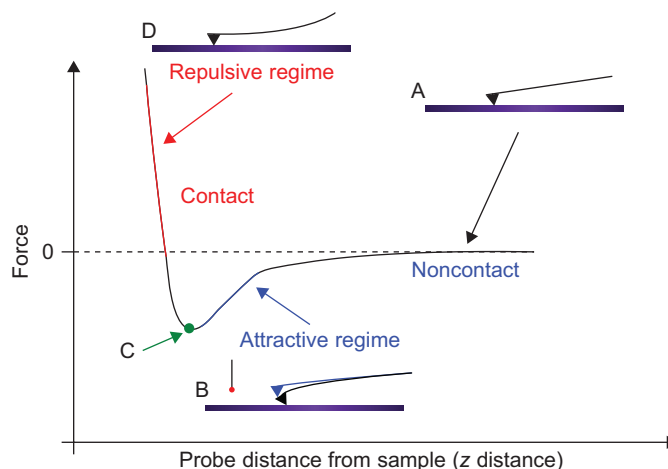


FIGURE 4.1

Interatomic force versus distance curve.

to the sample atoms. Even if you design a very stiff cantilever to exert large forces on the sample, the interatomic separation between the tip and sample atoms is unlikely to decrease much. Instead, the sample surface is likely to deform.

Contact Mode: The probe is essentially dragged across the sample surface while the force between the tip and the surface is kept constant during scanning. As the topography of the sample changes, a feedback loop maintains a constant deflection between the cantilever and the sample by vertically moving the scanner at each (x, y) data point to maintain a set deflection. By maintaining a constant cantilever deflection, the force between the tip and the sample remains constant. The computer stores the distance that the scanner moves vertically at each (x, y) data point to form the topographic image of the sample surface. To minimize the amount of applied force used to scan the sample, low spring constant ($k \leq \text{N/m}$) probes are normally used. However, significant deformation and damage of soft samples (e.g., biological and polymeric materials) often occur in contact mode during imaging in air because significant force must be applied to overcome the effects of surface contamination (e.g., adsorbed moisture). The combination of a significant normal force, the lateral forces created by the dragging motion of the probe tip across the sample, and the small contact areas involved result in high contact stresses that can damage either the sample or the tip or both. To overcome this limitation, contact mode imaging can be performed within a liquid environment, which essentially eliminates problems due to surface moisture so that much lower contact forces can be used. In fact, the ability to image samples in a liquid environment is often a desirable capability of AFM.

Noncontact Mode: The probe has no contact with the sample surface to reduce or eliminate the damaging forces associated with contact mode. The cantilever is oscillated near its first bending mode resonance frequency as the probe is raster scanned above the surface. In noncontact mode, both the tip-sample separation and the oscillation amplitude are in the order of 1–10 nm, such that the tip oscillates just above the surface contamination layer, essentially imaging the surface of the adsorbed surface moisture. The resonance frequency and amplitude of the oscillating probe decrease as the sample surface is approached due to interactions with van der Waals, and other long-range, forces extending above the surface. These types of forces tend to be quite small relative to the repulsive forces encountered in contact mode. Either a constant amplitude or constant resonance frequency is maintained through a feedback loop with the scanner and, like in contact mode, the motion of the scanner is used to generate the topographic image. To reduce the tendency for the tip to be pulled down to the surface by attractive forces, the cantilever spring constant is normally much higher compared with the contact mode cantilevers. The combination of weak forces affecting feedback and large spring constants causes the noncontact AFM signal to be small, which leads to unstable feedback and requires slower scan speeds than either contact mode or tapping mode. Also, the lateral resolution in noncontact mode is limited by the tip-sample separation and is normally lower than that in either contact mode or tapping mode. In practice, noncontact mode is rarely used considering its technical difficulties. However, it could be a potential solution for imaging very soft materials such as a living cell's membrane.

Tapping Mode: The tapping mode is also called the dynamic contact mode. Tapping mode tends to be more applicable to general imaging in air, particularly for soft samples, as the resolution is similar to contact mode while the forces applied to the sample are lower and less damaging. In fact, the only disadvantages of tapping mode compared with contact mode are that the scan speeds are slightly slower and the AFM operation is a bit more complex, but these disadvantages tend to be outweighed by the advantages. In tapping mode, the cantilever oscillates close to its first bending mode resonance frequency, as in noncontact mode. However, the oscillation amplitude of the probe tip is much larger

than that of noncontact mode, often in the range of 20–200 nm, and the tip makes contact with the sample for a short duration in each oscillation cycle. As the tip approaches the sample, the tip-sample interactions alter the amplitude, resonance frequency, and phase angle of the oscillating cantilever. During scanning, the amplitude at the operating frequency is maintained at a constant level (the set-point amplitude) by adjusting the relative position of the tip with respect to the sample. In general, the amplitude of oscillation during scanning should be large enough so that the probe maintains enough energy for the tip to tap through and back out of the surface contamination layer. Tapping mode AFM is the most useful scanning mode for almost all the applications considering its less destructive effects on both samples and tips. The loosely-attached nano-objects on the surface are often swept by the tip during contact mode scan but remain intact during tapping mode. Its manifold imaging type is another attractive feature for most users.

4.1.3 AFM-Based Nanomanipulation

The AFM probe used for collecting image data can also work as an end effector to modify the sample surface through the manipulation of pulling, scratching, pushing, and so on. In the last two decades, AFM has been proven to be a powerful manipulation tool, with users taking advantage of its high precision and high resolution. The pioneering work of AFM-based nanomanipulation can be tracked back to 1992 when Kim and Lieber demonstrated the rearrangement of thin oxide structures on the underlying surface by increasing the applied load during scanning with AFM [1]. In 1995, Junno et al. assembled GaAs particles with diameters of 30 nm into arbitrary nanostructures by controlled pushing under ambient conditions [2]. Schaefer et al. manipulated gold nanoparticles in HOPG surface into two-dimensional arrays of nanometer-sized clusters [3]. In 1998, Martin et al. assembled silver particle (with diameter 15 nm) into an “LTL” pattern with AFM in noncontact mode [4]. In 2003, Decossas et al. demonstrated they could straighten, bend, translate, reorient, and cut carbon nanotubes on glass substrate using contact AFM [5]. Yang and Sacher reported their research on the influence of set point in Cu particle manipulation with AFM [6]. In 2004, Muller et al. performed a 3-nm width lithography in mica surface with AFM [7]. In 2005, for the first time, Sugimoto et al. achieved Sn atom manipulation on the surface of Ge in normal temperature [8]. Although all the above research progress has proved the powerful ability of AFM as a manipulation tool, because AFM collects data for image by “feeling” rather than “looking,” there is no real-time visual feedback available during manipulation due to the slow speed of AFM scan. Thus, all the above work is carried out in the dark, and the operation result has to be verified by a new image scan after each step of the manipulation. Obviously, this scan–design–manipulation–scan cycle is very time-consuming and has low effectiveness.

To obtain the real-time feedback, some researchers tried to use a haptic technique and virtual reality interface to facilitate AFM-based nanomanipulation. In addition to providing a virtual reality interface for the operator, Sitti and Hashimoto linked a 1-DOF haptic device to the AFM system through which the operator can sense the vertical force acting on the probe during manipulation [9]. However, the 1-DOF force feedback may provide spurious force feeling because the manipulation force is mainly in the lateral direction instead of normal direction. Guthold et al. [10] connected the AFM to a PhantomTM stylus (a haptic device from Sensable Inc.) with the function of 3D force feedback. In imaging mode, the topography data from AFM are sent to the PhantomTM, and the operator can “feel” the topography of the sample. In manipulation mode, the PhantomTM can be used to move the tip over the surface while keeping the internal normal force feedback on. However, it is still not clear whether the mapping

from topography information to force information is helpful to the operation. Furthermore, although a virtual reality interface can display a static virtual environment and a dynamic tip position, it does not display the environment changes during manipulation. The operator is still “blind” because the environment changes are not updated in real time. Thus, any method that can show the real-time changes of manipulation result and provide more vivid 3D force feedback to the operator will significantly improve the efficiency and effectiveness of AFM-based nanomanipulation. The followed AFM-based nanorobotic system is a feasible way to approach this goal.

4.2 AFM-BASED AUGMENTED REALITY SYSTEM

The AFM-based nanorobotic system aims to provide both the 3D force feedback and real-time visual feedback to the operator. The mechanism of the nanorobotic system is shown in Fig. 4.2. It includes two subsystems which are connected through the ethernet: the AFM system and the augmented reality system. During manipulation, the operator can not only feel the real-time 3D manipulation force, but also directly control the 3D movement of AFM tip through the haptic device. At the same time, the visual feedback interface provides a movie-like display to show the real-time changes of the manipulation result. In this way, several steps of operation can be carried out without a image scan in between, which in turn significantly improves the effectiveness and efficiency of AFM-based nanomanipulation.

4.2.1 Principle for 3D Nanoforce Feedback

Real-time force feedback is a key factor for fully realizing the function of nanorobotic system, through which the operator can sense the interaction force between the AFM tip and the object. Since AFM itself is a force sensing tool, the real-time manipulation force can be mapped out by monitoring the cantilever deformation that is sensed through detecting the displacement of the reflected laser beam

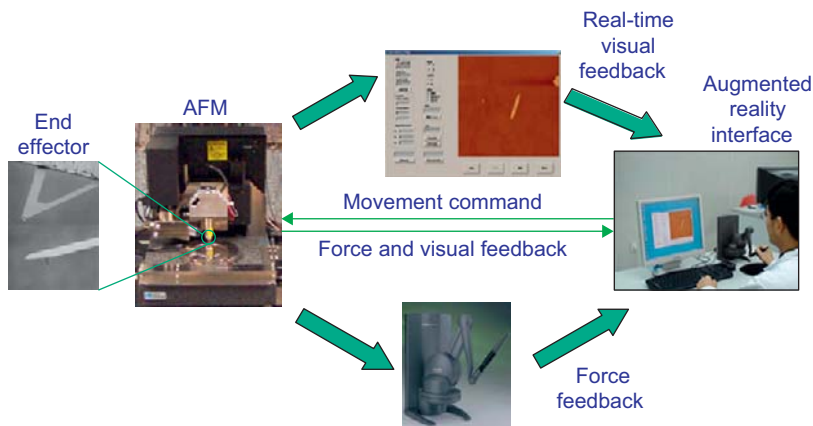


FIGURE 4.2

The AFM-based nanorobotic system.

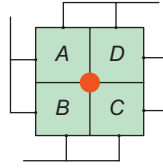


FIGURE 4.3

Quad photodiode detector: A , B , C , and D are the signal outputs of the quad photodiodes. Solid circle delegates laser position.

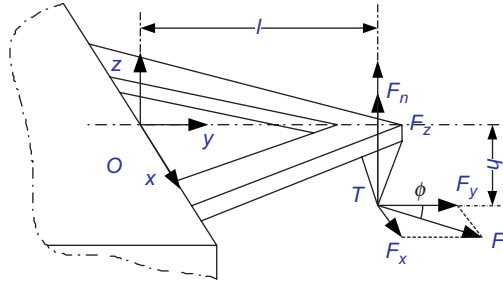


FIGURE 4.4

Force analysis model of the cantilever: l is the cantilever length; h is tip height which includes the thickness of the cantilever; and T is the tip apex.

with a split photodiode. The split photodiode consists of four regions (A , B , C , and D) with independent signal output as shown in Fig. 4.3. The signals on behalf of the cantilever deflection and the cantilever torsion S_n and S_l can be calculated respectively through the following equations:

$$\begin{cases} S_n = \frac{(A+B) - (C+D)}{A+B+C+D} \\ S_l = \frac{(A+C) - (B+D)}{A+B+C+D} \end{cases} \quad (4.1)$$

While PSD only provides the information of cantilever deformation in normal and lateral directions, it is necessary to model the cantilever to obtain a 3D force from this 2D PSD signal. Since the size of the objects under manipulation is usually small compared with the size of the cantilever-tip body, therefore, the force applied to the tip by the object can be considered as a point force on the tip apex. Then the force model of the cantilever can be expressed as shown in Fig. 4.4. O is the origin of cantilever frame; l is the length of the cantilever; h is tip height which includes the thickness of the cantilever; T is the tip apex. The normal force applied to the AFM tip can be calculated from cantilever deflection according to the spring model of the cantilever,

$$F_n = k\delta_z \quad (4.2)$$

where F_n is the pseudo normal force that is defined in Eq. (4.4), k is the spring constant of the cantilever, δ_z is the cantilever deflection in z direction. Once the deflection and spring constant are known, the normal force can be calculated.

The lateral force F_x will twist the cantilever around its axis with a angle θ_x , the relationship in between can be expressed as

$$F_x = \frac{k_t}{h} \theta_x \quad (4.3)$$

where k_t is the torsional constant of the cantilever.

The pseudo normal force F_n is the combination effect of force F_z and F_y both of which cause a vertical deflection of the cantilever. The relationship among F_n , F_z , and F_y can be expressed as

$$F_n l = F_y h + F_z l \quad (4.4)$$

Suppose the tip lateral motion direction has an angle ϕ with respect to the y axis of the cantilever frame, then the lateral force, F_l , must be opposite to the direction of the tip motion and its amplitude can be found by

$$F_l = \frac{F_x}{\sin \phi} \quad (4.5)$$

Then the lateral force along y axis can be expressed as

$$F_y = F_x \cot \phi \quad (4.6)$$

The relationship between σ_z and S_n , θ_x , and S_l is

$$\delta_z = K_N S_n \quad (4.7)$$

$$\theta_x = K_T S_l \quad (4.8)$$

where K_N and K_T are system constants that need to be calibrated; more detailed information for the calibration of these two parameters can be found in [11, 12].

Substituting Eq. (4.7) and Eq. (4.2) into Eq. (4.4), we can get the following equations for calculating the 3D manipulation forces:

$$\begin{cases} F_x = \frac{k_t K_T S_l}{h} \\ F_y = F_x \tan(\frac{\pi}{2} - \phi) \\ F_z = k K_N S_n - \frac{h}{l} F_y \end{cases} \quad (4.9)$$

By feeding the 3D forces $[F_x; F_y; F_z]^T$ to the haptic device, the operator can sense the forces, which are proportional to the actual forces acting on the cantilever. One thing need to be pointed out is that there will be a minor change for force calculation if the AFM frame is different from the cantilever frame, such as the AFM scanned the sample with a nonzero angle φ . The 3D forces need to be multiplied by a rotational matrix that is determined by the angle φ before they are output to the haptic device for force feedback [12].

4.2.2 Principle for Real-Time Visual Feedback Generation

In addition to providing the real-time force feedback to the operator, real-time visual feedback is also needed to improve the efficiency and effectiveness of AFM-based nanomanipulation. Since the manipulated object is often in the size of just over 10 nanometers, the traditional optical microscopy cannot observe these very tiny objects. Although AFM does have a resolution down to nanometer scale, it cannot perform image scans and manipulation simultaneously. Thus, the real-time feedback is not available during manipulation due to the slow speed of the image scan. Here we adopt a model-based simulation method to generate a movie-like visual display that mimics the real-time changes of the true nanoenvironment. This visual display is calculated based on the previously scanned image, off-line model, and real-time forces. Figure 4.5 shows the generation mechanism of the real-time visual feedback. From this picture, we can see that the behavior model of the object is one of the prerequisites to generate the video feedback. Refs [12] and [13] provide a detailed analysis to the movement of the nanorod and nanoparticle respectively, during the tip-based manipulation. While any model may be different to the true environment, the modeling error may lead to a false visual display and a failed manipulation. We will discuss a strategy to overcome this problem in Section 4.3.

4.2.3 Experimental Testing and Discussion

In this section, we will show some experimental results that demonstrate the increased efficiency and effectiveness of the AFM-based nanomanipulation with the proposed methods.

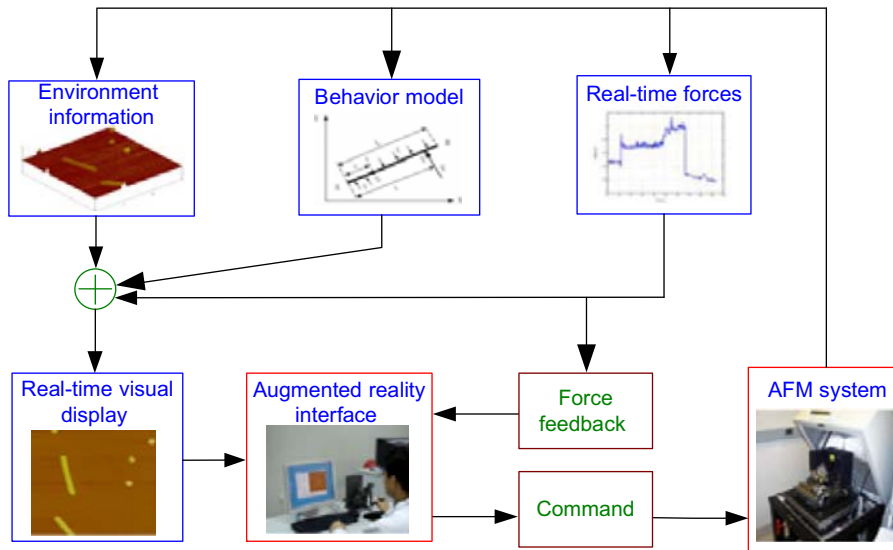
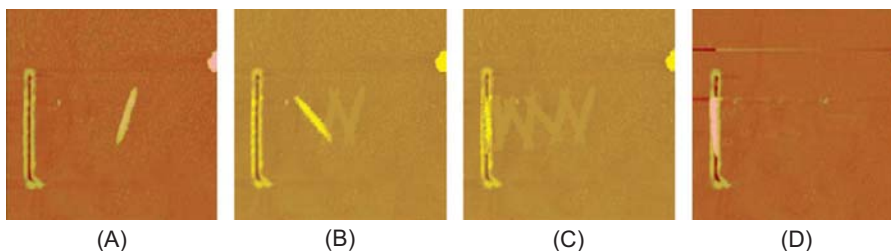


FIGURE 4.5

Schematic diagram for building real-time visual feedback.

**FIGURE 4.6**

(A) Silver nanowire with diameter of 100 nm and length of 1.3 μm on a smooth polycarbonate surface in scanning range of 5 $\mu\text{m} \times 5 \mu\text{m}$. The trench is created in advance on the surface by inscribing the tip into the surface. (B) and (C) Image displayed in the augmented reality interface. The pushing operation on nanowire drives the wire into the fixture. (D) AFM image by a new scan after the final pushing operation.

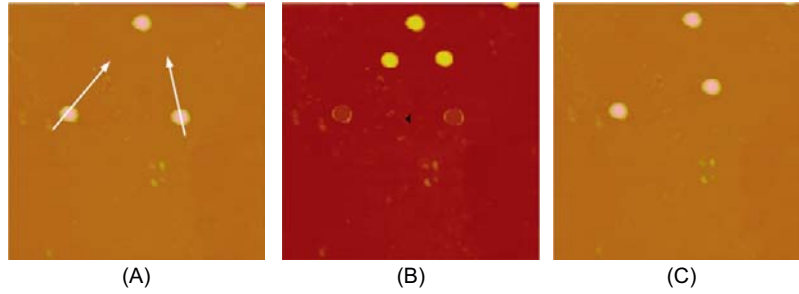
A. Nanomanipulation with Augmented Reality System

Nanorods are manipulated to demonstrate the efficiency and effectiveness of the AFM-based nanorobotic system. Figure 4.6A shows a silver nanorod (diameter 100 nm, length 1.3 μm) deposited on the surface of polycarbonate with a trench created in advance. Figure 4.6B and C is the real-time visual feedback displayed in the augmented reality system. The visual display shows that the nanowire has been pushed into the trench successfully. The real result from a new AFM image, as shown in Fig. 4.6D, has the same result as in the augmented reality interface, as shown in Fig. 4.6C. From these pictures, we can see the visual display can match the true manipulation result very well. Several steps of manipulation can be performed successively without an image scan in between, which in turn shows the increased efficiency and effectiveness of AFM-based nanomanipulation.

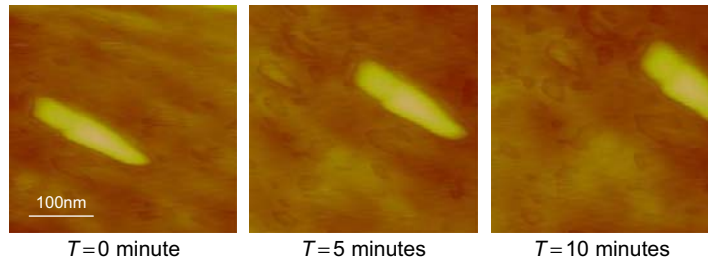
B. Discussion: Limitations of Augmented Reality System

Although the augmented reality system has greatly improved the efficiency and effectiveness of AFM-based nanomanipulation through providing the real-time force and visual feedback to the operator, there are still several shortcomings that hinder its wide application.

The first problem is the poor reliability of the real-time visual feedback. Although the augmented reality system can provide a real-time visual feedback to the operator, this kind of real-time visual display is not the true manipulation results, but graphical simulation based on the behavior models. Because any model may be different to the true environment, especially in the nanoworld, microforces such as surface tension, the van der Waals force, capillary forces, and so on are very complex and interact with each other. It is difficult to ascertain the accurate behavior model of nano-object, which in turn results in an inaccurate visual display and a failed manipulation. Figure 4.7 is such an example; two nanoparticles are manipulated along the arrow direction to form a triangle pattern as shown in Fig. 4.7A. Figure 4.7B is the manipulated results displayed in the real-time visual feedback and shows that the triangle pattern is formed very well. Figure 4.7C is the true manipulation result obtained from a new image scan. Through these pictures we can see the real-time visual display may not match the true result during manipulation. This phenomenon is common in nanomanipulation with augmented reality system especially for nanoparticle manipulation. Thus, it is very important to find a way to solve this problem and improve the reliability of the real-time visual feedback.

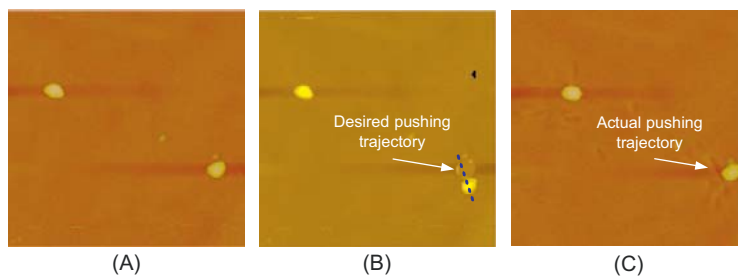
**FIGURE 4.7**

An inaccurate model leads to a faulty visual display and a failed nanomanipulation. Operation area: $7\ \mu\text{m} \times 7\ \mu\text{m}$, latex radius: 175 nm. (A) Manipulating two particles along the arrow directions. (B) The image of manipulation result displayed in the real-time visual feedback interface. (C) A new scanned AFM image after final manipulation.

**FIGURE 4.8**

Three images are scanned continuously with 5-minute interval.

The second problem is the positioning error caused by the random drift. Random drift is caused by many factors such as the contraction and expansion of the mechanical system, temperature variety, humidity change, and so on [14–16]. Due to random drift, nanomanipulation can be likened to using AFM to manipulate a nano-object that is in a conveyor. Random drift accompanies the manipulation process all the time. Figure 4.8 shows a sequential image scan with time interval of 5 minutes. Even with the scanning parameters kept constant, there is still an obvious drift between the AFM tip and the sample. Since all the AFM-based nanomanipulation is performed based on the previously scanned image, the random drift will cause a position error between the current manipulation coordinates and the true environment. Furthermore, if the random drift is larger than the size of the nano-object, the AFM tip may not be able to touch the object at all during manipulation. In Fig. 4.9B, the dashed line shows the desired push trajectory of the nanoparticle. The visual feedback shows that the particle has been pushed away by the AFM tip. But due to random drift, there was a positioning error between the display coordinates and the manipulation coordinates. Figure 4.9C is the true manipulation result from a new image scan. Comparing (B) with (C), we can see there is a rightward drift during manipulation,

**FIGURE 4.9**

Tip positioning error caused by thermal drift.

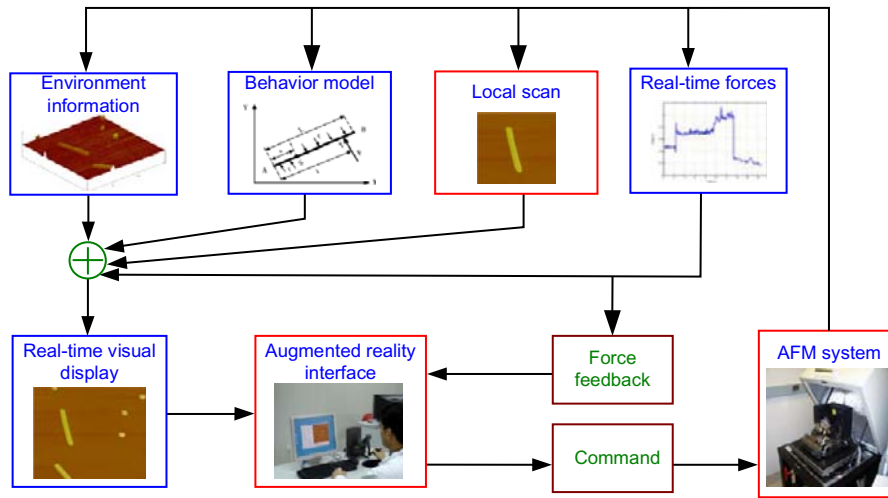
which causes the tip to shave the particle instead of pushing it away. Thus, it is critical to compensate the positioning error arising from random drift to perform a successful manipulation.

4.3 AUGMENTED REALITY SYSTEM ENHANCED BY LOCAL SCAN

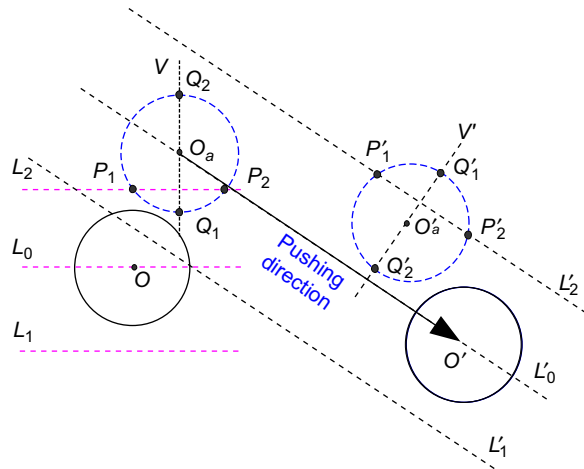
As discussed in last section, random drift and faulty visual feedback are the main issues hindering the efficiency and effectiveness of any AFM-based augmented reality system. In this section, a local scan algorithm is developed and implemented to the former-developed augmented reality system for solving these problems. The local scan algorithm mainly includes two subprocess: Local Scan Before Manipulation (LSBM) and Local Scan After Manipulation (LSAM). LSBM is used to detect and compensate for the positioning error caused by the random drift. LSAM is used to sense the true manipulation result and correct the faulty visual display aroused from the modeling errors. After the local scan algorithm is implemented into the augmented reality system, the schematic diagram for generating the visual display has changed from what we saw in Fig. 4.5, to that shown in Fig. 4.10. In this configuration, the real-time visual display not only relies on the behavior models but also depends on the real-time sensing result from local scan. In this way, the positioning error caused by random drift and faulty display arising from modeling errors can be moved out in manipulation. The following section will give a detailed explanation for the local scan algorithm by assuming that nanoparticles and nanorods are manipulated objects. But the algorithm is not limited to these two shapes, it can be expanded to objects with different shapes through a minor change of the local scan pattern.

4.3.1 Local Scan Mechanism for Nanoparticle

A round nanoparticle is one of the fundamental particles for building nanodevices and nanostructures. The location of a nanoparticle can be determined by its center position and radius. The radius of each nanoparticle can be obtained through the scanned image taken before the manipulation. But due to random drift and model errors, the displayed position may not represent the actual position. The actual center of a nanoparticle can be recovered by two local scan actions before and after each manipulating operation. The LSBM can eliminate the thermal drift, whereas the LSAM mainly minimizes the effects of model errors, correcting the final position of the nanoparticle in the visual display.

**FIGURE 4.10**

Schematic diagram of the new real-time display supported by local scan.

**FIGURE 4.11**

Online sensing patterns to identify the actual position of a nanoparticle. The arrow indicates the pushing direction. Reproduced with permission from IEEE [17].

Figure 4.11 shows the online sensing process whilst manipulating a particle. The solid circle O represents the particle position on the AFM image before manipulation. Since there is random drift, the particle is actually at the position of the dashed circle O_a . To find this real position, the LSBM needs to scan at least two lines: one or more horizontal lines and one vertical line. First, AFM scans

along Line L_0 , which passes through point O , the displayed center of the particle on the image. If the particle was not found, then the scanning line moves up and down alternatively by a distance of $3R/2$ until the particle is found, where R is the radius of particle. Once the particle is found, the scanning line forms two intersection points with the boundary of the particle, P_1 and P_2 . A vertical line V , which goes through the midpoint between P_1 and P_2 and is perpendicular to the previous scanning line, is scanned to find the center of the particle. The vertical scanning line has two intersection points with the boundary of the particle, Q_1 and Q_2 . The center of the nanoparticle O_a is located at the midpoint between Q_1 and Q_2 . The length of the scanning line L is determined by the maximum random drift such that $L > 2(R + rmax)$, where $rmax$ is the maximum random drift distance and is determined through experiments.

After manipulating the particle along the pushing direction, the solid circle O' represents the model-calculated location of the particle. Since there may be some difference between the calculated location based on model and the real location, a LSAM is performed to correct the position errors in the visual display. At least two scanning lines are needed for the LSAM as shown in the right side of Fig. 4.11. First, AFM scans along line L'_0 , which passes through the initial actual center and along the tip motion direction. If the particle was not found, then the scanning line moves up and down along the direction perpendicular to line L'_0 alternatively by a distance of $3R/2$ until the particle is found. Once the particle is found, the scanning line forms two intersection points with the boundary of the particle, P'_1 and P'_2 . Another line V' , which goes through the midpoint between P'_1 and P'_2 and is perpendicular to the previous scanning line, is scanned to find the actual center of the particle. The last scan line has two intersection points with the boundary of the particle, Q'_1 and Q'_2 . The final actual center of the nano-particle O'_a , is located at the midpoint between Q'_1 and Q'_2 . The length of the scanning line L' is determined by the maximum random drift and the pushing distance such that $L' > \Delta + 2(R + rmax)$, where Δ is the pushing distance. The visual display is updated immediately after the actual position obtained.

4.3.2 Local Scan Mechanism for Nanorod

Nanorods and nanowires are fundamental shapes for forming nanodevices and nanostructures. The location of a nanorod is determined by its width and two ends in a local scan for convenience. The initial displayed rod width and ends are identified from a previously-captured AFM image before the manipulation. Due to the random drift, the displayed position may not represent the actual position. The random drift usually causes translational error, whereas the modeling error causes both translational and rotation errors. Local scan algorithm is required to determine the actual center position and orientation of the nanorod. The location of a nanorod can be recovered by two local scan actions, before and after each manipulating operation. The LSBM eliminates the random drift, whereas the LSAM mainly minimizes the effects of model errors, correcting the final position of the rod in the visual display.

Figure 4.12 shows the online sensing processes during manipulating a rod. The solid rectangle A represents the rod location on the AFM image before manipulation. Due to random drift, the rod is actually at the location of dashed rectangle B . To find this real position, the LSBM needs to scan at least two lines: one or more lines perpendicular to the rod orientation and one line parallel to the rod orientation. First, AFM scans along Line L_0 , which passes through the displayed center of the rod and perpendicular to the rod orientation. If the rod is not found, then the scanning line moves up and down alternatively by a distance of $L/4$ until the rod is found, where L is the length of the rod. Once the rod is

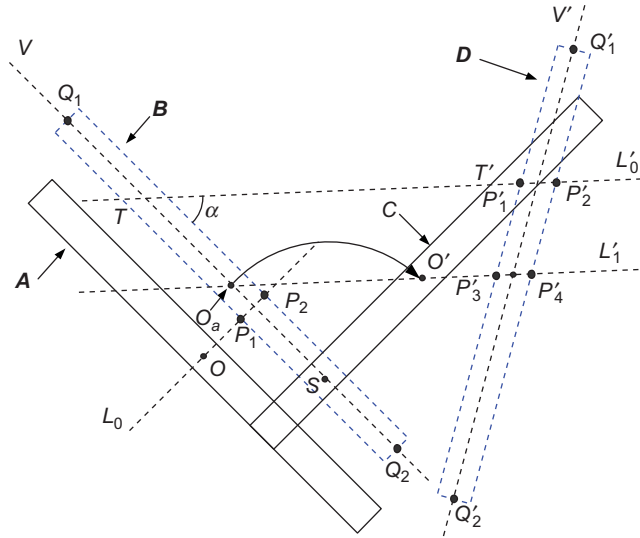


FIGURE 4.12

Online sensing patterns to identify the actual location of a nanorod. Reproduced with permission from IEEE [17].

found, the scanning line forms two intersection points with the boundary of the rod, P_1 and P_2 . Another line V , which passes through the midpoint between P_1 and P_2 and is parallel to the rod orientation, is scanned to find the actual two ends of the rod. The scanning line V has two intersection points with the boundary of the rod, Q_1 and Q_2 . These two points are the actual two ends of the rod. The actual rod center, orientation can be calculated from these two points. The visual display is updated immediately with the actual location of the rod. The length of the scanning line L_0 is determined by the maximum random drift such that $L_0 > 2d + rmax$, where d is the width of the rod, and the length of the scanning line V is determined by the length of the rod such that $V = 2L$, where L is the length of the rod.

After manipulating the nanorod along the pushing direction, the solid rectangle C represents the model-calculated location of the rod after manipulation. Because any model may be different to with the true manipulation result, the actual position is not exactly at C . The dashed rectangle D represents the real rod position. To find this real position, LSAM needs to scan at least three lines. First, as shown in Fig. 4.12, the AFM scans along Line L'_0 , which passes through the initial pushing point, T , and along the direction $\overrightarrow{O_a O'}$. If the rod was not found, then the scanning line goes along line $O_a O'$. If the rod is still not found, the scanning action continues by moving the scan line up and down by a distance of $(L \sin \alpha)/4$ until two scan lines can locate the rod, where α is the angle between the pushing direction and the initial rod orientation. Each of the two scan lines has two intersection points with the boundary of the rod. For example P'_1 and P'_2 for L'_0 , P'_3 and P'_4 for L'_1 . Another line V' , which goes from the midpoint between P'_1 and P'_2 to the midpoint between P'_3 and P'_4 , is scanned to locate the two actual ends of the rod. The scanning line V' has two intersection points with the boundary of the rod, Q'_1 and Q'_2 , which are the actual ends of the rod. The actual rod center will locate at the midpoint between Q'_1 and Q'_2 . The orientation of the rod will along the direction $\overrightarrow{Q'_1 Q'_2}$. The length of the scanning Line L'_0 is

determined by the maximum random drift and the pushing distance such that $L_0 > \Delta + d/\sin\alpha + r_{max}$, where Δ is the pushing distance. The length of the scanning Line V' is $2L$, where L is the length of the rod. The visual display is updated immediately after the actual position is obtained.

4.3.3 Nanomanipulation with Local Enhanced Augmented Reality System

Manipulation of nanoparticles and nanorods are performed to demonstrate the advantages of the local scan algorithm.

A. Manipulation of Nanoparticles

In this experiment, Nanoparticles are manipulated to validate the effect of OSD method. As shown in Fig. 4.13A, several latex particles with diameter around 110 nm were randomly distributed on a flat polycarbonate surface (scanning range: $3.1\ \mu\text{m} \times 3.1\ \mu\text{m}$). Before nanomanipulation, a LSBM was performed to eliminate the random drift. Since random drift occurred between the whole image and the AFM tip, the position error obtained from the LSBM existed between every particle and the AFM tip. Thus, instead of updating the visual display image with the new position of particles, the drift displacement was added onto the motion command of AFM tip as an offset value.

As shown in Fig. 4.13B, one particle was pushed along the arrow direction. The indent in the rectangle is the visual displayed final particle position based on the behavior model. Because there are a lot of uncertainties with nanoscales, the visual display may not be true due to a modeling error. A local scan was immediately performed after the manipulation. The position obtained from local scan is shown as the circle in Fig. 4.13B. Figure 4.13C shows a new captured AFM image after manipulation. The good match of these two pictures proves that the OSD method identified the actual particle position correctly. The scanning pattern in this experiment is generated as shown in Fig. 4.14A. The topography information of the scanning lines is shown in Fig. 4.14B. The actual position of the nanoparticle can be easily identified based on the topography information along the scan lines as described in Section 4.3.1.

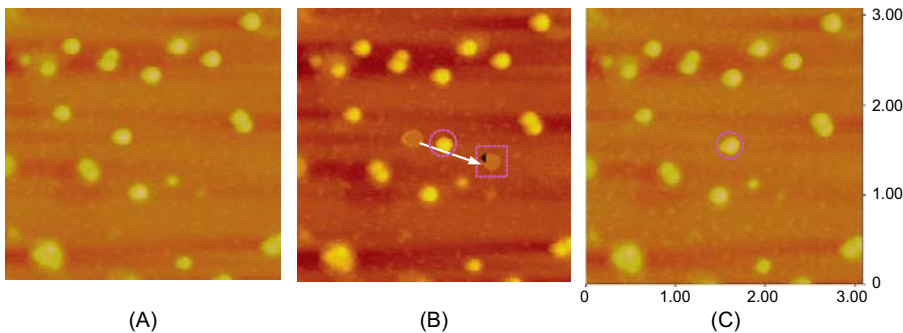
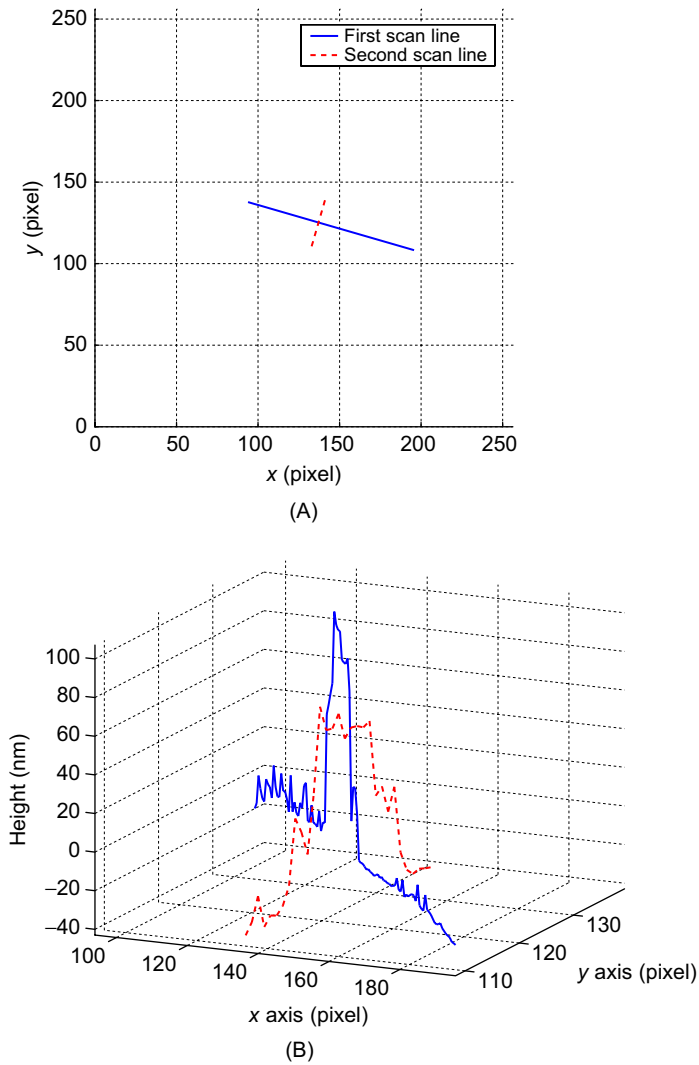


FIGURE 4.13

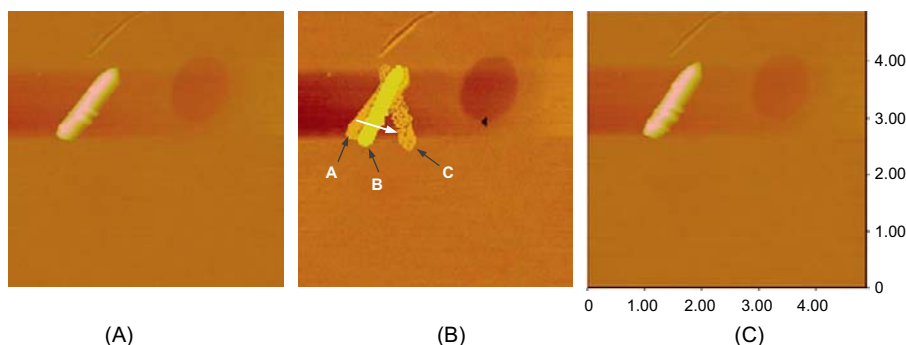
Manipulating a nanoparticle on a polycarbonate surface with scanning range $3.1\ \mu\text{m} \times 3.1\ \mu\text{m}$. (A) Latex particle with diameter 110 nm on polycarbonate surface before manipulation. (B) Real-time display on the visual feedback interface. (C) A new scanned AFM image after manipulation. Reproduced with permission from IEEE [17].

**FIGURE 4.14**

Local scan pattern and result for the nanoparticles. (A) The scan pattern of LSAM for nanoparticles. (B) The topography information along the scanning lines. Reproduced with permission from IEEE [17].

B. Manipulation of Nanorods

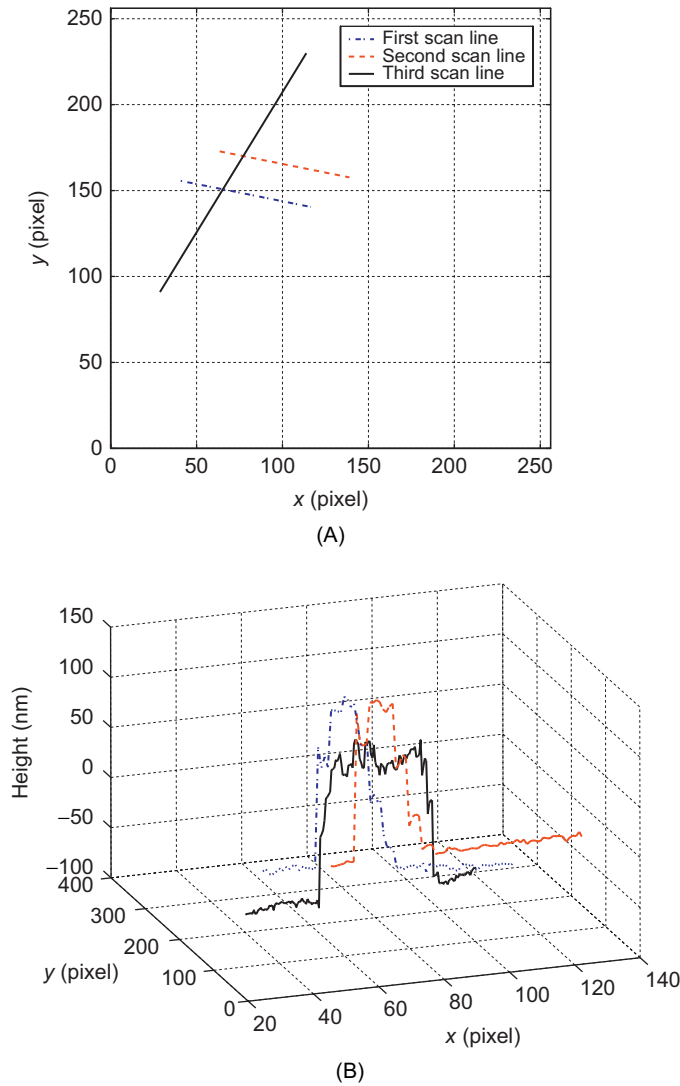
Experiments with manipulating nanorods were also carried out to verify the effectiveness of the local scan algorithm. As shown in Fig. 4.15A, a nanorod with a diameter of 170 nm was deposited on the polycarbonate surface (scanning range $5\ \mu\text{m} \times 5\ \mu\text{m}$). Figure 4.15B shows the rod being pushed from one end and rotated around the other end as predicted by the model in [12]. The final position of

**FIGURE 4.15**

Manipulating a nanorod on the polycarbonate surface with scanning range $5\mu\text{m} \times 5\mu\text{m}$. (A) A silver rod with diameter 170 nm deposited on polycarbonate surface before nanomanipulation. (B) Real-time display on the visual feedback interface. (C) A new AFM image after manipulation. Reproduced with permission from IEEE [17].

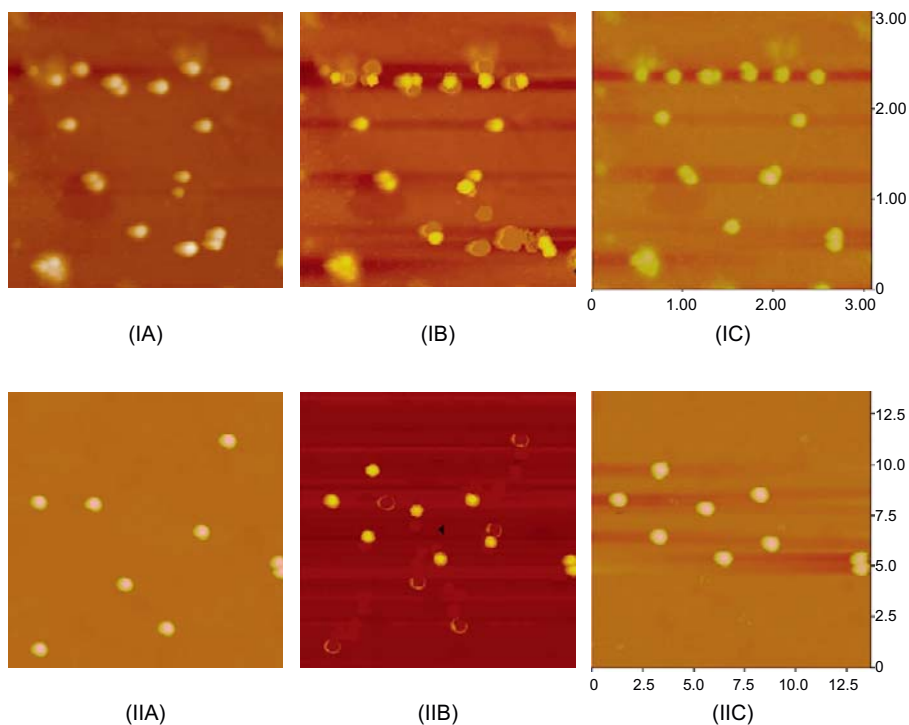
visual display is shown as C in Fig. 4.15B. But through local scanning, the real position of the rod was identified as B. Figure 4.15C shows a new captured AFM image after manipulation. The good match of the two pictures proves that the actual location of the rod can be accurately identified by online sensing. The scanning pattern for nanorods is generated as shown in Fig. 4.16A. The topography information along the scanning lines is shown as in Fig. 4.16B. From the topography information, the actual location of the nanorod can be obtained. Here the different max height between the first two scan lines and the third scan line is due to the data process for removing the offset and eliminating the tilt, but the relative height along the scanning line keeps constant. The same reason is for Fig. 4.13B.

Both Figs 4.13 and 4.15 show a common situation in AFM-based manipulation: the AFM tip is easy to slip over or slip away from the object. This situation is more serious during nanoparticle manipulation. Without local scan algorithm, a new image scan is needed to find the actual position of the lost particle. With the assistance of a local scan algorithm, the object's actual position can be obtained without a new image scan. The reliability of the visual feedback is greatly enhanced. Since only several lines are scanned, the local scan process can be finished without interrupting manipulation. Operators can immediately know the result after each step of manipulation. Figure 4.17 shows particles with different diameter are manipulated under the assistance of a local scan. The real-time AFM image is displayed in the augmented reality interface as shown in Figs 4.17IB and IIB. A new scanning image after manipulation is shown as in Figs 4.17IC and IIC. The two pictures show that the final result matches well with the display in the visual feedback interface. Although these two pictures match well with each other, there is still a small error of the latex particles final position between the visual display and the final result. This is mainly due to the bending of the cantilever in a normal direction existing in manipulation, while not in a local scan. The bending will cause a lateral displacement along the length direction of the cantilever [13]. The reason that the diameter of the particle in Fig. 4.17IIC looks bigger than IIA because the tip has been contaminated during manipulation. Figure 4.18 shows another example where a nanorod with diameter 170 nm is manipulated with the assistance of a local scan

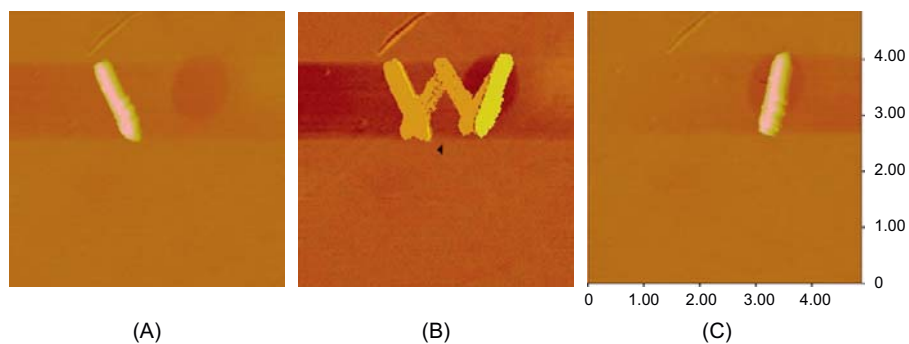
**FIGURE 4.16**

Local scan pattern and result for nanorod. (A) The scan pattern of LSAM for nanorods. (B) The topography information of the scanning lines. Reproduced with permission from IEEE [17].

algorithm, and the display result matches the new image scan. All of these experiments are finished continuously in a couple of minutes. From these experimental studies, it can be seen that assembly of nanostructures using the AFM-based nanomanipulation system becomes very straightforward and highly efficient.

**FIGURE 4.17**

Manipulating nanoparticles with different diameter (I: 110 nm, II: 350 nm) on polycarbonate surface. The operation range is $3.1\ \mu\text{m} \times 3.1\ \mu\text{m}$ in I and $13.6\ \mu\text{m} \times 13.6\ \mu\text{m}$ in II. (A) Image of latex particles on a polycarbonate surface before manipulation. (B) The image of manipulation result displayed in the real-time visual feedback interface. (C) A new scanned AFM image after final manipulation. Reproduced with permission from IEEE [17].

**FIGURE 4.18**

(A) Silver nanowire with length of $1.5\ \mu\text{m}$ on a smooth polycarbonate surface. (B) The image of manipulation result displayed in the real-time visual feedback interface. (C) A new scanned AFM image after final manipulation. Reproduced with permission from IEEE [17].

4.4 CAD-GUIDED AUTOMATED NANOASSEMBLY

In order to increase the efficiency and accuracy in nanomanufacturing, automated CAD-guided nanoassembly is desirable. A general framework for automated nanoassembly is developed to manufacture nanostructures and nanodevices, as illustrated in Fig. 4.19. Based on the distribution of nano-objects on a surface from an AFM image, the CAD model of a nanostructure is designed. The tip path planner generates manipulation paths to manipulate nano-objects. The paths are fed to a user interface to simulate the manufacturing process and then to the AFM system to perform the nanomanufacturing process.

The AFM tip path planner is the core of the general framework. Figure 4.20 shows the architecture of the tip path planner. Nano-objects on a surface are first identified based on the AFM image.

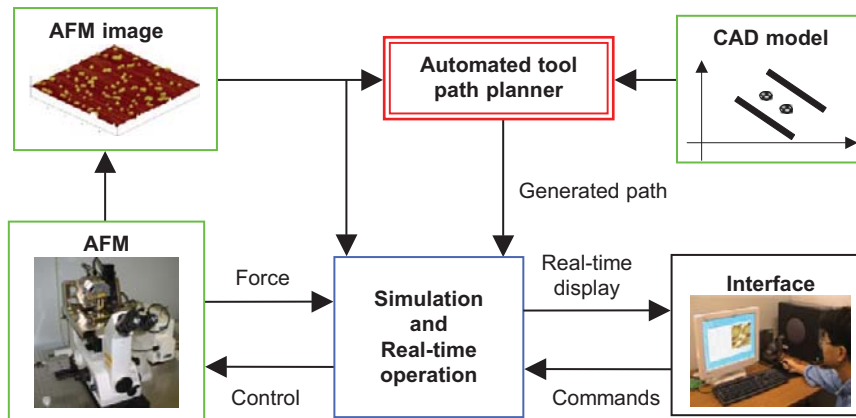


FIGURE 4.19

The general framework for an automated path generation system. The bottom left is the AFM system and the bottom right is the augment reality interface used for simulation and real-time operation.

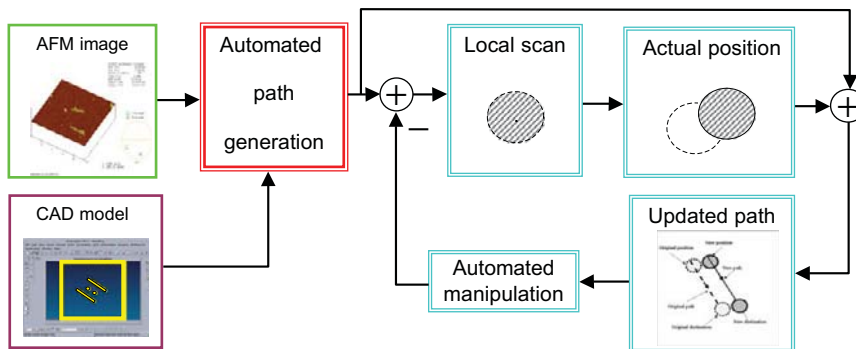


FIGURE 4.20

Automated tip path planner. Initial paths are generated based on the CAD model. Each path is adjusted individually according to each local scanning results.

A nanostructure is then designed using the available nano-objects. Initial collision-free manipulation paths are then generated using the CAD model of a designed nanostructure. In order to overcome the drift, a local scanning method is then applied to identify the actual position of a nano-object before its manipulation. Each manipulation path is then adjusted accordingly based on its actual position. The regenerated path is then sent to the AFM system to manipulate the nano-object. The process continues until all nano-objects are processed. A nanostructure is finally fabricated. Therefore, there are several problems that have to be solved to automatically manufacture nanostructures: identification of nano-objects; design of a nanostructure; automatic generation of manipulation paths and drift compensation. These problems will be discussed in the following sections.

4.5 MODELING OF NANOENVIRONMENTS

Because the nano-objects are randomly distributed on a surface, the position of each nano-object has to be determined in order to generate a manipulation path. Also the nano-objects have different shapes, such as nanoparticles and CNTs. They have to be categorized before the manipulation because the manipulation algorithms for these nano-objects are different.

After an AFM image is obtained, as shown in Fig. 4.21, the nano-objects can be identified and categorized.

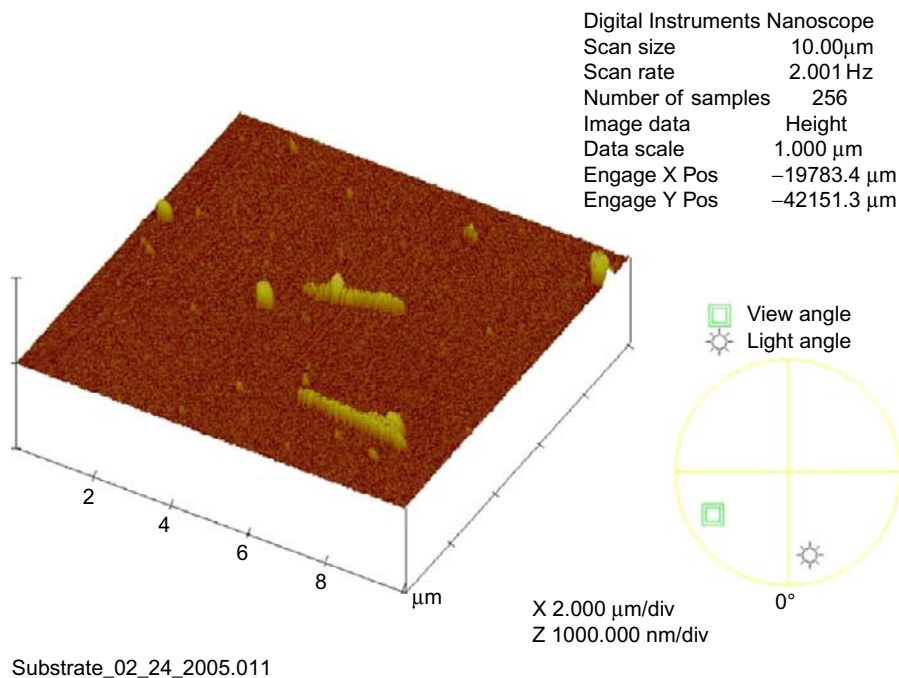


FIGURE 4.21

An image obtained from an AFM.

The (x, y) coordinates and the height information of each pixel can be obtained from the AFM image. First, a threshold related to the average height of the surface is set. The pixels with a height larger than the threshold are identified. Using the neighboring relationship of pixels, objects can then be identified. Straight lines are then fitted to each object using the following equations:

$$\begin{aligned} x &= my + b & \Delta x < x_0 \\ y &= mx + b & \Delta x \leq x_0 \end{aligned} \quad (4.10)$$

where x and y are the coordinates of a pixel; Δx is the difference between the maximum and minimum x coordinates of the nano-object; x_0 is a set value; m and b are parameters to be identified. The length of a nano-object can then be calculated by finding the intersecting points between the straight line and the object boundary. The width can be computed using the perpendicular line and the object boundary. If the length–width ratio is larger than a set value, it is considered as a CNT, otherwise, a nanoparticle.

It is difficult for the AFM tip to manipulate nanoparticles in big or small sizes because small objects are easy to be lost while large objects are hard to manipulate. Furthermore, using nano-objects with different sizes may cause gaps between components. Therefore, the size of a particle must be in a certain range to be considered as a nano-object; otherwise, it is an obstacle, i.e.,

$$\text{Nanoparticle} = \begin{cases} \text{Obstacle} & S_p \leq \alpha_1 \text{ or } S_p \geq \alpha_2 \\ \text{Object} & \alpha_1 < S_p < \alpha_2 \end{cases} \quad (4.11)$$

Similarly, a CNT can be considered as an object or an obstacle depending on its radius and length.

Since nano-objects are building blocks for assembly nanostructures, the nanostructures have to be designed based on the available nano-objects. Figure 4.22 shows a two-dimensional CAD model, designed with Unigraphics, for a nanostructure comprised of nanoparticles and CNTs. Because the

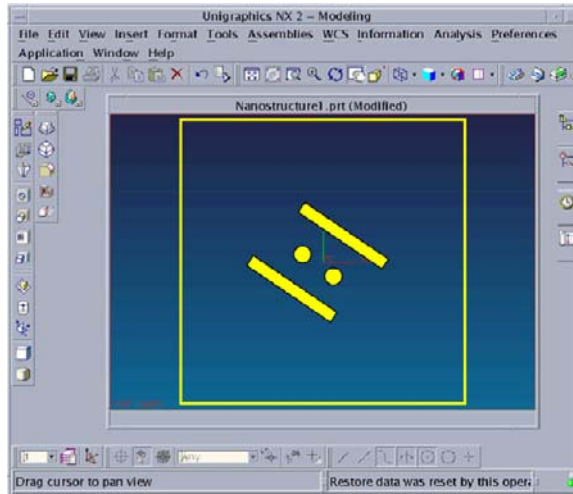


FIGURE 4.22

A two-dimensional CAD model for an exemplary nanostructure that may be constructed using nanoparticles and CNTs.

position of a nano-object in the CAD model is the destination where the nano-object is manipulated, it has to be identified before a manipulation path can be generated. The CAD model of the nanostructure is rendered into triangles first. The boundary of each nano-object is identified. The nano-object can then be categorized and its position can be determined using the boundary information.

4.6 AUTOMATED MANIPULATION OF CNT

The manipulation of a CNT is much more complicated than that of a nanoparticle because there is only translation during manipulating a nanoparticle, while there are both translation and rotation during manipulating a CNT. A CNT can only be manipulated to a desired position by applying force alternatively close to its ends. From an AFM image, CNTs can be identified and represented by their radius and two end points. Each end point on a CNT has to be assigned to a corresponding point on the destination. The starting pushing point is important because it determines the direction along which the object moves. By choosing a suitable step size, an AFM tip path can then be generated. Therefore, the steps of automated manipulation of CNT are:

- Find the initial position destination of a CNT;
- Determine the corresponding points;
- Find the starting pushing point;
- Calculate the pushing step and plan the tip trajectory.

The following are the details of the steps.

To automatically manipulate a CNT, its behavior under a pushing force has to be modeled. When a pushing force is applied to a CNT, the CNT starts to rotate around a pivot if the pushing force is larger than the friction force. Figure 4.23B shows the applied pushing force and the pivot. The CNT rotates around point D when it is pushed at point C by the AFM tip. The CNT under pushing may have different kinds of behavior, which depends on its own geometry property. If the aspect ratio of a CNT

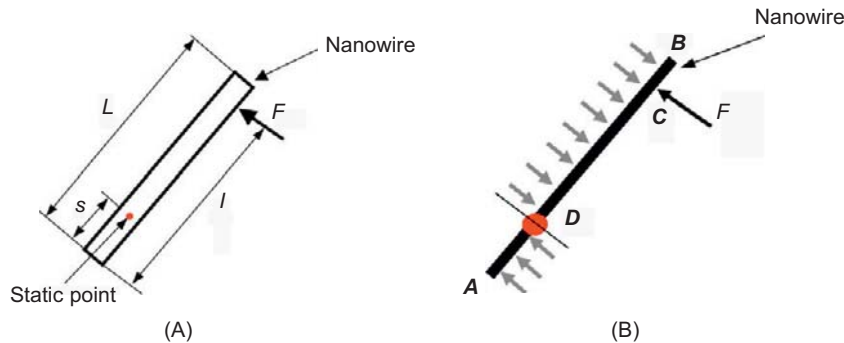


FIGURE 4.23

The behavior of a CNT under a pushing force: (A) F is the applied external force. (B) The detailed force model. D is the pivot where the CNT rotates, C the pushing point, and L the length of the CNT.

is defined as

$$\sigma = d/L \quad (4.12)$$

then a CNT with aspect ratio of $\sigma > 25$ usually behaves like a rod, which will deform or bend under pressure. The rotation behavior was observed for CNTs with aspect ratio of $\sigma < 15$. In this case, the pushing force F from the tip causes the friction and shear force $F' = \mu_{ot}F + \nu F_{ot}^a$ along the rod axis direction when the pushing direction is not perpendicular to the rod axis, where μ_{ot} and ν are the friction and shear coefficients between the tip and the CNT which depends on the material properties and the environment, F_{ot}^a is the adhesion force between the tip and the CNT.

Fortunately, it is easy to prove that the force F' hardly causes the rod to move along the rod axis direction. Assume that the shear forces between rod and surface are equal along all directions during moving, therefore

$$fL = f'_{max}d \quad (4.13)$$

Because the shear force is usually proportional to the contact area and the contact area between a CNT and surface is much greater than that between the tip and the CNT, therefore

$$\nu F_{ot}^a < f'd \quad (4.14)$$

Also note that

$$F < fL = f'_{max}d \quad (4.15)$$

and because μ is usually very small, finally it is reasonable to assume that

$$f'd = F'\mu F + \nu F_{ot}^a < f'_{max}d \quad (4.16)$$

This means that the rod will have no motion along the axis direction, therefore, the static point D must be on the axis of the CNT. Considering the above analysis, the CNT can be simplified as a rigid line segment. The external forces applied on the CNT in surface plane can be modeled as shown in Fig. 4.23B. The pivot D can be either inside the CNT or outside the CNT. First assume that D is inside the CNT. In this case, all the torques around D are self balanced during smooth motion.

$$F(l-s) = \frac{1}{2}f(L-s)^2 + \frac{1}{2}fs^2 \quad (4.17)$$

where F is the applied external force; f is the evenly distributed friction and shear force density on the CNT; L is the length of the CNT; s is the distance from one end of the CNT (point A in Fig. 4.23B) to the pivot D; l is the distance from A to C, where the external force is applied. Equation (4.17) can be written as

$$F = \frac{f(L-s)^2 + fs^2}{2(l-s)} \quad (4.18)$$

The pivot can be found by minimizing F with respect to s , i.e.,

$$\frac{dF}{ds} = 0 \Rightarrow s^2 - 2ls + lL - L^2/2 = 0 \quad (4.19)$$

Since we have assumed that $0 < s < L$, a unique solution of the pivot for any $0 < l < L$ except $l = L/2$ can be determined by

$$s = \begin{cases} l + \sqrt{l^2 - lL + L^2/2} & l < L/2 \\ l - \sqrt{l^2 - lL + L^2/2} & l > L/2 \end{cases} \quad (4.20)$$

When $l = L/2$, there is no unique solution. A detailed analysis will show that S can be anywhere when the force F is applied in the exact middle of the rod, the point T becomes a bifurcation point. Now, assume the static point D is outside of rod and on the left side. Noting that $s < 0$ now, the self-balanced torque equation becomes

$$f(l - s) = fL(L/2 - s) \quad (4.21)$$

namely

$$F = \frac{fL(L/2 - s)}{2(l - s)} \quad (4.22)$$

It can be seen that F can only be minimized at $l = L/2$

$$\frac{dF}{ds} = 0, \text{ for } l = L/2 \quad (4.23)$$

Similarly, if S is in the right side, the analysis results should be the same. Practically, it is hard to keep T at this bifurcation point ($l = L/2$). Therefore, during manipulation, it is better to avoid pushing the exact middle of the rod because it is hard to predict its behavior.

The corresponding points between a CNT and its destination have to be matched in order to plan a manipulation path. Figure 4.24 shows the initial position and the destination of a CNT. P_{s1} and P_{s2} are the initial positions; P_{d1} and P_{d2} are the destinations.

The CNT rotates anti-clockwise and moves downward if the starting pushing point is close to P_{s2} . Similarly, the CNT rotates clockwise and moves upward if the starting pushing point is close to P_{s1} . The starting pushing point can be determined by the angle β as shown in Fig. 4.24. If $\beta > 90^\circ$, the starting pushing point should be close to P_{s2} . Otherwise, P_{s1} . Figure 4.25 shows the process for manipulating a CNT from its initial position to its destination. The manipulation scheme of a CNT has to go through a zigzag strategy in order to position the CNT with specified orientation.

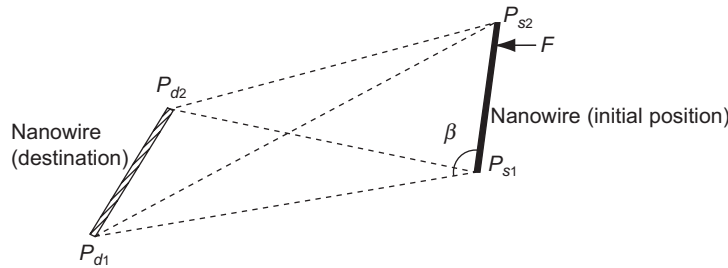


FIGURE 4.24

The initial position of the CNT and the destination where it is manipulated.



The coordinates used to compute the AFM tip pushing position at each step.

$$L_p = \frac{d}{N}, \quad 0 < L_p < 2L_1 \quad (4.24)$$
$$\theta = 2a \cos\left(\frac{L_p}{2L_1}\right) \quad (4.25)$$

The rotation angle θ stays the same during manipulation. The initial pushing angle θ_1 and the final pushing angle θ_2 in Fig. 4.25 can be calculated by finding the starting position and the ending position. After θ is determined, the pivots P_i and Q_i ($i = 1, \dots, N$) can be calculated. The pushing points can then be determined. Here we show how to determine the pushing points when a CNT rotates around the pivot P_i as an example. Figure 4.26 shows the frames used to determine the tip position.

The following transformation matrix can be easily calculated. The transformation matrix of the frame originated at P_s relative to the original frame is \mathbf{T}_s . The transformation matrix of the frame originated at P_i relative to the frame originated at P_s is \mathbf{T}_i . Suppose the rotation angle is β ($0 < \beta \leq \theta$), the transformation matrix relative to the frame originated at P_i is $\mathbf{T}_{\beta i}$. β can be obtained by setting a step size of manipulation. The coordinates of the pushing point can then be calculated

$$\begin{bmatrix} X_F \\ Y_F \\ 1 \end{bmatrix} = \mathbf{T}_s \mathbf{T}_i \mathbf{T}_{\beta i} \begin{bmatrix} 0 \\ L - 2s \\ 1 \end{bmatrix} \quad (4.26)$$

Similar steps can be followed to determine the pushing position for a CNT rotating around the pivot Q_i , $i \in [1, N]$. After the coordinates of the pushing point is obtained, the manipulation path for a CNT can then be generated.

4.7 SUMMARY

In conclusion, nanomanipulation using AFM-based augmented reality system has been introduced to overcome traditional shortcomings, through which the operator can not only feel the interaction forces, but also observe the real-time changes of the nano-environment. To further enhance the reliability of the visual feedback, a local scan strategy is proposed to obtain the true manipulation result and be updated onto the visual feedback display. Moreover, to fully automate the AFM-based nanomanipulation and improve its efficiency, the general framework of computer-aided design (CAD)-guided automated nanoassembly has been further developed. The experimental results demonstrate that AFM-based nanomanipulation has become very straightforward through the developed techniques and methods, in turn leading to a significantly-improved effectiveness and efficiency.

References

- [1] Y. Kim and C. M. Lieber. Machining oxide thin films with an atomic force microscope: pattern and object formation on the nanometer scale. *Science*, 257(5068):375–377, 1992.
- [2] T. Junno, K. Deppert, L. Montelius, and L. Samuelson. Controlled manipulation of nanoparticles with an atomic force microscope. *Appl. Phys. Lett.*, 66(26):3627–3629, 1995.
- [3] D. M. Schaefer, R. Reifengerger, A. Patil, and R. P. Andres. Fabrication of two-dimensional arrays of nanometer-size clusters with the atomic force microscope. *Appl. Phys. Lett.*, 66(8):1012–1014, 1995.
- [4] M. Martin, L. Roschier, P. Hakonen, U. Parts, M. Paalanen, B. Schleicher, and E. I. Kauppinen. Manipulation of ag nanoparticles utilizing noncontact atomic force microscopy. *Appl. Phys. Lett.*, 73(11):1505–1507, 1998.

- [5] S. Decossas, L. Patrone, A. M. Bonnot, F. Comin, M. Derivaz, A. Barski, and J. Chevrier. Nanomanipulation by atomic force microscopy of carbon nanotubes on a nanostructured surface. *Surf. Sci.*, 543(1-3):57–62, 2003.
- [6] D. Q. Yang and E. Sacher. Local surface cleaning and cluster assembly using contact mode atomic force microscopy. *Appl. Surf. Sci.*, 210(3-4):158–164, 2003.
- [7] M. Muller, T. Fiedler, R. Gröger, T. Koch, S. Walheim, C. Obermair, and T. Schimmel. Controlled structuring of mica surfaces with the tip of an atomic force microscope by mechanically induced local etching. *Surf. Interface Anal.*, 36(2):189–192, 2004.
- [8] Y. Sugimoto, M. Abe, S. Hirayama, N. Oyabu, O. Custance, and S. Morita. Atom inlays performed at room temperature using atomic force microscopy. *Nat. Mater.*, 4(2):156–159, 2005.
- [9] M. Sitti and H. Hashimoto. Tele-nanorobotics using atomic force microscope. In *Proceedings of 1998 IEEE/RSJ International Conference on Intelligent Robots and Systems*, volume 3 of *Intelligent Robots and Systems, 1998. Proceedings, 1998 IEEE/RSJ International Conference*, pages 1739–1746 vol. 3, 1998.
- [10] M. Guthold, M. R. Falvo, W. G. Matthews, S. Paulson, S. Washburn, D. A. Erie, R. Superfine, F. P. Brooks, and R. M. Taylor. Controlled manipulation of molecular samples with the nanomanipulator. *IEEE/ASME Trans. Mechatronics*, 5(2):189–198, 2000.
- [11] J. L. Hutter and J. Bechhoefer. Calibration of atomic-force microscope tips. *Rev. Sci. Instrum.*, 64(7):1868–1873, 1993.
- [12] G. Li, N. Xi, H. Chen, C. Pomeroy, and M. Prokos. “Videolized” atomic force microscopy for interactive nanomanipulation and nanoassembly. *IEEE Trans. Nanotechnol.*, 4(5):605–615, 2005.
- [13] G. Li, N. Xi, M. Yu, and W. Fung. Development of augmented reality system for AFM-based nanomanipulation. *IEEE/ASME Trans. Mechatronics*, 9(2):358–365, 2004.
- [14] D. Alliata, R. Staub, and C. Nicolini. Drift elimination in the calibration of scanning probe microscopes. *Rev. Sci. Instrum.*, 66(3):2513–2516, 1995.
- [15] J. T. Woodward and D. K. Schwartz. Removing drift from scanning probe microscope images of periodic samples. *J. Vac. Sci. Technol. B*, 16(1):51–53, 1998.
- [16] B. Mokaberi and A. A. Requicha. Drift compensation for automatic nanomanipulation with scanning probe microscopes. *IEEE Trans. Autom. Sci. Eng.*, 3(3):199–207, 2006.
- [17] L. Lui, J. Zhang, G. Li, and N. Xi. On-line sensing and display in atomic force microscope based nanorobotic manipulation. In *2007 IEEE/ASME International Conference on Advanced Intelligent Mechatronics*, ETH Zurich, Switzerland, pages 1–6, 2007.

On-Chip Band Gap Engineering of Carbon Nanotubes

King Wai Chiu Lai*, Ning Xi*, Carmen Kar Man Fung†, Hongzhi Chen*, Tzyh-Jong Tarn**, and Yilun Luo††

*Department of Electrical and Computer Engineering, Michigan State University, Michigan

†Hong Kong Productivity Council, Hong Kong

**Department of Electrical and Systems Engineering, Washington University in St. Louis, Missouri

††Department of Biosystems Engineering, Michigan State University, Michigan

CHAPTER OUTLINE

5.1 Introduction	81
5.2 Quantum Electron Transport Model	82
5.2.1 Nonequilibrium Green's Functions	82
5.2.2 Poisson's Equation and Self-Consistent Algorithm	84
5.3 Electrical Breakdown Controller of a CNT	85
5.3.1 Extended Kalman Filter for Fault Detection	85
5.4 Effects of CNT Breakdown	87
5.4.1 Current-Voltage Characteristics	87
5.4.2 Infrared Responses	89
5.5 Summary	91
References	91

5.1 INTRODUCTION

Thus far, we have discussed several processes to form CNT-based structure, including CNT classification, DEP manipulation, and AFM robotic assembly. The majority of this book is about the development of nanomaterials in optoelectronics. A nano-sized quantum optical sensor is one of the important components of the nano-optoelectronic system. The band gap of a semiconducting material is size-dependent, which is important for optical nanosensor applications. Classical band gap materials are inherently limited by their atomic and lattice structures. For carbon nanotubes, the electron transport is confined to one dimension and the wave function has a periodicity in the circumferential direction [1], so the band gap of a CNT is determined by its diameter and chirality as discussed in Chapter 2. It is known that the diameter of CNTs is inversely proportional to the band gap [2]. We have developed a quantum infrared (IR) detector using CNTs [3], and CNTs have been used for nanotransistors as reported in the literature [4]. Obviously, the band gap of nanotubes is the main determinant of

the performance of nanodevices. Further processing, such as band gap engineering, is required to set the limits of the optoelectronic behavior of nanodevices.

However, the band gap of current CNT varies over a wide range. To improve the consistency of the electronic properties of CNTs, various CNT synthesis processes can be applied as has already been discussed [5–7], but this still falls short of being able to reliably control CNT performance. Instead, a band gap engineering method was proposed to break down the outer layer of multiwalled CNTs (MWCNTs) electrically [8]. If the diameter of a CNT decreases, fewer wave vectors are allowed in the circumferential direction and thus the band gap of the CNT increases [9].

In this chapter, an electrical breakdown system for MWCNTs will be discussed to control the band gap of the MWCNT. The system plays an important role in the nanomanufacturing of CNT-based devices, and can be used as a reliable posttreatment after the CNTs are deposited on the metal electrodes. The development of the system includes research into a real-time CNT electrical breakdown controller and an extended Kalman filter (EKF) for fault detection, which determines the breakdown status [10]. By controlling the diameter of a MWCNT, a specific band gap material can be generated. The MWCNT consists of multilayer of carbon shells and can be either semiconducting or metallic. Theoretical and experimental studies have shown that the outermost layer of the MWCNT dominates the electrical conductivity of the MWCNT [11]. To precisely adjust the band gap, we start with a MWCNT with a relatively large diameter and small band gap. The electrical breakdown process is then used to remove the outermost layer of the MWCNT.

5.2 QUANTUM ELECTRON TRANSPORT MODEL

First, we developed the electrical current model of a CNT [10]. A quantum electron transport model for the current-voltage characteristics of a CNT has been derived to precisely control the electrical breakdown process. Breakdown of the shell of nanotubes happens when the current induces the development of a defect on the nanotubes, with breakdown usually starting from this point. The electronic properties and the band structure of the nanotube change after losing the outermost conducting carbon layers. By considering CNT as a semiconducting material, the current transport includes free electrons and holes in both conduction and valence bands. However, energy levels are quantized in the conduction and valence bands because of the special crystalline structure of CNTs. Therefore, the model is developed from studying the current-voltage characteristics of a single nanotube.

5.2.1 Nonequilibrium Green's Functions

Current-voltage characteristics of a semiconducting material can be derived and predicted based on the self-consistent method by solving the nonequilibrium Green's functions (NEGF) and electrostatics [12]. This formulation can be used to solve Schrödinger's equation under nonequilibrium conditions and is capable of treating the contact coupling effect and dissipative scattering process in the channel.

Let's consider a single MWCNT bridging between two metal electrodes with small overlap area. The structure can be modeled as shown in Fig. 5.1. From Schrödinger's equation (5.1), the quantum

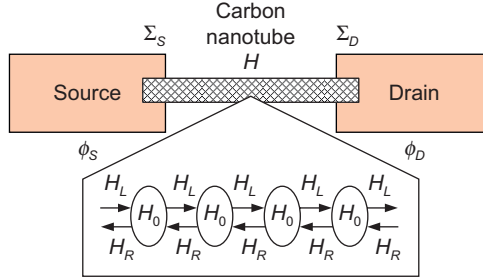


FIGURE 5.1

The quantum model derived for the the electrical breakdown device. The electron transport inside a carbon nanotube is injected by source and drain electrodes with potential ϕ_S and ϕ_D .

energy states and electron wave function inside the CNT can be modeled by the Hamiltonian matrix H in Eq. (5.2).

$$\left[-\frac{\hbar^2}{2m} \nabla^2 + U(\vec{r}) \right] \Psi = E(\vec{r}) \Psi \quad (5.1)$$

$$H \Psi = E \Psi \quad (5.2)$$

where \hbar is the Dirac constant; m is the electron mass; \vec{r} is the position vector; $U(\vec{r})$ is the potential energy; and Ψ is the wave function.

The CNT is composed of unit carbon rings along the translational direction following its periodic lattice structure as shown in Fig. 5.1. Hamiltonian matrix H for the whole CNT can be derived by the Hamiltonian matrix of the unit ring H_0 based on the Bloch's theory [13] and the tight binding approximation [14]. The left and right coupling from the neighboring units can be considered as H_L and H_R , respectively. Because the electron transport is mainly contributed by the contacts of the outermost carbon shell with the electrodes [8], the quantum tunneling and quantum effect between the layers in the MWCNT can be neglected.

$$H = \begin{bmatrix} H_0 & H_R & 0 & & \dots \\ H_L & H_0 & H_R & 0 & \dots \\ 0 & H_L & H_0 & H_R & 0 & \dots \\ & 0 & H_L & H_0 & H_R & 0 & \dots \\ & & & \dots & & & \dots \end{bmatrix} \quad (5.3)$$

In the channel of a nanotube, the empty quantum energy states were occupied by electrons with high electrochemical potential in the source, so electrons are pulled out from the drain, which has lower electrochemical potential, to establish equilibrium. Because of the coupling effect by the contact, the quantum states from the channel and metal will diffuse to the other materials, so this broadens the allowed quantum energy levels. The self-energy matrix, Σ_S and Σ_D , describes the electron flow through the contact between metal electrodes and a nanotube.

The source-drain current can be derived from Eq. (5.4), which can be thought as the difference of the electron transmission contributed from the source and the drain.

$$I = \frac{4e}{h} \int T(E)[f_0(E - \phi_S) - f_0(E - \phi_D)]dE \quad (5.4)$$

where e is the electron charge; h is the Planck constant; f_0 is the Fermi-Dirac function, which represents the possibility of an electron to occupy an available quantum state in the channel; and $\phi_{S(D)}$ is the electrostatic potential at the source (drain). The transmission matrix $T(E)$ is defined in Eq. (5.5), which is proportional to the densities of states at given energy levels.

$$T(E) = \text{Trace}(\Gamma_S G \Gamma_D G^+) \quad (5.5)$$

The energy level broadening due to CNT-electrode contact at the source and the drain can be defined as in Eq. (5.6)

$$\Gamma_S = i(\Sigma_S - \Sigma_S^+) \text{ and } \Gamma_D = i(\Sigma_D - \Sigma_D^+), \quad (5.6)$$

The retarded Green's function G matrix is derived for the lifetime of the quantum energy state and the broadening of the density of states [12].

$$G(E) = [(E + i0^+)I - H - \Sigma_S - \Sigma_D]^{-1} \quad (5.7)$$

However, the derivation of the Hamiltonian matrix H requires the electrostatic potential $\phi(\vec{r})$ at each periodic carbon ring. The quantum state inside the nanotube channel will be affected by carrier propagation flux due to potential difference between the source and the drain.

5.2.2 Poisson's Equation and Self-Consistent Algorithm

The electrostatic potential ϕ of a carbon nanotube can be calculated by Poisson's equation (5.8)

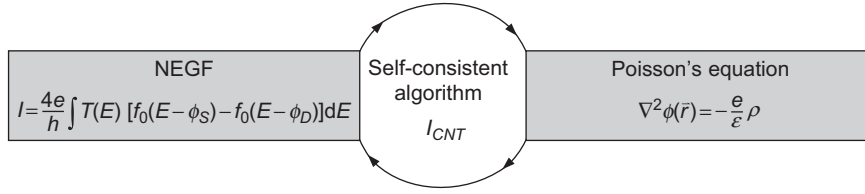
$$\nabla^2 \phi(\vec{r}) = -\frac{e}{\epsilon} \rho \quad (5.8)$$

where e is the electron charge; ϵ is the dielectric constant; and ρ is for the charge density. By solving the NEGF formulas, the charge density ρ within the channel of the nanotube can be derived as

$$\rho = \int dE G^n(E)/2\pi \quad (5.9)$$

where $G^n(E)$ is the contact correlation function at energy E , which causes inscattering into the channel [12]. By solving the the NEGF formulas and Poisson's equation iteratively, the electron transport of the CNT device can be obtained. Each iteration will estimate an improved result for the next step. When the self-consistency is achieved, the numerical solution to the NEGF transport equation can be obtained as shown in Fig. 5.2.

The NEGF formulas and Poisson's equation can be derived based on the actual geometrical information of the specific structure. With the help of atomic force microscopy, the detailed three-dimensional information can be measured. We can calculate the Hamiltonian matrix H according to the diameter and channel length of the CNT. The self-energy matrix Σ for the nanotube contact can be obtained from the electrode size and contact length. For a given source-drain voltage, the current across the CNT can be evaluated using the self-consistent NEGF formulas.

**FIGURE 5.2**

Self-consistence loop for the numerical calculation of the NEGF formalism and Poisson's equation.

5.3 ELECTRICAL BREAKDOWN CONTROLLER OF A CNT

Because the electron transmission model gives the optimal estimation of the current-voltage characteristic of a specific device, it can be employed as the state space model for electrical breakdown current control [12]. In the real-time application, the quantum electron transport model is simplified by fitting it with the effective mass transport model and the self-consistent result in Eq. (5.10) [15]. Although this semiclassical model may lose accuracy when large drain voltage is applied, the modeling error is tolerable after combining the NEGF solution [16]. The semiclassical model also follows the characteristic features of curvature, which helps us to estimate the breakdown voltage. Therefore, the current of a CNT-based device (I_{CNT}) is given by,

$$I_{CNT} = (4e/h)k_B T \left\{ \ln \left[\frac{1 + \exp(\eta_{FS}/k_B T)}{1 + \exp(\eta_{FD}/k_B T)} \right] \right\} \quad (5.10)$$

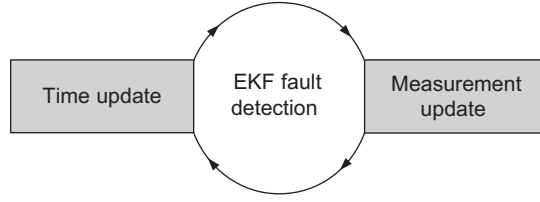
where e is the electron charge; h is the Planck constant; k_B is the Boltzmann constant; and T is the temperature in Kelvin. $\eta_{F,S(D)} = \phi_{S(D)} - \phi_{\text{barrier}}$ denotes the potential difference between the source (drain) and the barrier height of the metal-semiconductor contact. In the band gap engineering process, the source is grounded and ϕ_S equals zero, and ϕ_{barrier} can be calculated by the optimal fitting from the NEGF result. Thus, I_{CNT} is completely determined by the drain voltage ϕ_D .

5.3.1 Extended Kalman Filter for Fault Detection

The design of the controller is based on EKF, which is a real-time nonlinear recursive algorithm. EKF estimates the state of a dynamic system from discrete and noise measurements [17], and it is least-square optimal based on maximum *a posteriori* probability (MAP) [17]. When a voltage is applied to a CNT by controller, the corresponding current is measured simultaneously. The rapid change in current, which indicates the beginning of the breakdown process, can be detected as the system fault based on the robust parameter estimation approach [18]. The breakdown voltage is stopped immediately once the fault residual exceeds the threshold to prevent cascade breakdowns [19].

The iterative process of the EKF includes two key steps as shown in Fig. 5.3. The time update step projects the current system state and its statistical information forward in time according to system plant. The measurement update step adjusts the propagated estimate by an actual measurement based on statistical decision theory and the least-square method.

The system state x is defined using the potential difference between the source and the drain, $U_{S(D)}$. The polynomial quantum electron transport model $h_p(x)$ is integrated in the measurement update stage.

**FIGURE 5.3**

The recursive iteration for an Extended Kalman filter: time update and measurement update.

During the electrical breakdown process, the voltage across the nanotube is increased by small steps u . Thus, the extended Kalman filter loop can be written in continuous time form as Eqs (5.11) and (5.12),

$$\dot{x} = u \quad (5.11)$$

$$z = h_p(x) \quad (5.12)$$

For real-time control, the discrete EKF is derived according to the above dynamic system. The time update of the extended Kalman filter is obtained as Eqs (5.13) and (5.14),

$$\hat{x}_k^- = \hat{x}_{k-1} + u_k \quad (5.13)$$

$$P_k^- = P_{k-1} + Q \quad (5.14)$$

where \hat{x} is the system state for the source-drain potential difference generated by the controller. The control variable u_k is the potential change in each iteration step. P is the error covariance matrix. Q is the covariance of the modeling error. The measurement update of the EKF can be obtained as Eqs (5.15)–(5.17).

$$K_k = P_k^- H^T (H P_k^- H^T + R)^{-1} \quad (5.15)$$

$$\hat{x}_k = \hat{x}_k^- + K_k (z_k - H \hat{x}_k^-) \quad (5.16)$$

$$P_k = (I - K_k H) P_k^- \quad (5.17)$$

where K is the Kalman gain; R is the measurement noise covariance; z is the measurement of the current flow through the CNT device; and H is the observation matrix, which is the Jacobean matrix derived from the quantum electron transport model in Eq. (5.18).

$$H = \left. \frac{\partial h_p}{\partial x} \right|_{\hat{x}_{k-1}, u_k} = - \frac{4q \exp(\zeta_{DB})}{h \{ \exp(1 + \zeta_{DB}) \}} \quad (5.18)$$

$$\zeta_{DB} = \hat{x}_k^- - \phi_{barr} \quad (5.19)$$

Therefore, the control voltage of the CNT is optimally propagated based on the statistical information from the previous measurement, while the incoming current measurement data are used to adjust the projected estimation. The Gaussian random noise in modeling and measurement is filtered during iteration. Any rapid change of the current in the nanotube can be detected as the system fault

in the quantum transport controller by exploring the analytical redundancy information of the system space [18]. The fault observer is modeled by generating the Mahalanobis distance in Eq. (5.20). The breakdown voltage is stopped immediately once r exceeds a fault threshold to prevent cascade breakdown.

$$r = (z_k - H\hat{x}_k^-)^T P_k^{-1} (z_k - H\hat{x}_k^-) \quad (5.20)$$

5.4 EFFECTS OF CNT BREAKDOWN

The reliability of the controller was verified experimentally. Individual CNTs were manipulated between two metal electrodes by dielectrophoretic manipulation (see Chapter 2) and AFM-based assembly (see Chapter 4). After the MWCNT was deposited on the metal electrodes, the band gap of the MWCNT was tuned by the electrical breakdown system as shown in Fig. 5.4A. The breakdown controller was implemented in a computer, and a curve tracer (Agilent 4156C precision semiconductor parameter analyzer) was used to measure the current of individual nanotubes. As mentioned earlier, the current was used as a real-time current feedback, so the optimal breakdown voltage was generated by the EKF. When the fault detection algorithm detected the rapid change of current, it indicated the beginning of the breakdown process. Therefore, the system stopped applying the voltage immediately to prevent the cascade breakdown as shown in Fig. 5.4B. The fault threshold was experimentally optimized to minimize the false alarm and maintain a quick response. Multiple breakdown processes were performed on the MWCNT to remove outer shells, and the band gap of the MWCNT was increased consecutively as shown in Fig. 5.5A. Moreover, the diameter of the MWCNT decreased after the breakdown process as shown in Figs 5.5B and D. Thus, the breakdown process can be used for on-chip modification of CNT band structures.

5.4.1 Current-Voltage Characteristics

It is also found that CNT electrical breakdown happens at a particular region on a CNT [20]. A single MWCNT was placed on three pairs of gold microelectrodes as shown in Fig. 5.6A. Current-voltage

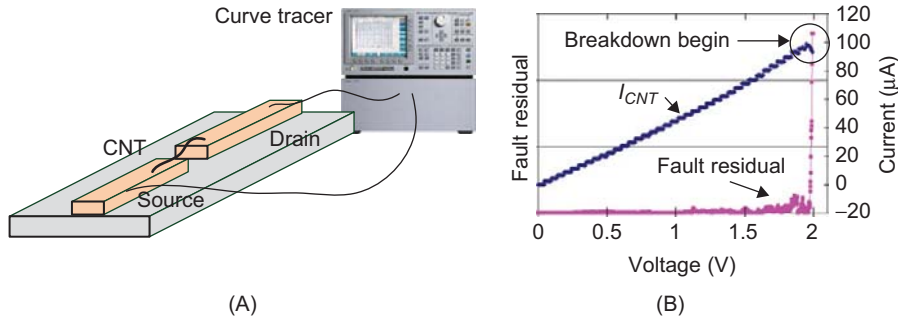
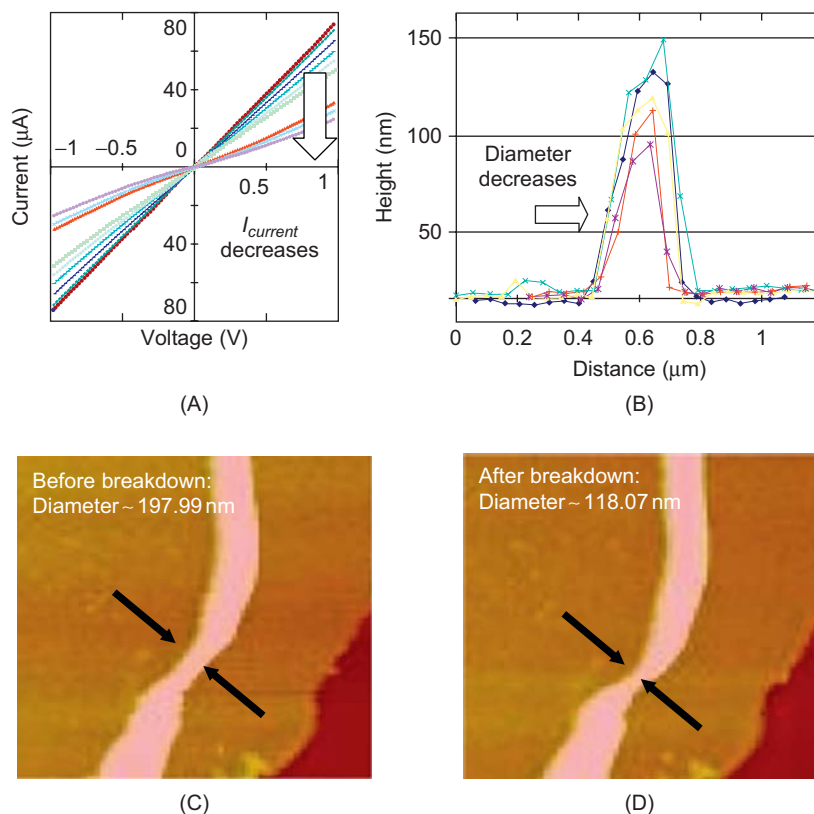


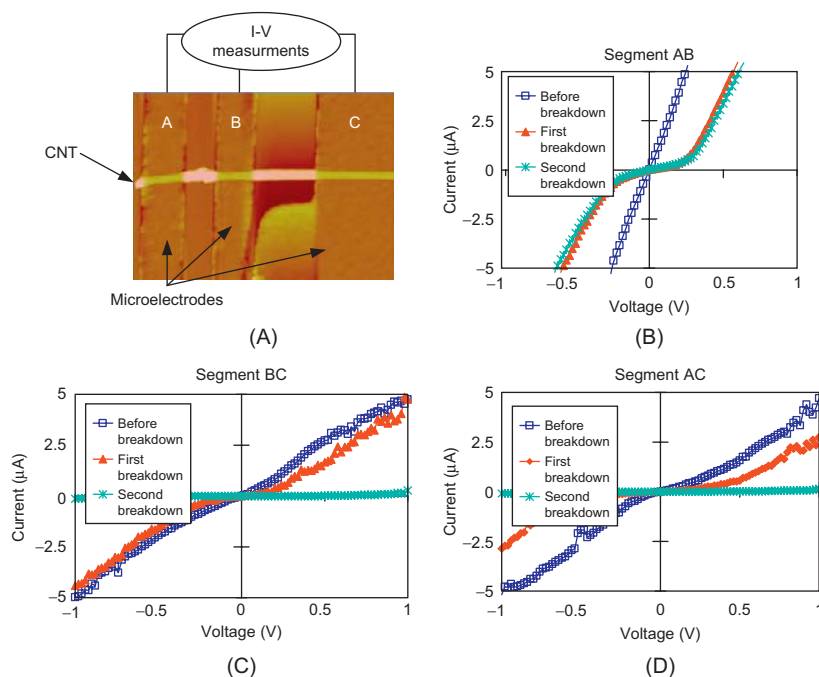
FIGURE 5.4

(A) Illustration of a curve tracer connected with a CNT-based device. (B) Experimental data of the fault residual and the current of the CNT [10].

**FIGURE 5.5**

(A) I-V characteristics of the CNT after multiple breakdown processes. (B) The AFM cross-section high data show the diameter of the CNT reduced after the breakdown processes. AFM images of a nanotube before breakdown (C) and after breakdown (D) [10].

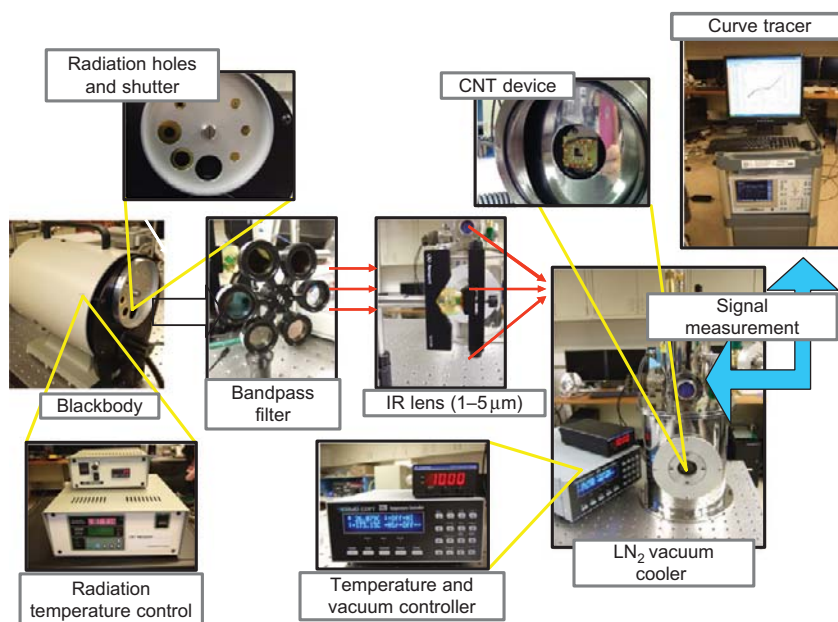
characteristics of different segments (AB, BC, and AC) of the nanotube were measured and compared before and after the breakdown process as shown in Fig. 5.6. When a voltage was applied to the segment AB, the first CNT breakdown occurred within the segment AB. We observed a significant change in the current–voltage curve of the segment AB, whereas no obvious change in the current–voltage curve of the segment BC occurred. Because the segment AC included both the segments AB and BC, the current–voltage curve of the segment AC was also affected. Similarly, when the voltage was applied to the segment BC, the second CNT breakdown occurred within the segment BC, and the current–voltage curve between the segment AB remained unchanged because the breakdown occurred on the segment BC only. This experimental results clearly indicated that the breakdown position of a CNT can be adjusted by applying the electrical current at specific locations.

**FIGURE 5.6**

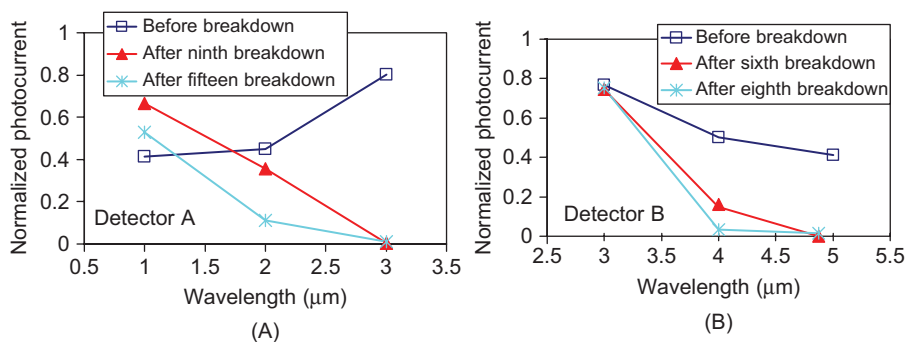
(A) An AFM image of a single MWCNT connected to three gold microelectrodes. I-V characteristics of the MWCNT at different segments: (B) segment AB, (C) segment BC, and (D) segment AC [20].

5.4.2 Infrared Responses

As the band gap of nanotubes can be adjusted through the aforementioned process, the sensitivity of a CNT-based infra-red (IR) detector sensor was studied under the breakdown conditions. The detector was made using the techniques discussed earlier. The sensing principle of the detector is based on the photovoltaic effect in the CNT-metal structure. When IR photons hit the CNT, electrons and holes inside the CNT are generated by the photons with energy larger than the band gap of the CNT. The electron-hole pairs are then separated by the built-in potential and contribute to the photocurrent at the contact. The IR sensing capability is affected by band gap of the CNT because the photon energy is inversely proportional to the wavelength, and therefore CNTs of small band gap are desired and chosen to detect the IR signal with less photon energy and longer wavelength, such as middle-wave IR (MWIR) signal. As a result, controlling the band gap of a CNT is important to design MWIR sensors. A detailed design of CNT-based IR detectors will be given in Chapter 7. Here, the CNT-based IR detector was tested under IR irradiation from a black body, which emits a temperature-dependent spectrum of light (from visible light to the MWIR region). The detector was placed in a detector chamber and connected to the curve tracer for signal measurement and on-chip band gap tuning as shown in Fig. 5.7. To measure the photoresponses of the detector at a specific wavelength, different

**FIGURE 5.7**

Experimental setup of the band gap tuning experiment with different frequencies of IR radiation.

**FIGURE 5.8**

Photocurrent responses of the CNT-based detector at specific wavelengths [20].

narrow bandpass filters (1 μm , 2 μm , 3.2 μm , 4 μm , and 5 μm , Spectrogon US, Inc.) were used and placed between the black body and the detector. The photocurrent responses of two detectors were measured with different bandpass filters before and after each breakdown stage as shown in Fig. 5.8. Obviously, the optical spectrum of both detectors changed during the breakdown process. For example, detector A was sensitive to an IR signal of 3 μm at the beginning, but it became sensitive to an IR signal

of 1 μm after the breakdown processes commenced. This further proves that the band gap of the CNT was increased through each stage of the CNT breakdown. As a result, a photovoltaic material with a band gap can be produced by using this procedure.

5.5 SUMMARY

In conclusion, on-chip CNT band gap engineering has been developed. This provides a steady and high-yield on-chip band gap engineering approach to adjust the band structure of a nanomaterial, which is important for manufacturing the next generation of nano-IR sensors. The experimental results indicated that the desired band gap of a MWCNT can be tuned by utilizing the electrical breakdown process; hence, the sensitivity of the nano-optical detector at specific wavelengths can be adjusted. The electrical breakdown process can be further exploited to fabricate multispectrum optical detectors.

References

- [1] R. Saito, M. Fujita, G. Dresselhaus, and M. S. Dresselhaus. Electronic structure of chiral graphene tubules. *Appl. Phys. Lett.*, 60(18):2204–2206, 1992.
- [2] M. S. Arnold, A. A. Green, J. F. Hulvat, S. I. Stupp, and M. C. Hersam. Sorting carbon nanotubes by electronic structure using density differentiation. *Nat. Nanotechnol.*, 1:60–65, 2006.
- [3] J. Zhang, N. Xi, H. Chen, K. Lai, G. Li, and U. C. Wejinya. Design, manufacturing, and testing of single-carbon-nanotube-based infrared sensors. *IEEE Trans. Nanotechnol.*, 8(2):245–251, 2009.
- [4] H. J. Dai, A. Javey, E. Pop, D. Mann, and Y. R. Lu. Electrical transport properties and field effect transistors of carbon nanotubes. *Nano*, 1:1–13, 2006.
- [5] Y. Li, D. Mann, M. Rolandi, W. Kim, A. Ural, S. Hung, A. Javey, J. Cao, D. Wang, E. Yenilmez, Q. Wang, J. F. Gibbons, Y. Nishi, and H. Dai. Preferential growth of semiconducting single-walled carbon nanotubes by a plasma enhanced cvd method. *Nano Lett.*, 4(2):317–321, 2004.
- [6] S. M. Bachilo, M. S. Strano, C. Kittrell, R. H. Hauge, R. E. Smalley, and R. B. Weisman. Structure-assigned optical spectra of single-walled carbon nanotubes. *Science*, 298(5602):2361–2366, 2002.
- [7] M. J. O'Connell, S. M. Bachilo, C. B. Huffman, V. C. Moore, M. S. Strano, E. H. Haroz, K. L. Rialon, P. J. Boul, W. H. Noon, C. Kittrell, J. Ma, R. H. Hauge, R. B. Weisman, and R. E. Smalley. Band gap fluorescence from individual single-walled carbon nanotubes. *Science*, 297(5581):593–596, 2002.
- [8] P. G. Collins, M. S. Arnold, and P. Avouris. Engineering carbon nanotubes and nanotube circuits using electrical breakdown. *Science*, 292(5517):706–709, 2001.
- [9] M. S. Dresselhaus, G. Dresselhaus, and P. C. Eklund, editors. *Science of Fullerenes and Carbon Nanotubes: Their Properties and Applications*. Academic Press, New York, 1996.
- [10] Y. Luo, N. Xi, L. Liu, and J. Zhang. Modeling and control of electrical breakdown process of carbon nanotubes. *Proceedings of the 17th International Federation of Automation Control World Congress*, Vol. 17. 10468–10473, Korea, 2008.
- [11] B. Q. Wei, R. Vajtai, and P. M. Ajayan. Reliability and current carrying capacity of carbon nanotubes. *Appl. Phys. Lett.*, 79(8):1172–1174, 2001.
- [12] S. Datta, editor. *Quantum Transport: Atom to Transistor*. Cambridge University Press, New York, 2005.
- [13] N. W. Ashcroft and D. Mermin, editors. *Solid State Physics*. Holt, Reinhart and Winston, New York, 1976.
- [14] J. Han, L. Yang, M. P. Anantram, and J. P. Lu. Effect of small uniaxial and torsional strain. *Phys. Rev. B*, 60:13874–13878, 1999.

- [15] R. Tamura and M. Tsukada. Analysis of quantum conductance of carbon nanotube junctions by the effective-mass approximation. *Phys. Rev. B*, 58(12):8120–8124, 1998.
- [16] S. O. Koswatta, N. Neophytou, D. Kienle, G. Fiori, and M. S. Lundstrom. Dependence of dc characteristics of CNT mosfets on bandstructure models. *IEEE Trans. Nanotechnol.*, 5(4):368–372, 2006.
- [17] R. E. Kalman. A new approach to linear filtering and prediction problems. *Trans. ASME J. Basic Eng.*, 82:35–45, 1960.
- [18] P. M. Frank. Fault diagnosis in dynamic systems using analytical and knowledge-based redundancy: a survey and some new results. *Automatica*, 26(3):459–474, 1990.
- [19] K. Lai, N. Xi, Y. Luo, C. K. M. Fung, J. Zhang, and H. Chen. Development of carbon nanotube based spectrum infrared sensors. In *Proc. IEEE Sensors*, 1600–1603, 2008.
- [20] K. W. C. Lai, N. Xi, C. K. M. Fung, H. Chen, and T.-J. Tarn. Engineering the band gap of carbon nanotube for infrared sensors. *Appl. Phys. Lett.*, 95(22):221107, 2009.

Packaging Processes for Carbon Nanotube-Based Devices

6

King Wai Chiu Lai*, Ning Xi*, Carmen Kar Man Fung[†], and Hongzhi Chen*

*Department of Electrical and Computer Engineering, Michigan State University, Michigan

[†]Hong Kong Productivity Council, Hong Kong

CHAPTER OUTLINE

6.1 Introduction	93
6.2 Thermal Annealing of Carbon Nanotubes	94
6.3 Electrical and Optical Responses of Carbon Nanotubes After Thermal Annealing	96
6.4 Parylene Thin Film Packaging	100
6.5 Electrical and Optical Stability of the CNT-Based Devices After Packaging	101
6.6 Summary	103
References	104

6.1 INTRODUCTION

In this chapter, we present a thermal annealing method to control oxygen doping in carbon nanotube (CNT) and polymer-based packaging to improve the stability of related CNT-based devices, and the processes can be considered as the final processes for the nanomanufacturing of CNT-based nano devices. As we discussed earlier, CNTs have been found to be promising nano-materials due to their unique and superb electrical and optical properties [1, 2] and various types of nano-optoelectronic devices can be built with this novel material [3–7]. However, it has been found that the electrical behaviors of nanotube devices are affected by many factors such as the contact condition and contact resistance of the materials. Due to the large absorption area of nanotubes, the tubes are very sensitive to small gaseous molecules in the working environment. The exposure of single-walled CNT (SWCNT) samples to oxygen appeared to have a strong influence on their electronic transport properties [8, 9]. Besides, it is reported that the oxygen adsorption of CNTs modified the barriers at the CNT–metal interfaces [10]. Therefore, various methods to maintain and improve stability of the CNT-based devices have been explored. As our interests in the book are design and fabrication of nano-optoelectronics, we put our focus on the influence of contact resistance on the photocurrent and explore the methods to improve the stability of the CNT-based optical detector in this chapter.

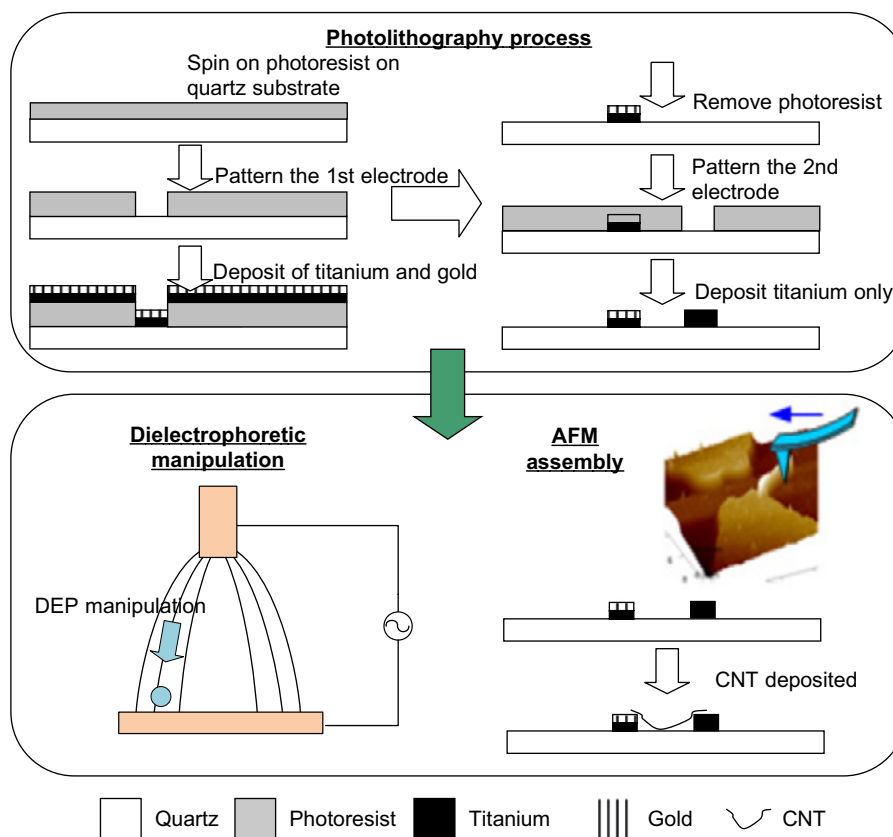
Recently, the applications of using the nanostructural material for optical detection have been explored. The photovoltaic effect of CNTs was investigated and a sensitive CNT-based infrared (IR) sensor was developed [11–13]. When a semiconducting CNT is manipulated between two metal

electrodes, Schottky barriers are formed at the CNT-metal interfaces. Photocurrent is induced at the barriers by the photovoltaic effect when it is exposed to IR light. Regarding the CNT-based IR sensor, the electronic properties of the CNT sensing element are easily altered by oxygen absorption, which results in changing the contact resistance at Schottky contacts. The Schottky barrier plays an important role in IR detection as the photocurrent is generated at the Schottky contacts, thus the stability of the CNT device is also influenced by oxygen contamination.

In the following sections, the effect of the thermal annealing process on the performance of CNT-based IR sensors, such as electronic behaviors, photoresponses, and the stability, are investigated under different conditions. I-V characteristic of an de-doped (out-gassed) CNT-based IR detector is measured after the thermal annealing process and compared with the IR detector before thermal annealing. The photonic behavior of the oxygen-doped and de-doped CNT device are also studied and compared. Experimental results show that the photocurrent and dark current of the CNT-based IR sensors are changed after the thermal annealing process. Besides, the de-doped CNT-based IR sensor is coated with a layer of parylene C polymer thin film. The thin film acts as an oxygen barrier to isolate the detector from the ambient environment and prevents oxygen absorption on the CNT again. The parylene C packaged CNT-based IR detector is fabricated and tested under near IR radiation. Current results indicate that the CNT-based IR detector coated with parylene C is capable of sensing IR radiation and exhibits repeatable IR responses. The photoresponse of the IR detector is tested over a period of time and the results indicated that the de-doped and packaged CNT detector exhibit more stable performance.

6.2 THERMAL ANNEALING OF CARBON NANOTUBES

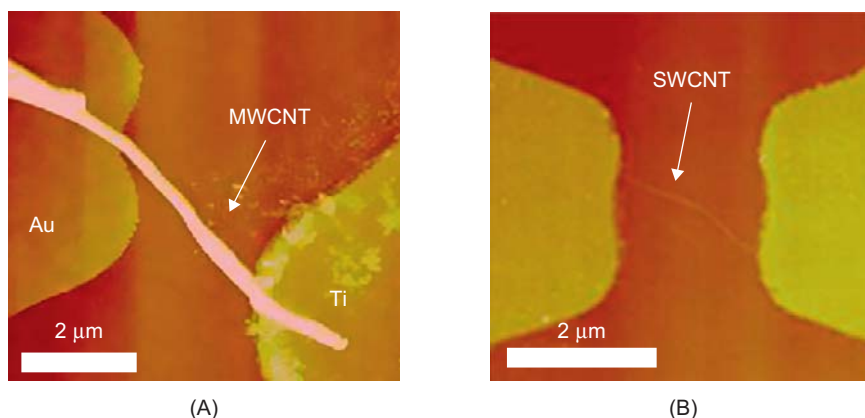
It is commonly known that thermal annealing has been used in Silicon-based industries [14], and preliminary result of effect of thermal annealing of multi-walled carbon nanotubes was reported [15]. Here, we experimentally studied the thermal annealing process of carbon nanotubes [21]. In the experiment, heterogeneous electrodes (gold [Au] and titanium [Ti]) were chosen to achieve two different contact conditions on a carbon nanotube. The electrodes were fabricated on a quartz substrate by a standard photolithography process as shown in Fig. 6.1. First, a layer of AZ5214E photoresist with thickness of $1.5\ \mu\text{m}$ was put onto a 0.5×0.5 -inch quartz substrate. Second, the photoresist was patterned by an AB-M mask aligner and was developed in the AZ300 developer. Third, a layer of Ti with thickness of $30\ \text{\AA}$ was deposited by a thermal evaporator, followed by depositing a layer of Au with thickness of $30\ \text{nm}$. Fourth, the photoresist was removed by acetone and the first layer of Au metal electrode was formed. The second layer of metal electrode was fabricated in a similar process. A new layer of photoresist was spun first and patterned on the substrate. A layer of Ti with thickness of $30\ \text{nm}$ was then deposited. Finally, the photoresist was removed by acetone and the second Ti electrode was fabricated. The gap distance between two electrodes was designed to be $2\ \mu\text{m}$, a CNT was then formed between the two electrodes by dielectrophoretic (DEP) manipulation (Refer to Chapter 2 if you are searching for details) [16, 17]. Before the DEP manipulation of nanotubes, CNT suspensions were prepared before the processes. Single-walled carbon nanotube (SWCNT) powder (BU-203, Bucky USA/Nanotex Corp.) and multi-walled CNT (MWCNT) powder (BU-201, Bucky USA/Nanotex Corp.) were dispersed in an alcohol liquid medium, respectively. The length of the

**FIGURE 6.1**

Fabrication and assembly process of forming carbon nanotubes across heterogeneous electrodes.

SWCNT and the MWCNT are 0.5–4 and 1–10 μm , respectively. Both the SWCNT and MWCNT suspensions were ultrasonicated for 10–15 minutes. Afterwards, a droplet of the CNT suspension was deposited on the heterogeneous electrodes. At the same time, an AC voltage of 1.5 V peak-to-peak with frequency of 1 kHz was applied to the electrodes for 2 seconds, so a DEP force was induced to attract the CNT to the electrodes. In the deposition process, the yield to form a single CNT between two electrodes was controlled by adjusting the concentration of the CNT suspension, the frequency, and the amplitude of the AC voltage. However, impurities or more than one CNT were trapped between the electrodes in some cases. Therefore, an atomic force microscopic (AFM) based nanomanipulation system [18] was employed to push some misconnected CNTs away from the electrodes. Finally, a single CNT was bridged between the electrodes and typical MWCNT- and SWCNT-based devices are shown in Fig. 6.2.

After depositing a single MWCNT on the heterogeneous Au–Ti electrodes, I–V characteristic of the MWCNT-based device was measured as shown in Fig. 6.3A. The I–V characteristic indicated the

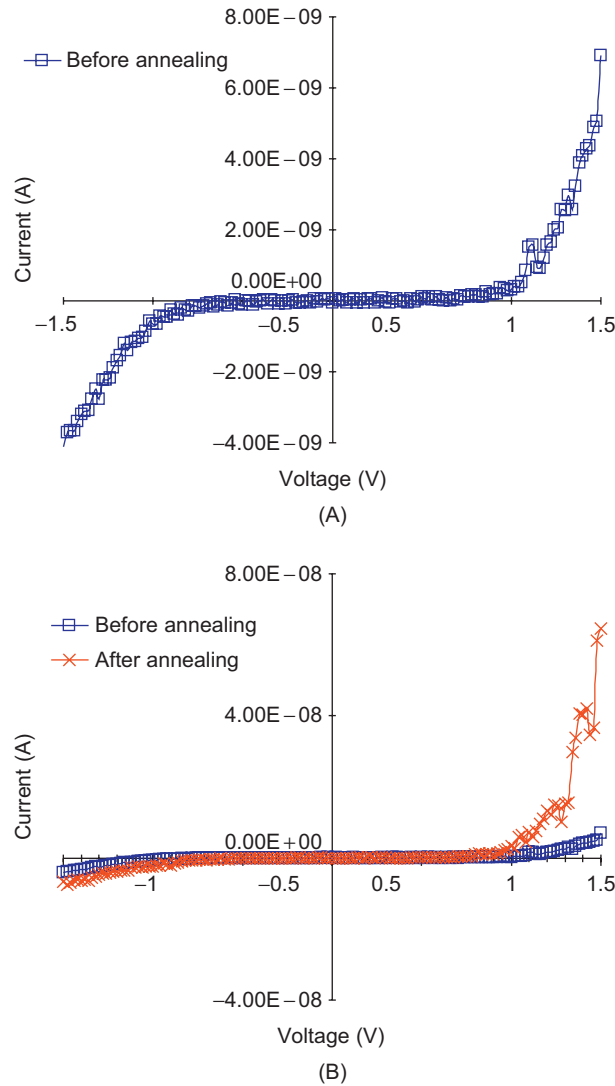
**FIGURE 6.2**

AFM images of (A) an MWCNT and (B) a SWCNT. The CNTs were deposited and bridged between the metal electrodes.

connection and electronic behavior of the CNT, and the MWCNT-based device behaved with two different contact conditions, and their difference can be found by comparing the current when the voltages are 1.5 and -1.5 V, respectively. The asymmetric currents were generated at the heterogeneous metal contacts with the value of 7 and -4 nA at the bias voltages of 1.5 and -1.5 V, respectively. As mentioned earlier, the MWCNT was exposed in air and the contact resistance was influenced by oxygen molecules. Therefore, the de-doping process was conducted through thermal annealing to remove the oxygen molecules from the nanotubes. The oxygen-doped MWCNT-based device was annealed at 400°C in a vacuum furnace for 1 hour. I-V characteristic of the de-doped MWCNT-based device was measured and also compared with the oxygen-doped MWCNT-based device as shown in Fig. 6.3B. It clearly indicated that the current of the de-doped MWCNT-based device was increased to 63 nA when the bias voltage was 1.5 V. The increasing conductivity is due to the decreasing contact resistance at the CNT-metal interface by removing the oxygen molecules on the MWCNT during the thermal annealing process. Based on this result, the thermal annealing process can be used to enhance the conductivity of the CNT-based device.

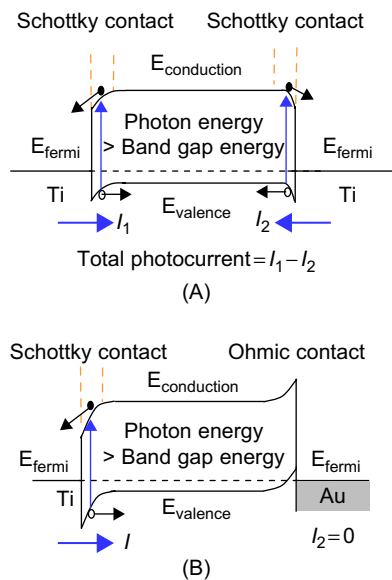
6.3 ELECTRICAL AND OPTICAL RESPONSES OF CARBON NANOTUBES AFTER THERMAL ANNEALING

In order to verify the optical behavior of oxygen-doped and de-doped CNTs, the MWCNT-based device was tested under illumination of an IR laser source (UH5-30G-830-PV, World Star Tech, optical power: 30 mW; wavelength: 830 nm), and photocurrents were generated at the electrodes, so the device can be considered as an optical sensor. The sensing mechanism is based on the photovoltaic effect [11–13] and the design of the CNT-metal contact is important to achieve an optimum photonic behavior. Here, let us introduce the simple design of CNT-based optical sensors first, and a more comprehensive discussion of the design of CNT-based nano Schottky photodiodes will be given in Chapter 7. As mentioned

**FIGURE 6.3**

(A) I-V characteristic of the MWCNT-based device which was made from two different contacts. (B) I-V characteristics of the MWCNT-based device before and after annealing. The current was significantly increased when the voltage was 1.5V. ([21], © [2008] IEEE)

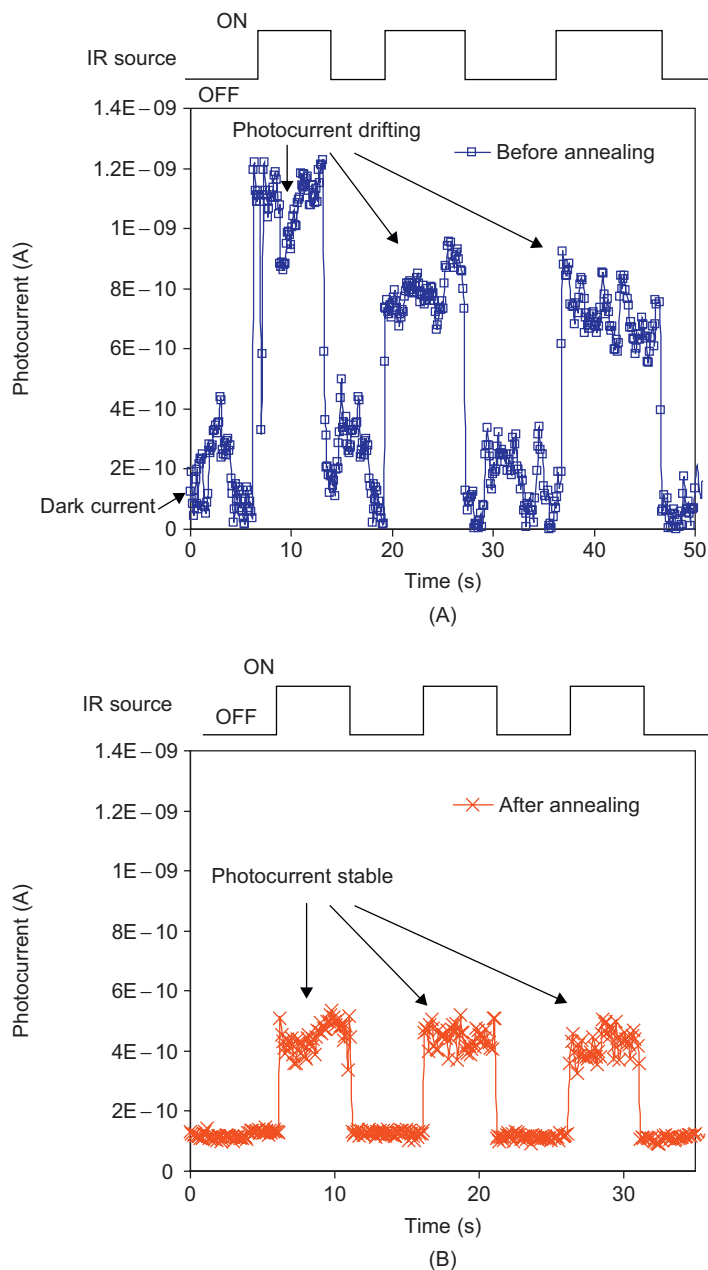
earlier, the contact condition is one of the factors to affect the photo responses of CNT-based devices. As shown in Fig. 6.4, when a semiconducting CNT is connected between a pair of metal electrodes, two Schottky barriers are formed and the total photocurrent is equal to $I_1 - I_2$, where I_1 and I_2 are the currents generated at the two CNT-metal contacts, respectively. If a CNT is deposited on a pair of

**FIGURE 6.4**

Energy band diagram of the CNT Schottky contacts on heterogeneous electrodes.

homogenous electrodes (i.e., the electrodes are made by the same material), the two Schottky barriers are reversely connected. When they are illuminated under an IR source, photo-generated electrons and holes generate almost the same photocurrent at two sides and two currents will cancel each other. As a result, the total photocurrent is very small. On the contrary, the total photocurrent is bigger when a CNT is deposited on a pair of heterogeneous electrodes (i.e., the electrodes are made by two different materials). The difference between two CNT-metal contacts directly affects the efficiency and sensitivity of the CNT device. In the heterogeneous design, a Schottky contact is formed at one of the CNT-metal interface and an ohmic contact is formed at another CNT-metal interface, therefore, the total photocurrent can be enhanced. Au and Ti are chosen as the heterogeneous electrodes because they have different work functions ($\text{Au} = 5.2 \text{ eV}$ and $\text{Ti} = 4.3 \text{ eV}$), and the resulting photocurrent is significantly increased.

After the discussion of the simple structure of the optical sensor, we can also study optical behavior of the CNT-based optical sensors before and after the annealing process. When the IR light source, which was controlled to be ON and OFF periodically, was illuminated to the sensor, the temporal photoresponses of the oxygen-doped MWCNT-based optical sensor and de-doped MWCNT-based optical sensor were compared as shown in Fig. 6.5. For the oxygen-doped MWCNT, the dark current was about 0.2 nA with a signal noise of 0.3 nA and the photocurrent was drifting from 1.2 to 0.8 nA. For the de-doped MWCNT, the dark current and the photocurrent were maintained at 0.1 and 0.5 nA, respectively. The result clearly indicated that the photocurrent drifting and signal noise of the de-doped MWCNT-based optical sensor was decreased after the thermal annealing process and the sensor provided more stable performance after the annealing treatment.

**FIGURE 6.5**

Temporal photoresponses of (A) the de-doped (before annealing) and (B) the oxygen-doped (after annealing) MWCNT-based IR detector. The oxygen-doped MWNT based IR detector exhibited signal drifting before the annealing process, which is a very unstable performance.

6.4 PARYLENE THIN FILM PACKAGING

Parylene C thin film is employed as a conformal pinhole free insulating layer for current electronics [19]. And we have developed a packaging process of carbon nanotube device by using this polymer thin film as a oxygen barrier to protect the CNT-based devices [20]. Since our interests are using the devices for optical sensing, the transmission properties of parylene C thin film were studied to find the optimal thickness of the parylene C thin film for using as a packaging material. It is important to find a suitable thickness of parylene C layer which is not only acting as an oxygen barrier, but also contributing the least optical absorption, such that the packaged CNT-based optical sensor can detect the optical signal effectively. In the experiment, different thicknesses of parylene C layers (from 0.8 to 12 μm) were coated on raw quartz substrates and then placed between the IR source and the CNT-based IR sensor, respectively, as shown in Fig. 6.6. The corresponding current change from the sensor was obtained and shown in Fig. 6.7. The photo-generated current of the IR sensor was changed when IR laser source was configured to switch on and off periodically. The current percentage change from the sensor was 62.7 when a raw quartz substrate was put between the IR source and the CNT-based IR sensor, and it was used as a reference value because the raw quartz substrate absorbed some IR laser radiation and deflected the IR laser path. The experimental results indicated that the sensing current decreased as the thickness of parylene increased as shown in Fig. 6.7. However, the thickness of parylene C layer cannot be too small; otherwise, it cannot isolate CNTs from surrounding environment. Based on the results, the thickness was estimated and the IR absorption of parylene should be the least if the thickness is less than 1 μm .

Here, we demonstrated the packaging result of a CNT-based IR sensor. A single SWCNT was deposited on a pair of heterogeneous electrodes and was then annealed at 400°C in a vacuum furnace for 1 hour to remove the oxygen molecules first. Afterwards, a parylene C thin film layer with thickness

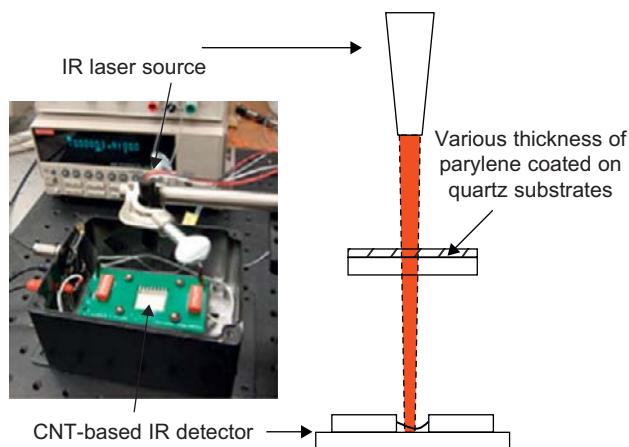
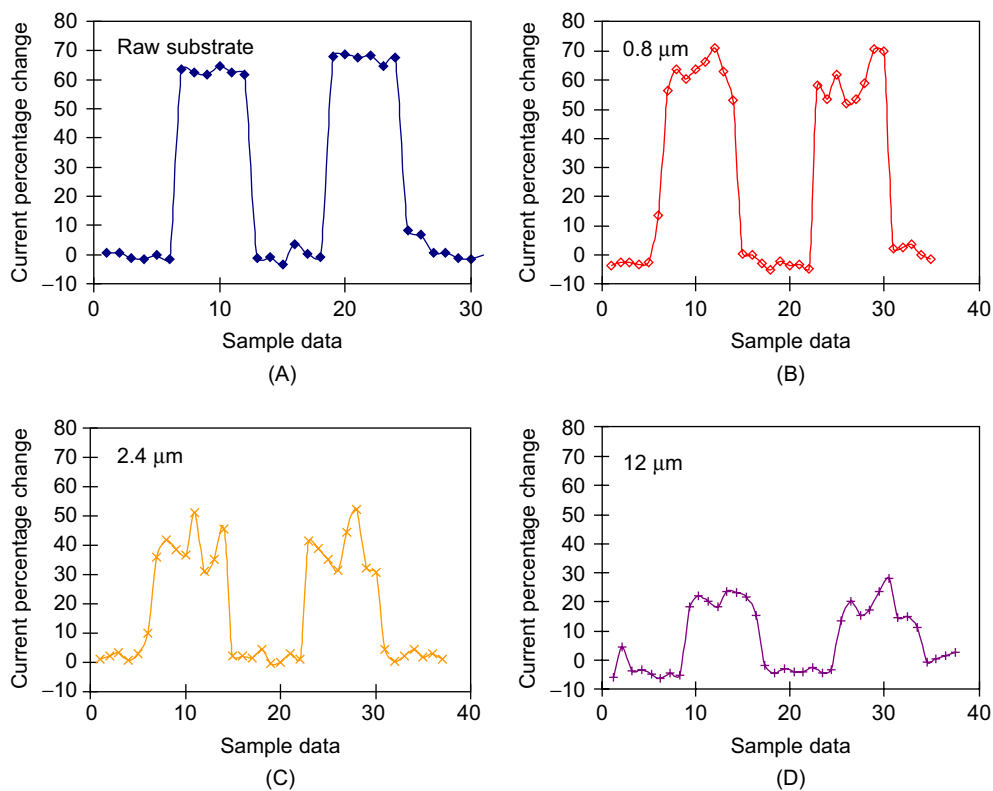


FIGURE 6.6

Experimental setup IR response measurement of the CNT-based IR sensor under quartz substrate coated with different thicknesses of parylene C. ([20], © [2007] IEEE)

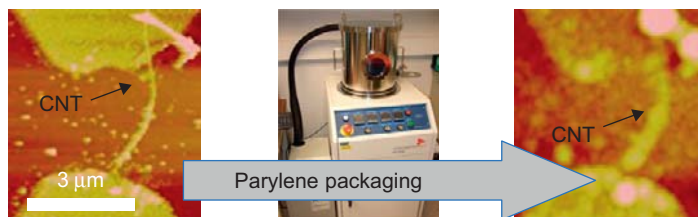
**FIGURE 6.7**

Current percentage change of the CNT-based detector device when different thicknesses of parylene C thin film layers were coated on the substrate: (A) raw substrate; (B) 0.8 μm ; (C) 2.4 μm ; and (D) 12 μm .

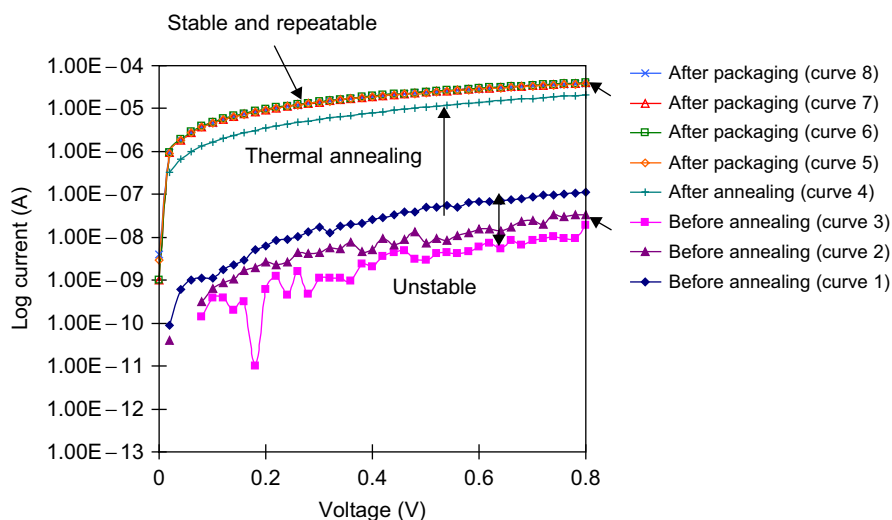
of 1 μm was deposited on the sensor so as to protect SWCNT from oxygen contamination. In order to verify the formation of SWCNT between the micro electrodes, AFM images were taken to observe the formation of SWCNTs before and after parylene C coating as shown in Fig. 6.8. It indicated that SWCNTs were successfully formed between the micro electrodes.

6.5 ELECTRICAL AND OPTICAL STABILITY OF THE CNT-BASED DEVICES AFTER PACKAGING

Since parylene C layer isolated CNT-based devices from ambient environment, the electrical behavior was not affected by surrounding environment. When compared with the CNT-based IR detector without parylene protection, the stability was significantly increased after parylene packaging. The result

**FIGURE 6.8**

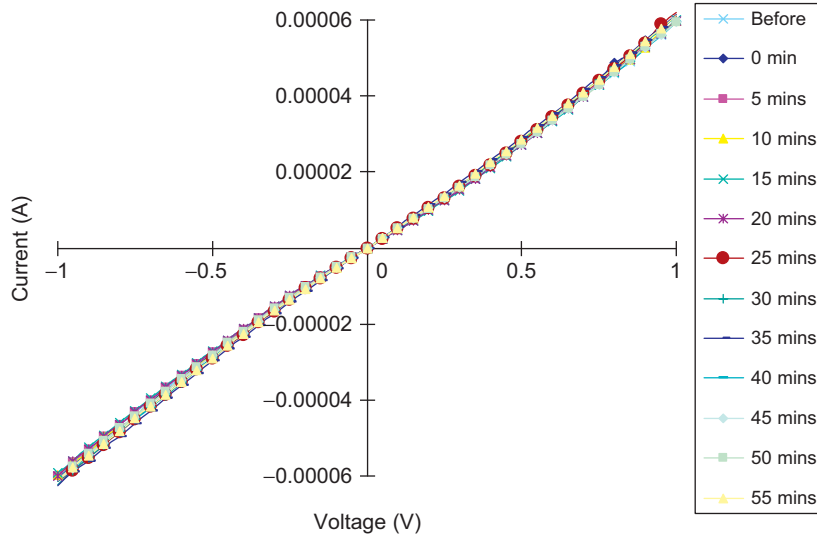
AFM images showing a bundle of SWCNTs were placed between electrodes before and after parylene C coating.

**FIGURE 6.9**

I-V characteristic of the CNT IR detector during the thermal annealing process and the parylene C packaging process. ([21], © [2008] IEEE)

indicated that parylene C acted as an excellent packaging material, which not only transmitted to IR signal, but also maintained the reliability of the CNT device. It also indicated that it is possible to prevent oxygen doping to CNT devices by coating a layer of parylene C thin film, and the electronic property of the CNT-based devices can be maintained. As shown in Fig. 6.9, I-V characteristics of a CNT-based IR detector at different status of the de-doping processes were obtained. Before the thermal annealing process, fluctuation in conductivities and unstable performance of the detector were observed (curves 1–3 in Fig. 6.9). The conductivities of the detector increased significantly after the thermal annealing process (curve 4 in Fig. 6.9). Finally, the I-V characteristics of the detector became very stable after the parylene C packaging process and the signal was repeated over a couple days (curves 5–8).

In order to further investigate the stability and reliability of the CNT-based device after parylene C coating, an experiment was performed to measure the I-V characteristic of the device under abnormal

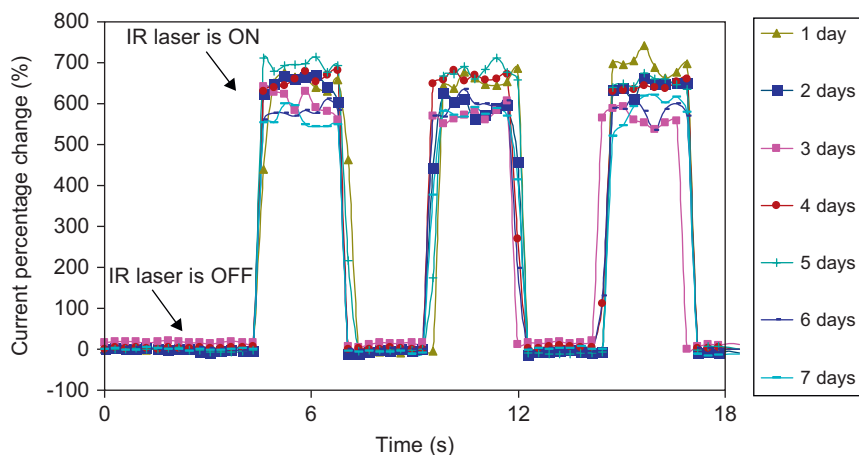
**FIGURE 6.10**

I-V characteristics of the packaged CNT sensor which was surrounded by dry ice for 55 minutes. ([20], © [2007] IEEE)

condition for a period of time. The CNT-based IR sensor was coated with the parylene C thin film and was then surrounded by dry ice for 55 minutes. Since the temperature of surrounding environment was decreased by the dry ice, a thin layer of moisture was condensed on top of the chip. The I-V curves of the corresponding CNT IR sensor was measured every 5 minutes. As seen from the experimental results in Fig. 6.10, repeatable I-V curves in different cycles were obtained, which implied that the performance of the CNT device after parylene C coating was very stable and further proved that parylene C is a very good moisture barrier. Moreover, the IR detection experiment was performed to investigate its stability and the experiment was repeated in several cycles for 1 week. As shown in Fig. 6.11, the photocurrent changed and responded repeatedly to IR radiation for a period of time.

6.6 SUMMARY

A systemic approach to maintain, control, and prevent the oxygen doping of CNT-based IR detectors was presented. It included two different processes: (1) oxygen removal by the vacuum thermal annealing and (2) oxygen prevention by parylene C packaging. The photonic behavior of the oxygen-doped and the de-doped CNT-based IR detector were studied. The oxygen molecules removal by thermal annealing process provides significant improvement in the performance of the CNT-based devices and the contact resistances at the CNT-metal interfaces. The fabrication, thermal annealing process, and packaging process of CNT-based IR detectors have been presented. The CNT-based IR detectors were successfully fabricated and their IR responses and I-V characteristics were investigated. Experimental results indicated that the IR sensing ability of the packaged device. Moreover, the packaged CNT-based

**FIGURE 6.11**

IR response of the CNT IR detector coated with parylene C thin film with thickness of $1\ \mu\text{m}$. The IR detection experiment was performed and repeated in several cycles for a period of time. ([21], © [2008] IEEE)

device was able to sustain and exhibit repeatable photoresponses for a long period of time, which could not be observed from the results of CNT-based devices without parylene C coating. It indicated that parylene C acted as an excellent packaging material, which not only protected CNT-based devices from oxygen contamination, but also improved the stability of the CNT device. Based on the current results, the thermal annealing process and packaging process may potentially become efficient methods to fabricate a CNT-based IR detector array with reliable performance.

References

- [1] S. J. Tans, A. R. M. Verschueren, and C. Dekker. Room-temperature transistor based on a single carbon nanotube. *Nature*, 393:49–52, 1998.
- [2] A. Javey, J. Guo, Q. Wang, M. Lundstrom, and H. Dai. Ballistic carbon nanotube field-effect transistors. *Nature*, 424:654–657, 2003.
- [3] I. A. Levitsky and W. B. Euler. Photoconductivity of single-wall carbon nanotubes under continuous-wave near-infrared illumination. *Appl. Phys. Lett.*, 83:1857–1859, 2003.
- [4] H. Chen, N. Xi, K. W. C. Lai, C. K. M. Fung, and R. Yang. Development of infrared detectors using single carbon-nanotube-based field-effect transistors. *IEEE Trans. Nanotechnol.*, 9:582–589, 2010.
- [5] L. Liu and Y. Zhang. Multi-wall carbon nanotube as a new infrared detected material. *Sens. Actuators A*, 116:394–397, 2004.
- [6] D. Liu, M. Fina, J. Guo, X. Chen, G. Liu, S. G. Johnson, and S. S. Mao. Organic light-emitting diodes with carbon nanotube cathode-organic interface layer. *Appl. Phys. Lett.*, 94:013110, 2009.
- [7] J. A. Misewich, R. Martel, P. Avouris, J. C. sang, S. Heinze, and J. Tersoff. Electrically induced optical emission from a carbon nanotube fet. *Science*, 300:783–786, 2003.
- [8] P. G. Collins, K. Bradley, M. Ishigami, and A. Zettl. Extreme oxygen sensitivity of electronic properties of carbon nanotubes. *Science*, 287:1801–1804, 2000.

- [9] L. Valentinia, I. Armentanoa, L. Lozzib, S. Santuccib, and J. M. Kenny. Interaction of methane with carbon nanotube thin films: role of defects and oxygen adsorption. *Mater. Sci. Eng. C*, 24:527–533, 2004.
- [10] V. Derycke, R. Martel, J. Appenzeller, and Ph. Avouris. Controlling doping and carrier injection in carbon nanotube transistors. *Appl. Phys. Lett.*, 80:2273–2275, 2002.
- [11] J. Zhang, N. Xi, H. Chen, K. Lai, G. Li, and U. C. Wejinya. Design, manufacturing, and testing of single-carbon-nanotube-based infrared sensors. *IEEE Trans. on Nanotechnol.*, 8(2):245–251, 2009.
- [12] J. Zhang, N. Xi, K. W. C. Lai, H. Chen, Y. Luo, and G. Li. Single carbon nanotube based photodiodes for infrared detection. In *Proceedings of the 7th IEEE International Conference on Nanotechnology*, pages 1156–1160, 2007.
- [13] H. Chen, N. Xi, K. W. C. Lai, C. K. M. Fung, and R. Yang. Development of infrared detectors using single carbon-nanotube-based field-effect transistors. *IEEE Trans. on Nanotechnol.*, 9(5):582–589, 2010.
- [14] L. H. Allen, J. R. Phillips, D. Theodore, C. B. Carter, R. Soave, J. W. Mayer, and G. Ottaviani. Two-dimensional Si crystal growth during thermal annealing of Au/polycrystalline-Si bilayers. *Phys. Rev. B*, 41(12):8203–8212, 1990.
- [15] Y. Ochiai, R. Enomoto, S. Ishii, K. Miyamoto, Y. Matsunaga, and N. Aoki. Thermal annealing effect in multi-wall carbon nanotubes. *Physica B: Condens. Matter*, 323(1-4):256–258, 2002. *Proceedings of the Tsukuba Symposium on Carbon Nanotube in Commemoration of the 10th Anniversary of its Discovery*.
- [16] K. W. C. Lai, N. Xi, C. K. M. Fung, J. Zhang, H. Chen, Y. Luo, and U. C. Wejinya. Automated nanomanufacturing system to assemble carbon nanotube based devices. *Int. J. Rob. Res.*, 28(4):523–536, 2009.
- [17] K. W. C. Lai, C. K. M. Fung, V. T. S. Wong, M. L. Y. Sin, W. J. Li, and C.-P. Kwong. Development of an automated microspotting system for rapid dielectrophoretic fabrication of bundled carbon nanotube sensors. *IEEE Trans. Autom. Sci. Eng.*, 3(3):218–227, 2006.
- [18] G. Li, N. Xi, and M. Yu. Development of augmented reality system for afm based nanomanipulation. *IEEE/ASME Trans. Mechatronics*, 9:358–365, 2004.
- [19] *Parylene Data Sheet*. Specialty Coating Systems, Indianapolis.
- [20] K. W. C. Lai, N. Xi, J. Zhang, G. Li, and H. Chen. Packaging carbon nanotube based infrared detector. In *Proceedings of the 7th IEEE Conference on Nanotechnology*, pages 778–781, 2007.
- [21] K. W. C. Lai, N. Xi, C. K. M. Fung, H. Chen, J. Zhang, and Y. Luo. Photonic Effect on Oxygen-doped and De-doped Carbon Nanotubes. In *Proceeding of the 8th IEEE International Conference on Nanotechnology*, pages 251–254, 2008.

Carbon Nanotube Schottky Photodiodes

7

Hongzhi Chen, Ning Xi, and King Wai Chiu Lai

Department of Electrical and Computer Engineering, Michigan State University, Michigan

CHAPTER OUTLINE

7.1 Introduction	107
7.2 Review of CNT Photodiodes	108
7.3 Design of CNT Schottky Photodiodes	111
7.4 Symmetric Schottky Photodiodes	112
7.5 Asymmetric Schottky Photodiodes	117
7.6 Summary	121
References	121

7.1 INTRODUCTION

Owing to their outstanding physical, electrical, and mechanical properties, carbon nanotubes (CNTs) have been widely used as functional materials for biosensors [1, 2], gas sensors [3, 4], pressure sensors [5, 6], and transistors [7, 8]. In particular, the one-dimensional (1D) hollow cylindrical structure of CNTs possesses exceptional optoelectronic properties, which enables them to function as core materials for light emitters [9] and photodetectors [10, 11].

Semiconductor CNT is a direct band-gap material, which is essential for high-performance photodetectors. The noise of 1D photodetectors using CNTs can be extremely low because of phonon scattering suppression [12] and size shrinkage [13]. The quantized energy level and phonon bottleneck in the CNT give prolonged carrier life time [14]. The 1D structure with high surface-to-volume ratio can inherently increase the signal-to-noise ratio with shortened carrier transit time [15], which may lead to a higher operating temperature that is significant for long-wavelength photodetectors. It has been demonstrated that CNT-based middle-wave IR sensors can operate at room temperature [16]. The peak responsivity of the detectors can be tuned to the desired wavelength by controlling the diameter of CNTs, since the bandgap energy is inversely proportional to the diameter in quantum-confined structures [17], and the diameter of CNTs can be easily tailored by electrical breakdown [18]. As a result, the CNT detector can cover the spectrum from UV to long-wave infrared. The dominant Fermi level pinning effect in planar contact is trivial in the 1D structure [19], and therefore, the performance of CNT infrared detectors can be improved by selecting proper metals. In addition, multiple electron-hole pair generation in nanostructures could potentially increase the sensitivity of

CNT detectors [20]. Photodetector operation typically involves three consecutive processes to transform the optical signal into electrical signal, namely carrier generation, carrier separation, and carrier transport. In other words, photodetectors with high sensitivity require high quantum efficiency, low noise, long carrier life, and short carrier transit time. Therefore, CNTs have the potential to outperform their bulkier counterparts if their unique features are fully utilized in the sensor design. However, there are three aspects that limit manufacturing of high-performance nanosensors. First of all, current technologies are still incapable of synthesizing CNTs with identical properties. Second, the diameter of CNTs can be as small as subnanometer size, making it extremely difficult to assemble CNTs in desired locations. Finally, the underlying physics of the nanomaterial is not fully understood, which impedes sensor design with optimized structure.

In previous chapters, we introduced selecting CNTs with desired properties using DEP, and efficiently assembled CNTs by using a DEP deposition system coupled with an AFM manipulation system. In order to gain a better understanding of the working principles and underlying physics of CNT photodiodes, which is essential for obtaining sensors with desired functionality, a systematic study of CNT photodiodes based on Schottky barriers between metals and CNTs is introduced in this chapter. First, some typical CNT photodiode structures are reviewed, followed by the design of the CNT Schottky photodiodes. Both symmetric and asymmetric Schottky photodiodes are examined, and their performance is compared to explore the underlying physics of the CNT photodiode.

7.2 REVIEW OF CNT PHOTODIODES

After depositing a CNT thin film between two pre-patterned electrodes with an insulating gap, infrared detection was first realized by observing the conductance change with infrared irradiation of the device as shown in Fig. 7.1 [21]. However, not only did the mixture of metallic and semiconductor CNTs in the film severely degrade the response of the thin-film photodiode, but also the adsorbed oxygen in the film decreased the photo-sensitivity. In order to improve the performance of the thin-film detector, CNTs were embedded into the polycarbonate nanocomposite [22]. This insulating polymer matrix dramatically enhanced the photoresponse, since the nanocomposite changed the detection mechanism from a thermal effect into a photo effect.

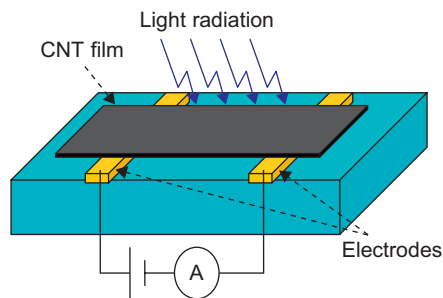
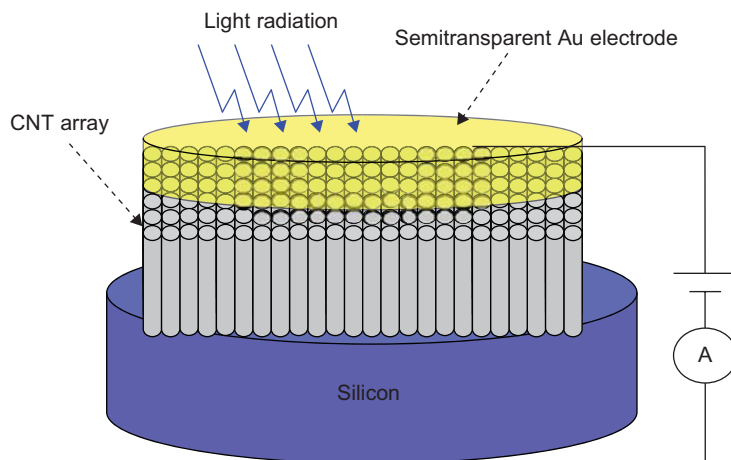


FIGURE 7.1

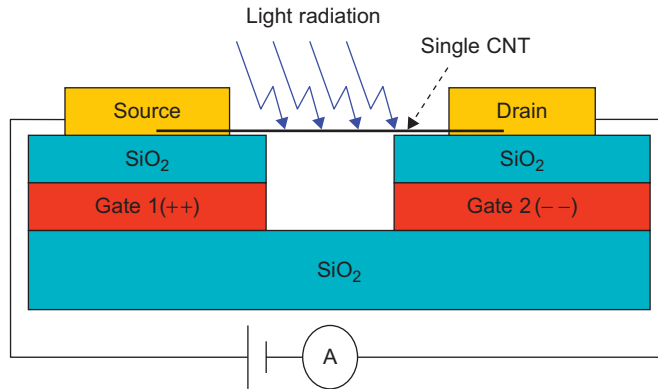
The structure of a CNT thin-film photodetector.

**FIGURE 7.2**

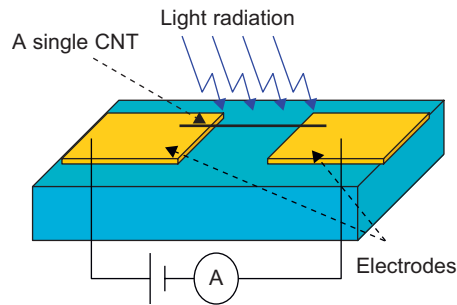
The structure of a silicon–CNT heterojunction photodetector with nanoporous anodic aluminum oxide (AAO) template to separate the vertical CNT array.

Instead of connecting a CNT film to the metal electrodes, detectors can also be fabricated by stacking CNT films onto the bulk silicon substrate [23]. In this structure, the contact between CNTs and silicon forms heterojunctions, which are responsible for the photocurrent generation. Nanophotoelectronic devices using films or sheets will lose some particular properties and advantages due to the interaction between nanotubes. By growing CNTs on a nanoporous anodic aluminum oxide (AAO) template, the interaction of CNTs can be eliminated, as shown in Fig. 7.2 [24]. This synthesis method will form a periodic dense array of CNTs that are parallel to one another and perpendicular to the silicon substrate. In this heterojunction system, several mechanisms may contribute to the photoresponse. It is very difficult to fully understand its underlying operation mechanism, since the two materials are very dissimilar in band gap, work functions, and dimensionality, and the synthesized CNTs may have varied properties.

A single CNT is a perfect 1D system. Studying single-CNT-based photodetectors can help us understand the real operation principle of 1D detectors, which enables fabrication of photodetectors with optimized performance. Photoconductivity of a single-CNT-based p–n junction photodiode was observed by fabricating two split gates underneath both ends of a semiconductor nanotube, as illustrated in Fig. 7.3 [25]. By applying opposite gate voltages with high amplitude to the split gates, the CNT at both ends will be electrostatically doped into p and n type semiconductors, resulting in the formation of a p–n junction in the CNT. The fabrication begins with a thick thermal oxide grown on a heavily doped Si wafer. Split gates were formed using Mo. Using the split gate metal as an etch mask, part of oxide was dry etched. Next, a thin layer of silicon oxide was deposited, forming the gate dielectric for the split gate. The source and drain contacts were then lithographically defined. Finally, CNTs were grown on top of the source and drain metals. In the center of the device, where the built-in field is greatest, photogenerated electron and hole pairs become separated, causing currents to flow. This photodiode provides some insights into CNT detectors and shows some promising results [25]. However, the fabrication process of the device is too complicated, which will hinder its wide-ranging

**FIGURE 7.3**

The structure of a single CNT-based p-n junction photodiode.

**FIGURE 7.4**

The structure of a single-CNT-based Schottky photodiode.

application. Therefore, a CNT detector with a simpler structure is needed. CNT Schottky photodiodes emerge as a perfect alternative.

When metal and CNT come into contact, whether or not a Schottky barrier is formed depends on the Fermi energy alignment. The Schottky barrier determines the electrical and optical properties of CNT devices; however, the importance of the Schottky barrier was neglected in the early days of developing CNT-based devices, when researchers attributed the electrical properties of these devices to the intrinsic properties of CNTs [26] rather than to the contacts. With the development of CNT field effect transistors (CNTFETs), increasing evidence suggests that the Schottky barrier plays a key role in determining the characteristics of nanodevices [27]. It was demonstrated that Schottky diodes between an individual SWCNT and metals were responsible for photocurrent generation under continuous infrared illumination [28]. Figure 7.4 shows the structure of a Schottky photodiode that has a much simpler configuration than a p-n junction photodiode.

The main cause of generation of photocurrent in the CNT Schottky barrier photodiode is the depletion regions of the barrier. Photons with energy higher than the band gap of CNT can produce electron

and hole pairs or excitons in the entire CNT, whereas the current flow is distributed only to the depletion region, since the built-in potential in the depletion region (and within diffusion length) can separate the photo-generated e–h pairs, and thus produce photocurrent, while the e–h pairs outside the depletion region will recombine shortly.

Understanding the one-dimensional (1D) Schottky barrier within the CNT is important. The traditional Schottky barrier theory for planar contact between metal and bulk semiconductor is well established, and can help in the design of optimized photodiodes. However, the conventional understanding of the Schottky barrier cannot be applied to 1D Schottky barriers between metal and nanotubes, since the planar contacts are dominated by the metal-induced gap states (MIGS), whereas the MIGS-induced Fermi level pinning is trivial for the 1D structure [29] because of quantum confinement. Therefore, the physics and fundamentals of 1D Schottky barriers within a CNT need to be reexamined. In the following sections, the design, fabrication, testing and analysis of CNT Schottky photodiodes are introduced so as to understand their working principles.

7.3 DESIGN OF CNT SCHOTTKY PHOTODIODES

After photons are absorbed by semiconductor CNTs, photo-generated electrons are separated by the electric field within the Schottky barrier, and need to tunnel through the barrier before contributing to the photocurrent. The Schottky barrier width determines the effective absorption area, while the built-in potential within the barrier determines the speed of separated carriers, and both barrier width and height define the carrier tunneling probability. The basic structure of a CNT Schottky photodiode is shown in Fig. 7.4, in which a single semiconductor CNT bridges two metal electrodes to form the Schottky barriers. Figure 7.5A shows the energy alignment between a metal (take Au as example) and CNT. CNT was reported as a p-type material in air with a Fermi energy of around 5 eV [17] due to oxygen doping or some accidental doping during synthesis [30]. The work functions (Fermi energy) of Au is also close to 5 eV, and it can be slightly lower or higher than 5 eV because of the environmental differences [31] (in the Fig. 7.5A, the Fermi energy of Au is slightly smaller than that of CNT). The

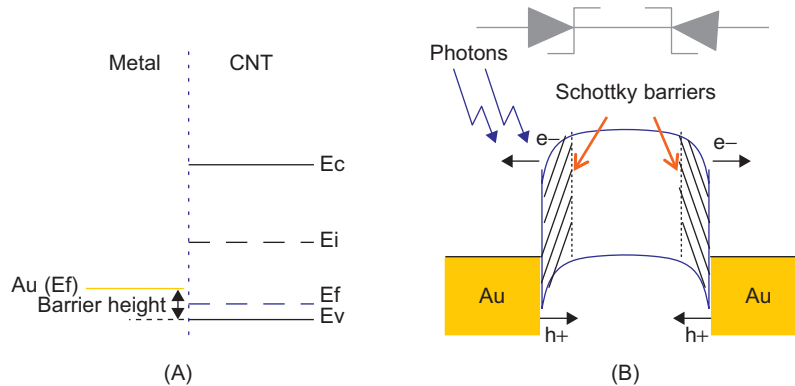
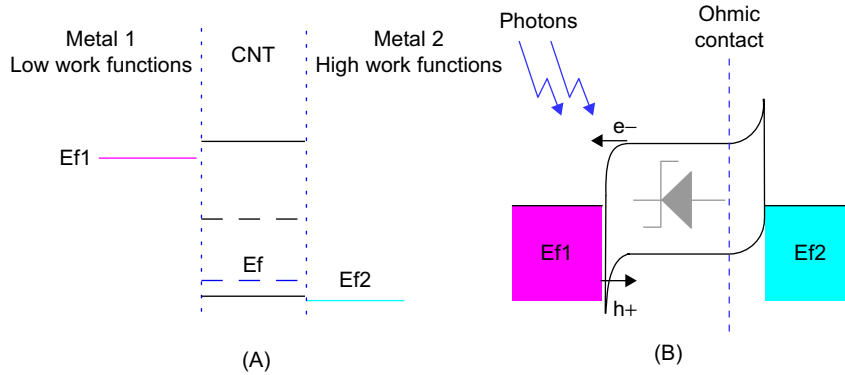


FIGURE 7.5

(A) Energy alignment of Au and CNT. (B) Band diagram of a symmetric CNT photodetector. E_c = conduction band energy; E_v = valence band energy; E_f = Fermi energy; E_i = intrinsic energy.

**FIGURE 7.6**

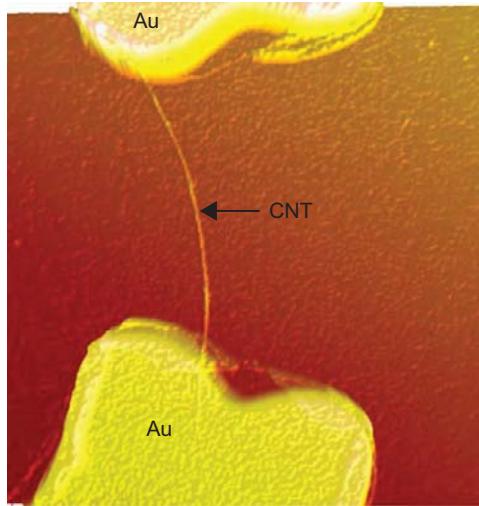
(A) Energy alignment of metals with high/low work functions and CNT. (B) Band diagram of the asymmetric CNT photodetector.

majority of carriers of the semiconductor CNT are holes, and therefore, the energy difference between the Au work functions and the CNT valence band (E_v) is indicated as the barrier height. When CNT connects two Au electrodes at both ends, denoted as a symmetric photodetector, two symmetric Schottky barriers will be formed at the contacts as shown in Fig. 7.5B. This structure results in a photodiode that consists of two Schottky barriers inversely connecting to each other. When the photons with energy higher than the CNT bandgap strike the CNT, electron and hole pairs will be generated and separated in the depletion region, as indicated in Fig. 7.5B. Hence, the total photocurrent under zero bias is calculated by $I_{\text{photo}} = I_{\text{left}} + I_{\text{right}} = i_{b1} - i_{b2}$. These symmetric barriers significantly reduce the sensitivity of the photodetector, since the separated carriers need to tunnel through another barrier before being collected. What is more, this structure detects the signal intensity difference between two contacts, resulting in poor performance.

Asymmetric photodetectors, using metals with high/low work functions to connect two ends of a single CNT, can be used to improve the performance of the detectors. The energy alignment and resulting band diagram are shown in Fig. 7.6. On the left contact, the metal has a work functions that is smaller than that of the CNT and forms a Schottky barrier, while on the right contact, the metal work functions is higher than that of the CNT and forms an Ohmic contact. The electrical and optical properties of this device will be determined by one Schottky barrier. Thus the total photocurrent will depend only on one Schottky barrier rather than on the difference between the photocurrent of two barriers as in the symmetric structure. Moreover, by transferring one of the Schottky barriers into Ohmic contact, the photo-generated electron holes at the Schottky barrier will be able to transport through the contact easily. As a result, the photoresponse of the CNT photodetector is expected to be highly enhanced in the asymmetric structure.

7.4 SYMMETRIC SCHOTTKY PHOTODIODES

An AFM image of a symmetric CNT Schottky photodiode with Au electrodes is shown in Fig. 7.7. An individual single wall CNT (SWCNT) connects two Au electrodes on top of a quartz substrate. The

**FIGURE 7.7**

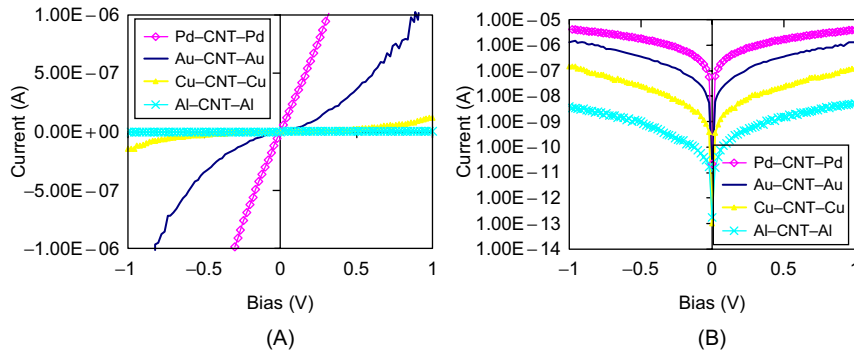
An AFM image of a symmetric CNT detector with Au electrodes.

fabrication process begins with making two Au electrodes with an insulating gap of approximately $1\text{ }\mu\text{m}$ by photolithography, thermal evaporation, and lift-off. After that, a droplet of SWCNT suspension (ethanol) is dropped into the gap between electrodes that connects with the dielectrophoresis (DEP) deposition system [32]. An individual SWCNT was deposited between the electrodes by optimizing the suspension concentration, and assisted by the atomic force microscope (AFM) manipulation system [33–35]. A more detailed fabrication process was discussed in previous chapters and [36, 37].

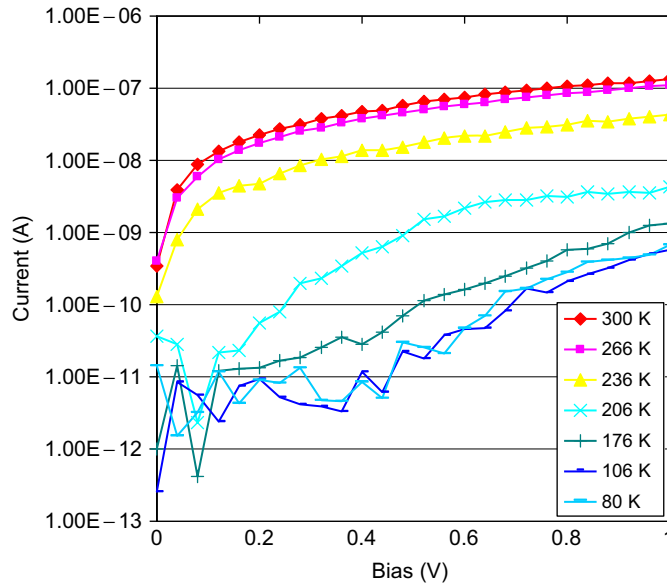
The properties of the Schottky barriers are determined by the energy alignment between the metals and SWCNT; thus Schottky photodiodes made of different metals were investigated to understand the importance of the metal work functions.

The I-V characteristics of symmetric Schottky photodiodes with four different metals (Pd, Au, Cu and Al) were studied. Their typical I-V curves are shown in Fig. 7.8, which are based on more than 100 devices tested in our laboratory.

Figure 7.8 shows that the I-V characteristics for positive and negative biases are symmetric, indicating symmetric barriers at both ends, while the conductance of these devices varied significantly. The Pd–CNT–Pd diode shows linear I-V characteristics, implying an Ohmic contact or very weak Schottky barrier, which has been verified in [38]. A quasi-metallic I-V characteristic of Au–CNT–Au (weak parabolic) was observed, which resulted from two small Schottky barriers reversely connecting between the source and drain, since Au and SWCNT have similar work functions. While Cu and Al have much smaller work functions than SWCNT; the contacts between these metals with CNT form larger Schottky barriers, which is illustrated by the band diagram shown in Fig. 7.5B. Consequently, the Cu–CNT–Cu and Al–CNT–Al photodiodes have much smaller conductance. The highest conductance magnitude difference for these 1D photodiodes was approximately four orders, indicating the importance of the metal work functions. In conventional planar contacts, metal-induced gap states (MIGS)

**FIGURE 7.8**

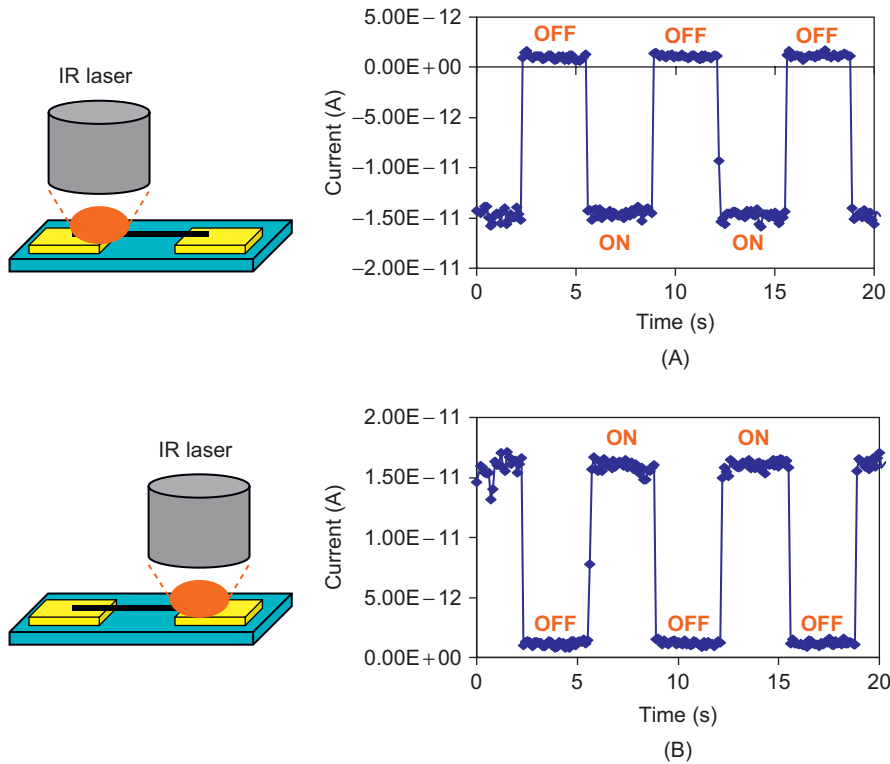
(A) I-V characteristics of CNT Schottky diodes with four different metals (Pd, Au, Cu, and Al). (B) The I-V characteristics shown on a logarithmic scale.

**FIGURE 7.9**

I-V characteristics of a Au-CNT-Au diode at different temperatures.

dominate the contacts, which weakens the role of metal work functions in determining the properties of 3D Schottky barriers. That is to say, 1D Schottky contacts have a much greater flexibility in terms of regulating the performance of the detectors via selection of proper metals.

In a conventional bulk Schottky diode, carrier injection is dominated by thermionic emission, while thermal-assisted tunneling dominates carrier injection in the 1D Schottky barrier [39]. Temperature-dependent I-V characteristics of a Au-CNT-Au photodiode is shown in Fig. 7.9. The conductance

**FIGURE 7.10**

The IR responses of a Au–CNT–Au Schottky photodiode by irradiating (A) the left electrode and (B) the right electrode. ([42], © [2010] IEEE)

was reduced significantly as the temperature decreased from 300 to 80 K, resulting in dark current suppression, since decreased temperature depresses the tunneling probability of carriers through the barriers.

The IR responses of the Schottky photodiodes were also investigated. The testing system consisted of a 830-nm IR laser, irradiating a CNT detector housed in a chamber, after passing through an IR window, which was schematically depicted in [40]. The current signal was measured using an Agilent 4156-C semiconductor analyzer by periodically switching the IR source ON and OFF. All measurements were conducted at zero bias. Figure 7.10 shows the IR response of a SWCNT Au–CNT–Au photodiode by radiating IR photons on its left and right contacts. One distinct characteristic is that the photocurrent changed direction but kept similar magnitude (1.5×10^{-11} A) when the laser illuminated two different contacts. This is caused by two symmetric Schottky diodes between Au and CNT inversely connecting to each other, as indicated in the band diagram in Fig. 7.5B. A more detailed discussion can be found in [28].

The typical IR responses of four CNT Schottky photodiodes with different metals are shown in Fig. 7.11, in which an IR laser irradiated one contact.

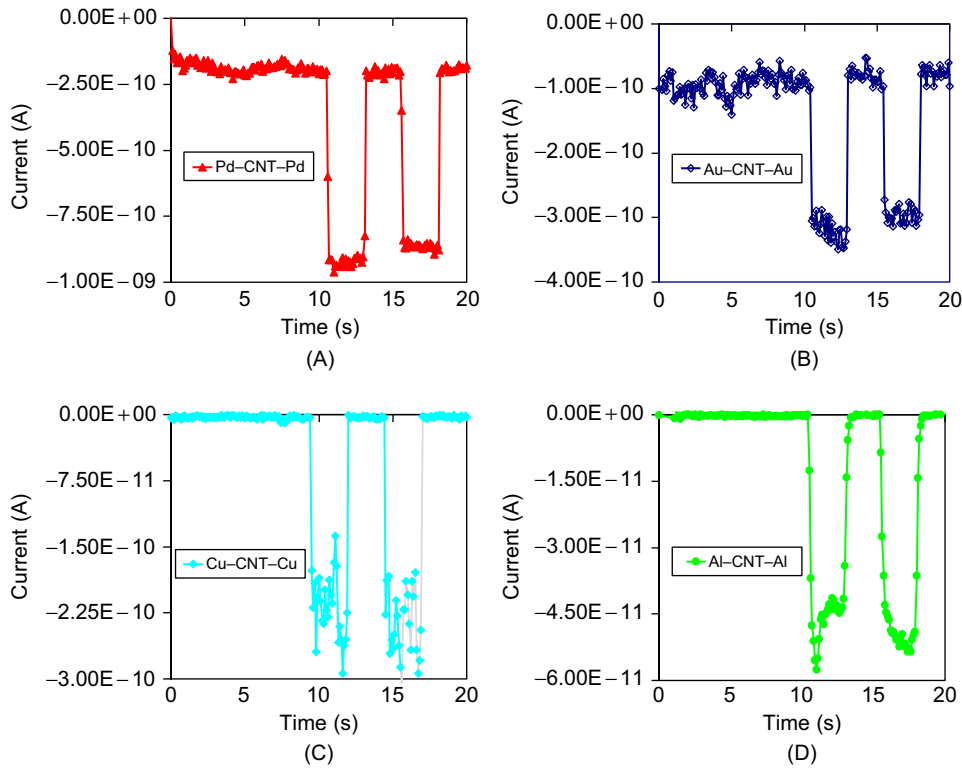
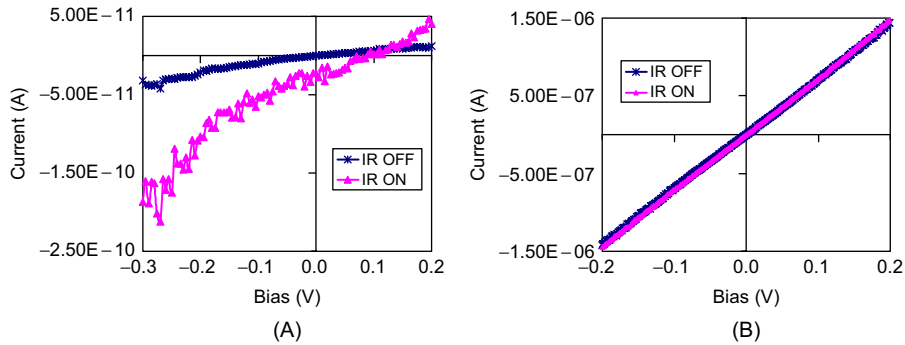


FIGURE 7.11 The IR responses of four CNT Schottky photodiodes with different metals (A) Pd-CNT-Pd, (B) Au-CNT-Au, (C) Cu-CNT-Cu, and (D) Al-CNT-Al.

Table 7.1 Performance of Four Detectors with Different Metals		
SWCNT IR Detectors	Dark Current (A)	I_{photo} (A)
Pd-CNT-Pd	2.0×10^{-10}	7.0×10^{-10}
Au-CNT-Au	1.0×10^{-10}	2.0×10^{-10}
Cu-CNT-Cu	2.0×10^{-12}	2.3×10^{-10}
Al-CNT-Al	9.0×10^{-13}	4.5×10^{-11}

The dark current and photocurrent (I_{photo}) (current difference between IR ON and OFF) of these devices are summarized in Table 7.1. Pd-CNT-Pd and Au-CNT-Au photodiodes had relatively high dark current and photocurrent. This can be explained both injected and photo-generated carriers are easily tunneling through the weak barriers. In contrast, the Al-CNT-Al photodiode had two strong

**FIGURE 7.12**

The IR responses of CNT Schottky photodiodes with bias (A) Cu-CNT-Cu and (B) Au-CNT-Au.

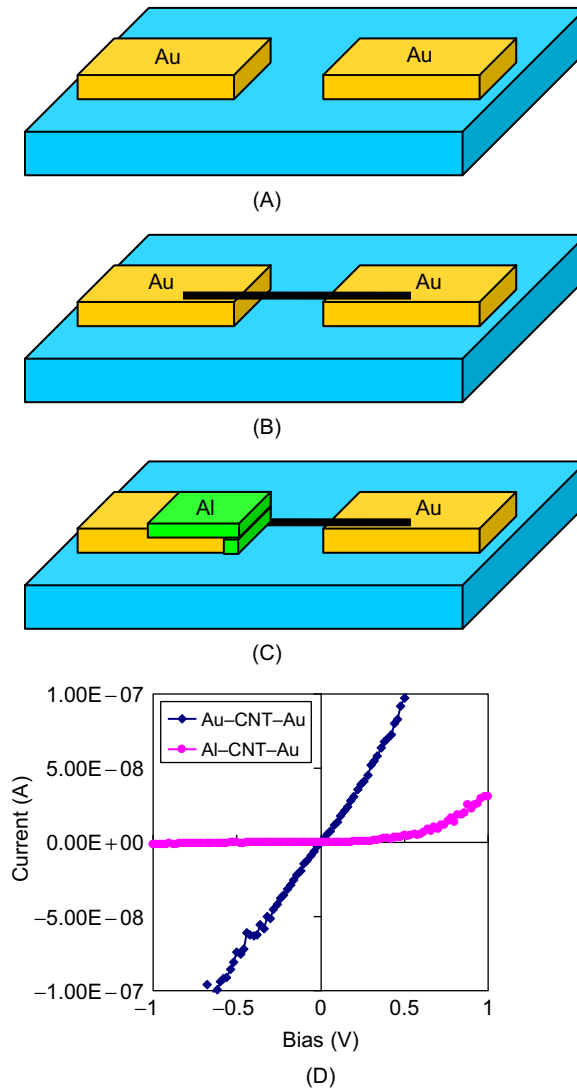
barriers, rendering the carriers difficult to tunnel through. As a result, it has relatively low dark current and photocurrent. The Cu-CNT-Cu photodiode had moderate Schottky barriers, resulting in the highest signal-to-noise ratio.

The importance of the signal-to-noise ratio of nanodevices needs to be emphasized here. It is difficult for nanophotodetectors to have photocurrent comparable to that of bulk photodiodes due to the small fill factor. However, the open circuit voltage (V_{oc}) is determined by the ON/OFF ratio (the ratio between IR ON and OFF), which can be high, even absorbing small amount of photons, because the dark current can be extremely low because of its nanoscale size and phonon scattering suppression in the 1D structure. The typical IR responses of Cu-CNT-Cu and Au-CNT-Au with applied bias are shown in Fig. 7.12. The bias-dependent photoresponse of Cu-CNT-Cu shows photovoltaic characteristics: negative bias increases the photocurrent by widening the barrier, while positive bias reduces the photocurrent because of the shrinkage of the barrier. A V_{oc} of 100 mV was observed when injected carriers were equal to photo-generated carriers, resulting in zero net current. The short circuit current of this device is only -5×10^{-11} A, which is negligible compared to conventional photodiodes, but it corresponds to 100 mV V_{oc} , which is on the same order as other traditional photodiodes. The photocurrent of Au-CNT-Au with bias is difficult to observe, since the dark current dominates the current flow.

In this section, the performance and characteristics of symmetric photodiodes using different metal electrodes were introduced. Pd-CNT-Pd, Au-CNT-Au, and Al-CNT-Al detectors have low signal-to-noise ratio, since they have either too small or large Schottky barriers at both ends. The Cu-CNT-Cu detector has moderate Schottky barriers, generating a high signal-to-noise ratio and V_{oc} .

7.5 ASYMMETRIC SCHOTTKY PHOTODIODES

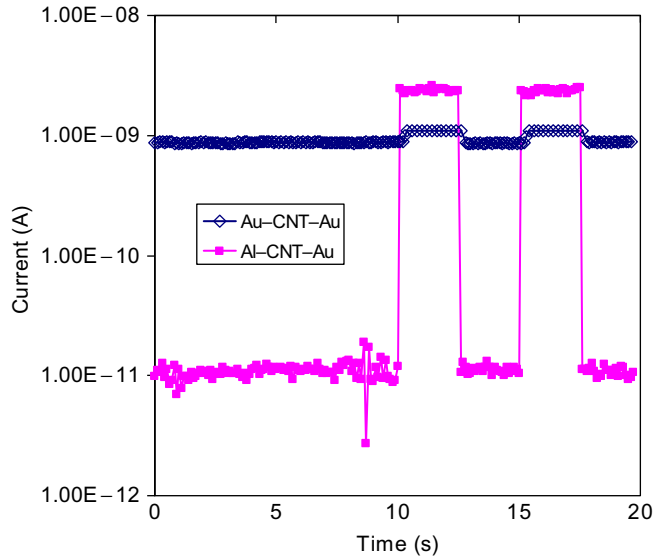
The symmetric structure of two reversely connecting Schottky diodes will significantly suppress photocurrent generation, since the two diodes are close to each other, and the photocurrents generated at the two contacts will cancel each other. In addition, the photo-generated carriers need to tunnel through another barrier before being collected. In order to address these problems, asymmetric Schottky diodes

**FIGURE 7.13**

(A–C) Fabrication process of Au–CNT–Au and Al–CNT–Au photodiodes using a single CNT. (D) Their I–V characteristics.

using metals with high/low work functions at two ends were designed. The band diagram is shown in Fig. 7.6.

In order to verify the concept of this asymmetric infrared detector, a fabrication process was designed to measure the electrical properties and IR responses of both Au–CNT–Au and Al–CNT–Au photodiodes using a single CNT. The process began with fabricating two Au electrodes with a gap

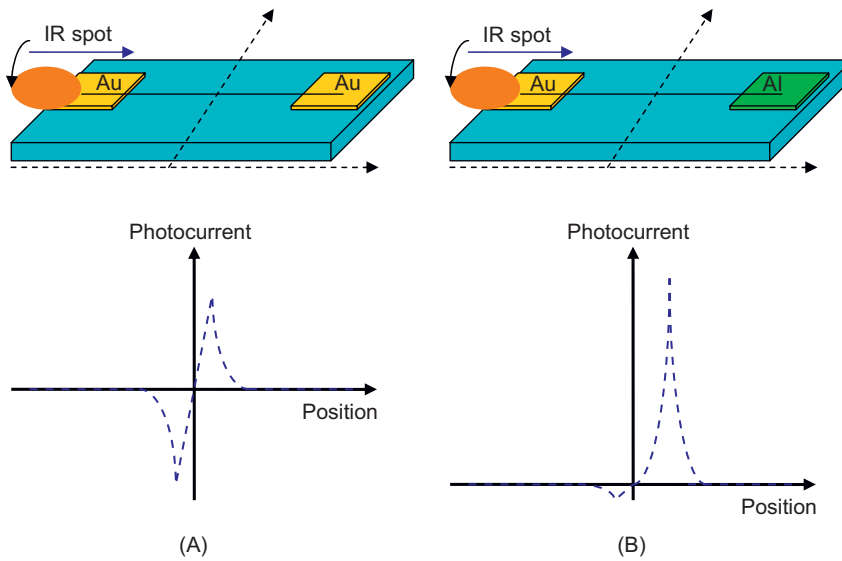
**FIGURE 7.14**

IR responses of Au-CNT-Au and Al-CNT-Au using a single CNT.

of $1.2\ \mu\text{m}$ using e-beam lithography on top of a quartz substrate as shown in Fig. 7.13A. This was followed by depositing an individual SWCNT bridging these two electrodes using the DEP and AFM manipulation system (Fig. 7.13B). The I-V characteristics were measured, denoted as Au-CNT-Au in Fig. 7.13B. Thereafter, further e-beam lithography was used to pattern an Al electrode that covered one of the Au electrodes and extended $0.2\ \mu\text{m}$ into the gap, making the device structured in the form of Al-CNT-Au with a gap of $1.0\ \mu\text{m}$ as shown in Fig. 7.13C. Its electrical characteristics were measured as shown in Fig. 7.13D, denoted as Al-CNT-Au. The Au-CNT-Au showed symmetric and quasi-metallic electrical characteristics (weak parabolic I-V characteristics with higher bias), while typical diode electrical characteristics were observed in the Al-CNT-Au structure. The electrical properties of the device changed significantly because of the replacement of an Au electrode. Therefore, there must be a higher barrier between Al and nanotube that dominates the optoelectronic properties of the detector [41].

The IR responses of Au-CNT-Au and Al-CNT-Au are also compared as shown in Fig. 7.14. The dark current decreased from 8.8×10^{-10} to 1.1×10^{-11} A, while the photocurrent increased from 2.1×10^{-10} to 2.4×10^{-9} A. The photocurrent enhancement increased the responsivity (photocurrent/infrared power) and quantum efficiency (number of generated electrons/number of photons), and both dark current suppression and photocurrent enhancement contributed to the improvement of the noise equivalent power (NEP)(noise/responsivity) and noise equivalent temperature difference (NETD). In other words, the asymmetric structure greatly increased the sensitivity and efficiency of the CNT-based IR detector.

In order to further understand the working principle of CNT Schottky diodes, the position-dependent photocurrent of symmetric and asymmetric detectors were compared as shown in Fig. 7.15. By moving the IR laser spot from left to the right in the symmetric Schottky photodiode (Fig. 7.15A),

**FIGURE 7.15**

The position-dependent IR response of (A) Au–CNT–Au and (B) Au–CNT–Al when the IR laser was moved from left to right.

the photocurrent was increased (negative values) gradually at the beginning, and the amplitude was maximized when the spot approached the left CNT–Au contact. The photocurrent was decreased and vanished when the spot moved to the middle of the CNT. By further moving the laser spot to the right, the photocurrent increased in amplitude but in a different direction (values became positive), and the positive photocurrent was maximized when the laser illuminated on the right CNT–Au contact. The photocurrent decreased to zero gradually by further moving the laser to the right. This measurement corresponds to the results shown in Fig. 7.10. This photoresponse can be explained by two symmetric Schottky barriers formed at two contacts.

The same measurement was done on the asymmetric photodiode, and a significantly different photoresponse was observed as shown in Fig. 7.15B. When the laser spot moved from the left to the Au–CNT contact, photocurrent was also increased gradually, and reached a maximum amplitude (negative values), but with a much smaller value than that in the symmetric structure. The reason is that the generated electron–hole pairs needed to tunnel through a large barrier (Al–CNT) in order to contribute to the photocurrent. The negative photocurrent vanished when the laser irradiated the middle of the CNT. By further moving the laser spot to the right, the photocurrent increased in amplitude with positive values, and the positive photocurrent was maximized when the laser moved to the CNT–Al contact; however, the photocurrent amplitude was much larger than that in the symmetric structure, since the generated electron–hole pairs at the CNT–Al contact only needed to tunnel through a small barrier between Au–CNT in order to contribute to the photocurrent. The photocurrent decreased to zero when the laser was moved to the right. The measurement results in Fig. 7.15 verify the design and analysis given in Section 7.3, and we can conclude that the asymmetric structure can greatly

enhance the photoresponse of CNT-based Schottky photodiodes. A more detailed discussion can be found in [28].

7.6 SUMMARY

In this chapter, the fabrication and investigation of CNT-based Schottky photodiodes using different metals and structures was dealt with. It was found that the work functions of metals play an important role in determining the properties of the photodiodes. Symmetric Schottky photodiodes using different metals have varied dark current and photocurrent of several orders of magnitude. Low built-in potentials resulted in large dark current and photocurrent, while high built-in potentials caused smaller dark current and photocurrent. This can be explained by two Schottky barriers reversely connecting with each other in the symmetric metal structure, which was verified by position-dependent photocurrent measurements. In order to improve the performance of CNT-based Schottky photodiodes, asymmetric structure photodiodes using metals with high/low work functions at two contacts were fabricated. Compared to the symmetric photodiodes, asymmetric photodiodes had lower dark current and higher photocurrent.

References

- [1] N. Sinha and J. T.-W. Yeow. Carbon nanotubes for biomedical applications. *NanoBioscience IEEE Trans.*, 4(2):180–195, 2005.
- [2] K. Besteman, Jeong.-O. Lee, F. G. M. Wiertz, Hendrik A. Heering, and C. Dekker. Enzyme-coated carbon nanotubes as single-molecule biosensors. *Nano Lett.*, 3:727–730, 2003.
- [3] L. Valentini, I. Armentano, J. M. Kenny, C. Cantalini, L. Lozzi, and S. Santucci. Sensors for sub-ppm no2 gas detection based on carbon nanotube thin films. *Appl. Phys. Lett.*, 82:961–963, 2003.
- [4] J. Li, Y. Lu, Q. Ye, M. Cinke, J. Han, and M. Meyyappan. Carbon nanotube sensors for gas and organic vapor detection. *Nano Lett.*, 3:929–933, 2003.
- [5] J. R. Wood and H. D. Wagner. Single-wall carbon nanotubes as molecular pressure sensors. *Appl. Phys. Lett.*, 76(20):2883–2885, 2000.
- [6] C. Y. Li and T. W. Chou. Strain and pressure sensing using single-walled carbon nanotubes. *Nanotechnology*, 15(11):1493–1496, 2004.
- [7] S. J. Wind, J. Appenzeller, R. Martel, V. Derycke, and P. Avouris. Vertical scaling of carbon nanotube field-effect transistors using top gate electrodes. *Appl. Phys. Lett.*, 80:3817–3819, 2002.
- [8] A. Javey, J. Guo, D. B. Farmer, Q. Wang, D. Wang, R. G. Gordon, M. Lundstrom, and H. Dai. Carbon nanotube field-effect transistors with integrated ohmic contacts and high-k gate dielectrics. *Nano Lett.*, 4(3):447–450, 2004.
- [9] J. A. Misewich, R. Martel, P. Avouris, J. C. Tsang, S. Heinze, and J. Tersoff. Electrically induced optical emission from a carbon nanotube FET. *Science*, 300(5620):783–786, 2003.
- [10] M. E. Itkis, F. Borondics, A. Yu, and R. C. Haddon. Bolometric infrared photoresponse of suspended single-walled carbon nanotube films. *Science*, 312(5772):413–416, 2006.
- [11] C. K. M. Fung, N. Xi, B. Shanker, and K. W. C. Lai. Nanoresonant signal boosters for carbon nanotube based infrared detectors. *Nanotechnology*, 20(18), 2009.
- [12] U. Bockelmann and G. Bastard. Phonon scattering and energy relaxation in two-, one-, and zero-dimensional electron gases. *Phys. Rev. B*, 42(14):8947–8951, 1990.

- [13] D. M. Kuo, A. Fang, and Y. C. Chang. Theoretical modeling of dark current and photo-response for quantum well and quantum dot infrared detectors. *Infrared Phys. Technol.*, 42:422–433, 2001.
- [14] S. Sanguinetti, M. Guzzi, E. Grilli, M. Gurioli, L. Seravalli, P. Frigeri, S. Franchi, M. Capizzi, S. Mazzuccato, and A. Polimeni. Effective phonon bottleneck in the carrier thermalization of InAs/GaAs quantum dots. *Phys. Rev. B*, 78(8):085313, 2008.
- [15] C. Soci, A. Zhang, B. Xiang, S. A. Dayeh, D. P. R. Aplin, J. Park, X. Y. Bao, Y. H. Lo, and D. Y. Wang. ZnO nanowire UV photodetectors with high internal gain. *Nano Lett.*, 7:1003–1009, 2007.
- [16] K. W. C. Lai, N. Xi, C. K. M. Fung, H. Chen, and T.-J. Tarn. Engineering the band gap of carbon nanotube for infrared sensors. *Appl. Phys. Lett.*, 95(22):221107, 2009.
- [17] P. G. Collins, M. S. Arnold, and P. Avouris. Engineering carbon nanotubes and nanotube circuits using electrical breakdown. *Science*, 292(5517):706–709, 2001.
- [18] K. W. C. Lai, N. Xi, C. K. M. Fung, H. Chen, and T. J. Tarn. Advancements in complementary carbon nanotube field effect transistors. In *Nanotechnology Materials and Devices Conference, 2009. NMDC '09. IEEE*, pages 130–135, 2003.
- [19] F. Léonard and J. Tersoff. Role of Fermi-level pinning in nanotube Schottky diodes. *Phys. Rev. Lett.*, 84(20):4693–4696, 2000.
- [20] N. M. Gabor, Z. Zhong, K. Bosnick, J. Park, and P. L. McEuen. Extremely efficient multiple electron-hole pair generation in carbon nanotube photodiodes. *Science*, 325(5946):1367–1371, 2009.
- [21] I. A. Levitsky and W. B. Euler. Photoconductivity of single-wall carbon nanotubes under continuous-wave near-infrared illumination. *Appl. Phys. Lett.*, 83:1857–1859, 2003.
- [22] B. Pradhan, K. Setyowati, H. Liu, D. H. Waldeck, and J. Chen. Carbon nanotube–polymer nanocomposite infrared sensor. *Nano Lett.*, 8(4):1142–1146, 2008.
- [23] W. B. Euler, P.-L. Ong and I. A. Levitsky. Carbon nanotube-Si diode as a detector of mid-infrared illumination. *Appl. Phys. Lett.*, 96(3):033106, 2010.
- [24] M. B. Tzolov, T.-F. Kuo, D. A. Straus, A. Yin, and J. Xu. Carbon nanotube-silicon heterojunction arrays and infrared photocurrent responses. *J. Phys. Chem. C*, 111(15):5800–5804, 2007.
- [25] J. U. Lee. Photovoltaic effect in ideal carbon nanotube diodes. *Appl. Phys. Lett.*, 87:073101, 2005.
- [26] R. Martel, T. Schmidt, H. R. Shea, T. Hertel, and P. Avouris. Single- and multi-wall carbon nanotube field-effect transistors. *Appl. Phys. Lett.*, 73(17):2447–2449, 1998.
- [27] S. Heinze, J. Tersoff, R. Martel, V. Derycke, J. Appenzeller, and P. Avouris. Carbon nanotubes as Schottky barrier transistors. *Phys. Rev. Lett.*, 89(10):106801, 2002.
- [28] J. Zhang, N. Xi, H. Chen, K. W. C. Lai, G. Li, and U. Wejinya. Photovoltaic effect in single carbon nanotube-based Schottky diodes. *Int. J. Nanoparticles*, 1(2):108–118, 2008.
- [29] F. Léonard and J. Tersoff. Novel length scales in nanotube devices. *Phys. Rev. Lett.*, 83(24):5174–5177, 1999.
- [30] J. Zhao, J. Han, and J. P. Lu. Work functions of pristine and alkali-metal intercalated carbon nanotubes and bundles. *Phys. Rev. B*, 65(19):193401, 2002.
- [31] X. D. Cui, M. Freitag, R. Martel, L. Brus, and P. Avouris. Controlling energy-level alignments at carbon nanotube/Au contacts. *Nano Lett.*, 3(6):783–787, 2003.
- [32] K. W. C. Lai, N. Xi, and U. C. Wejinya. Automated process for selection of carbon nanotube by electronic property using dielectrophoretic manipulation. *J. Micro-Nano Mechatronics*, 4(1-2):37–48, 2008.
- [33] G. Y. Li, N. Xi, and M. Yu. Development of augmented reality system for AFM based nanomanipulation. *IEEE/ASME Trans. on Mechatronics*, 9:358–365, 2004.
- [34] J. Zhang, N. Xi, G. Li, H. Y. Chan, and U. C. Wejinya. Adaptable end effector for atomic force microscopy based nanomanipulation. *IEEE Trans. Nanotechnol.*, 5:628–642, 2006.
- [35] J. Zhang, N. Xi, L. Liu, H. Chen, K. Lai, and G. Li. Atomic force yields a master nanomanipulator. *Nanotechnol. Mag. IEEE*, 2(2):13–17, 2008.

- [36] J. Zhang, N. Xi, H. Chen, K. Lai, G. Li, and U. C. Wejinya. Design, manufacturing, and testing of single-carbon-nanotube-based infrared sensors. *Nanotechnol. IEEE Trans.*, 8(2):245–251, 2009.
- [37] K. W. C. Lai, N. Xi, C. K. M Fung, J. Zhang, H. Chen, Y. Luo, and U. C. Wejinya. Automated nanomanufacturing system to assemble carbon nanotube based devices. *Int. J. Rob. Res.*, 28(4):523–536, 2009.
- [38] A. Javey, J. Guo, Q. Wang, M. Lundstrom, and H. Dai. Ballistic carbon nanotube field-effect transistors. *Nature*, 424:654–657, 2003.
- [39] J. Appenzeller, M. Radosavljević, J. Knoch, and P. Avouris. Tunneling versus thermionic emission in one-dimensional semiconductors. *Phys. Rev. Lett.*, 92(4):048301, 2004.
- [40] J. Zhang, N. Xi, H. Chan, and G. Li. Single carbon nanotube based infrared sensor. *Electro-Optical and Infrared Systems: Technology and Applications III, SPIE Proc.*, 6395:63950A, 2006.
- [41] M. H. Yang, K. B. K. Teo, and W. I. Milne. Carbon nanotube schottky diode and directionally dependent field-effect transistor using asymmetrical contacts. *Appl. Phys. Lett.*, 87:253116, 2005.
- [42] H. Chen, N. Xi, K. W. C. Lai, C. K. M. Fung, and R. Yang. Development of infrared detectors using single carbon nanotube-based field effect transistors. *IEEE Trans. Nanotechnology*, 9(5):582–589, 2010.

Carbon Nanotube Field-Effect Transistor-Based Photodetectors

Hongzhi Chen, Ning Xi, and King Wai Chiu Lai

Department of Electrical and Computer Engineering, Michigan State University, Michigan

CHAPTER OUTLINE

8.1 Introduction	125
8.2 Back-Gate Au–CNT–Au Transistors	127
8.3 Back-Gate Ag–CNT–Ag Transistors	130
8.4 Back-Gate Au–CNT–Ag Transistors	132
8.5 Middle-Gate Transistors	136
8.6 Multigate Transistors	139
8.7 Detector Array Using CNT-Based Transistors	146
8.8 Summary	147
References	148

8.1 INTRODUCTION

In the previous chapter, we demonstrated that 1D Schottky photodiodes between an individual CNT and metals are responsible for the photocurrent (I_{photo}) generation under continuous IR illumination. The optoelectronic characteristics of CNT-based IR detectors are determined by the Schottky barriers, which depend on the Fermi energy (workfunction) alignment between the CNTs and metals, and, therefore, photoresponse can be improved by selecting appropriate metals. However, the choices of metals are limited, especially those that are both compatible with current technology (e.g., CMOS) and have desired workfunctions. In addition, the performance of CNT Schottky photodiodes is constrained by workfunction variation caused by technical difficulties in controlling CNT synthesis [1]. Therefore, it is more effective to control the Fermi energies of CNTs in order to optimize the performance of CNT detectors, instead of changing workfunctions by selecting proper metals. CNT field-effect transistors (CNTFETs) can be considered as CNT Schottky diodes with an external terminal, called a gate, capacitively coupled to the CNT channel to electrostatically doped CNT by applying gate voltages (V_g). In other words, the Fermi energies of CNTs can be controlled by CNTFETs through their gates.

To begin with, a brief history of CNTFETs is given. Conventional metal-oxide-semiconductor field-effect transistor (MOSFET) technologies have been improved dramatically in the past decades by

downscaling, which results in better performance. Downscaling of the MOSFET has recently led to a device size below 35 nm, but owing to current leakage, the ultimate limit will be reached in the near future. Therefore, there is intense interest in finding alternative materials and devices. CNT is very promising in this respect, because its exceptional electrical properties, such as high current-carrying capability and excellent carrier mobility, make it a potential candidate for replacing traditional semiconductors. CNTFETs have been demonstrated to operate in the ballistic transport regime at room temperature [2]. In addition, CNT essentially conducts current on its surface, where all the chemical bonds are saturated and stable. Thus, it is compatible with high- k gate dielectrics, and there is no need to passivate the interface between the CNT channel and the gate dielectric.

The first CNTFET was reported in 1998 [3, 4]. The researchers fabricated the CNTFET by dispersing CNTs in a solvent, separating bundles in an ultrasonic bath, and depositing the CNTs onto a Si/SiO₂ surface with prefabricated metal electrodes. A few of the semiconducting CNTs would bridge two electrodes and define a conducting channel between them. Modulation of the transistor conduction was achieved by applying voltages to the silicon back-gate. During the first few years after the report of CNTFETs, their working principle was not well understood. They were analyzed like MOSFETs, barrier injection transit time (BARITT) diodes, or double 1D Schottky barrier transistors. The dominant Schottky barriers were experimentally confirmed in CNT cross-junctions made of one semiconducting and one metallic CNT in 2000 [5]. Since then, the performance of CNTFETs has been greatly improved by decreasing the thickness of dielectric layer [6], using high- k materials as gate of the dielectrics [7], and eliminating barriers by forming ohmic contacts [2].

Although CNTFETs have been extensively developed, CNTFET-based IR detectors are not well understood, since high-performance CNTFETs functioning as switches may not perform as well as IR detectors. They require different characteristics: CNTFETs working as switches need high switching speed, low subthreshold slope, and high transconductance, while IR detectors require low noise, fast response, and large effective absorption area. In addition, although the theory of planar contact between metals and traditional semiconductors has been fully developed and understood, it cannot be applied to 1D structures because of their unique characteristics, which arise from quantum confinement. That is to say, the behavior of CNT detectors may differ from those of traditional photovoltaic devices even though they share similar structures. Therefore, IR detectors using CNTFETs need to be investigated to understand their working principles so as to optimize their performance.

CNTFET-based IR detectors have been fabricated to investigate their photoconductivity by modulating the Fermi energy of CNT through silicon back-gates [8, 9], as illustrated in Fig. 8.1. In this configuration, a semiconductor CNT contacts two metal electrodes on a heavily doped Si/SiO₂ substrate. The metals serve as source and drain electrodes, while the conducting substrate acts as a gate

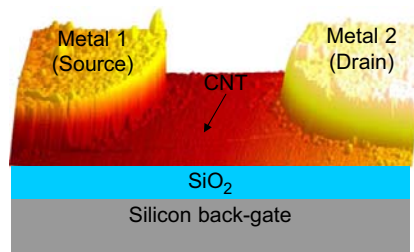


FIGURE 8.1

An AFM image of the structure of CNTFET with a silicon back-gate.

terminal, which is used to control the Schottky barriers by modulating the Fermi level of the CNT. However, these CNTFETs were used to focus on exploring the physics of the CNTs, rather than concentrating on optimizing performance of CNT photon-detectors. In this chapter, optimization of the design and performance of CNTFET-based IR detectors is discussed.

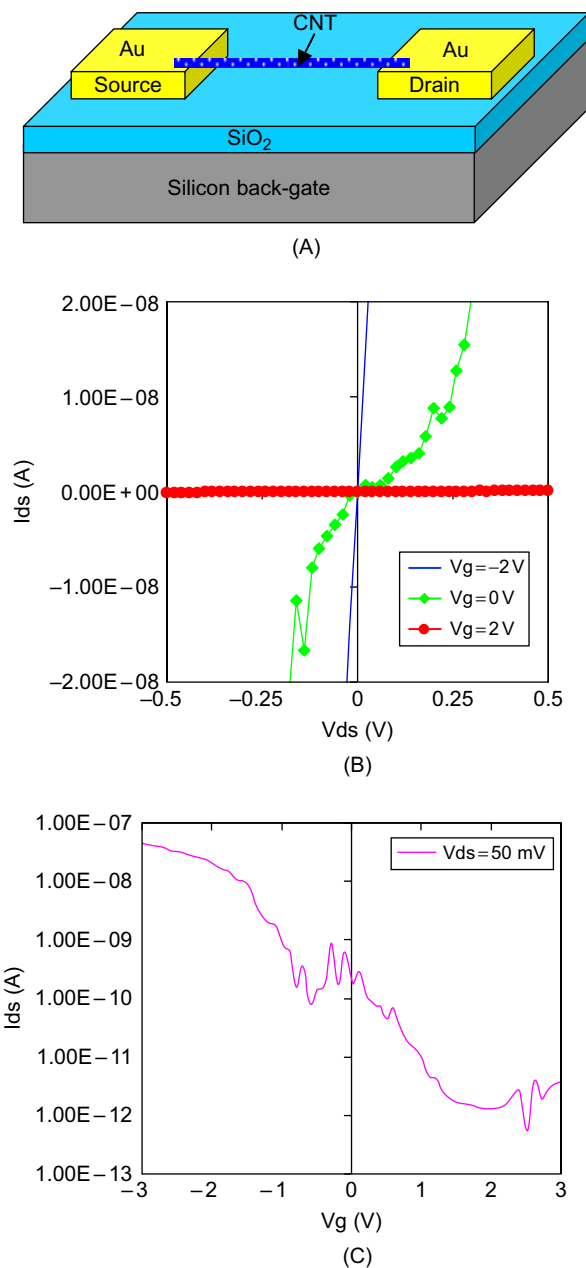
We have already studied the performance of CNT-based Schottky photodiodes in the previous chapter. However, in order to optimize the design and performance of CNTFET-based detectors, three questions remain to be answered: (1) how does the V_g affect the detector performance?; (2) is an asymmetric metal structure is suitable for CNTFETs?; and (3) what is the optimal gate structure?. Five different CNTFETs are introduced in the following sections to find the answers to these questions. A back-gate CNTFET with the Au–CNT–Au structure is introduced first, and its photoresponses are compared with back-gate CNTFETs with the Ag–CNT–Ag configuration, so as to understand the roles of metal workfunctions and V_g in determining the detector performance. Asymmetric back-gate CNTFET with the Ag–CNT–Au structure was then investigated, and both high photocurrent and open circuit voltage (V_{oc}) were obtained. The back-gate structure, albeit simple, provides valuable information to guide the design of CNTFET-based IR detectors. However, the back-gate structure cannot be applied to a large-scale detector array, since its component devices will be modulated simultaneously. Individual gate is required for each single detector. A middle-gate CNTFET consisting of an Al/Al₂O₃ gate between source and drain was examined, showing the capability to control detectors independently. Eventually, an asymmetric multigate CNTFET was investigated to find the optimal gate structure. The multigate CNTFET comprises four different gates: back-gate, gates for source and drain, and middle-gates for the CNT channel.

8.2 BACK-GATE Au–CNT–Au TRANSISTORS

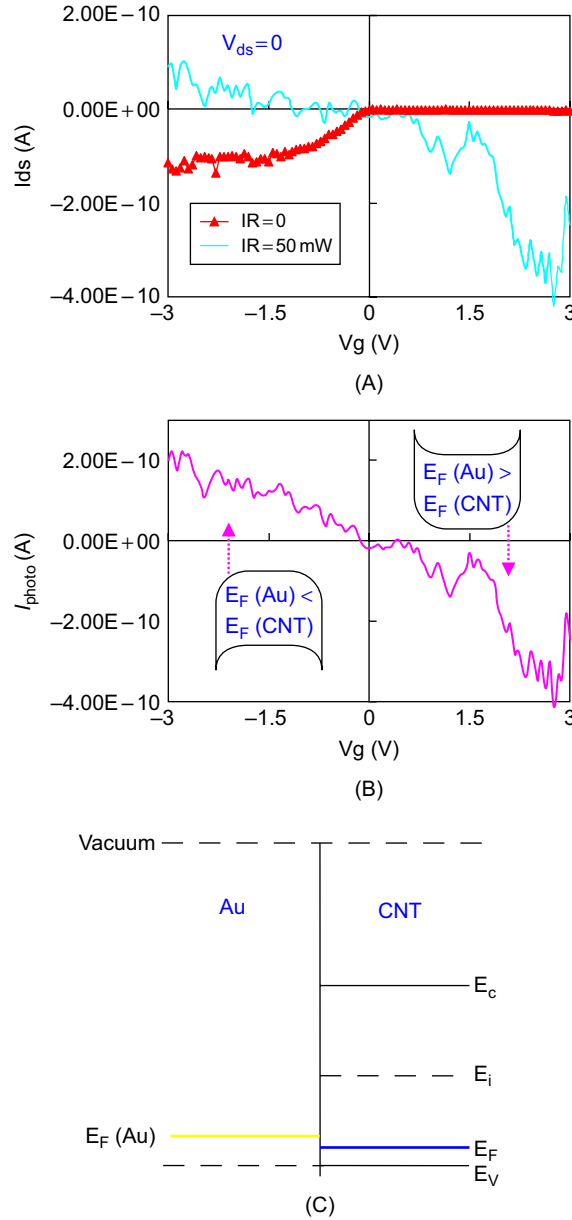
Figure 8.2A shows the configuration of a back-gate Au–CNT–Au CNTFET. The fabrication process of this device began with making two Au electrodes with a gap of around 1 μm using photolithography, thermal evaporation, and lift-off on top of a heavily doped Si substrate covered with 200-nm SiO₂. This was followed by dropping a droplet of CNT suspension between the electrodes that connect to the DEP system [10]. An individual CNT can be deposited between the electrodes by adjusting the suspension concentration, assisted by an AFM manipulation system [11, 12].

Conductance of the CNTFET was varied by applying V_g to the back-gate, which changes the tunneling probability through the Schottky barriers. The I–V characteristics of a CNTFET using CNT with three different V_g are shown in Fig. 8.2B. A weak parabolic I–V characteristic was observed without V_g , because of two small Schottky barriers reversely connecting between the source and the drain. When no V_g was applied, the Fermi energy of Au is close to that of CNT (~ 5.0 eV) [13]. By applying different V_g to the gate, p-type transistor characteristics were observed: positive V_g reduced the conductance, while negative V_g increased the conductance, as shown in Fig. 8.2C. An exceptional characteristic is that negative V_g caused a linear I–V relationship, while positive V_g resulted in strong parabolic I–V characteristics. In 1D barriers, thermally assisted tunneling dominates the carrier injection [14], and therefore, the linear I–V characteristics indicated an extreme thin or zero barrier, while strong parabolic I–V characteristics were caused by a strong barrier.

The photoresponses of the CNTFET were measured by focusing an IR laser with a wavelength of 830 nm and a maximum power of 50 mW, on one barrier. A more detailed introduction to the testing system can be found in [15]. The transfer characteristics of the device at zero bias with IR laser off and on (50 mW) are shown in Fig. 8.3A. When the IR source was off, the conductance had

**FIGURE 8.2**

(A) Structure of the back-gate Au-CNT-Au CNTFET. (B) The I-V characteristics of the CNTFET. (C) Transfer characteristics of the CNTFET at $V_{ds} = 50$ mV.

**FIGURE 8.3**

(A) Transfer characteristics of the Au–CNT–Au CNTFET with IR source off (IR = 0) and on (IR = 50 mW) at zero bias. (B) The relationship between gate voltage and photocurrent and corresponding band diagrams at negative and positive gate voltages. (C) The energy levels of Au and CNT. ([26], © [2010] IEEE)

similar correspondence to V_g as in Fig. 8.2B. However, markedly different transfer characteristics were observed when the IR laser was turned on. This indicated that excess carriers were generated by IR illumination, and contributed to current flow. The current difference between IR on and off status is denoted as photocurrent (I_{photo}) in the following discussion. The relationship between V_g and I_{photo} is shown in Fig. 8.3B. The I_{photo} at zero V_g was approximately -17.5 pA. The I_{photo} was positive and enhanced by increasing positive V_g , while it became negative when negative V_g was applied. This can be explained by the band diagram shown in Fig. 8.3B, and the energy level alignment shown in Fig. 8.3C (CNT is p type material in the air [16]). When positive V_g was applied, the Fermi energy of the CNT became lower than that of Au. In contrast, sufficient negative V_g increased the Fermi energy of the CNT beyond that of Au. As a result, the direction of the Schottky barrier changed, which inversed the sign of I_{photo} .

The magnitude of I_{photo} was enhanced by increasing the magnitude of both positive and negative V_g . However, the I_{photo} to dark current ratio (denoted as ON/OFF ratio in the following discussion) at positive V_g was much higher than that at negative V_g , as explained in the following discussion.

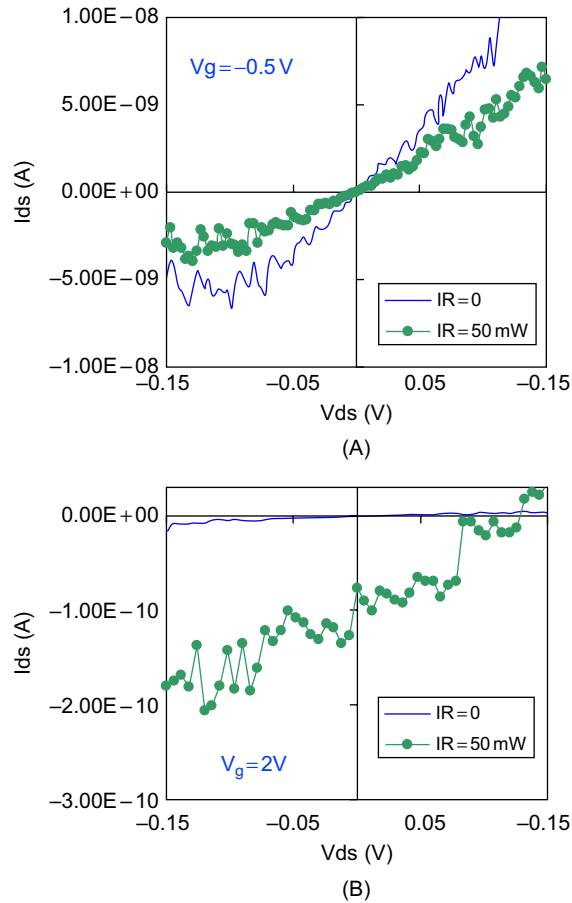
For negative V_g , increasing V_g caused higher built-in potential and p-doping levels (assume that Au and CNT have the same Fermi energy). The additional p-doping may turn the CNT into a degenerated p-doped semiconductor. This is supported by the linear I-V characteristics at negative V_g (Fig. 8.2). The bias-dependent I_{photo} values at $V_g = -0.5$ V are shown in Fig. 8.4A. One particular feature is that the current decreased with IR illumination, which was caused by the contradictory nature of the separated photo-generated carriers and injection carriers. Higher bias decreased carrier transit time, leading to photoconductive gain, resulting in higher I_{photo} .

For positive V_g , larger bias resulted in higher built-in potential but lower p-doping level. Note that the ON/OFF ratio at positive V_g was greatly improved because of the suppression of dark current and enhancement of I_{photo} . The bias-dependent measurement at $V_g = 2$ V (Fig. 8.4B) clearly showed the photovoltaic characteristics. At $V_{\text{ds}} = 0.12$ V, I_{photo} was equal to the current produced by the bias, resulting in zero net current. This bias is the open-circuit voltage, denoted as V_{oc} . Simulation has shown that depletion width varies exponentially with inverse doping [17] and built-in potential [18]. Therefore, the I_{photo} at positive V_g was increased by the widened depletion width, which enlarged the effective absorption area.

8.3 BACK-GATE Ag–CNT–Ag TRANSISTORS

It was demonstrated that applying proper voltages to the back-gate can improve the performance of CNT detectors in the Au–CNT–Au structure. In order to achieve that, both high built-in potential and low doping level are desired. However, the built-in potential in the Au–CNT–Au structure is limited by the workfunction of Au, which is close to that of CNTs. In addition, the barrier height using Au is small because the majority consists of holes, as shown in Fig. 8.3C. In 3D bulk material, the Schottky barrier properties are dominated by the Fermi level pinning effect, which makes metal workfunction insignificant in determining Schottky barriers, but this effect is trivial in 1D structures [19]. Therefore, using a metal with lower workfunction ($\text{Ag} = 4.2\text{--}4.5$ eV) [20] for the electrodes can form a higher built-in potential and barrier height, as shown in Fig. 8.5.

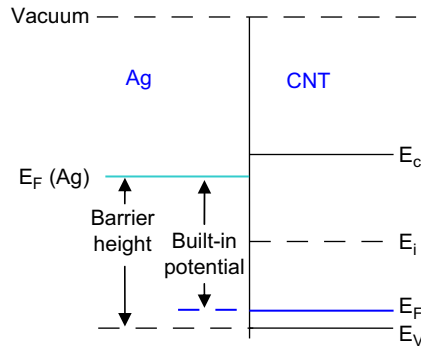
A back-gate CNTFET using Ag electrodes was fabricated to investigate the role of metal workfunction (Fig. 8.6A). The fabrication process was the same as for the Au–CNT–Au CNTFET, but

**FIGURE 8.4**

The bias-dependent measurement of the Au–CNT–Au CNTFET with $IR = 0$ and $IR = 50$ mW at (A) $V_g = -0.5$ V and (B) $V_g = 2$ V. ([26], © [2010] IEEE)

Ag was deposited instead of Au. Figure 8.6B shows the electrical characteristics of the Ag–CNT–Ag CNTFET with an individual CNT of 1.4-nm diameter. P-type transistor transfer characteristics were also observed in this device. In addition, negative V_g caused linear I–V characteristics, while positive V_g resulted in current rectifying. However, one distinct feature was that the conductance was ~ 1 –2 orders of magnitude smaller than in the Au–CNT–Au CNTFET, resulting in smaller dark current. This can be explained by a decreased tunneling probability through stronger Schottky barriers between Ag and CNT. The dark current of this detector was changed corresponding to the conductance change: increased by negative V_g , but decreased by positive V_g , as shown in Fig. 8.6C.

The relation between V_g and I_{photo} is shown in Fig. 8.7A. Positive V_g not only reduced dark current, but also increased I_{photo} , resulting in an enhanced ON/OFF ratio. The V_{oc} at zero V_g was small; however, a V_{oc} of 0.3 V was observed when a V_g of 3 V was applied to the back-gate with

**FIGURE 8.5**

The energy levels of Ag and CNT.

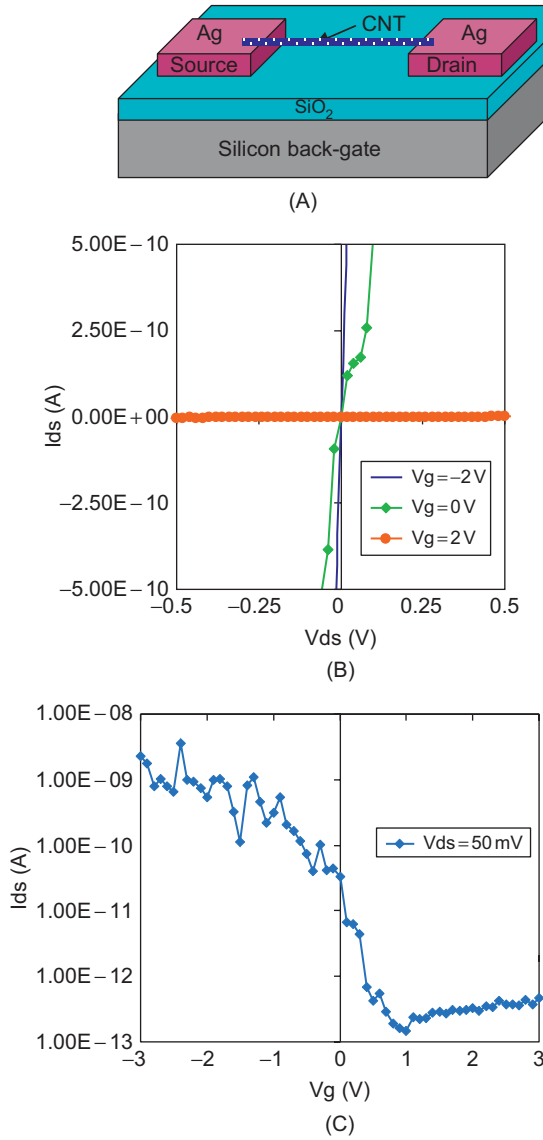
50 mW IR illumination (Fig. 8.7B). Bias-dependent measurement with four different power outputs was conducted. Typical photovoltaic characteristics were measured: I_{photo} was linearly proportional to the output power, while V_{oc} was exponentially proportional to the output power.

One particular feature is that the highest I_{photo} of the Ag–CNT–Ag CNTFET at IR = 50 mW (5×10^{-11} A) was smaller than that of the Au–CNT–Au CNTFET (1×10^{-10} A) in the bias-dependent measurements, but V_{oc} was much higher. This can be explained by the symmetric metal structure: a higher built-in potential in Ag–CNT contacts resulted in wider absorption width (depletion width) and lower dark current, but the separated electrons and holes at one barrier needed to tunnel through a wider barrier in order to contribute to I_{photo} generation. The comparison between these two CNTFETs indicates that metal selection plays a vital role in determining detector performance. Ag has lower work function than Au, resulting in a higher built-in potential and barrier height in the metal–CNT contacts. As a result, a higher V_{oc} was obtained in the back-gate Ag–CNT–Ag CNTFET.

8.4 BACK-GATE Au–CNT–Ag TRANSISTORS

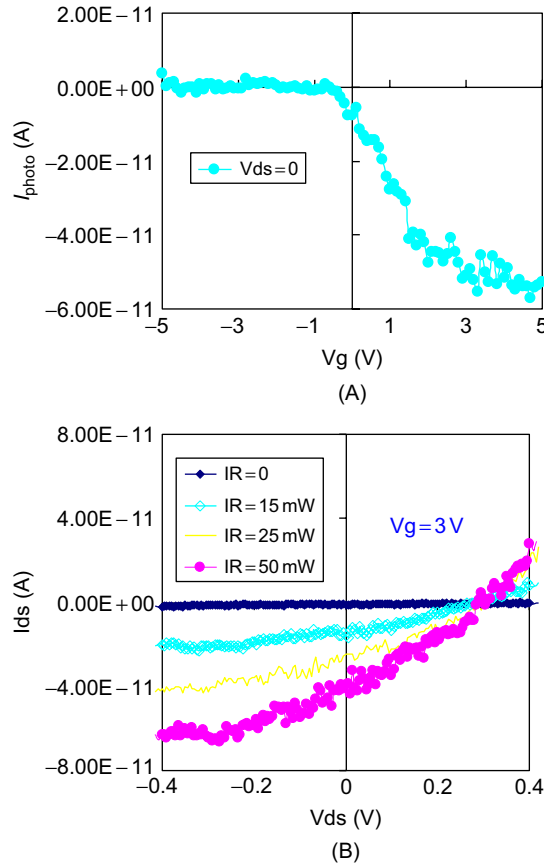
Electrostatic doping in two symmetric CNTFETs has been demonstrated in previous sections as an effective method to improve detector performance by depressing dark current and enhancing I_{photo} with widened Schottky barriers. However, the symmetric structure depressed photocurrent generation, since the separated electrons and holes need to tunnel through a wide barrier before contributing to current flow. Motivated by this problem, a back-gate Au–CNT–Ag CNTFET was fabricated, as shown in Fig. 8.8A. CNT and Au form a quasi-ohmic contact, while CNT and Ag form a Schottky barrier. As a result, this detector becomes a Schottky diode. By irradiating the device with IR photons, photore-sponse can be improved, since the separated electrons and holes do not need to pass through as strong a barrier (Ag–CNT) as in the symmetric structure. The fabrication process began with making an Au electrode, followed by fabricating an Ag electrode with a gap of 1 μm from the Au electrode after fine alignment.

Figure 8.8B shows the transfer characteristics of the Au–CNT–Ag CNTFET with and without IR illumination. The dark current showed p-type transistor characteristics. I_{photo} was highly improved

**FIGURE 8.6**

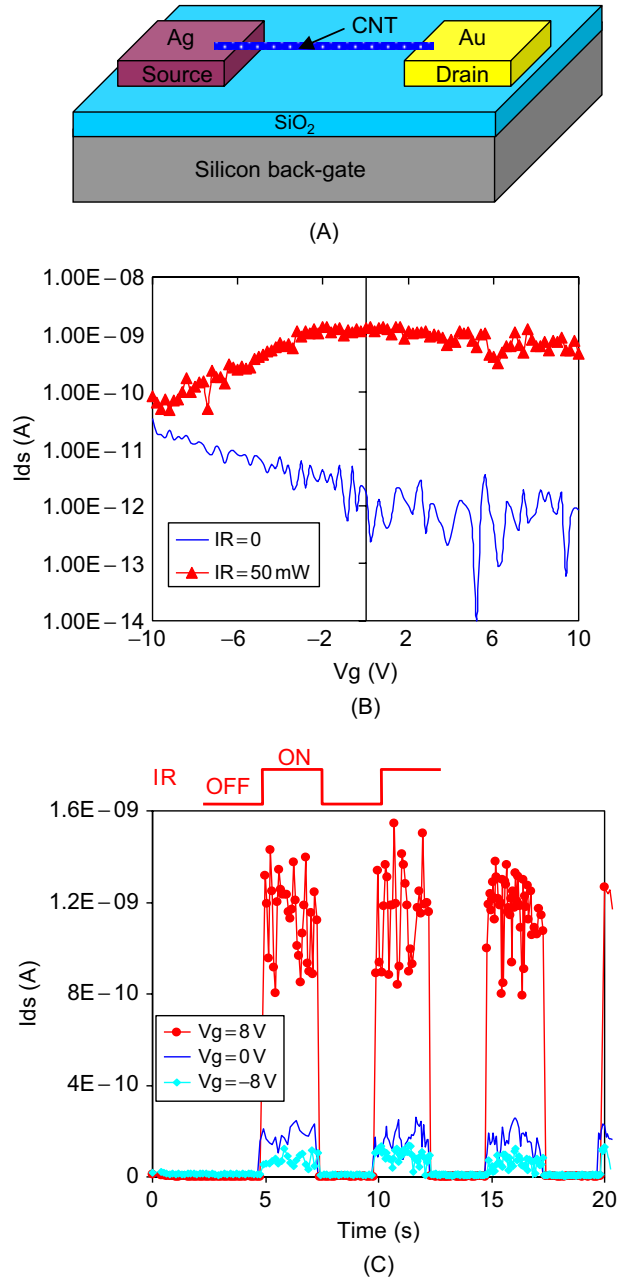
(A) The structure of back-gate Ag–CNT–Ag CNTFET. (B) I–V characteristics of the CNTFET. (C) Transfer characteristics of the CNTFET at $V_{ds} = 50$ mV.

with positive V_g , although no obvious improvement is apparent in Fig. 8.8C because of the hysteresis effect [21]. By measuring the temporal photoresponse, it is shown that the I_{photo} was increased from 2×10^{-11} ($V_g = 0$) to 1.2×10^{-9} A ($V_g = 8$ V) (Fig. 8.8C). The highest I_{photo} value, around 1 nA, was an order of magnitude higher than that for symmetric detectors.

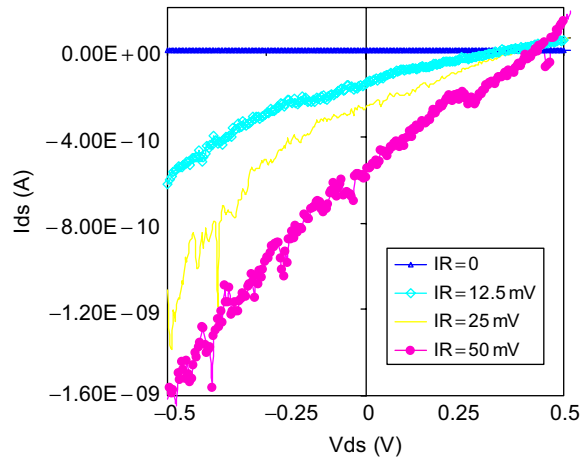
**FIGURE 8.7**

(A) The relation between gate voltage and photocurrent of the Ag-CNT-Ag CNTFET. (B) Bias-dependent measurement with IR at four different output power levels at $V_g = 3$ V. ([26], © [2010] IEEE)

A high ON/OFF ratio was obtained with positive V_g , and thus, the V_{oc} was expected to improve. The bias-dependent measurement with four different output power levels at $V_g = 5$ V is shown in Fig. 8.9. This is a typical photovoltaic photoresponse: negative bias enlarged the Schottky barrier that increased the I_{photo} , while positive bias shrank the depletion region that suppressed the I_{photo} . In addition, the I_{photo} is proportional to the output power, while the V_{oc} is exponentially proportional to the output power. A V_{oc} around 0.45 V was observed with 50-mW IR illumination, which is the highest V_{oc} reported to date for an individual CNT-based photodetector. In contrast to the I_{photo} , which is linearly dependent on the absorbed photons, the V_{oc} is determined by the ON/OFF ratio. Therefore, although the detector absorbs small amounts of photons, V_{oc} can still have a high value because the dark current can be extremely low in 1D structures because of the phonon scattering suppression and its nanoscale size.

**FIGURE 8.8**

(A) Structure of the back-gate Au–CNT–Ag CNTFET. (B) Transfer characteristics of the asymmetric CNTFET with and without IR illumination. (C) Temporal photoresponse with three different gate voltages at IR = 50 mW. ([26], © [2010] IEEE)

**FIGURE 8.9**

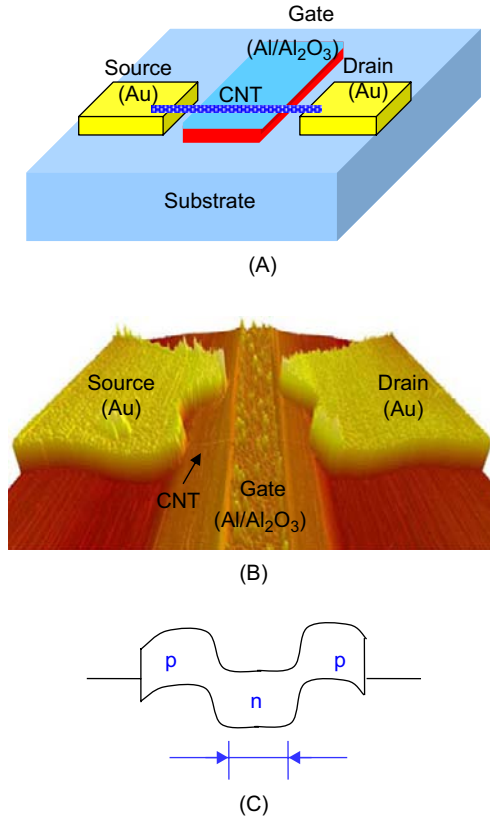
Bias-dependent measurement with IR at four different output power levels at $V_g = 5$ V. ([26], © [2010] IEEE)

8.5 MIDDLE-GATE TRANSISTORS

Previous CNTFETs showed promising improvement by using a back-gate to modulate the Schottky barriers between metals and a CNT. However, back-gates cannot be used in large-scale detector arrays, since all the devices will be modulated simultaneously. In this section, a middle-gate CNTFET, which has the capability to control each individual detector independently, is introduced.

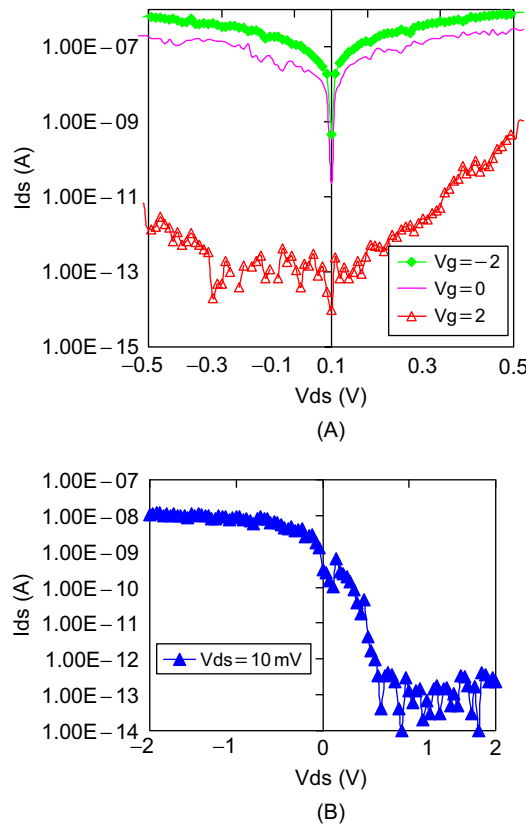
The structure of the middle-gate CNTFET and its AFM image are shown in Fig. 8.10. A CNT bridges two Au electrodes as source and drain, and an Al/Al₂O₃ middle-gate is made underneath the CNT and partially couples it. The fabrication process begins with making two Au electrodes with an insulating gap of 2 μ m. A 1- μ m-wide Al electrode is fabricated in between the source and the drain by e-beam lithography, thermal evaporation, and lift-off. The sample is then bombarded by oxygen plasma, and a thin layer of Al₂O₃ grown on the Al as the insulator for the gate. The last step is to deposit a CNT to connect the two Au electrodes using the DEP deposition system and the AFM manipulation system. Two inversely connecting p–n junctions (p–n–p) will be formed by applying proper V_g to the middle-gate, as shown by the band diagram in Fig. 8.10C.

The I–V characteristics of the middle-gate CNTFET with three different V_g are shown in Fig. 8.11A. P-type transistor characteristics were observed. Its conductance slightly increased with negative V_g , but decreased significantly with positive V_g . Current was linearly dependent on the bias without V_g , implying that ohmic contact is most probably between the CNT and Au. This was further verified by the no photoresponse at $V_g = 0$ V. The increased conductance with negative V_g may have resulted from the fringing field effect to the contacts. Positive V_g converts the middle of the CNT into n-type material, forming a p–n–p structure, which can be considered as two inversely connected p–n junctions. Thus, diode-like I–V characteristics are shown at $V_g = 2$ V in Fig. 8.11A. The transfer characteristics at $V_{ds} = 10$ mV are shown in Fig. 8.11B with a 200 mV/dec subthreshold slope.

**FIGURE 8.10**

(A) Structure of the middle-gate CNTFET. (B) AFM image of the middle-gate CNTFET. (C) Band diagram of the working status of the middle-gate CNTFET.

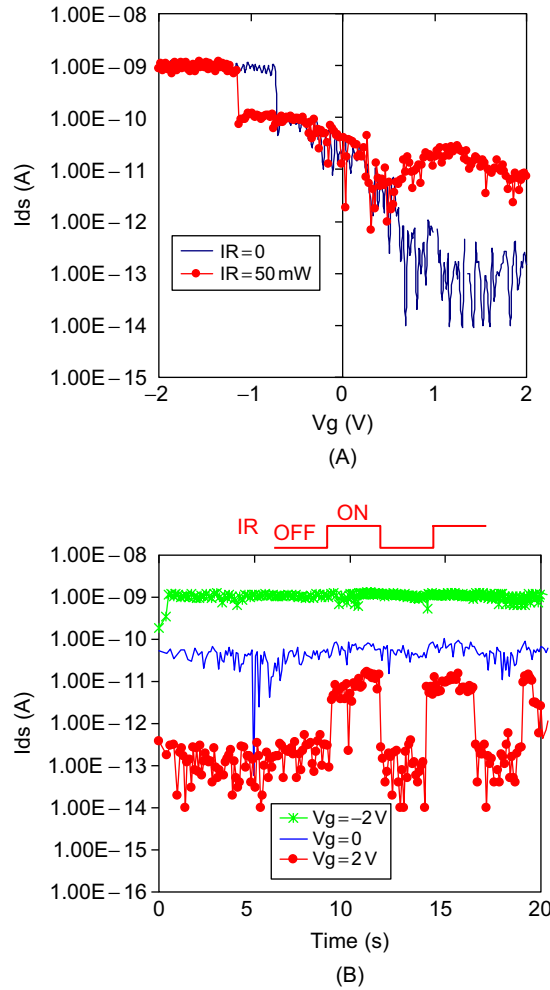
The transfer characteristics, at $V_{ds} = 0$ V with IR on and off, were shown (Fig. 8.12A) by sweeping the V_g from -2 V to 2 V. Dark current of the CNTFET decreased from 5×10^{-11} (zero V_g) to 5×10^{-14} A with increasingly positive V_g , since the electrons needed to tunnel through two p-n junctions in the CNT in order to contribute to the dark current. When 50 mW IR illuminated the CNT, similar transfer characteristics were observed with negative and small positive V_g , indicating that no I_{photo} was produced. I_{photo} was observed with V_g values larger than $+0.5$ V, as shown in Fig. 8.12A. There was a sudden drop of the current signal at a V_g of around -1 V, which may have been caused by defects in the CNT. Hysteresis characteristics in current versus gate voltage was observed in this device [21]. In order to eliminate the effect of the hysteresis, we measured the temporal photoresponse at fixed V_g by switching IR on and off at 0.2 Hz, as shown in Fig. 8.12B. No I_{photo} was generated at $V_g = 0$ V and $V_g = -2$ V, and the dark currents were large compared to those with positive V_g . When a $+2$ V

**FIGURE 8.11**

(A) I-V characteristics of the middle-gate CNTFET at three V_g in log-scale. (B) Transfer characteristics of the CNTFET with $V_{ds} = 10$ mV. ([27], © [2009] IEEE)

V_g was applied, I_{photo} with a value of 1×10^{-11} A was generated, and an ON/OFF ratio of around two orders was observed. Although the I_{photo} is small, the V_{oc} is determined by the ON/OFF ratio and operating temperature. We investigated the V_{oc} by measuring bias-dependent current at $V_g = 2$ V, as shown in Fig. 8.13. A typical photovoltaic photoresponse was observed, and a 0.1 V V_{oc} was obtained.

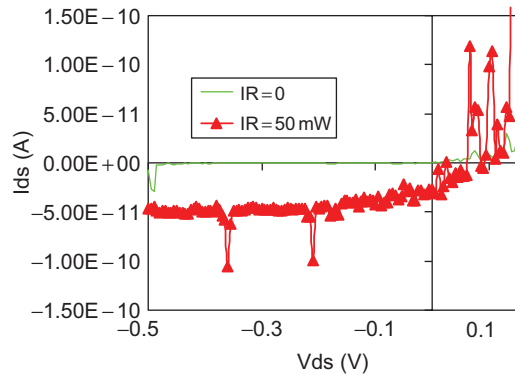
By introducing a middle-gate to the CNTFET, each individual detector in a large-scale array can be controlled separately. However, this structure has some limitations that prevent optimal performance. First of all, the I_{photo} generation is based on two inversely connecting p-n junctions, which is similar to the case of CNTFET with symmetric Schottky barriers. The detected I_{photo} reflects the signal intensity difference between two junctions that are only $1 \mu\text{m}$ away from each other. What is more, although ohmic contact can be formed between a CNT and metals by selecting the appropriate metal, the fringe field from the middle-gate may produce a barrier that suppresses the generation of I_{photo} .

**FIGURE 8.12**

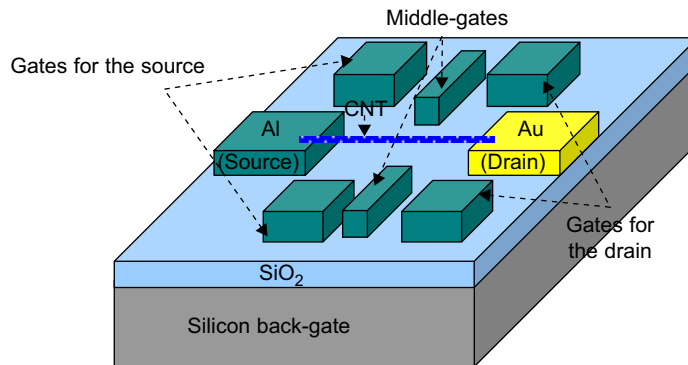
(A) Transfer characteristics of the middle-gate CNTFET with IR on and off at zero bias. (B) Temporal photoresponse measurement by switching IR on and off at 0.2 Hz. ([27], © [2009] IEEE)

8.6 MULTIGATE TRANSISTORS

In previous sections, we demonstrated that both an asymmetric metal structure and electrostatic doping using a back-gate can improve the performance of the CNT detectors by manipulating the energy alignment between metals and a CNT, but a back-gate modulates all the detectors simultaneously. In order to control detectors independently, a middle-gate CNTFET was fabricated and investigated. However, all these CNTFETs have their limitations for optimum performance.

**FIGURE 8.13**

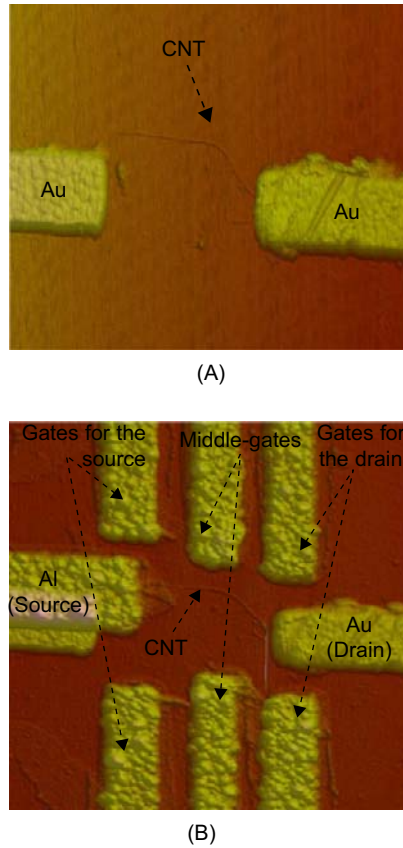
Bias-dependent measurement with IR at two output powers at $V_g = 2$ V. ([27], © [2009] IEEE)

**FIGURE 8.14**

Structure of the asymmetric multigate CNTFET. ([28], © [2010] IEEE)

In order to optimize the design of the CNT detectors, an asymmetric multigate CNTFET-based IR detector was fabricated, integrating an asymmetric metal structure (Au–CNT–Al) with multiple gates, which allow of controlling the Fermi energies at source, drain, and CNT channel independently. The structure of the asymmetric multigate CNTFET is shown in Fig. 8.14. It consists of a CNT connecting to Al and Au electrodes, a back-gate, and three pairs of gates located beside the source, the drain and the CNT. The gates next to the source and drain control the carrier injection of Schottky barriers independently, while the middle-gates can not only shield the source (drain) gate effects from the drain (source), but also modulate the Fermi energy of the CNT. In other words, this structure can guarantee control of the source, drain, and CNT channel independently.

The fabrication process of this device began with making two Au electrodes on top of a Si/SiO₂ substrate using e-beam lithography, thermal evaporation, and lift-off. The distance between the electrodes was around 1 μm . An individual CNT was deposited around the electrodes by using the DEP deposition

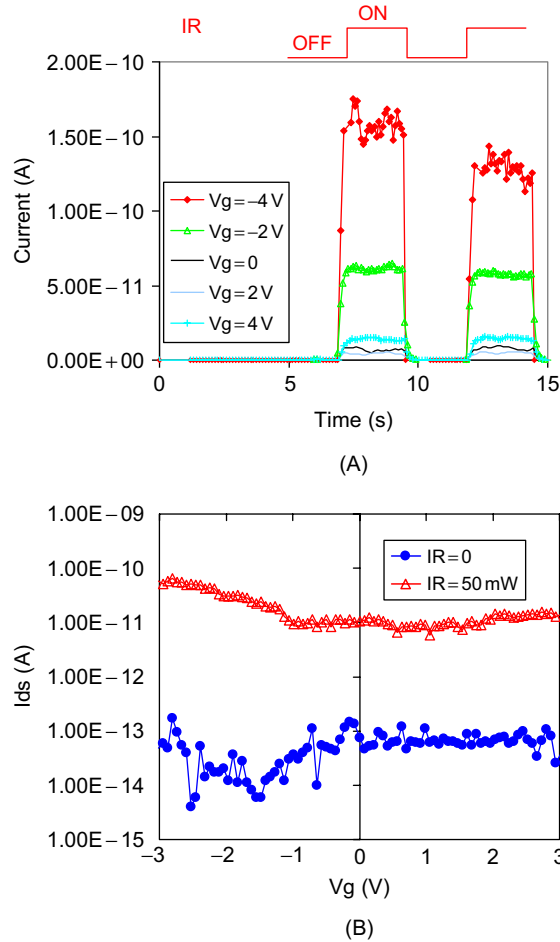
**FIGURE 8.15**

AFM image of the fabrication process. (A) A CNT was deposited close to the Au electrodes. (B) The AFM image of the device after depositing Al as the source, and three pairs of gates.

system and the AFM manipulation system, as shown in Fig. 8.15A. Further e-beam lithography, thermal evaporation (Al), and lift-off were used to fabricate the asymmetric structure (Au–CNT–Al) and three pairs of gates, as shown in Fig. 8.15B. The pattern of this e-beam lithography was adjusted on the basis of the position of the CNT. At the end, a thin layer of Parylene-C was deposited on the device to prevent environmental influence, since both Al and CNT are very sensitive to oxygen.

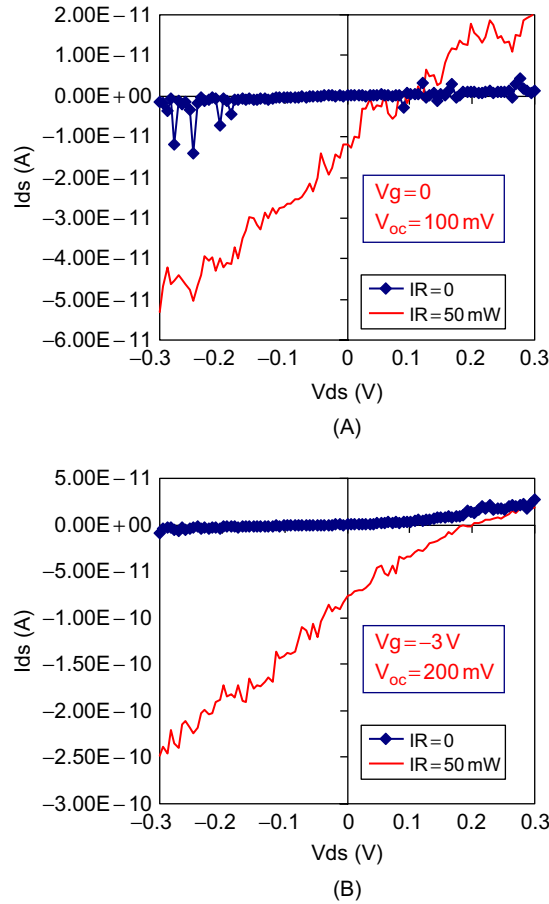
Au has a Fermi energy similar to that of CNT (5.0 eV), while Al (4.1 eV) has a much lower Fermi energy than does CNT [22]; therefore, a large Schottky barrier forms between Al and CNT, while a small or no barrier forms between Au and CNT. As a result, this CNTFET exhibits the current-rectifying characteristics of a traditional diode.

In order to understand the gate-dependent photoresponses of this CNTFET, we first measured the I_{photo} and V_{oc} by applying V_g to the gates of drain. The temporal I_{photo} measurement with five different V_g is shown in Fig. 8.16A by switching the IR on and off at 0.2 Hz. I_{photo} was highly enhanced from

**FIGURE 8.16**

Photoresponses of the multigate CNTFET by applying gate voltages to the gates of drain: (A) Temporal photoresponse measurement with five different gate voltages. (B) Transfer characteristics by applying gate voltages from -3 V to 3 V with two IR output powers. ([28], © [2010] IEEE)

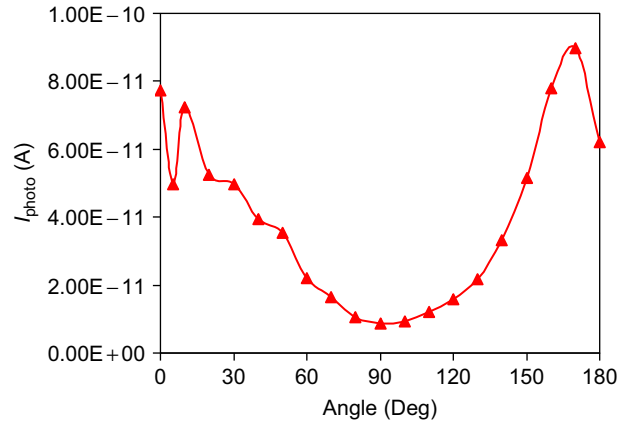
$\sim 8 \times 10^{-12}\text{ A}$ ($V_g = 0\text{ V}$) to $\sim 1.5 \times 10^{-10}\text{ A}$ ($V_g = -4\text{ V}$) by applying negative V_g , but changed only slightly with positive V_g . By sweeping V_g from -3 V to 3 V , the transfer characteristics of this device were also investigated, as shown in Fig. 8.16A. Negative V_g not only depressed the dark current, but also increased I_{photo} , while positive V_g only slightly changed both the dark current and I_{photo} . This can be explained by the change of the Schottky barriers due to the applied electrical field. The CNT was connecting to Au and Al electrodes, and the Au–CNT contact showed p-type transistor characteristics [3], while the Al–CNT contact showed n-type transistor characteristics [23]. The optoelectronic

**FIGURE 8.17**

Open circuit voltage (V_{oc}) measurement (A) without gate voltage and (B) with -3 V V_g . ([28], © [2010] IEEE)

properties of this detector were dominated by the Al contact because of a larger Fermi energy difference. In the Al-CNT contact, negative V_g can increase the built-in potential by pulling up the Fermi energy, resulting in the dark current suppression and I_{photo} enhancement. A larger built-in potential will result in a wider depletion region, which is the effective absorption area of the detector, thus producing a larger photocurrent. V_{oc} is also expected to be improved with negative V_g , since the value of V_{oc} is proportional to the ON/OFF ratio [24]. Bias-dependent photoresponse measurements were conducted by applying V_g with values of 0 V and -3 V to the detector, as shown in Fig. 8.17. The V_{oc} was doubled from 100 mV (no V_g) to 200 mV ($V_g = -3$ V).

The polarization-dependent I_{photo} was recorded in order to further understand its working principle. The I_{photo} was measured by changing the relative angle between the CNT axis and laser polarization. I_{photo} was highest when the CNT axis was parallel to the laser polarization, while the lowest I_{photo} was

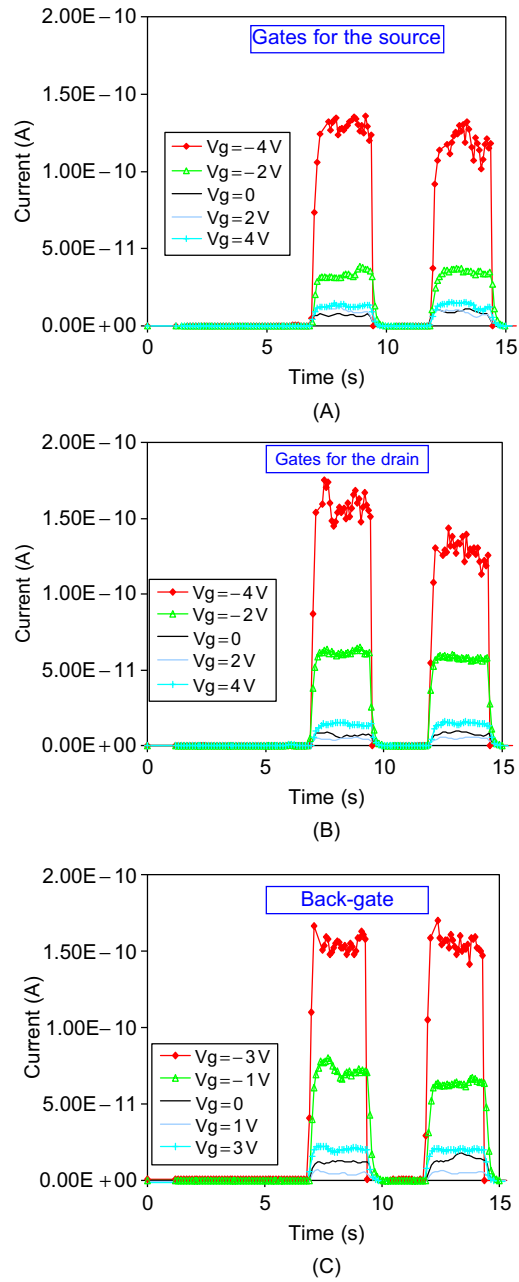
**FIGURE 8.18**

Photocurrent measurement with different angles between CNT axis and laser polarization. ([28], © [2010] IEEE)

recorded when CNT was perpendicular to the polarization, as shown in Fig. 8.18. The polarization ratio (highest/lowest I_{photo}) was approximately 10. Dielectric contrast between the CNT and surrounding environment was explained as the cause of this polarization anisotropy [25]. However, the quantum effects should not be neglected. According to the selection rule, the electrons excited from the ground state to the excited state need to conserve angular momentum, which depends on the photon polarization. The generation of I_{photo} inside the Schottky barrier also relates to the polarization. The energy of photons is stored as a vibrating electric field in electromagnetic waves, but forward and reverse biases in the Schottky barrier generate a different I_{photo} , therefore net current will be generated by the vibrating electric field when the polarization is not perpendicular to the CNT. A more sophisticated model is needed to fully understand this polarization anisotropy.

In order to find out optimal gate structure, temporal photoresponses of the multigate CNTFET were measured by applying V_g to back-gate, gates for source, and gates for drain, with IR laser OFF and ON at 0.2 Hz. The back-gate controls the Fermi energy of the whole CNT channel, while gates for source and drain control the Fermi energy of the left and right contacts. Therefore, the expected V_g -dependent values of I_{photo} should be very different. However, the device had similar photoresponses when applying voltages to the gates at different positions, as shown in Fig. 8.19. This similarity may have been caused by the full depletion in the CNT channel, since the charge distribution of the 1D Schottky barrier has an exponentially decreasing charge tail extending throughout the CNT [17]. In other words, the whole CNT channel becomes a depletion region that contributes to the photon absorption and separation.

It should be noted that the “full depletion” in CNT is actually partial depletion due to the unique charge distribution in 1D structures. This is the reason why dark current and photoresponse still can be modulated by V_g , but they differ only by about one order of magnitude. This property makes the asymmetric multigate CNTFET a poor switch, but an excellent IR detector. The results from this CNTFET indicate that the CNT-based detector can be simplified into an asymmetric metal structure with only a single gate.

**FIGURE 8.19**

Comparison of the temporal photoresponse by applying V_g to the gates of (A) source, (B) drain, and (C) back-gate.

8.7 DETECTOR ARRAY USING CNT-BASED TRANSISTORS

In previous sections, we demonstrated that gates at different positions can deliver the same improvement in the asymmetric multigate CNTFET. Thus, multiple gates can be replaced by one pair of gates, as shown in Fig. 8.20. This simplification can not only make the device smaller, but also avoid the electric field influence from neighboring devices.

A 3×3 CNT detector array was fabricated, as shown in Fig. 8.21, which also shows the AFM image of the structure of one of its pixels. For this array, two Au electrodes of each detector were fabricated with a gap of $1 \mu\text{m}$ using e-beam lithography, thermal evaporation, and lift-off. A single CNT was then deposited between the electrodes using the DEP deposition system and the AFM manipulation system, followed by fabricating two gates and replacing one of the Au electrodes with Al. At the end, the whole device was packaged using a Parylene-C layer in order to protect the device from environmental contamination. The pitch size of this array is $15 \mu\text{m}$. Each individual detector in the array can be controlled independently using its own gates. We first measured the photoresponse of each detector separately, and then calibrated proper values of V_g for each individual detector in order to make them generate the highest I_{photo} .

By irradiating the detector array with IR photons from a laser, I_{photo} of all detectors was measured. The images obtained from the measurement are shown in Fig. 8.22. The color lightness shows the magnitude of I_{photo} , which was normalized. In the images, the darker the color, the higher the I_{photo} . Fig. 8.22A shows that the highest intensity light of the laser is radiating on Pixel5. Other pixels have smaller I_{photo} , and the value of I_{photo} decreased as the distance between the detector and laser spot increased. Figure 8.22B shows that when the laser was moved toward the top left, the highest intensity point moved to Pixel1. This detector array can be considered a small focal plane array in an IR imaging system. If the CNT detector array had a larger number of detectors, a higher resolution IR image could be obtained.

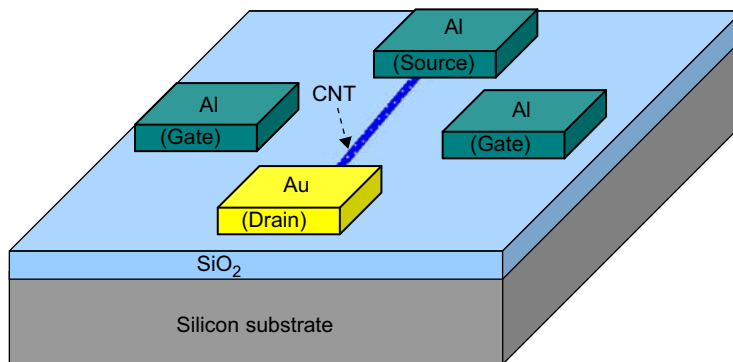
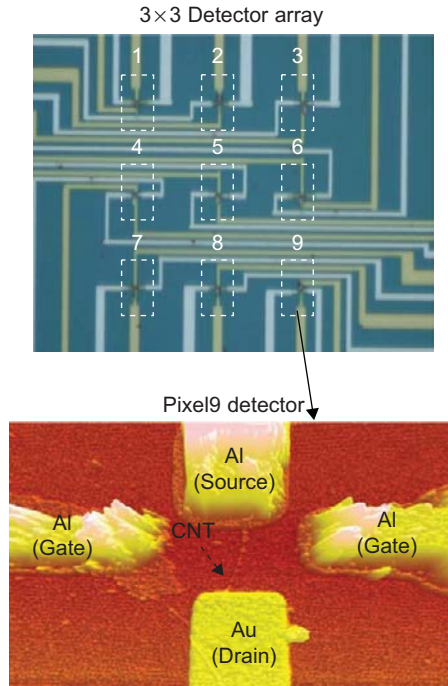


FIGURE 8.20

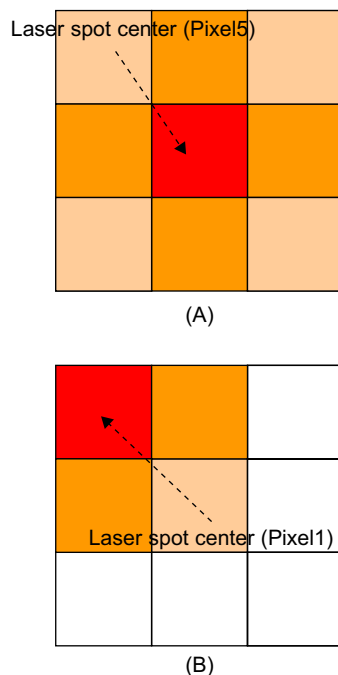
Asymmetric CNTFET with simplified gate structure.

**FIGURE 8.21**

The image of a 3×3 detector array and the AFM image of the Pixel9.

8.8 SUMMARY

Five types of CNTFETs were discussed in this chapter to investigate and improve the performance of CNT-based IR detectors. In the Au–CNT–Au CNTFET back-gate, the detector performance was improved by applying voltages to the back-gate, resulting in smaller dark current and higher I_{photo} . Back-gate is capacitive-coupled to the CNT, and thus, application of V_g can electrostatically modulate the Fermi energy of CNT so as to control the Schottky barriers that are responsible for I_{photo} generation. The Ag–CNT–Ag CNTFET back-gate produced higher V_{oc} under IR illumination, since the built-in potential between Ag and CNT is higher than that of Au and CNT, showing the significance of metal workfunction. The two CNTFETs have symmetric metal structures, that constrained the performance of the detectors, because separated electrons and holes from one Schottky barrier need to tunnel through another barrier. In the Au–CNT–Ag CNTFET back-gate, an asymmetric metal structure was used, and both I_{photo} and V_{oc} were highly improved. The reason is that the electrons and holes from the Ag–CNT interface only needed to pass through a small barrier between Au and CNT before being collected. CNTFET with back-gate structure is easy to fabricate and provide valuable information for improving detector performance. However, the back-gate structure is not suitable for larger scale detector arrays, because the back-gate will modulate all detectors simultaneously. A middle-gate

**FIGURE 8.22**

The image is obtained from the detector, and color lightness shows the magnitude of photocurrent. The laser spot center is on (A) Pixel5 and (B) Pixel1.

CNTFET was fabricated in order to control each detector independently. But a CNT detector with middle-gate structure and symmetric metal structure could not deliver optimal performance. In order to find the optimal detector design, an asymmetric multigate CNTFET was introduced, with asymmetric metal structure and multiple gates, including back-gate, gates for source and drain, and middle gates. The experimental results show that gates at different positions can deliver the same improvement for the CNT detector because of full depletion in the CNT channel. Therefore, CNT detectors can be simplified to use a single gate structure. A 3×3 focal plane array using the asymmetric CNT detector with one pair of side-gates was fabricated, effectively detecting laser intensity distribution.

References

- [1] H. Dai. Carbon nanotubes: synthesis, integration, and properties. *Acc. Chem. Res.*, 35:1035–1044, 2002.
- [2] A. Javey, J. Guo, Q. Wang, M. Lundstrom, and H. Dai. Ballistic carbon nanotube field-effect transistors. *Nature*, 424:654–657, 2003.
- [3] R. Martel, T. Schmidt, H. R. Shea, T. Hertel, and P. Avouris. Single- and multi-wall carbon nanotube field-effect transistors. *Appl. Phys. Lett.*, 73(17):2447–2449, 1998.

- [4] S. J. Tans, A. R. M. Verschueren, and C. Dekker. Room-temperature transistor based on a single carbon nanotube. *Nature*, 393(6680):49–52, 1998.
- [5] M. S. Fuhrer, J. Nygard, L. Shih, M. Forero, Y. G. Yoon, M. S. C. Mazzoni, H. J. Choi, J. Ihm, S. G. Louie, A. Zettl, and P. L. McEuen. Crossed nanotube junctions. *Science*, 288(5465):494–497, 2000.
- [6] S. J. Wind, J. Appenzeller, R. Martel, V. Derycke, and P. Avouris. Vertical scaling of carbon nanotube field-effect transistors using top gate electrodes. *Appl. Phys. Lett.*, 80:3817–3819, 2002.
- [7] A. Javey, J. Guo, D. B. Farmer, Q. Wang, D. Wang, R. G. Gordon, M. Lundstrom, and H. Dai. Carbon nanotube field-effect transistors with integrated ohmic contacts and high-k gate dielectrics. *Nano Lett.*, 4(3):447–450, 2004.
- [8] M. Freitag, Y. Martin, J. A. Misewich, R. Martel, and P. Avouris. Photoconductivity of single carbon nanotubes. *Nano Lett.*, 3:1067–1071, 2003.
- [9] X. Qiu, M. Freitag, V. Perebeinos, and P. Avouris. Photoconductivity spectra of single-carbon nanotubes: Implications on the nature of their excited states. *Nano Lett.*, 5:749–752, 2005.
- [10] K. W. C. Lai, N. Xi, and U. C. Wejinya. Automated process for selection of carbon nanotube by electronic property using dielectrophoretic manipulation. *J. Micro-Nano Mechatronics*, 4(1-2):37–48, 2008.
- [11] G. Y. Li, N. Xi, and M. Yu. Development of augmented reality system for AFM based nanomanipulation. *IEEE/ASME Trans. Mechatronics*, 9:358–365, 2004.
- [12] J. Zhang, N. Xi, G. Li, H. Y. Chan, and U. C. Wejinya. Adaptable end effector for atomic force microscopy based nanomanipulation. *IEEE Trans. Nanotechnology*, 5:628–642, 2006.
- [13] M. Shiraishi and M. Ata. Work function of carbon nanotubes. *Carbon*, 39(12):1913–1917, 2001.
- [14] J. Appenzeller, M. Radosavljević, J. Knoch, and P. Avouris. Tunneling versus thermionic emission in one-dimensional semiconductors. *Phys. Rev. Lett.*, 92(4):048301, 2004.
- [15] J. Zhang, N. Xi, H. Chen, K. Lai, G. Li, and U. C. Wejinya. Design, manufacturing, and testing of single-carbon-nanotube-based infrared sensors. *IEEE Trans. Nanotechnol.*, 8(2):245–251, 2009.
- [16] D. Kang, N. Park, J. Ko, E. Bae, and W. Park. Oxygen-induced p-type doping of a long individual single-walled carbon nanotube. *Nanotechnology*, 16(8):1048–1052, 2005.
- [17] F. Léonard and J. Tersoff. Novel length scales in nanotube devices. *Phys. Rev. Lett.*, 83(24):5174–5177, 1999.
- [18] C. Chen, W. Zhang, E. S.-W. Kong, and Y. Zhang. Carbon nanotube photovoltaic device with asymmetrical contacts. *Appl. Phys. Lett.*, 94(26):263501, 2009.
- [19] F. Léonard and J. Tersoff. Role of fermi-level pinning in nanotube Schottky diodes. *Phys. Rev. Lett.*, 84(20):4693–4696, 2000.
- [20] M. Chelvayohan and C. H. B. Mee. Work function measurements on (110), (100) and (111) surfaces of silver. *J. Phys. C: Solid State Phys.*, 15(10):2305–2312, 1982.
- [21] W. Kim, A. Javey, O. Vermesh, Q. Wang, Y. Li, and H. Dai. Hysteresis caused by water molecules in carbon nanotube field-effect transistors. *Nano Lett.*, 3:193–198, 2003.
- [22] Z. H. Chen, J. Appenzeller, J. Knoch, Y. M. Lin, and P. Avouris. The role of metal-nanotube contact in the performance of carbon nanotube field-effect transistors. *Nano Lett.*, 5(7):1497–1502, 2005.
- [23] A. Javey, Q. Wang, W. Kim, and H. Dai. Advancements in complementary carbon nanotube field-effect transistors. In *Electron Devices Meeting, 2003. IEDM '03 Technical Digest. IEEE International*, pages 31.2.1–31.2.4, 2003.
- [24] J. U. Lee. Photovoltaic effect in ideal carbon nanotube diodes. *Appl. Phys. Lett.*, 87:073101, 2005.
- [25] J. F. Wang, M. S. Gudiksen, X. F. Duan, Y. Cui, and C. M. Lieber. Highly polarized photoluminescence and photodetection from single indium phosphide nanowires. *Science*, 293(5534):1455–1457, 2001.
- [26] H. Chen, N. Xi, K. W. C. Lai, C. K. M. Fung, and R. Yang. Development of infrared detectors using single carbon nanotube-based field effect transistors. *IEEE Trans. Nanotechnology*, 9(5):582–589, 2010.

- [27] H. Chen, N. Xi, K. W. C. Lai, C. K. M. Fung, and R. Yang. CNT infrared detectors using schottky barriers and p-n junctions based FETs. In *Nanotechnology Materials and Devices Conference*, pages 91–95, 2009.
- [28] H. Chen, N. Xi, K. W. C. Lai, C. K. M. Fung, and R. Yang. Improving the detectability of CNT based infrared sensors using multi-gate field effect transistor. In *IEEE Conference on Nanotechnology*, pages 727–731, 2010.

Nanoantennas on Nanowire-Based Optical Sensors

9

Carmen Kar Man Fung*, Ning Xi[†], Balasubramaniam Shanker[†], and King Wai Chiu Lai[†]

**Hong Kong Productivity Council, Hong Kong*

[†]Department of Electrical and Computer Engineering, Michigan State University, Michigan

CHAPTER OUTLINE

9.1 Introduction	151
9.2 Nanoantenna Design Consideration for IR Sensors	152
9.2.1 Optical Nanoantennas Combined with CNT-Based IR Sensors	152
9.3 Theoretical Analysis: Nanoantenna Near-Field Effect	153
9.4 Fabrication of Nano Sensor Combined with Nanoantenna	154
9.5 Photocurrent Measurement on Nano Sensor Combined with Nanoantenna	157
9.6 Summary	158
References	160

9.1 INTRODUCTION

The discovery of nanostructural materials, such as carbon nanotubes (CNTs), opens the way to a myriad of potential sensing applications. As is well known, the electrical properties of CNTs depend on the geometry; for instance, armchair CNTs exhibit ballistic transport over micrometer-length scales. On the other hand, semiconducting CNTs exhibit a narrow bandgap in the near to middle wave infrared (IR) regime. Therefore, there were earlier attempts to develop IR detectors based on semiconducting CNTs. The advantage of employing CNTs as IR sensing elements is their low noise level. However, the signal received is extremely small, which results in low quantum efficiency. Thus, the principal question is the development of the means through which this signal may be boosted using near-field enhancement structures. Since the diameter of CNTs is only in the order of few nanometers, it makes the incorporation of these enhancement structures into such ultra-small sensing elements extremely difficult. The focus of this chapter will be on exploiting the physics of developing an enhancement technology that will increase the number of photons absorbed at the CNTs and thereby achieve higher quantum efficiency. It has been recently found that using a nano resonance structure called a nanoantenna is one promising approach to solving this problem [1].

In this chapter, the theoretical and experimental issues considered for the development of nanoantenna-integrated CNT-based IR sensors will be discussed [1]. The theoretical part will focus on

the development of a comprehensive mathematical model that accounts for the quantum-confinement effects on the conductivity and dielectric function of the nanoscale antenna, to theoretically predict the electric field-enhancement effect for different configurations of the antenna structure and the CNT sensor, and to optimize the design parameter. Reliable nanomanufacturing techniques and fabrication flow for creating CNT-based sensors with a nanoantenna will then be presented.

9.2 NANOANTENNA DESIGN CONSIDERATION FOR IR SENSORS

In recent years, optical nanoantennas have been increasingly investigated and used as near-field enhancement structures and plasmonic devices in near-IR range [2–5]. These resonance structures behave differently when compared with those traditional antennas where photon confinement happened in the near-field region but not in the radiated field. The basic principle behind their operation relies on the surface plasmonics (or field localization in the vicinity) due to shape singularity and impedance matching of the structures, which are formed by a feed gap between the antenna arms [2].

9.2.1 Optical Nanoantennas Combined with CNT-Based IR Sensors

Here, a locally resonant structure is studied and used for boosting the electric field intensity that is incident on the CNT sensing element. The conceptual design of the nanoantenna with the CNT sensor is illustrated in Fig. 9.1. This comprises a metallic pattern around the sensor. The sensor is formed by placing the CNT between a pair of metal microelectrodes. The near field of the antenna depends on several parameters including location, antenna geometry, size of metallization, etc. Therefore, there is a need to develop a theoretical approach to predict the radiation properties and the electric field distribution of different antenna topologies.

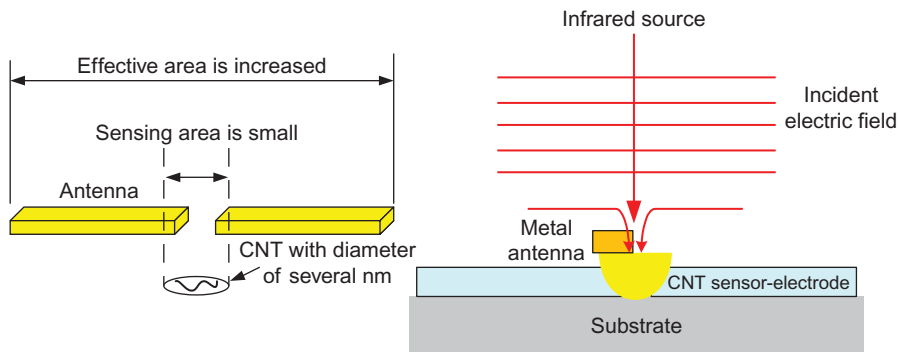


FIGURE 9.1

Illustration showing the configuration of a CNT-based IR detector with a nanoscale antenna.

9.3 THEORETICAL ANALYSIS: NANOANTENNA NEAR-FIELD EFFECT

Before looking at constructing the sensor, we will carry out a theoretical analysis to better understand the underlying physics that can be used to optimize the sensors as well as obtain insight into developing others. The key to developing efficient sensors is to understand the field localization. Thus, the principal objective of this task is the analysis of field localization in biased semiconductors with features on the nanoscale. This will be performed using a combination of classical and quantum mechanical methods. The latter will be used to obtain parameters that will be fed into the former.

Recently, several approaches have been used to investigate the nanoantenna theoretically [6, 7]. At the macroscopic level, it is well known that the behavior of the electromagnetic field in antennas is described by classical Maxwell equations. Purely full-wave analysis results are scant as several numerical and analytical challenges are posed. Most of the analysis techniques employed have centered on using the Finite Difference Time Domain technique. These are ideal for proof of concept studies, as it is well known that this numerical technique is plagued with errors when the object under analysis is electrically large and/or if the spatial discretization required to characterize the fields in the medium is small; the latter is always the case, as one needs to have sufficient samples to characterize field propagation through small metallic or non-metallic particles. Integral equation-based techniques offer considerably more accurate models albeit at a higher computational cost. Our approach to solving this problem has been different; we have resorted to using a layered medium Green's function that considerably reduces the unknown count at the expense of making the evaluation of the Green's function more complicated [8] and at the same time, we considered the quantum effect of the antenna structure.

In atomic physics, the spatial scale of the potential function is generally set by the fundamental length scale of the Bohr radius. As a result, configurations of antennas on the nanoscale will have very different physical properties. Therefore, the quantum effect in the field enhancement should be considered in the theoretical analysis. Here, Wood–Ashcroft theory [9, 10] is employed to find the conductivity of the antenna when it is illuminated by IR radiation. The electric current and resulting total electric field on the metallic structures can then be found based on the Green's function technique for the Maxwell equations of the total electric field [11].

To start with, the Hamiltonian of a system of electrons is defined as follows [9, 10]:

$$H = \frac{1}{2m_e} \left(\hat{p} + \frac{e}{c} A \right)^2 + V(r) \quad (9.1)$$

where m_e is the electron mass, e is the elementary charge, c is the speed of light in free space, \hat{p} is the momentum operator, A is the vector potential of the wave, and $V(r)$ is the one-electron effective potential in the absence of the field.

In all analysis presented here, the antenna is considered as a metallic nano thin film where the length a and the width b of the antenna is much larger than the thickness L . In this case, the conductivity can be described as follows [10]:

$$\sigma(\omega) = \frac{iNe^2}{m_e\omega\Omega} + \frac{ie^2}{m_e^2\omega\Omega} \sum_{ij} \frac{f_i - f_j}{\varepsilon_{ij} - \hbar\omega} |\langle i | \hat{p}_E | j \rangle|^2 \quad (9.2)$$

where N is the number of conduction electrons and Ω is the film volume; f_i is the occupation number of the state ε_i and supported by:

$$f_i = \left\{ \exp \left(\frac{\varepsilon_i - \mu}{k_B T} \right) + 1 \right\}^{-1} \quad (9.3)$$

where μ is the chemical potential of electrons, T is the temperature, and k_B is the Boltzmann constant.

Once the conductivity of the antenna is found, the current $J(r)$ is obtained by solving an integral equation as follows [11]:

$$(E^i + E^s) = E^{\text{total}} \quad (9.4)$$

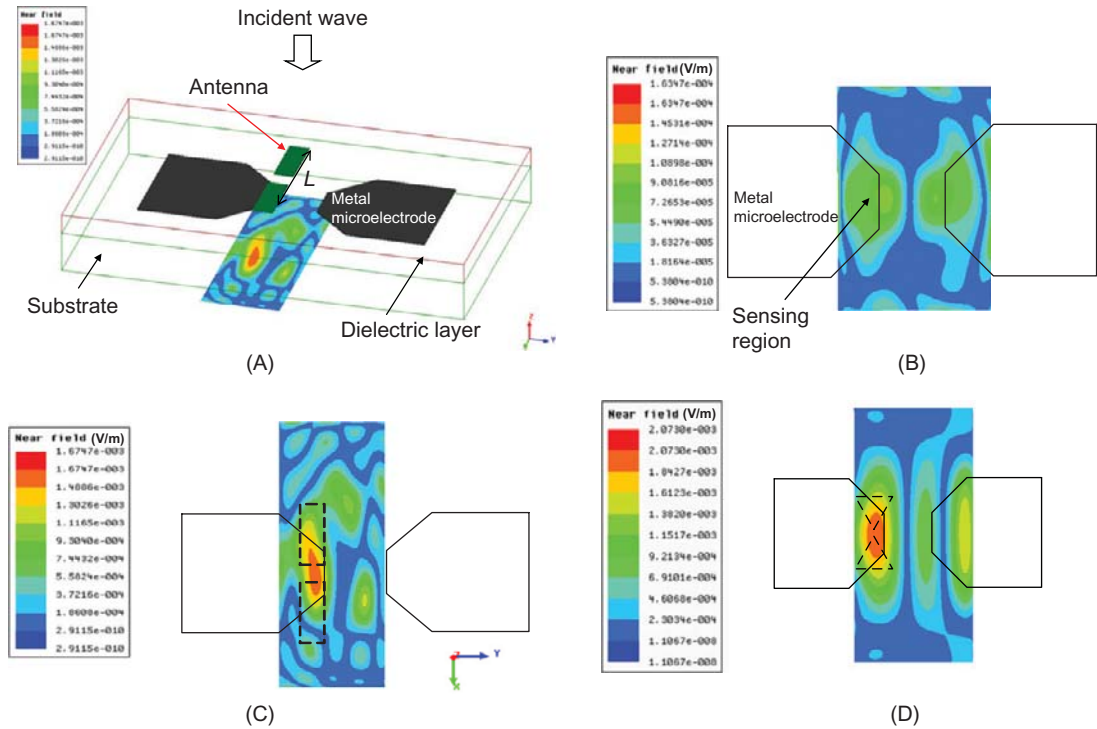
$$E^s = \overline{\overline{G}}(r) \times J(r) \quad (9.5)$$

where $\overline{\overline{G}}$ is the layered medium Green's function. E^s and E^{total} are the scattered and the total field, respectively. As a result, the total electric field, $E^{\text{total}}(r) = E^i(r) + E^s(r)$ on the metallic structures can be found from the current generated on the antenna.

By using the above approach, the electric field distribution along the plane of the IR detector with two different antenna geometries (dipole and bowtie) are obtained and compared. As shown in Fig. 9.2, the maximum electric field intensity occurred at the center of both the dipole (Fig. 9.2C) and bowtie (Fig. 9.2D) antenna and was enhanced by more than an order of magnitude when compared with the field without putting the antenna (Fig. 9.2B). In addition, the field-enhancement factor from the bowtie antenna is higher than that for the dipole antenna.

9.4 FABRICATION OF NANO SENSOR COMBINED WITH NANOANTENNA

The substantial interest in carbon nanotubes has been due in large part to their unique electronic properties, predicted to be either metallic or semiconducting depending on circumferential boundary conditions [12]. Indexing tubes by the number of lattice vectors around a circumference, theory predicts that $(n; n)$ tubes are metals, $(n; n + 3i)$ tubes (with i an integer) are small gap semiconductors with $E_{\text{gap}}/1 = R$, and other tubes have larger gaps proportional to $1 = R$ [13]. The semiconducting bandgap can be controlled through the range of sub-100 meV to a few 100 meV by varying the diameter. This makes it a potential candidate for infrared sensors. As reported in the literature [14], the CNT sensor is designed as a Schottky diode for IR detection. When the CNT is connected between a pair of metal electrodes, a Schottky barrier is formed at the CNT and metal contact. The electrons and holes pairs are excited by the photons and photocurrent is generated at the CNT-metal Schottky contact upon illumination with the IR light. Thus, the photocurrent depends strongly on the number of photon carriers generated at the CNT-metal contact. The film of the single-wall carbon nanotube (SWNT) has been used for photodetection. Since it is difficult to make all CNTs in a CNT film with the same properties, the performance of CNT films is significantly limited. Theoretical studies have shown that the photoconductivity of individual SWNTs is much better than that of CNT films. However, the fabrication

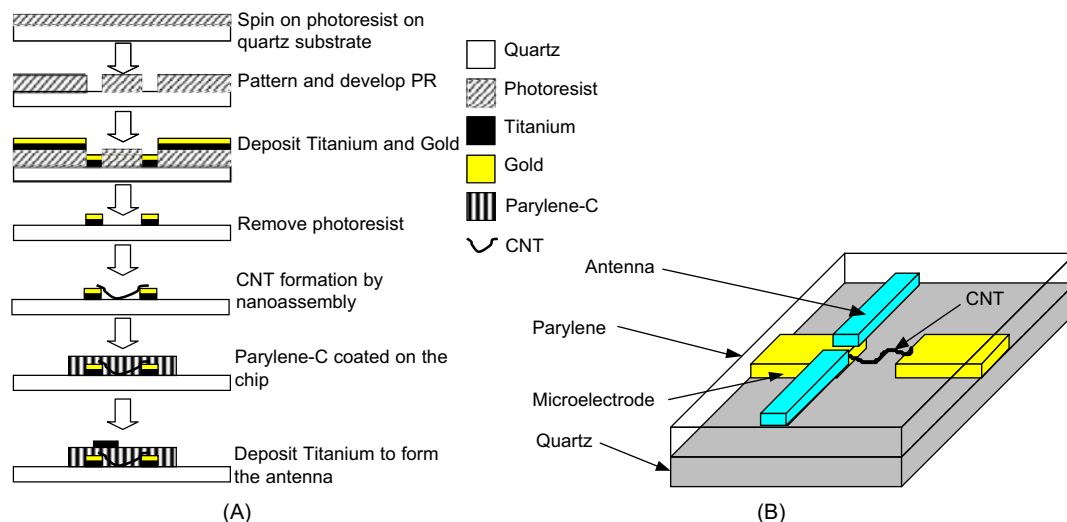
**FIGURE 9.2**

(A) Geometry of the structure for analysis, where L is the length of the antenna arm. Amplitude of the Y component of the electric field calculated when the length of the antenna is zero (B); for the dipole antenna with the length of the antenna is $4\ \mu\text{m}$ (width: $500\ \text{nm}$ and thickness: $30\ \text{nm}$) (C); and for the bowtie antenna, under the incident plane wave excitation (wavelength, $\lambda = 800\ \text{nm}$) (D). The field is calculated in a plane that is coincident with the metal microelectrode (unit: V/m). Titanium is chosen as the antenna material.

process for individual SWNT-based detectors is usually complicated and inefficient. As a result, the scope of the research into and applications of single CNT-based IR detectors has been limited. Enabled by our newly developed atomic force microscopy-based nanorobotic manipulation system, a deterministic manufacturing process has been developed to reliably and efficiently fabricate single CNT-based nano-infrared detectors [14].

The fabrication process to form the CNT Schottky diode and place the CNT-metal contact at the position of maximum field output near the antenna is shown in Fig. 9.3. It is expected that the increasing IR intensity at the CNT-metal contact would result in the enhancement of photocurrent.

Before fabricating the nanoantenna, a nanomanufacturing process is employed to fabricate the CNT-based IR detector [15]. After coating a pair of microelectrodes on the substrate, an AC voltage is applied and CNT suspension is dispersed. CNTs are then formed between the small gap (from 1

**FIGURE 9.3**

(A) Fabrication process and (B) schematic structure of a CNT-based IR detector with a nanoscale antenna.

to $3\text{ }\mu\text{m}$) of the microelectrodes by dielectrophoresis (see Chapter 2) and atomic force microscopy (AFM) nanomanipulation (see Chapter 4). The CNT is randomly formed, the position of the CNT-metal contact being confirmed by the AFM image taken after CNT formation. After the CNT sensor is successfully formed, an insulating layer is deposited on top of the sensor to separate the sensor and the nanoantenna and also protect the CNT sensing element. Parylene C is selected as the material of this insulating layer because it can be deposited conformally at room temperature. In addition, the Parylene does not completely block the IR and the CNT can still sense the IR after Parylene packaging as reported in [16].

E-beam lithography is used to pattern the nanoantenna and also align it to the CNT-metal contact. The nanoantenna produces a stronger field-enhancement effect if it is placed closer to the sensing region. Hence, the thickness of the Parylene thin film is controlled to be smaller than 500 nm. During the e-beam alignment process, a layer of polymethylmethacrylate (PMMA) resist is spin-coated and patterned with the desired geometry of the antenna. As predicted from the theoretical analysis, the maximum field occurs at the center of the antenna. By using the fabrication process presented here, the position of the nanoantenna can be precisely controlled; a typical fabricated device with dipole and bowtie antenna is shown in Fig. 9.4. It is seen that the antenna is aligned and placed on one of the symmetric CNT-metal contacts.

The above fabrication can also be used to integrate the antenna to CNT sensor with heterogeneous asymmetric metal electrodes. As explained in [14], the metal contacts with two different materials are fabricated to form the Schottky barrier and Ohmic contact, respectively. Since the photocurrent is only generated at the Schottky contact, the total photocurrent can be increased by putting the antenna on top of the Schottky contact.

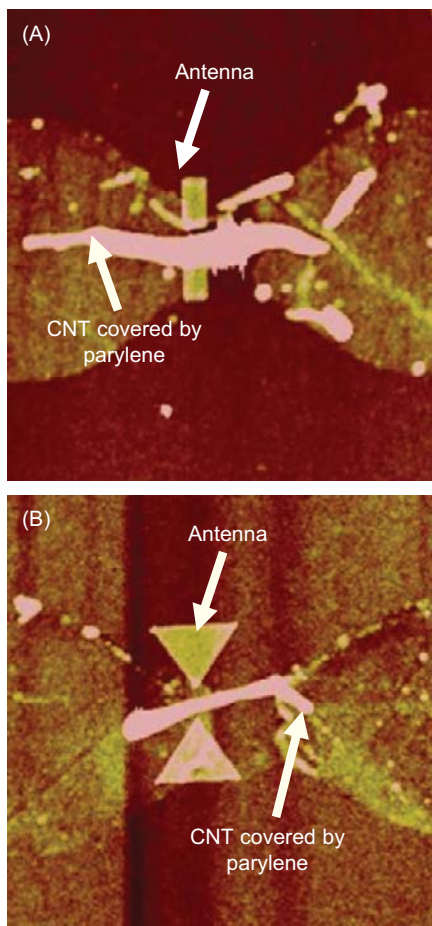
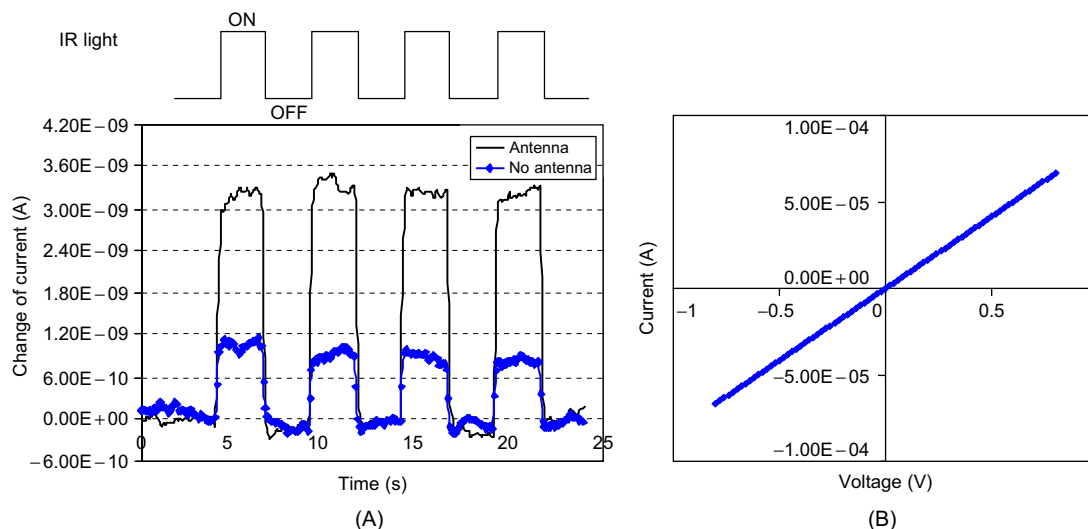


FIGURE 9.4

AFM images of the fabricated CNT IR detector with (A) the nano dipole antenna and (B) the bowtie antenna. Parylene thin film was coated between the antenna and the CNT. A pair of antennae are aligned to one of the symmetric metal contact electrodes.

9.5 PHOTOCURRENT MEASUREMENT ON NANO SENSOR COMBINED WITH NANOANTENNA

To validate the field-enhancement effect on the CNT sensor with the nanoantenna, an IR sensing experiment was performed and the photocurrent was measured before and after adding the antenna. The sensor chip was connected to a measurement circuit and the photocurrent was measured under laser illumination. The IR response to multiple on/off cycles of the CNT sensor is shown in [Fig. 9.5A](#).

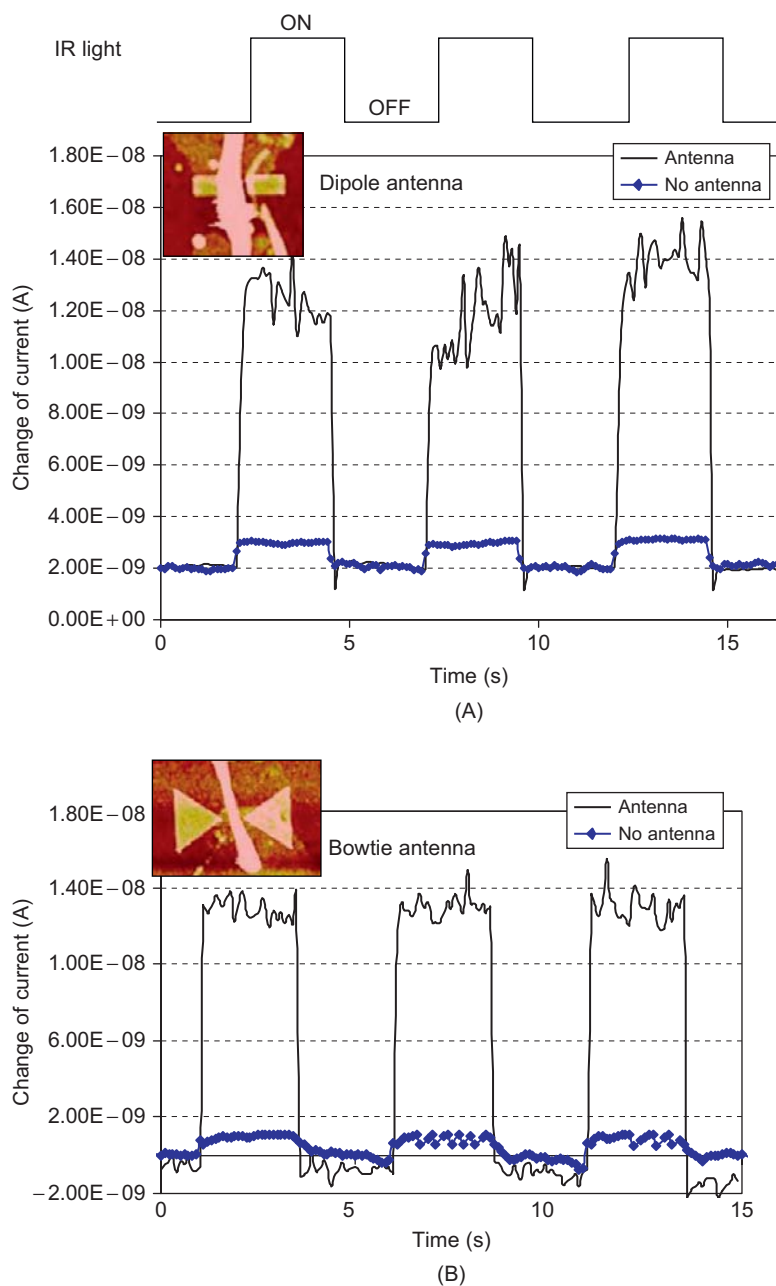
**FIGURE 9.5**

(A) Comparison of the temporal photocurrent response plots of the CNT-based IR detector with and without nanoantennae. (B) I-V characteristics of the CNT IR detector with nanoantenna.

By comparing with the photocurrent response obtained from the detector without the nanoantenna, the photocurrent change was seen to be enhanced after adding the nanoantenna. Before adding the antenna, the current change of the original CNT-based IR detector was small, which implied the low sensitivity of the sensor. On the other hand, the CNT-based sensor with the nanoantenna was more sensitive to IR because the incident power was enhanced by the antenna. I-V characteristics of the sensor after adding the antenna were also investigated as shown in Fig. 9.5B. Moreover, we studied the field enhancement of two different types of antenna structure, and it can be seen that the detector with bowtie antenna produces higher gain (Fig. 9.6). This implies the CNT detectors can be incorporated into different antenna structures and the response of the detector can be increased.

9.6 SUMMARY

Theoretical analysis and experimental study with regard to nanoantennas for use with CNT-based IR sensors has been reported. A comprehensive mathematical model was presented – that accounts for the quantum-confinement effects on the conductivity and dielectric function of the nanoscale antenna – to theoretically predict the electric field-enhancement effect for different configurations of the antenna structure and the CNT sensor. In addition, the design and fabrication process for nanoantennas for quantum IR detectors has been presented. By integrating the nanoantenna, the incident electric field at the sensor was enhanced such that the photocurrent of the sensor was greatly increased. Several factors for affecting the gain of the antenna were discussed and their effects were demonstrated by comparing the response of the detector with antennas of different geometries. Based on the above

**FIGURE 9.6**

Comparison of the temporal photocurrent response plots of a CNT-based IR detector with and without (A) dipole and (B) bowtie antennas.

study, the developed enhancement technology provides a dramatic improvement in the performance of infrared sensors.

In the future, we anticipate gaining greater insight into the localization of light and its control relating to semiconductor nanostructures. To date, localization of light has only been achieved using metallic nanostructures. The ability to control localization and manipulate the field structure on the surface of semiconductors could lead to the development of novel devices; highly sensitive sensors being just one of them. Likewise, given advances in IC technology, such devices can be manufactured both reliably and quickly. Finally, understanding the surface plasmon propagation might hold the key to the development and the design of ultra-compact integrated photonic systems with features on the nanoscale. These systems might be employed either alongside, or in lieu of, electronic components. Fundamental to the progress in this area is the control of propagation of light on a very small scale. Surface plasmon polariton (SPP) optics offers a promising avenue of development toward this end. Additionally, we anticipate that the tools developed herein can be used to facilitate development of integrated optical devices leading to better methods in optical computing and communications, and a quantitative description of SPP optics will enable improved imaging in SPP-based microscopy and spectroscopy. These imaging methods have subsequent impact across a broad range of fields including chemistry, biology, and medicine.

References

- [1] C. K. M. Fung, N. Xi, B. Shanker, and K. W. C. Lai. Nanoresonant signal boosters for carbon nanotube based infrared detectors. *Nanotechnology*, 20(18):185201, 2009.
- [2] P. Mühlschlegel, H. J. Eisler, O. J. F. Martin, B. Hecht, and D. W. Pohl. Resonant optical antennas. *Science*, 308:1607–1609, 2005.
- [3] P. Biagioni, J. S. Huang, L. Duò, M. Finazzi, and B. Hecht. Cross resonant optical antenna. *Phys. Rev. Lett.*, 105:256801, 2009.
- [4] J. Alda, J. M. Rico-Garcia, J. M. Lopez-Alonso, and G. Boreman. Micro- and nano-antennas for light detection. *Egypt. J. Solids*, 28:1–13, 2005.
- [5] Y. Wang, K. Kempa, B. Kimball, J. B. Carlson, G. Benham, W. Z. Li, T. Kempa, J. Rybczynski, A. Herczynski, and Z. F. Ren. Receiving and transmitting light-like radio waves: antenna effect in arrays of aligned carbon nanotubes. *Appl. Phys. Lett.*, 85(13), 2004.
- [6] G. W. Hanson. Fundamental transmitting properties of carbon nanotube antennas. *IEEE Trans. Antennas Propag.*, 53(11):3426–3435, 2005.
- [7] P. J. Burke, S. Li, and Z. Yu. Quantitative theory of nanowire and nanotube antenna performance. *IEEE Trans. Nanotechnol.*, 5(4):314–334, 2006.
- [8] G. Kobidze, B. Shanker, and D. P. Nyquist. Novel algorithm for analysis of surface plasmon polariton. *Phys. Rev. E*, 72:056702, 2005.
- [9] D. M. Wood and N. W. Ashcroft. Quantum size effects in the optical properties of small metallic particles. *Phys. Rev. B: Condens. Matter*, 25:6255–6274, 1982.
- [10] V. P. Kurbatsky, A. V. Korotun, V. V. Pogosov, and E. V. Vasyutin. Size dependence of the transmittance for metal nanofilms in the infrared region. *Phys. Solid State*, 50(5):949–956, 2008.
- [11] K. A. Michalski and D. Zheng. Electromagnetic scattering and radiation by surfaces of arbitrary shape in layered media. *IEEE Trans. Antennas Propag.*, 38:335–344, 1990.
- [12] R. Saito, M. Fujita, G. Dresselhaus, and M. S. Dresselhaus. Electronic structure of chiral graphene tubules. *Appl. Phys. Lett.*, 60:2201–2206, 1992.

- [13] V. H. Crespi and M. L. Cohen. *In situ* band gap engineering of carbon nanotubes. *Phys. Rev. Lett.*, 75:2093–2096, 1997.
- [14] J. Zhang, N. Xi, H. Chen, K. W. C. Lai, and G. Li. Photovoltaic effect in single carbon nanotube based Schottky diodes. *Int. J. Nanoparticles*, 1(2):108–118, 2008.
- [15] K. W. C. Lai, N. Xi, C. K. M. Fung, J. Zhang, H. Chen, Y. Luo, and U. C. Wejinya. Automated nanomanufacturing system to assemble carbon nanotube based devices. *Int. J. Rob. Res. (IJRR)*, 28(4):523–536, 2009.
- [16] K. W. C. Lai, N. Xi, J. Zhang, G. Li, and H. Chen. Packaging carbon nanotube based infrared detector. In *7th IEEE International Conference on Nanotechnology (IEEE NANO)*, pages 778–781, 2007.

Design of Photonic Crystal Waveguides

10

Jianyong Lou*, Carmen Kar Man Fung[†], King Wai Chiu Lai**,
Hongzhi Chen**, Ning Xi**, and Zhengfang Zhou^{††}

*The State Key Laboratory of Electrical Insulation and Power Equipment, Xi'an Jiaotong University, China

[†]Hong Kong Productivity Council, Hong Kong

**Department of Electrical and Computer Engineering, Michigan State University, Michigan

^{††}Department of Mathematics, Michigan State University, Michigan

CHAPTER OUTLINE

10.1 Introduction	163
10.2 Review of the Photonic Crystal	164
10.3 Principle for Photonic Crystal	165
10.4 Photonic Band Gap of Photonic Crystal	166
10.4.1 Effect from Dielectric Constants	167
10.4.2 Effect from Different Structures	168
10.5 Photonic Crystal Cavity	173
10.5.1 Basic Design of Photonic Crystal Defect	173
10.5.2 Defect from Dielectric Constants	174
10.5.3 Defect from Dielectric Size	176
10.5.4 Effect from Lattice Number	177
10.6 Design and Experimental Results of Photonic Crystal Cavity	178
10.6.1 Design	178
10.6.2 Photoresponses of CNT-Based IR Sensors with Photonic Crystal Cavities	179
10.6.3 Photocurrent Mapping of the CNT-Based IR Sensors with Photonic Crystal Cavities ..	180
10.7 Summary	181
References	182

10.1 INTRODUCTION

In Chapters 7 and 8, we demonstrated that the carbon nanotube (CNT)-based infrared (IR) sensor offers exciting prospects for this type of device, which works at room temperature and is on the micron scale. CNT-based IR sensors consist of CNTs with a length of about 200 nm–2 μ m, two asymmetric microelectrodes, and a dielectric substrate. The two microelectrodes are connected by the CNT, and they are together fixed on the dielectric substrate. If the CNT and microelectrodes are directly exposed

to an infrared source, photon-electron coupling in the CNT and two asymmetric contacts of the CNT and two microelectrodes produces photocurrent. However, the photocurrent is still too low because of the small absorption area of the CNT-metal contacts.

How can the photocurrent of CNT-based IR sensors be increased? The basic idea is to trap many more infrared photons (light energy from an incident source) for the IR sensors so the infrared photon absorptency is increased. In Chapter 9, use of nanoantennas to increase the photocurrent of CNT-based IR sensors was discussed. By using electric field resonance of incident light near a nanoantenna, local electric field enhancement can be achieved. As a result, the photocurrent of CNT-based IR sensors is increased. However, the gain of the photocurrent of the CNT-based IR sensors with nanoantennas is still not sufficiently high. In this chapter, we will demonstrate use of the photonic crystal waveguide to increase the photocurrent of CNT-based IR sensors. By using photonic crystals with defective nanostructures, the crystal nanocavity can acquire many more infrared photons from the two-dimensional dielectric plane in the nanoscale central defective photon trapper. This means that the sensors can collect more infrared photons from the same size, and this method will be helpful for infrared sensors to obtain higher photocurrent. We consider that energy collection of incident light by photonic crystals is a challenging idea for CNT-based IR sensors. To achieve the goal of photon collection for infrared sensors, the central defective nanostructure of photonic crystal must be precisely aligned above the CNT and its two nearby asymmetric metal contacts, and then more confined infrared photons can be absorbed because of stronger photon-electron coupling, with increased gain of IR sensors photocurrent. In the following sections of this chapter, we will discuss making use of the photonic crystal waveguide with a central point defect to confine infrared photons and demonstrate the photonic crystal calculation principle, photonic band gap diagrams, photonic nanocavity design, infrared field profile, and the applications of photonic crystals for CNT-based IR detectors.

10.2 REVIEW OF THE PHOTONIC CRYSTAL

The photonic band gap of dielectric media and the definite location of photons in dielectric lattices with defect nanostructures has been known about since 1987 [1, 2], the photonic crystal thus becoming a hot research topic for optical nanodevices, being investigated in the areas of optical waveguide, optical filter, and optical communication in recent years. Photonic crystals to control light transmission and reflection properties in dielectric lattices for special frequency scales are used because of the band gap characteristics. The photonic crystal can be used as a directivity patch antenna [3], or can also be used in optical filters [4], or to form a special waveguide and bandwidth [5, 6]. By introducing a design incorporative line defect, the sharp bend waveguide is one obvious case of optical waveguide to obtain high transmission. For special optical filters of photonic crystal in the literature [7–9], point defects in photonic crystals [10, 11], or the special donor-type defects in two-dimensional photonic crystal are adopted [12]. Both point defect and donor-type defect can be treated as the differences from the periodic arrangement of dielectric media in photonic crystal. By using the point defect and the line defect, the maximum emission efficiency of channel drop filters is investigated with theoretical analysis and experimental verification, and for the same structure with acceptor-type point defect, the photonic crystal can be used as the surface-inputting channel-add filter.

Instead of optical filters of photonic crystal, the quantum resonant photonic cavity of photonic crystal has attracted much interest in photon confinement in recent years. By using point defects or

heterostructures, the photons can be strongly localized inside the photonic crystal, and this indicates that photons can be collected thereby. From some of the published articles on photonic crystal, point defects and the heterostructures are used to obtain high performance nanocavity [13, 14], and the key factors that can influence the Q (quality) factor of quantum resonant nanocavity, such as the air holes arrangement near the central defect, are analyzed. The effect of one-sided dielectric claddings for light leak from photonic crystal is considered [15], and the radiation loss and in-plane loss of transverse electric-transverse magnetic coupling are discussed. Methods to improve the Q factor are also discussed [16, 17]. By hybrid point defect and line defect [18], a high photon number in the point defect can be achieved. Because of the rapid progress in photonic nanocavity research, the photonic crystal with a point defect in the two-dimensional plane has been used in the waveguide laser. Here, for our research of CNT-based IR sensors, we are interested in the photonic nanocavity of the photonic crystal with a point defect in the two-dimensional plane, to collect photons in order to generate high photocurrent.

10.3 PRINCIPLE FOR PHOTONIC CRYSTAL

There are two typical designs of photonic crystals without disordered lattices, which are shown in Fig. 10.1. In Fig. 10.1A, the air holes with a triangle lattice arrangement are periodically distributed in the two-dimensional plane of the dielectric media, and in Fig. 10.1B, the photonic crystal has the triangle lattice arrangement of periodic dielectric rods in air.

In general, the photonic crystal waveguide is just the optical analog of electrons in atoms. When electrons propagate in atom lattices, the atoms have electrical potential, and the electrons will be modulated by the potential function of atoms. The basic solution for electrons in atoms is the Schrodinger equation. For photonic crystal, the electrons are replaced by photons in dielectric media, and atoms are

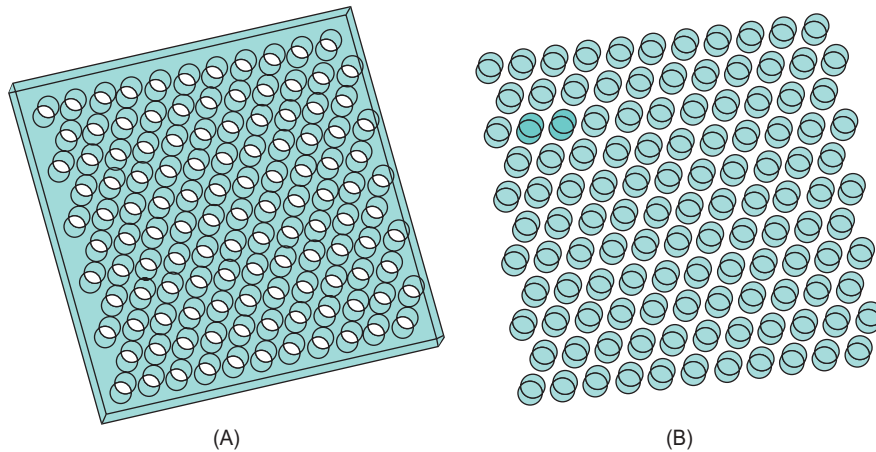


FIGURE 10.1

The full photonic crystal without defect. (A) Photonic crystal of air holes in a two-dimensional dielectric slab. (B) Photonic crystal of dielectric rods in air.

replaced by the periodic pattern media with different dielectric constants, and the electrical potential of atoms is replaced by the dielectric constants or equivalent refraction index. Initially, photon propagation in photonic crystal should also be solvable by the Schrodinger equation. But unfortunately, it is unrealistic to delineate the potential function of dielectric media for photons. Thus we are not able to solve light transmission in photonic crystal via the quantum mechanism. Hence we will have to look for help from Bloch's theorem for the solution of light transmission in photonic crystal. Basically, the incident light from an infrared source will be refracted and reflected in the interfaces of dielectric media (such as air hole and silicon dioxide) of photonic crystal, and light transmission in photonic crystal is controlled and modulated by the periodic dielectric media by light reflection and refraction principles. In the following, we will start from Maxwell's equations to obtain the governing equations for light transmission in photonic crystal.

$$\nabla \times E(r) - i\omega\mu_0 H(r) = 0 \quad (10.1)$$

$$\nabla \times H(r) + i\omega\epsilon_0\epsilon(r)E(r) = 0 \quad (10.2)$$

$$\hat{\Theta}H(r) = \left(\frac{\omega}{c}\right)^2 H(r) \quad (10.3)$$

$$\hat{\Theta}H(r) \triangleq \nabla \times \left(\frac{1}{\epsilon(r)} \nabla \times H(r) \right) \quad (10.4)$$

Maxwell's equations can be written in Eqs (10.1) and (10.2) [19]. The permeability of photonic crystal is considered to be one. For the polarization light of TE (transverse electrical field)-like mode or TM (transverse magnetic field)-like mode, it can be seen as the planar light wave. The magnetic field $H(r, t)$ of the incident polarization light is treated as a harmonic mode, which means that the magnetic field component of the incident source is the product of magnetic field pattern $H(r)$ and a time component. Then from Eqs (10.1) and (10.2), we will use the first equation to eliminate $E(r)$ by writing the electrical field pattern $E(r)$ in the item of magnetic field pattern $H(r)$. Then we substitute $E(r)$ into Eq. (10.2), and Eq. (10.3) can be obtained. In Eq. (10.3), the magnetic field $H(r)$ under the Hermitian operator equals a scale constant times magnetic field $H(r)$ itself. The constant in Eq. (10.3) is the square of angular frequency of incident light over c , the speed of light in space. The Hermitian operator is shown in Eq. (10.4); this operator includes the dielectric function of $\epsilon(r)$ to calculate the effect of periodic dielectric media in photonic crystal.

From Eqs (10.3) and (10.4), we can see that light transmission in photonic crystal can be thought of as an eigenvalue problem of electromagnetism. The eigenvalue is the square of ω/c . The electromagnetic principle for photonic crystal follows Bloch's theorem, and the field pattern is Bloch's state. The eigenvalue $H(r)$ of the magnetic field is modulated by the function of dielectric media. By solving the eigenvalue equations of photonic crystal, we can obtain the band gap diagrams of photonic crystal and field distribution of incident infrared light in the defective design of photonic crystal.

10.4 PHOTOTONIC BAND GAP OF PHOTONIC CRYSTAL

As we all know, photonic crystal has a photonic band gap, and if the frequency of incident light is inside the stop band of the band gap diagram of the crystal, the light from an infrared source is totally reflected by the crystal. The band gap characteristic of photonic crystal is related to the dielectric

constant, the contrast of two dielectric materials, and the dielectric lattice structure. Now we will show the band gap diagrams of different photonic crystals and analyze the factors that influence the band gap characteristics of possible photonic crystal design.

10.4.1 Effect from Dielectric Constants

The effect of dielectric constants on band gap characteristics of photonic crystal is shown in Fig. 10.2, which presents the band gap diagrams of various photonic crystals with the triangle lattice arrangement of air holes in the dielectric slab for the TE-like mode of the incident source. The dielectric materials of photonic crystal are polyimide (dielectric constant = 3.4), silicon nitride (dielectric constant = 7.8),

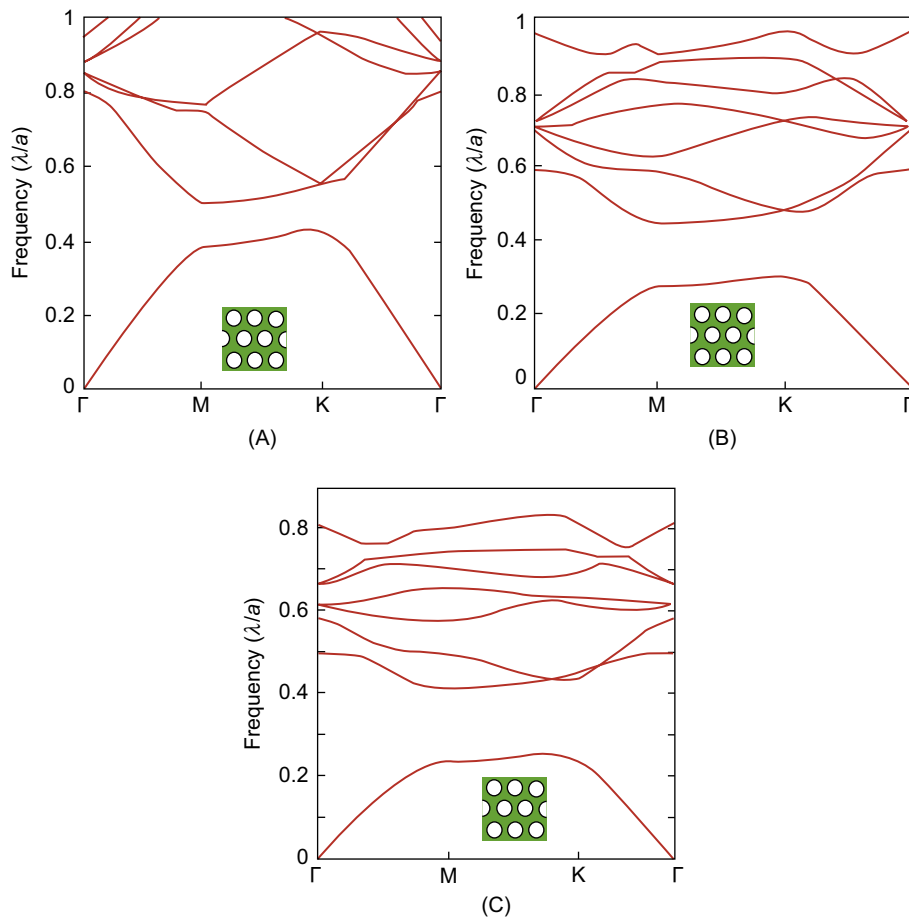


FIGURE 10.2

The band gap diagram of photonic crystal of different dielectric constants. The crystal has the lattice arrangement of air holes in a dielectric slab. (A) Polyimide photonic crystal. (B) Silicon nitride photonic crystal. (C) Silicon photonic crystal.

and silicon (dielectric constant = 12). The lattice constant of photonic crystal is a , and the radius of air holes over lattice constant is 0.4. The horizontal axis of the band gap diagram is Bloch's wave vector in the reciprocal space of the irreducible Brillouin zone of photonic crystal lattices. The vertical axis indicates the normalized frequency of incident light. For the TE-like mode of incident light, the transverse electrical field component $E(r)$ is inside the two-dimensional plane.

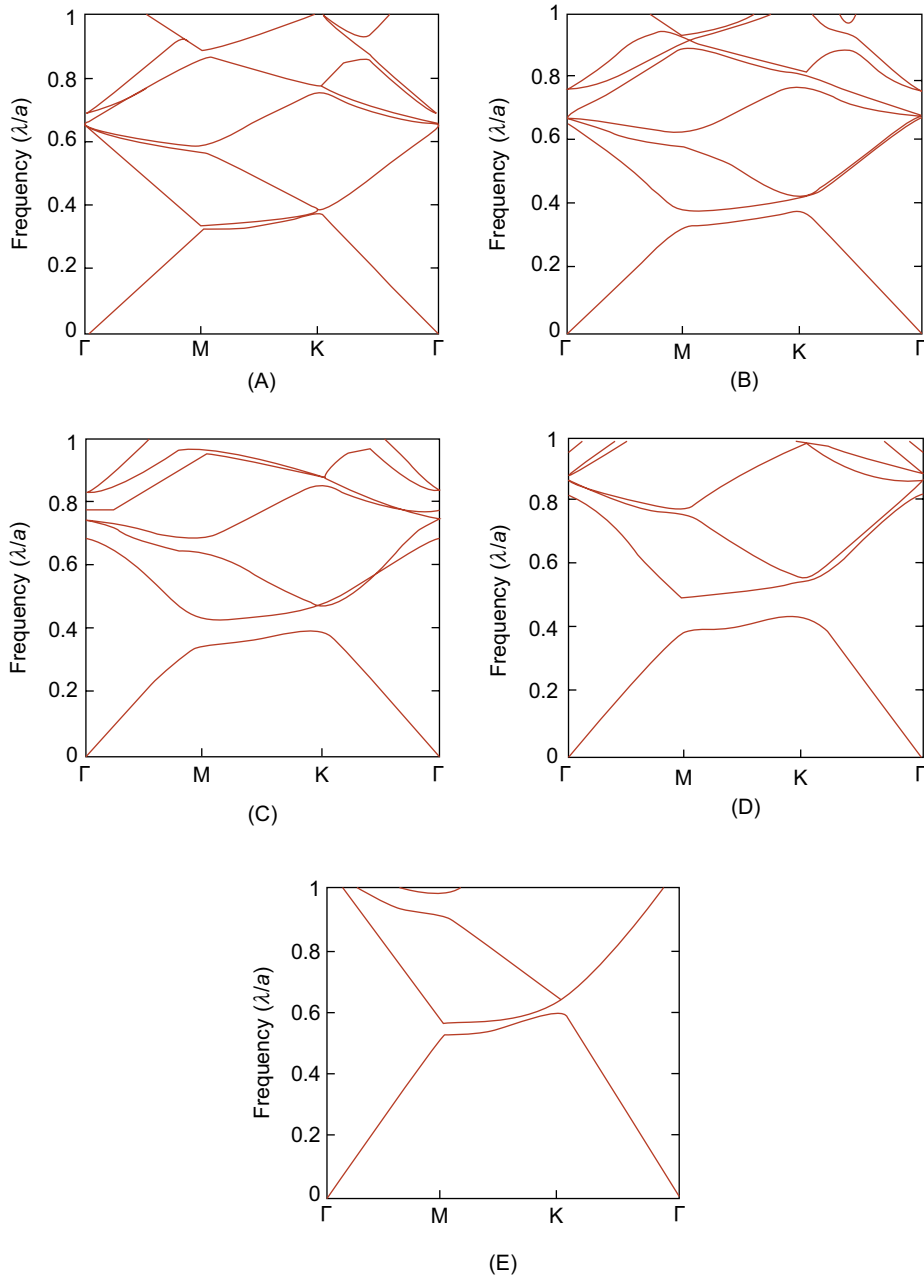
The band gaps of the TE-like mode of a polyimide photonic crystal, a silicon nitride photonic crystal, and a silicon photonic crystal shown in Fig. 10.2 are from 0.432 to 0.502, 0.301 to 0.446, and 0.246 to 0.405 of normalized frequency, respectively. We can see that the photonic crystal with a low dielectric constant has a smaller band gap (polyimide photonic crystal, $\varepsilon_r = 3.4$, 0.432 to 0.502 of normalized frequency), and the photonic crystal with a high dielectric constant has a bigger band gap (silicon photonic crystal, $\varepsilon_r = 12$, 0.246 to 0.405 of normalized frequency). In general, the difference between two dielectric materials is proportional to the width of the photonic band gap. For example, the dielectric constant of silicon slab is 12 for silicon photonic crystal, whereas the dielectric constant of air holes is 1. The silicon photonic crystal has the biggest band gap width, as shown in Fig. 10.2.

10.4.2 Effect from Different Structures

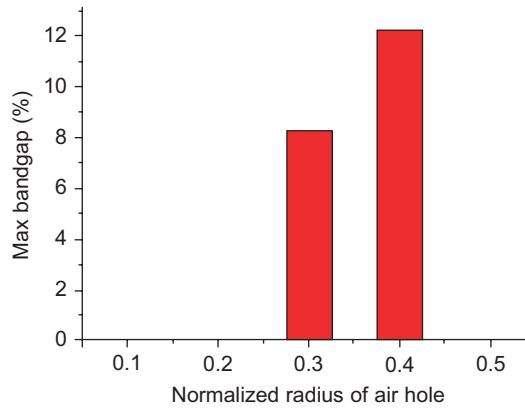
The effect of air hole size on the band gap characteristics of Parylene photonic crystal is shown in Fig. 10.3. The periodic air holes of Parylene photonic crystal also have the triangle lattice arrangement (see Fig. 10.1A), and the Parylene slab has a dielectric constant of 3.1. From Fig. 10.3A–E, the lattice constants of Parylene photonic crystal are the same, but the normalized radii (air hole radius over lattice constant) of the air holes are 0.1, 0.2, 0.3, 0.4, and 0.5, respectively. Using Fig. 10.3, we will show how air hole size can influence the band gap of Parylene photonic crystal of the TE-like mode of infrared source. In Fig. 10.3, we can see that there is no obvious band gap for Parylene photonic crystal when the normalized radii of air holes are 0.1, 0.2, and 0.5. For the case of a normalized air hole radius of 0.3, there is a small band gap from 0.399 to 0.435 of normalized frequency. For a normalized air hole radius of 0.4, there is a bigger band gap from 0.448 to 0.507 of normalized frequency. So we can conclude that Parylene photonic crystal has the biggest band gap, in Fig. 10.3D, when the radius of the air holes is 0.4.

To show the relationship of band gap width and air hole radius intuitively, we will use the concept of gap–midgap ratio to indicate the max band gap width [19]. The corresponding band gap would have a width $\Delta\omega$ in the band gap diagram of Parylene photonic crystal. Letting ω_m be the middle frequency of the stopband, we then define the gap–midgap ratio as $\Delta\omega/\omega_m$ in the expression of a percentage. For the Parylene photonic crystal shown in Fig. 10.3, the max band gap width in regarding a gap–midgap ratio for TE-like mode of incident light is shown in Fig. 10.4. For the case of a normalized air hole radius of 0.4, Parylene photonic crystal achieves the biggest band gap width for all lattice geometry size designs, which is 12.2% as regards gap–midgap ratio. For the case of normalized radius of 0.3, the max band gap width is about 8.3%.

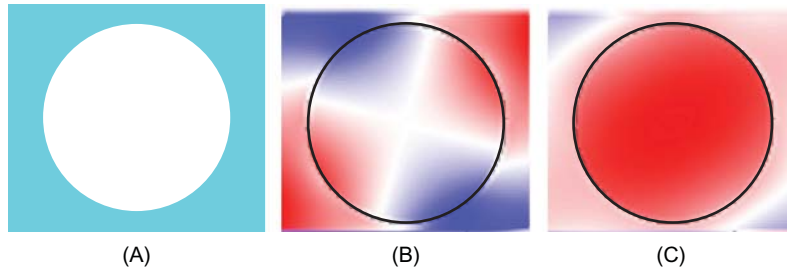
Why does Parylene photonic crystal achieve max band gap width at a normalized air hole radius of 0.4? In our understanding, the energy concentration contrast in the dielectric slab and air hole of two adjacent bands, under and above the band gap, is responsible for the appearance of the band gap. For the case of Figs 10.3 and 10.4, the energy concentration contrast in the Parylene slab and air holes of these two bands is the biggest for the lattice geometry structure of a normalized air hole radius of 0.4.

**FIGURE 10.3**

The band gap diagram of photonic crystal of air holes in Parylene slab for TE-like mode of incident source. (A–E): normalized radius of air hole is from 0.1 to 0.5 with an increment of 0.1.

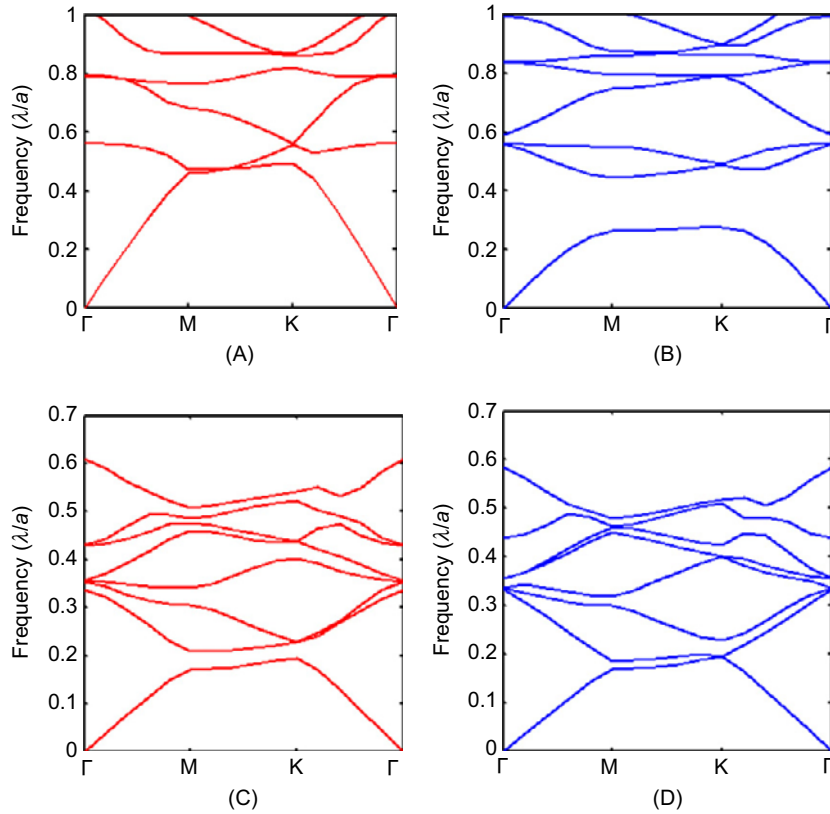
**FIGURE 10.4**

The max band gap width versus normalized radius of air hole for Parylene photonic crystal of TE-like mode.

**FIGURE 10.5**

The unity lattice and electric field profile of dielectric mode and air mode of Parylene photonic crystal of TE-like mode of incident light. (A) Unity lattice of air hole in Parylene slab. (B) Electrical field profile of first band (dielectric mode). (C) Electrical field profile of second band (air mode).

In the following, we will explain the relationship of band gap and energy contrast, referring to Fig. 10.5. In Fig. 10.3D, the band that is lower than the band gap is called the first band, and the band which is just above the band gap is called the second band. In Fig. 10.5A, the unity lattice cell is shown; the radius of air hole over lattice constant is 0.4, and the dielectric slab is Parylene. Figure 10.5B shows the electrical field profile of the first band in Fig. 10.3D, and Fig. 10.5C shows the electrical field profile of the second band of Fig. 10.3D. In Fig. 10.5B, we can see that there are two nodal planes of transmission light in the air hole region of Parylene photonic crystal, and this means that there is less energy distribution in the air holes, and most of the field energy of Fig. 10.5B is in the Parylene slab. This energy concentration mode is called the dielectric mode. In Fig. 10.5C, it is very obvious that most of the field energy is localized in the air hole region, and this energy concentration mode is called the air mode for the second band of Fig. 10.3D. When the normalized radius of air holes of Parylene

**FIGURE 10.6**

The band gap diagrams of two typical photonic crystals for TM-like and TE-like mode. (A) Bandgap of photonic crystal of silicon rods in air for TE-like mode. (B) Bandgap of photonic crystal of silicon rods in air for TM-like mode. (C) Bandgap of photonic crystal with air holes in silicon slab for TE-like mode. (D) Bandgap of photonic crystal with air holes in silicon slab for TM-like mode.

photonic crystal is 0.4, the energy concentration contrast of dielectric mode and air mode becomes greatest, and the max band gap width then appears.

The band gap characteristic of two typical photonic crystals and its relationship with the TE-like mode and TM-like mode of incident source is shown in Fig. 10.6. There are two basic designs of photonic crystal. The first typical one is photonic crystal with air holes in a dielectric slab (Fig. 10.1A). The second basic design is photonic crystal of dielectric rod in air (Fig. 10.1B). The two basic photonic crystals have totally different band gap characteristics for TE-like mode and TM-like mode. We will show these differences in the following sections using the case of silicon photonic crystal with a dielectric constant of 12. The band gap diagrams for photonic crystal of silicon rods in air are shown in Fig. 10.6A (for TE-like mode of incident source) and Fig. 10.6B (for TM-like mode). The silicon rods in air have a triangle lattice arrangement, and the radius of silicon rods over lattice constant is 0.2. In

Fig. 10.6A, there is a small band gap from 0.822 to 0.864 of normalized frequency for the TE mode. But there are two band gaps in Fig. 10.6B for the TM mode, and the first big band gap is from 0.275 to 0.446 of normalized frequency, and the second band gap is from 0.564 to 0.593. The band gap diagrams for photonic crystal of air holes in a silicon slab are shown in Fig. 10.6C (for the TE-like mode) and Fig. 10.6D (for the TM-like mode). The air holes have the triangle lattice arrangement too. The radius of air holes over lattice constant is also 0.2. In Fig. 10.6C, there is a small band gap from 0.195 to 0.208 of normalized frequency for the TE mode. But there is no obvious band gap in Fig. 10.6D for the TM mode. Therefore, it is concluded that the band gap for the TM-like mode is bigger than that for the TE-like mode for photonic crystal of dielectric rods in air, and the band gap for the TE-like mode appears more readily than with the TM-like mode for photonic crystal with air holes in a dielectric slab. If we compare the band gap diagram of Fig. 10.2C with that of Fig. 10.6C, we can see that the band gap of the TE-like mode will enlarge if we increase the normalized radius of air holes from 0.2 to 0.4.

The band gap width diagram for photonic crystal with air holes in a silicon slab is shown in Fig. 10.7. For the TM-like mode of incident light, biggest band gap width of 0.21 occurs when the normalized radius is 0.5, and band gap width is close to zero when the normalized radius is 0.1. For the TE-like mode of incident source, the band gap becomes biggest for a normalized radius 0.4, which is about 0.49. This band gap of TE-like mode is very large. For other normalized radii, the band gap becomes small, even reaching zero. By using this biggest band gap for a normalized radius of 0.4, we can design silicon photonic crystal to specification and confine infrared light over a wide frequency.

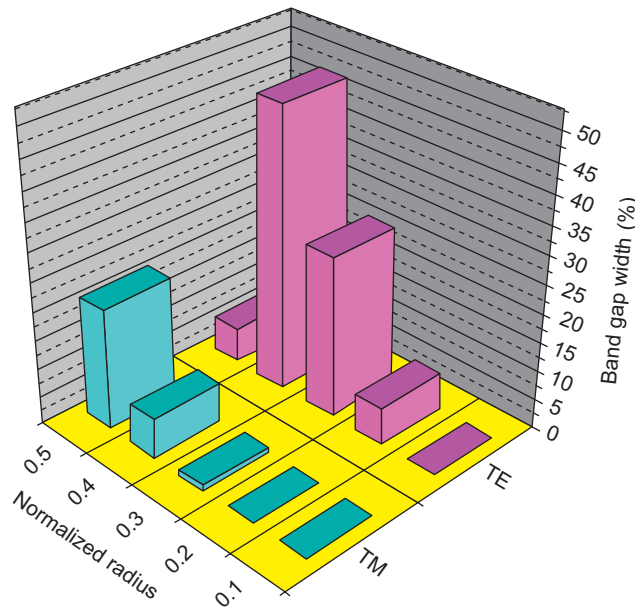


FIGURE 10.7

The band gap width for photonic crystal with air holes in a silicon slab.

10.5 PHOTONIC CRYSTAL CAVITY

10.5.1 Basic Design of Photonic Crystal Defect

The possible designs of photonic crystal for IR sensors are shown in Fig. 10.8. In Fig. 10.8A, the photonic crystal consists of dielectric rods in air, and the dielectric rods have same dielectric constant and geometry size. These familiar dielectric rods are arranged periodically in the two-dimensional plane. The dielectric rod in the central position of the photonic crystal has been removed. We can also change the radius and dielectric constant of the central rod to create a different defect. The photonic crystal in Fig. 10.8A has a triangular lattice arrangement, and we can also make it has a square lattice.

The antistructure photonic crystal of Fig. 10.8A is shown in Fig. 10.8B. There are periodic air holes in a two-dimensional dielectric slab. These air holes have triangular lattice arrangement, and the air hole in the central photonic crystal has been removed to form a point defect. We can also construct a point defect by setting a dielectric rod of different dielectric constant and size to replace the original air hole. We consider that photonic crystals with air holes in a dielectric slab is very similar to photonic crystal with dielectric rods in air. The difference between the two photonic crystals is only that the dielectric media distribution and contrast are reversed. The two types of photonic crystals will follow the same principle for light transmission, but they have different characteristics regarding band gap diagrams of polarization incident light.

Because there is a clear band gap in photonic crystal with air holes in a dielectric media for the TE-like mode in some cases of specific radius size of air holes, we can create central defective nanostructures inside this photonic crystal, and the defect can confine infrared photons, acting as a quantum resonant nanocavity. This is photonic crystal localization mode. How can we make this defect design for infrared light of special frequency to collect infrared photons? We will first consider that the frequency of the infrared source is close to the mid-frequency of the band gap and then decide the lattice constant and air hole size to make the actual band gap of the photonic crystal match the frequency of the infrared source.

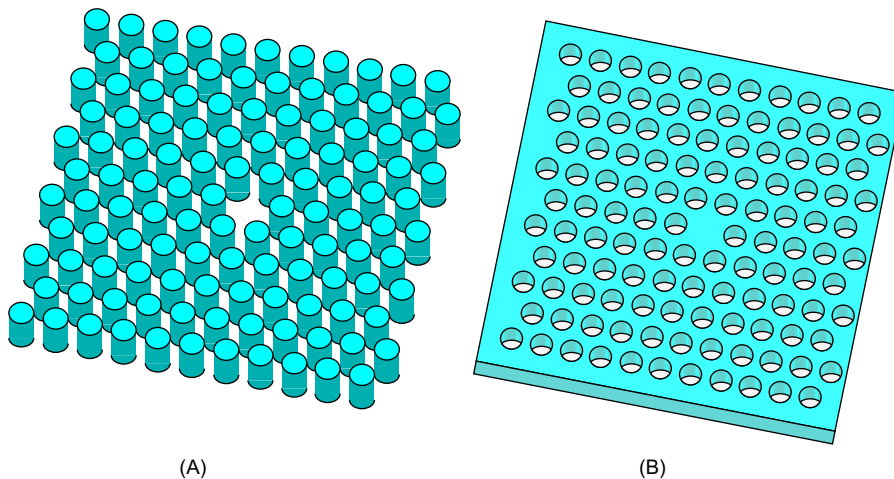
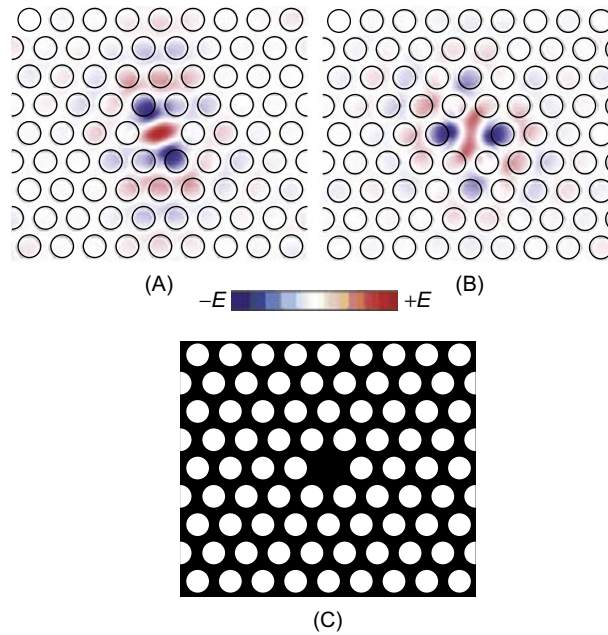


FIGURE 10.8

The basic design of photonic crystal nanocavity. (A) Dielectric rods in air. (B) Air holes in dielectric slab.

**FIGURE 10.9**

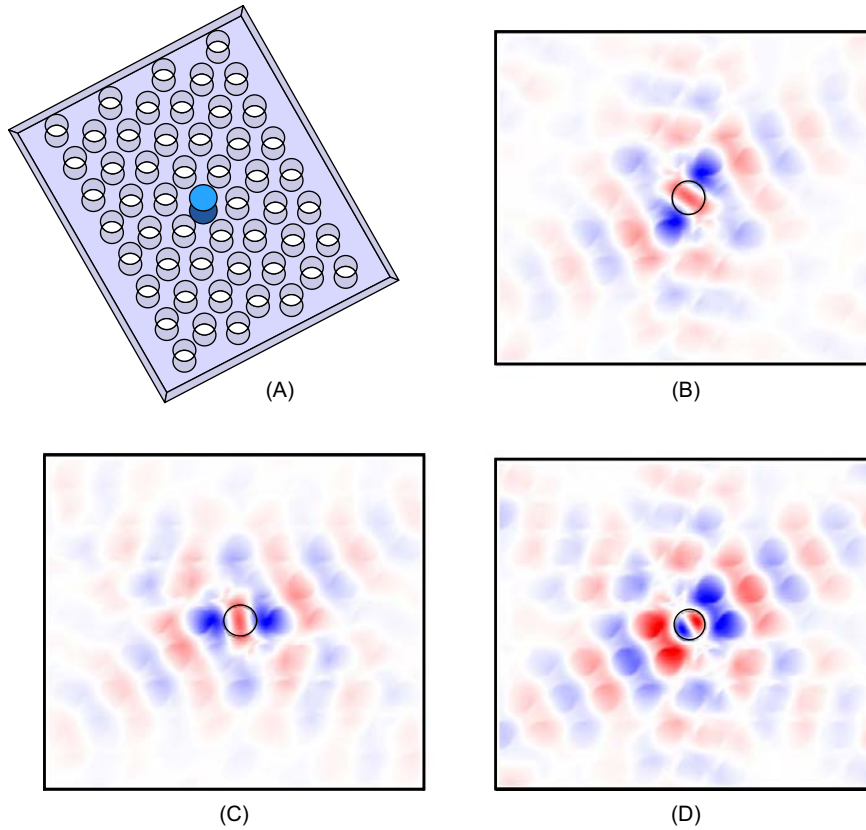
The field profile of silicon dioxide photonic crystal with removed air hole point defect. (A) E_x field. (B) E_y field. (C) Silicon dioxide (black) distribution.

First, we take the example of silicon dioxide photonic crystal to demonstrate the field profile feature of the photonic crystal nanocavity. The field profile of silicon dioxide photonic crystal with a central point defect is shown in Fig. 10.9. The black spot in Fig. 10.9C represents the dielectric substrate of silicon dioxide with a dielectric constant of 3.9, and the radius of air holes over lattice constant is 0.35. The central air hole has been removed to form the resonant nanocavity. The electrical field of the x component is shown in Fig. 10.9A, and the field of the y component is shown in Fig. 10.9B. The nodal planes of E_x and E_y fields of infrared light in photonic crystal are different, but in both fields, the electrical field in the central point defect is much higher than that in the air hole region of the photonic crystal. This field profile means that the incident infrared light is confined in the central point defect. The field energy inside the central point with an area having a diameter of the lattice constant is about a quarter of total energy in the photonic crystal plane. Therefore, we can say the infrared photons are collected in the point nanocavity by the photonic crystal.

What are the main factors that can influence the confinement efficiency of defective photonic crystal? We will now discuss the defect design by changing the dielectric constant and dielectric media sizes and also show the effect of different photonic crystal sizes.

10.5.2 Defect from Dielectric Constants

The effect of dielectric constants on the electrical field profile of silicon dioxide photonic crystal with a central point defect is shown in Fig. 10.10. The normalized air hole radius is 0.35, and the air holes

**FIGURE 10.10**

The field profile of silicon dioxide photonic crystal with point defect of different dielectric constants. (A) Design of defective phototonic crystal with central rods of different dielectric constants. (B) Point defect of silicon nitride rod. (C) Point defect of aluminium oxide. (D) Point defect of silicon.

have a triangular lattice geometry. In Fig. 10.10A, the dielectric substrate of photonic crystal is silicon dioxide, and the original central air hole has been replaced by dielectric rods (silicon nitride rod, Fig. 10.10B; aluminium oxide rod, Fig. 10.10C; silicon rod, Fig. 10.10D). The radius of the dielectric rods is the same as the radius of the removed central air hole. The only difference in photonic crystal of Fig. 10.10 is that the dielectric constants of defective rods are different.

The field profiles of Fig. 10.10B and C show that the confined mode has a monopole pattern in the point defect of dielectric rods, while the field profile of Fig. 10.10D has a dipole pattern with a nodal plane in the central line of the localized resonant mode. This means that the frequency of the confined mode of Fig. 10.10D is higher than that of Fig. 10.10B and C. In the defective dielectric rod with a normalized radius of 0.35, the confined energy of Fig. 10.10B–D is respectively 18.5%, 19.1% and 32.1% of total energy in the photonic crystal. We can see that the dielectric rod with a higher dielectric constant is more beneficial in terms of higher confinement efficiency and more greatly confined light energy.

10.5.3 Defect from Dielectric Size

The effect of defective rod size on the electrical field profile of silicon dioxide photonic crystal with silicon rod central point defect is shown in Fig. 10.11. The lattice structures of photonic crystal of Fig. 10.11 are the same as in Fig. 10.10D, but there is only one difference, which is the radius of the central silicon rod. In Fig. 10.11A–D, the normalized radius of central silicon rods is from 0.6 to 0.3 with an increment of -0.1 .

The field profiles of Fig. 10.11A–D show that the resonant modes of all have a dipole pattern with a nodal plane in the central point defect of the silicon rods. However, the resonant modes of Fig. 10.11A, C, and D are all localized only in the central silicon rod region. The resonant mode of Fig. 10.11B is partly outside the silicon rod. The confinement efficiency of photonic crystal is shown in Fig. 10.12. For the case of the normalized radius of silicon rod of 0.6, the photonic crystal with silicon rod central point defect achieves the best energy confinement efficiency of 62.7%. For the case of a normalized radius of 0.4, the silicon dioxide photonic crystal achieves the lowest energy confinement efficiency

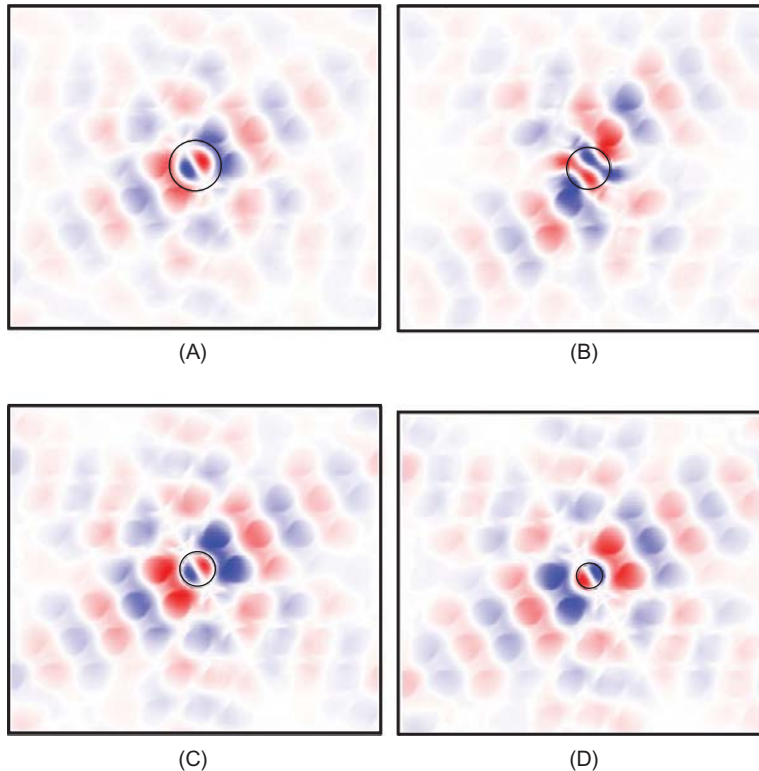
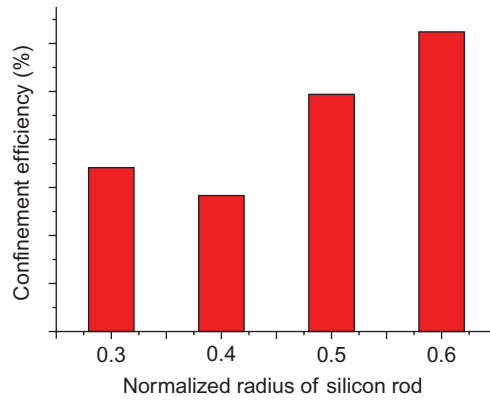
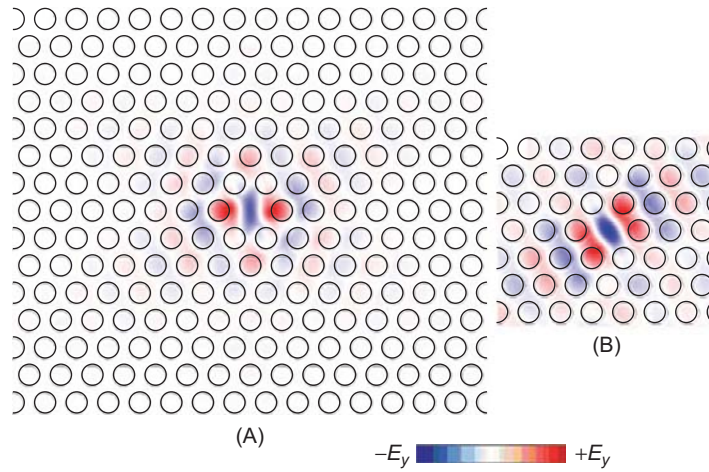


FIGURE 10.11

Field profile of silicon dioxide photonic crystal with point defect of silicon rods of different radii. (A) Normalized radius of silicon rod, 0.6. (B) Normalized radius of silicon rod, 0.5. (C) Normalized radius of silicon rod, 0.4. (D) Normalized radius of silicon rod, 0.3.

**FIGURE 10.12**

The confinement efficiency versus silicon rod radius of silicon dioxide photonic crystal with central defect of silicon rod.

**FIGURE 10.13**

The field profile of silicon dioxide photonic crystal with different lattice arrangements. (A) 15×15 lattices. (B) 7×7 lattices.

of 28.5%. We see that the silicon rod with a point defect with a bigger radius is useful for greater confinement efficiency.

10.5.4 Effect from Lattice Number

The electrical field profile of silicon dioxide photonic crystal with two different lattice arrangements is shown in Fig. 10.13. For Fig. 10.13A, there is a 15 by 15 lattice arrangement, and for Fig. 10.13B, there

is a 7 by 7 lattice arrangement. By our calculation, the energy in the point defect is about 0.258 of the total field energy in the photonic crystal for Fig. 10.13A and B, so we can say the point defect shown in Fig. 10.13A has a much higher energy density, because the total energy in Fig. 10.13A is higher than that in Fig. 10.13B. Intuitively, we can see from the field profile that the field in Fig. 10.13A is more concentrated in the point defect than that in Fig. 10.13B. It is clear that the bigger lattice is more effective in confining incident light, and the field decay from point nanocavity is faster.

10.6 DESIGN AND EXPERIMENTAL RESULTS OF PHOTONIC CRYSTAL CAVITY

10.6.1 Design

We now take the Parylene photonic crystal (air holes in Parylene slab) as an example to explain how photonic crystal can be used in CNT-based IR sensors. Photonic crystal has a photonic band gap, which is similar to the energy band gap of solid state crystals. When the frequency of light falls into the frequency of the photonic band gap of photonic crystal, it behaves as a perfect optical insulator, blocking light propagation, and it traps the corresponding light energy. The point defect breaks the symmetric arrangement of the photonic crystal, and the energy is released at the cavity. As a result, the photonic crystal cavity can perform as a microlens by placing it on top of a CNT-based IR sensor. The IR sensor design with photonic crystal is shown in Fig. 10.14. The two microelectrodes are connected by a CNT, and they are covered by a photonic crystal with the point defect above the CNT and the metal electrodes.

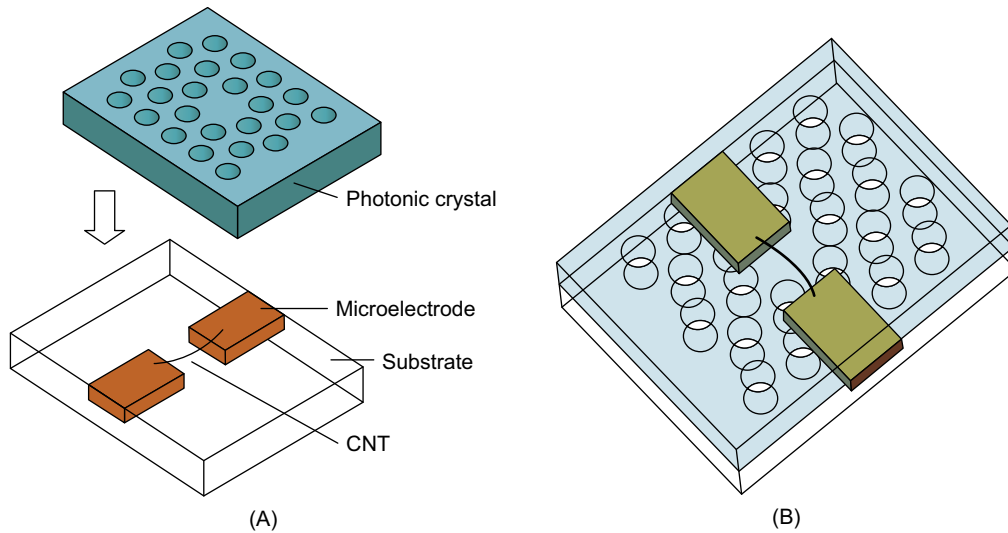


FIGURE 10.14

CNT-based IR sensor with photonic crystal. (A) Separated. (B) Assembled.

10.6.2 Photoresponses of CNT-Based IR Sensors with Photonic Crystal Cavities

A CNT-based IR sensor with Parylene photonic crystal was fabricated and is shown in Fig. 10.15A. In this device, the photonic crystal with air holes in Parylene slab is adopted. The Parylene has a dielectric constant of 3.1, and the air holes have a triangular lattice arrangement. The air hole radius over lattice constant is 0.4, the lattice constant is $1.434\text{ }\mu\text{m}$, and the air hole radius is $0.574\text{ }\mu\text{m}$. The CNT is connected by two microelectrodes, and the dielectric substrate is also Parylene. The CNT and

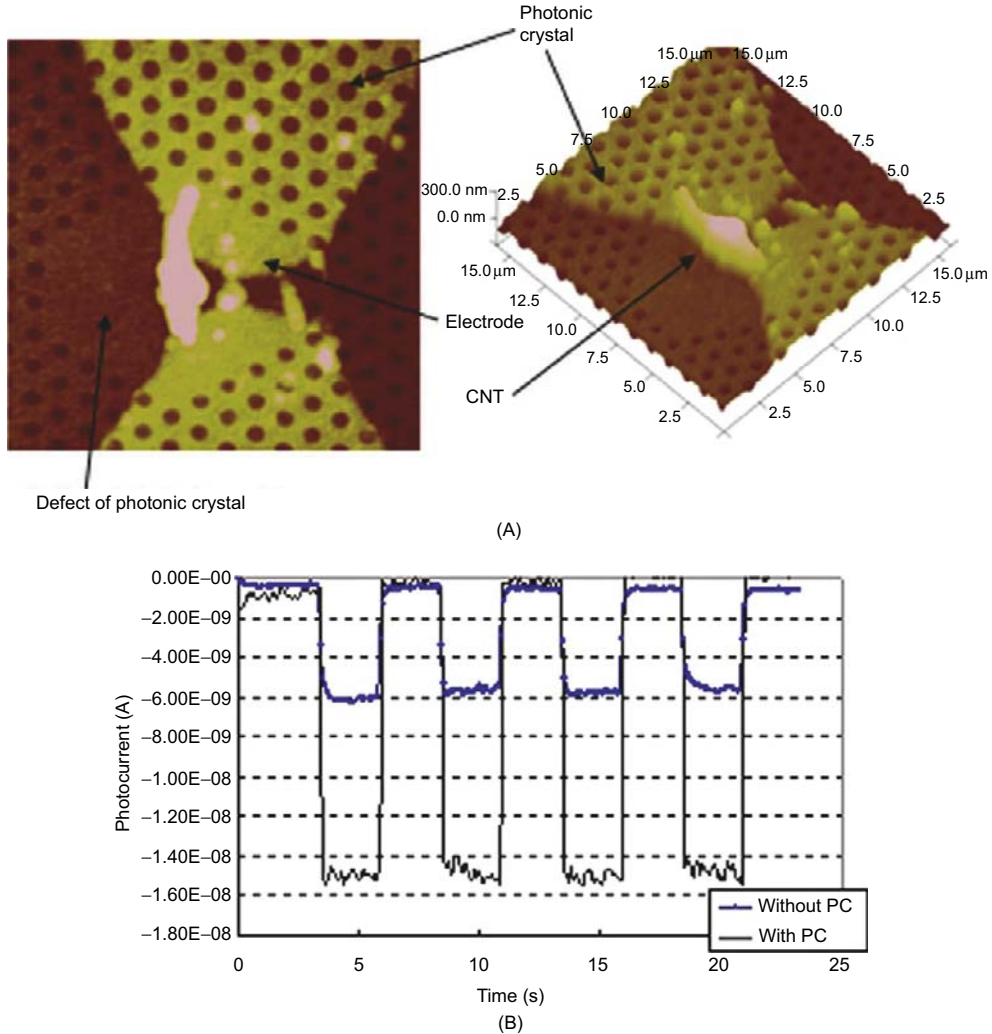


FIGURE 10.15

(A) AFM images of the photonic crystal cavity aligned on top of the CNT-based IR sensor. (B) Temporal photocurrent responses of the sensor with and without photonic crystal structure [20].

two microelectrodes are fixed inside Parylene substrate. The Parylene photonic crystal covers the CNT and the microelectrodes, and the point defect is just above the CNT. The device was illuminated by the incident IR light. The photocurrent response for multiple on/off IR illumination cycles was plotted (Fig. 10.15B). The photocurrent of the IR sensor without Parylene photonic crystal was about 6 nA, and the photocurrent was increased about threefold after adding the Parylene photonic crystal.

10.6.3 Photocurrent Mapping of the CNT-Based IR Sensors with Photonic Crystal Cavities

In the previous section, temporal photoresponses of the CNT-based IR sensor with absence and presence of photonic crystal cavities were measured, showing the photocurrent enhancement after adding photonic cavities. To have a better understanding of the photonic cavity as a microlens, photocurrent mapping of another CNT-based IR sensor with and without a photonic cavity was studied. Figure 10.16 illustrates the setup to obtain photocurrent mapping that indicates photocurrent distribution of the device. Laser spot scans around the CNT-based IR sensor along the scanning path. The first photocurrent mapping of the CNT-based detector was obtained without a photonic cavity. Thereafter, a photonic cavity made from Parylene slab was fabricated by aligning the cavity on top of the detector. The photocurrent distribution of the CNT-based IR sensor with photonic cavity was recorded by the laser scanning around the detector. A three-dimensional (3D) mapping of position-dependent photocurrent was obtained as shown in Fig. 10.17. Photocurrent was less than 1 nA without photonic cavity in a $20 \times 20 \mu\text{m}^2$ area. After the fabrication of the photonic cavity, photocurrent was enhanced to around 5 nA in the same area, indicating that the photonic cavity increases the light intensity approximately five times within the area of the detector. This result shows that photonic crystal cavity functioned as an effective microlens to increase the interaction of CNT-based IR sensors and light.

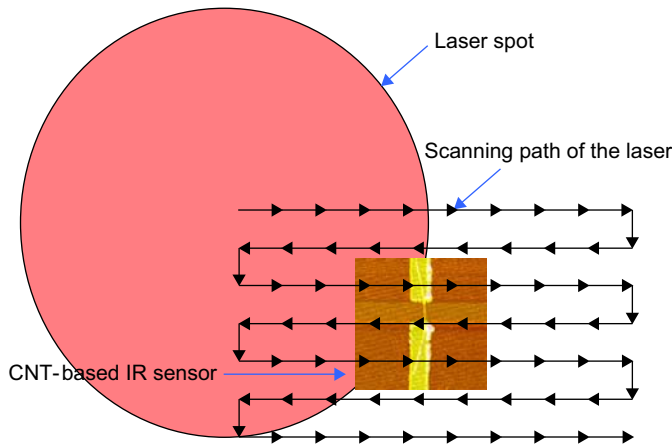
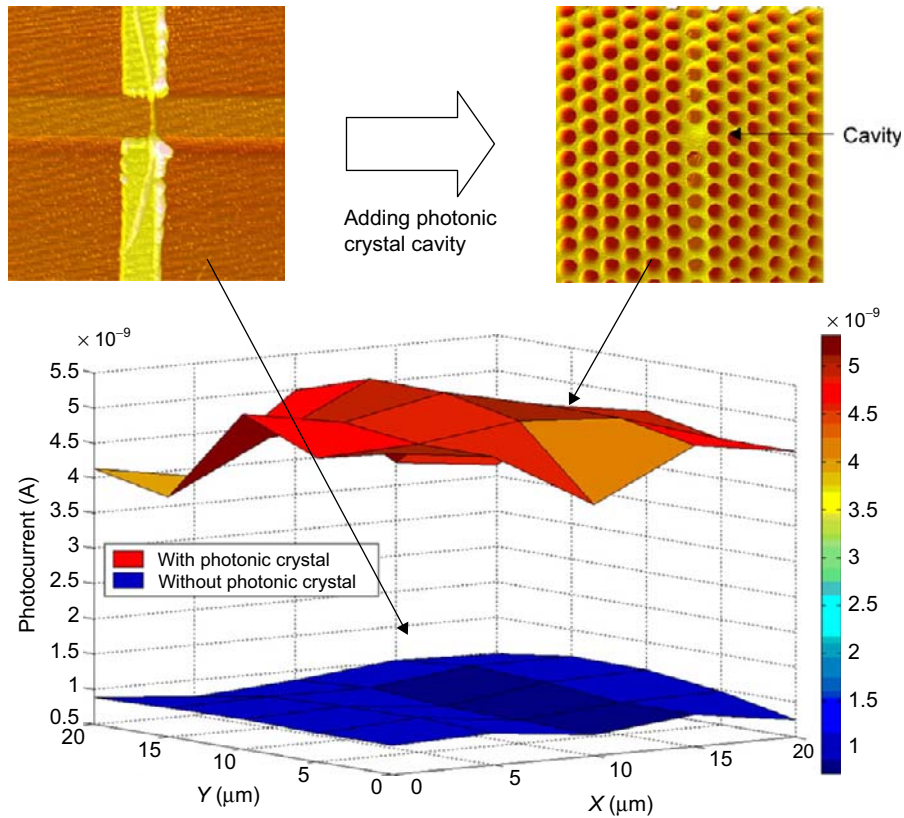


FIGURE 10.16

Experimental setup to obtain scanning photocurrent images.

**FIGURE 10.17**

Photocurrent mapping of the CNT-based IR sensor without and with photonic crystal. The insets are the AFM images of detectors without and with photonic cavity.

10.7 SUMMARY

In this chapter, we have demonstrated photon confinement by photonic crystal for CNT-based infrared sensors. The solution of light transmission in photonic crystal is an eigenvalue problem of electromagnetism. The photonic band gap of photonic crystal is related to the dielectric constant of two different dielectric media, lattice geometry and their sizes, and the TE- and TM-like modes of an incident source. The quantum resonant nanocavity of photonic crystal enables the control of localization of an infrared source in the nanoscale area for performance enhancement of optical sensors. While designing photonic crystal with defective cavity, we should consider (1) the dielectric constant contrast and size of point defect to match with the resonant state of infrared light and (2) the lattice size arrangement to obtain max light energy in the point defect. These factors determine the performance of CNT-based IR sensors with photonic crystal.

References

- [1] E. Yablonovitch. Inhibited spontaneous emission in solid-state physics and electronics. *Phys. Rev. Lett.*, 58: 2059–2062, 1987.
- [2] S. John. Strong localization of photons in certain disordered dielectric superlattices. *Phys. Rev. Lett.*, 58: 2486–2489, 1987.
- [3] S. He and M. Qiu. High-directivity patch antenna with both photonic banggap substrate and photonic bandgap cove. *Micro. Opt. Technol. Lett.*, 30:41–44, 2001.
- [4] Y. Akahane, Y. Tanaka, S. Noda, B.-S. Song, and T. Asano. Transmission and reflection characteristics of in-plane hetero-photonic crystals. *Appl. Phys. Lett.*, 85:4591–4593, 2004.
- [5] S. Noda and A. Chutinan. Waveguides and waveguide bends in two-dimensional photonic crystal slabs. *Phys. Rev. B.*, 62:4488–4492, 2000.
- [6] S. Noda, A. Chutinan, and M. Okano. Wider bandwidth with high transmission through waveguide bends in two-dimensional photonic crystal slabs. *Appl. Phys. Lett.*, 80:1698–1700, 2002.
- [7] T. Asano, H. Takano, and Y. Akahane. In-plane-type channel drop filter in a two-dimensional photonic crystal slab. *Appl. Phys. Lett.*, 84:2226–2228, 2004.
- [8] T. Asano, Y. Akahane, and M. Mochizuki. In-plane-type channel drop filter in a two-dimensional photonic crystal slab. *Appl. Phys. Lett.*, 82:1341–1343, 2003.
- [9] H. Takano, Y. Akahane, and T. Asano. Two-dimensional photonic-crystal-slab channel drop filter with flat-top response. *Opt. Express*, 13:2512–2530, 2005.
- [10] S. Noda, M. Okano, M. Imada, T. Asano, and M. Mochizuki. A channel drop filter using a single defect in a 2-D photonic crystal slab-defect engineering with respect to polarization mode and ratio of emissions from upper and lower sides. *J. Lightwave Technol.*, 21:1370–1376, 2003.
- [11] A. Chutinan, M. Imada, and S. Noda. Channel drop filter using a single defect in a 2-D photonic crystal slab waveguide. *J. Lightwave Technol.*, 20:873–878, 2002.
- [12] B.-S. Song, S. Noda, Y. Akahane, and T. Asano. Investigation of high-Q channel drop filters using donor-type defects in two-dimensional photonic crystal slabs. *Appl. Phys. Lett.*, 83:1512–1514, 2003.
- [13] B.-S. Song, S. Noda, Y. Akahane, and T. Asano. High-Q photonic nanocavity in a two-dimensional photonic crystal. *Nature*, 425:944–947, 2003.
- [14] B.-S. Song, S. Noda, Y. Akahane, and T. Asano. Fine-tuned high-Q photonic-crystal nanocavity. *Opt. Express*, 13:1202–1214, 2005.
- [15] R. Hatsuta, S. Noda, Y. Tanaka, and T. Asano. Investigation of point-defect cavity formed in two-dimensional photonic crystal slab with one-sided dielectric cladding. *Appl. Phys. Lett.*, 88:1–3, 2006.
- [16] T. Asano, S. Noda, T. Uesugi, and B.-S. Song. Investigation of optical nonlinearities in an ultra-high-Q Si nanocavity in a two-dimensional photonic crystal slab. *Opt. Express*, 14:377–386, 2006.
- [17] S. Noda, T. Asano, and B.-S. Song. Ultra-high-Q photonic double-heterostructure nanocavity. *Nat. Mater.*, 4:207–210, 2005.
- [18] S. Noda, A. Sugitatsu, and T. Asano. Line-defect–waveguide laser integrated with a point defect in a two-dimensional photonic crystal slab. *Appl. Phys. Lett.*, 86:1–3, 2005.
- [19] J. N. Winn, R. D. Meade, J. D. Joannopoulos, and S. G. Johnson. *Photonic Crystals Molding the Flow of Light*. Princeton University Press, Princeton and Oxford, 2008.
- [20] C. K. M. Fung, N. Xi, J. Lou, K. W. C. Lai, and H. Chen. Photonic crystal wave guide for non-cryogenic cooled carbon nanotube based middle wave infrared sensors. In *Proc. SPIE 7834*, page 78340L, 2010.

Organic Solar Cells Enhanced by Carbon Nanotubes

Guangyong Li and Liming Liu

*Department of Electrical and Computer Engineering,
University of Pittsburgh, Pennsylvania*

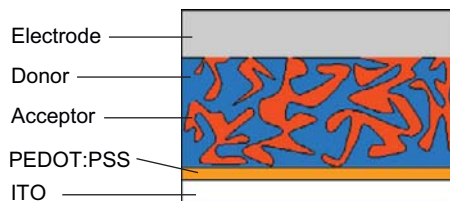
CHAPTER OUTLINE

11.1 Introduction	183
11.2 Application of Carbon Nanotubes in Organic Solar Cells	184
11.3 Fabrication of Carbon Nanotube-Enhanced Organic Solar Cells	185
11.4 Performance Analysis of OSCs Enhanced by CNTs	185
11.4.1 J-V of SWCNTs-Enhanced OSCs Under Illumination	186
11.4.2 J-V of SWCNTs-Enhanced OSCs in Dark	190
11.5 Electrical Role of SWCNTs in OSCs	193
11.6 Summary	197
References	197

11.1 INTRODUCTION

Carbon nanotubes (CNTs) have been widely used in different aspects of photovoltaics (PV). First, CNTs could be a good replacement for indium tin oxide (ITO) as the transparent electrode of solar cell devices [1, 2]; second, the multiple exciton generation (MEG) in CNTs, arising from the quantum-confinement effect in the low-dimensional materials, could increase the internal quantum efficiency and hence the short circuit current in CNT-based solar cells [3]; third, introduction of CNTs in solar cells could increase the carrier mobility because CNTs can provide a ballistic pathway for a photoexcited carrier to transport [4], etc.

Indium tin oxide coated glass is commonly used as a transparent electrode in solar cells. However, ITO glass is not only expensive in fabrication but also mechanically brittle, which increases the fabrication cost and also limits the flexibility of solar cell devices [2, 5]. Moreover, because of the rough surface of ITO glass, it is imperative to coat other materials as a buffer layer (such as PEDOT:PSS) to smooth the ITO surface in thin-film solar cells such as organic solar cells, which makes the fabrication procedure complex [5]. In addition, it has been pointed out that the conductivity of ITO is the major source of series resistance, which decreases the fill factor and thus degrades the performance of solar cells, especially for the application of large-area PVs [6]. Recently, it has been reported that a continuous film of single-walled carbon nanotubes (SWCNTs) with high purity could replace ITO glass as the transparent electrode in solar cell devices [1]. Compared with ITO coated glass by vacuum sputtering,

**FIGURE 11.1**

Organic solar cell with bulk heterojunctions.

it is much easier to fabricate transparent SWCNT electrodes, which is promising in terms of reducing the cost of PV fabrication. Other advantages are the relatively flat surface (10 nm roughness) and mechanical flexibility [2]. The flexibility of CNT electrodes paved the way to fabricate organic solar cells by roll-to-roll painting. However, the relative high sheet resistance (100 Ω) and low transmittance of CNT film in the visible region needs to be further balanced and optimized [7]. Multiple exciton generation (MEG) has been observed in a photodiode made of a single CNT [3]. However, there is still lack of evidence that this can be implemented in an everyday solar cell device.

Over the last ten years, organic solar cells have received much attention because of their numerous advantages. Compared with other solar cells made of inorganic materials such as silicon, organic photovoltaic (OPV) cells are less expensive alternatives because the thin and flexible organic solar cells (OSCs) can be fabricated onto the substrate with different shape by high-throughput, low-cost fabrication methods such as roll-to-roll painting, simple brushing, or ink jet printing [8–10]. Since the discovery of the photoinduced electron transfer from conjugated polymers to fullerene molecules [11], followed by the introduction of bulk heterojunction (BHJ) configuration as shown in Fig. 11.1 [12], OPV cells fabricated by blended conjugated polymer and fullerene have received much attention because of their promising low cost and mechanical flexibility. Unfortunately, wide application of OSCs has been hampered by their short lifetime and low power conversion efficiency. Considering one of the most critical factors to limit power conversion efficiency is the slow mobility arising from carrier hopping and tunneling in the disordered organic materials [13], it is expected that the introduction of CNTs in the active layer of OSCs will be able to optimize carrier transport through the ballistic pathway provided by CNTs [4, 14, 15]. In this chapter, we mainly focus on the utilization of CNTs in the active layer of organic solar cells to increase the carrier mobility.

11.2 APPLICATION OF CARBON NANOTUBES IN ORGANIC SOLAR CELLS

The first investigation of CNTs in OSCs can be traced back to 2002 when Kymakis and Amaratunga blended SWCNTs with poly(3-octylthiophene) (P3OT) to fabricate solar cell devices [4]. They claimed that there are mainly two effects of SWCNTs in the organic photovoltaic device. First, SWCNTs facilitate exciton dissociation at the interface between P3OT and SWCNTs; second, SWCNTs provide a ballistic pathway for the carrier to transport. However, the power conversion efficiency of P3OT/SWCNT OSCs is very low (<0.1%) because there is not enough interface area between P3OT and SWCNTs to sufficiently dissociate excitons due to the insolubility and low concentration of SWCNTs in OSCs (<1%) [16]. To tackle this problem, CNTs were functionalized to increase solubility and

then used to fabricate homogeneous thin-film OSCs with a high concentration of CNTs [17]. However, any improvement is limited, probably due to the increased carrier recombination in the functionalized CNTs.

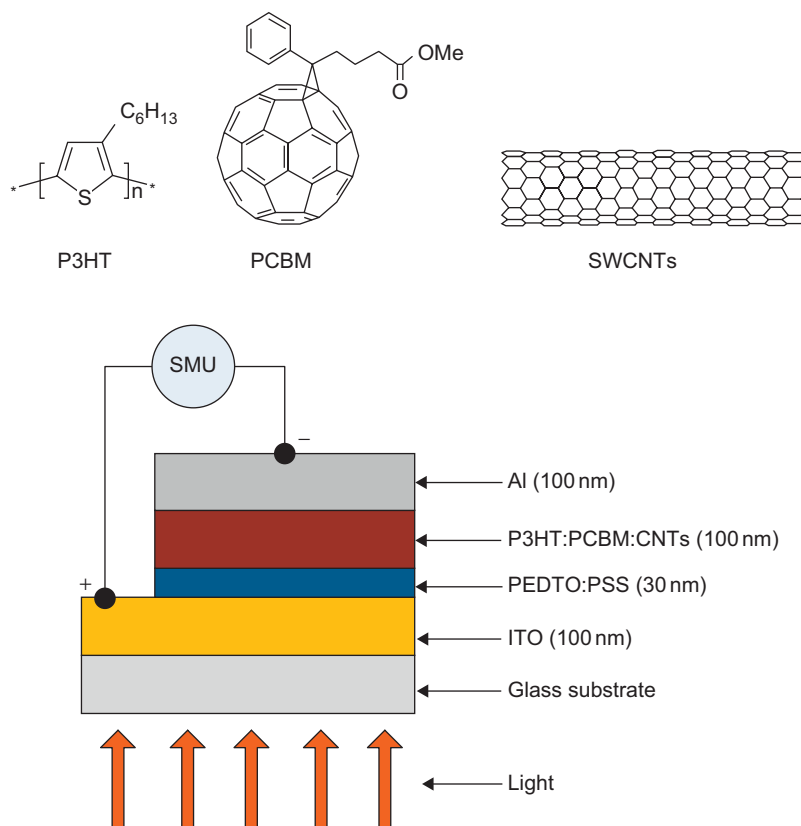
In recent studies, CNTs were introduced in polymer/fullerene organic solar cells because of the inherent problem of conjugated polymer/CNT solar cells (insufficient exciton dissociation). When CNTs are blended with conjugated polymer and fullerene, exciton dissociation is efficient at the polymer/fullerene interface because of the intimate blending between these two materials at the sub-nanometer scale; and meanwhile, free carriers transport through a ballistic pathway provided by CNTs with much lower resistance instead of intrinsic hopping between the disordered organic materials [15]. In this way, it is expected that the introduction of CNTs will improve the performance of polymer/fullerene BHJ OSCs. However, it has been observed that excessive CNTs decrease the performance of OSCs [18, 19]. Unfortunately, there is no convincing explanation for this based on theoretical analysis. In order to further optimize the performance of OSCs incorporated with CNTs, it is imperative to investigate the working mechanism of CNTs in OSCs.

11.3 FABRICATION OF CARBON NANOTUBE-ENHANCED ORGANIC SOLAR CELLS

To investigate the working mechanism of CNTs in OSCs, a series of organic solar cell devices with different CNT concentrations are fabricated. Regioregular poly 3-hexylthiophene (P3HT, conjugated polymer) and 6,6-phenyl C61-butyric acid methyl ester (PCBM, fullerene derivative) were chosen as the prototype of BHJ OSCs because this system has been extensively studied [12, 13]. The schematic structure of SWCNT-incorporated OSCs is shown in Fig. 11.2. SWCNTs (1–2 nm in diameter, 0.5–2 μm in length, as indicated in Fig. 11.3) as received from Sigma were dissolved in chloroform. After sonicated for 2 hours, SWCNTs were introduced into PCBM in chloroform and sonicated for another hour in order to blend SWCNTs and PCBM uniformly. Then P3HT in chloroform was added to the blended PCBM and SWCNT solution. After stirring for 2 hours, the solution was left to settle down in an inert atmosphere for about 48 hours to allow remaining impurities and some bundled SWCNTs to sediment out. Therefore, the actual concentration of SWCNTs should be much lower than the nominal value. The active layer was spun on ITO glass (8 Ω/square) coated with PEDOT:PSS of around 30 nm thickness. Four kinds of devices (50:50 wt.-% P3HT/PCBM) with different weight ratios of SWCNTs to P3HT (nominal 0%, 1%, 3%, and 5%) were fabricated. The thickness of active layers remained the same (100 nm) for all devices, checked by AFM scanning in tapping mode. Finally, aluminum (Al) was coated on top as the cathode by thermal evaporation using a shadow mask at a vacuum of 10^{-6} mbar, the area of the device was 10 mm², which was determined by the overlap between ITO and Al. It should be pointed out that the concentration value is not accurate because after preparing the active layer solution, it is moved to a vacuum box for 2 days in order to deposit insoluble carbon nanotubes on the bottom. The actual device is shown in Fig. 11.4.

11.4 PERFORMANCE ANALYSIS OF OSCs ENHANCED BY CNTs

By analyzing the current-voltage (J-V) characterizations of CNT-enhanced OSCs under both illumination and dark conditions, it can be seen that the carrier mobility in the CNT incorporated devices

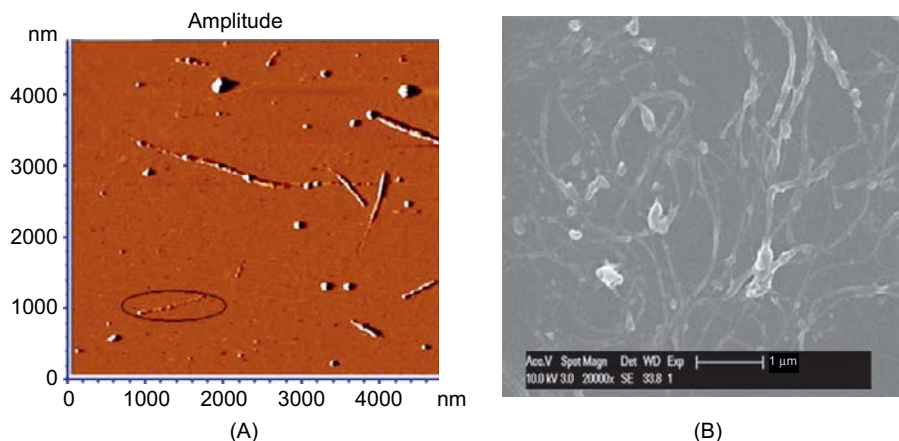
**FIGURE 11.2**

Chemical structure of P3HT, PCBM, and SWCNTs (top) and the schematic of a CNT incorporated photovoltaic device (bottom).

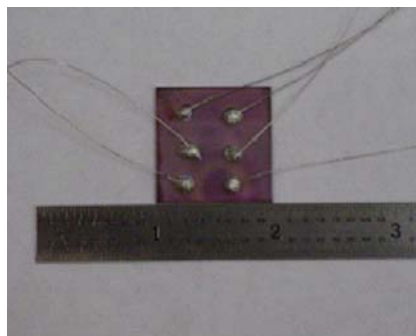
improved. By further analysis, effects of semiconducting and metallic SWCNTs in bulk heterojunction OSCs can also be identified.

11.4.1 J-V of SWCNTs-Enhanced OSCs Under Illumination

The current-voltage (J-V) characteristics of these four devices were measured under the same illumination intensity by a halogen lamp, and the results are shown in Fig. 11.5. The device with nominal 5% SWCNTs is short-circuited as the actual concentration of SWCNTs exceeds the percolation threshold. Therefore, the J-V curve for the device with nominal 5% SWCNTs is not shown in Fig. 11.5 and the performance of this device will not be further analyzed. It is observed that the short circuit current (J_{sc}) for the device with nominal 1% SWCNTs increased around 30% compared with the device without SWCNTs. However, for the device with nominal 3% SWCNTs, J_{sc} , the open circuit voltage (Voc) as well as the fill factor are all decreased. In order to further optimize the performance of OSCs

**FIGURE 11.3**

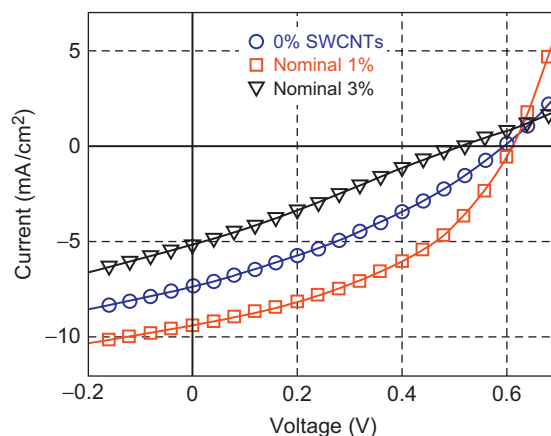
SWCNTs investigated by (A) AFM imaging and (B) SEM imaging. Some SWCNTs have a diameter of about 1–2 nm as shown in the black ellipse. The diameter of other SWCNTs is about 5 nm (bundled SWCNT).

**FIGURE 11.4**

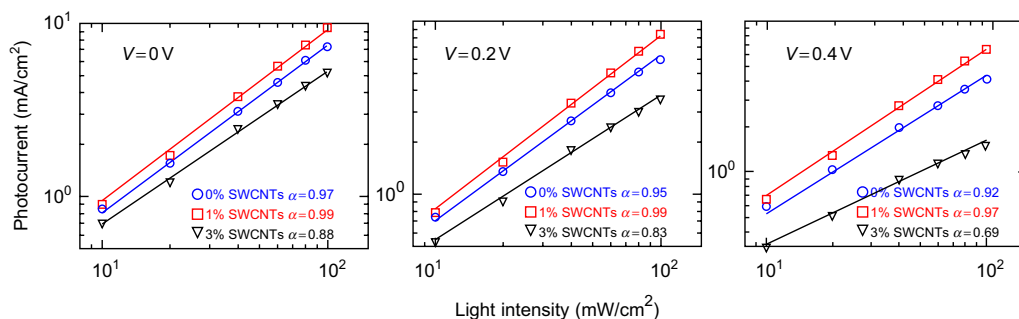
Real-life solar cell device.

incorporating SWCNTs, it is imperative to explore the underlying reason for the improved performance of the device with 1% SWCNTs as well as the decreased performance of the device with 3% SWCNTs.

Both theoretical analysis and numerical simulation have proved that [20], for the situation with non-negligible recombination loss (fill factor is less than 50%) as in Fig. 11.5, the fact that the constant α in $J_{ph} = I^\alpha$ (J_{ph} is photocurrent and I is the illumination intensity) equals 1 indicates that monomolecular recombination is dominant, while α decreases monotonically from unity with the increase of bimolecular recombination. For the details of intensity-dependent photocurrent, please refer to [20]. The dependence of photocurrent on light intensity measured by subtracting dark current from the respective current–voltage curves at three different applied voltages (0, 0.2, and 0.4 V) is presented in

**FIGURE 11.5**

J-V characteristics of OSCs with same thickness (100 nm) and different concentrations of SWCNTs under illumination intensity of 100 mW/cm².

**FIGURE 11.6**

Intensity dependence of the photocurrent for three devices at different applied voltages.

Fig. 11.6. For devices with 0% and nominal 1% SWCNTs, a value of α close to one at any bias voltage means that the bimolecular recombination for these two devices is negligible. But for the device with nominal 3% SWCNTs, α values are 0.88, 0.83, and 0.69 at 0, 0.2, and 0.4 V, respectively, indicating the strong bimolecular recombination in the device with a high concentration of SWCNTs.

In general, SWCNTs are grown as mixed bundles of semiconducting and metallic tubes according to different chirality [21]. Even though only about one-third are metallic, the detrimental effect of metallic SWCNTs in the active layer of OSCs is not negligible. Due to the presence of metallic SWCNTs, photoexcited free electrons in the PCBM phase and holes in the P3HT phase tend to recombine directly in metallic SWCNTs in the form of bimolecular recombination, instead of being totally extracted by external circuit as shown in the schematic diagram in Fig. 11.7. Therefore, it is reasonable to conclude that the degraded performance of the device with high concentration of SWCNTs (nominal 3%) is attributed to the abundance of metallic SWCNTs in the active layer.

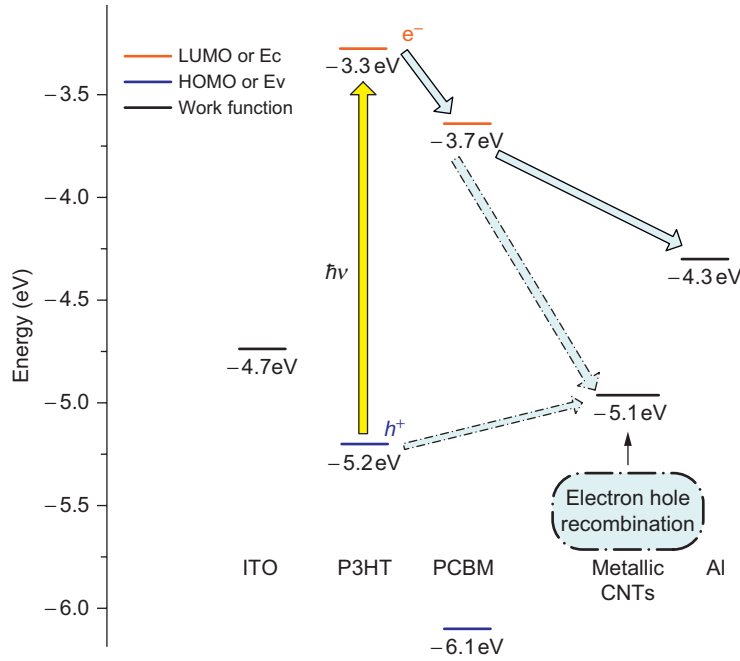


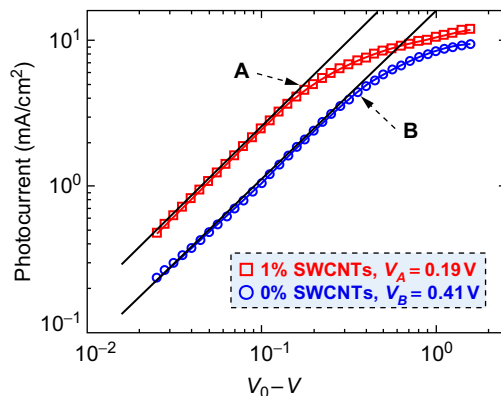
FIGURE 11.7

Schematic energy diagram to show that the presence of metallic SWCNTs causes serious bimolecular recombination of photoexcited electrons from PCBM and holes from P3HT.

To investigate the effect of semiconducting SWCNTs in OSCs, carrier mobility is studied under illumination. Figure 11.8 presents the reverse bias dependence of photocurrent for devices with 0% and nominal 1% SWCNTs under illumination intensity of 100 mw/cm² (only these two devices are analyzed because both of them have negligible bimolecular recombination as observed in Fig. 11.6, which makes them comparable) is plotted as a function of the effective applied voltage across the devices, where is flat band voltage, at which $J_{ph} = 0$. It is necessary to mention that the value of V_0 is not the same as V_{oc} , because the internal electric field at V_{oc} is not exactly zero such that drift current (proportional to electric field) can nullify the diffusion current. As shown in Fig. 11.8, at small effective potential, implying a small electric field in the device, the photocurrent is extraction limited and linearly increases with the electric field as described by [15]:

$$J_{ph} = qG(\mu_e\tau_e + \mu_h\tau_h) \frac{V_0 - V}{L} \quad (11.1)$$

where q is the electron charge, G is the generation rate of electron hole pairs, $\mu_e(\mu_h)$ is electron (hole) mobility, and $\tau_e(\tau_h)$ is the lifetime of electron (hole). When the electric field increases to a certain value at which carrier drift length, $\omega = \mu\tau E$, exceeds the device thickness L , all the photoexcited carriers are extracted by the external circuit. The photocurrent is then photoexcitation limited and saturated as $J_{ph} = qGL$ [22, 23]. At the turning point from linear to saturation region, carrier drift length ω is equal

**FIGURE 11.8**

J_{ph} of devices with 0% and 1% SWCNTs as a function of effective applied voltage at illumination intensity of 100 mW/cm^2 .

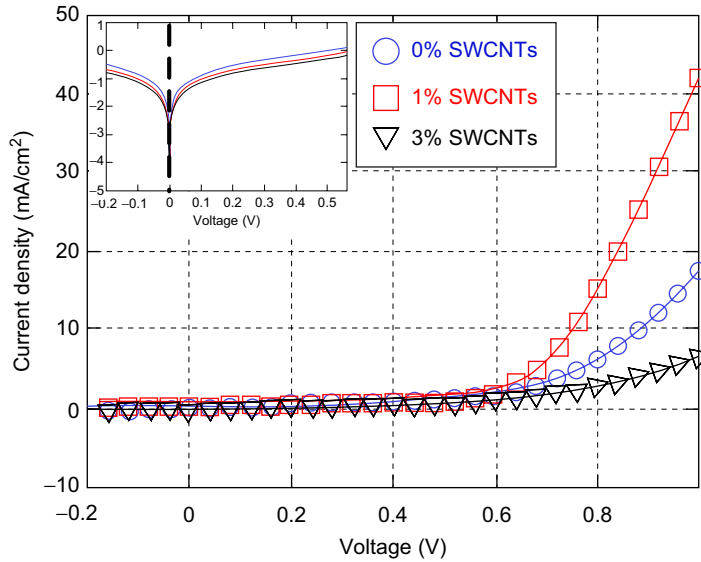
to the thickness of active layer L [23], i.e., $L = \omega = \mu\tau E$. Therefore, mobility can be expressed as:

$$\mu = \frac{L}{\tau E} = \frac{L^2}{\tau(V_0 - V)} \quad (11.2)$$

It is reasonable to assume that the carrier life time τ is the same for devices with 0% and nominal 1% SWCNTs, because the results of intensity-dependent photocurrent given above (Fig. 11.5) indicate that bimolecular recombination is negligible for both devices. The fabrication process guarantees that the thickness of the active layer L is also the same, which has been confirmed by AFM scanning. According to Eq. (11.2), for fixed τ and L , carrier mobility μ is reversely proportional to $(V_0 - V)$ at the turning point. As shown in Fig. 11.8, compared with a high voltage of turning point ($V_B = 0.41 \text{ V}$) of the device without SWCNTs, a lower voltage of turning point ($V_A = 0.19 \text{ V}$) of the device with nominal 1% SWCNTs shows that average carrier mobility is doubled ($\mu_A/\mu_B = V_B/V_A = 0.41/0.19 = 2.16$) after the introduction of SWCNTs into the active layer. Therefore, semiconducting SWCNTs are able to improve carrier mobility in OSCs through their ballistic pathways.

11.4.2 J-V of SWCNTs-Enhanced OSCs in Dark

The different effects of semiconducting and metallic SWCNTs have been studied through illumination J-V characterization. In the following, dark J-V measurements will be performed to further investigate SWCNTs-enhanced OSCs. Under illumination, carriers arise from photoexcitation; while for dark measurement, carriers arise from injection through the external circuit and the device behaves as a diode. For both situations, there are electrons and holes in the active layer which transport between two electrodes. Due to the presence of metallic SWCNTs in the active layer, the electron and hole will recombine in the metallic SWCNTs in the form of bimolecular recombination, whether the electrons and holes come from photoexcitation (under illumination) or injection (in the dark).

**FIGURE 11.9**

Dark J-V characteristics of OSCs with different concentration of SWCNTs. The inset is the logarithmic scale of J-V to show that all curves go through ($V = 0, J = 0$) point, which indicates that the capacitance effect is negligible in our solar cell devices.

Table 11.1 Fitting Parameters of Dark J-V Curves Based on Diode Equation

Concentration of SWCNTs (%)	0	1	3
Ideality factor n	3.2	3.09	6.51
Saturation current J_s (mA/cm ²)	3.7×10^{-4}	1.0×10^{-3}	2.47×10^{-6}

Figure 11.9 shows J-V characteristics in the dark for three devices with nominal 0%, 1%, and 3% SWCNTs. All devices show typical diode behavior without light illumination. The inset shows J-V on a logarithmic scale, which demonstrates all the devices go through the point of origin ($V = 0, J = 0$) and hence the capacitance effect due to SWCNTs is negligible. For the device with nominal 3% SWCNTs, the forward current is decreased compared with the other two devices shown because electron and hole, injected from the external circuit, will recombine together in the metallic SWCNTs in the form of bimolecular recombination. This observation for dark conditions is coincident with the results from J-V characteristics under illumination: excessive metallic SWCNTs cause serious bimolecular recombination, which decreases the performance of OSCs.

Dark J-V data then were fitted to the ideal diode equation, to determine the ideality factor n and saturation current density J_s , in which q represents unit electronic charge, V is the forward bias voltage, and kT is thermal energy. According to Ref. [24], carrier recombination results in the increase of ideality factor n . The fitting results at room temperature ($kT = 25.6$ meV) are shown in Table 11.1.

The ideality factors of the 0% SWCNT device ($n = 3.2$) and 1% SWCNT device ($n = 3.09$) are almost the same, which indicates that the recombination of carriers for these two devices is comparable. This is in coincidence with the illumination investigation in Fig. 11.6 (α is almost the same for devices with 0% and 1% SWCNTs, indicating the bimolecular recombination is comparable in these two devices). However, for the device with 3% SWCNTs, the ideality factor is much larger (twofold higher than that of devices with 0% and 1% SWCNTs). Therefore, the decreased forward current of the 3% SWCNT device is attributed to the increased ideality factor, which arises from the increased carrier recombination in metallic SWCNTs.

After investigation of ideal factor n , let us focus on the saturation current J_s . According to [25], the saturation current J_s is

$$J_s = \frac{qD_p p_{n0}}{L_p} + \frac{qD_n n_{p0}}{L_n} \quad (11.3)$$

in which L_p and L_n are diffusion length, which can be expressed as

$$L_{p(n)} = \sqrt{D_{p(n)} \tau_{p(n)}} \quad (11.4)$$

where $D_{p(n)}$ is the diffusion coefficient according to the Einstein relation

$$D_{p(n)} = \frac{kT}{q} \mu_{p(n)} \quad (11.5)$$

According to Eqs (11.3–11.5), the saturation current density J_s is related to carrier mobility $\mu_{p(n)}$ such that high mobility results in high saturation current density. According to Table 11.1, with increasing concentration of SWCNTs, J_s increases as well because the introduction of SWCNTs improves the carrier mobility. However, the device with 3% SWCNTs (highest mobility) did not have the best performance because even though the carrier mobility is increased, the carrier recombination is also increased significantly (high ideality factor) and the carrier recombination dominates the performance of the device with 3% SWCNTs.

The bimolecular recombination is negligible for both devices without SWCNTs and with nominal 1% SWCNTs, so dark J-V curves for these two devices are comparable. Because the presence of semiconducting SWCNTs provides ballistic pathways which have lower resistance compared with carrier hopping in the device without SWCNTs [15], introduction of SWCNTs with low concentration (nominal 1%) into the device improved the electrical conductivity of the active layer as demonstrated by the enhanced forward current under the same applied voltage compared with the device without SWCNTs.

In summary, the introduction of SWCNTs with small weight-ratio can improve the performance of BHJ OSCs as we expected. However, it has also been observed that excessive SWCNTs decreased the performance of OSCs. The different effects of semiconducting SWCNTs and metallic SWCNTs have been investigated by J-V characterizations both under illumination and in the dark. It is found that on one hand, the presence of semiconducting SWCNTs provides additional ballistic pathways for carriers to be extracted directly instead of slow hopping between disordered organic materials, which improves the performance of OSCs; on the other hand, metallic SWCNTs cause the electrons and holes to recombine, which decreases the efficiency of PV devices. This demonstrates the urgent need to enrich bulk SWCNTs with semiconducting SWCNTs extracted from either the fabrication or postfabrication processes.

11.5 ELECTRICAL ROLE OF SWCNTs IN OSCs

Introducing carbon nanotubes into BHJ OSCs has shown the ability to improve power conversion efficiency because carbon nanotubes are able to provide ballistic pathways for carriers to be transported instead of slow hopping and tunneling in disordered organic materials. However, the fundamental question, whether carbon nanotubes work as donors (hole rich) or acceptors (electron rich) in BHJ OSCs, remains controversial in the literature [18]. Some have assumed that nanotubes work as acceptor materials and photoexcited electrons transported into nanotubes [4]; while others have claimed that nanotubes are donor materials and become hole-rich after photoexcitation [24]; until now, direct measurement has not been available to support either side. Therefore, to further optimize the performance of the device, there is a critical need to fully understand the electrical role of SWCNTs in OSCs.

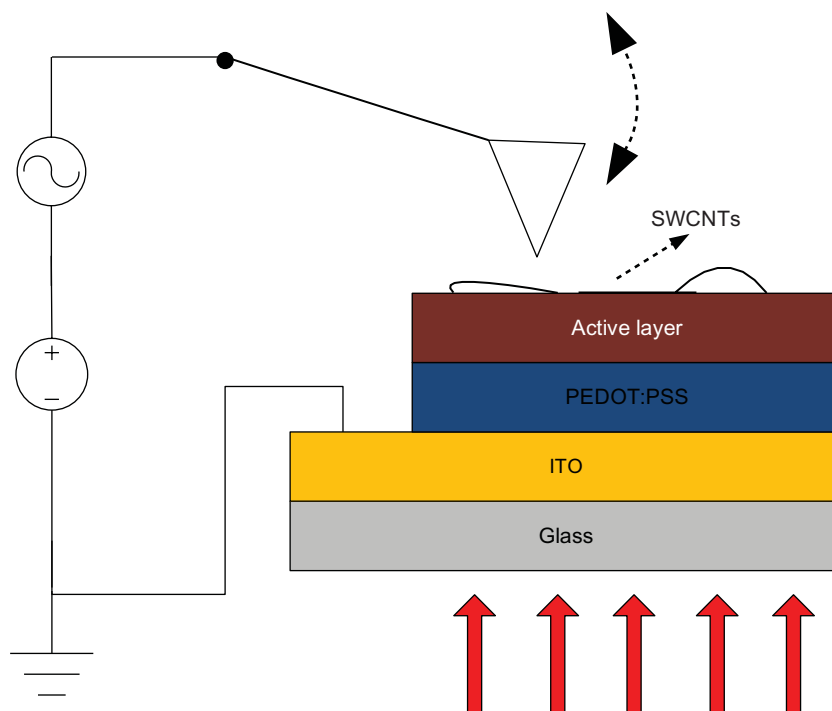
Even though many researchers still believe that SWCNTs are acceptors, two observations on the macroscopic scale suggest that SWCNTs are indeed donors, which transport holes in P3HT/PCBM OSCs.

The first observation is based on the experiment results in [26]. When nanotubes are placed between the active layer (P3HT/PCBM) and the cathode (Al), the performance degrades according to J-V illumination measurement, while the efficiency increases when SWCNTs are coated between PEDOT:PSS and the active layer. From this observation, it is assumed that carbon nanotubes are not acceptor materials. (Aluminum as the cathode, which is connected with SWCNTs, extracts electron.)

The second observation is based on the unbalanced carrier mobility in OSCs. For P3HT/PCBM BHJ OSCs, the electron mobility is about one order higher than the hole mobility [27, 28]. If nanotubes were acceptor materials, the electron mobility would increase further and the difference between electron and hole mobility would also increase, which would result in unbalanced carrier transport [27]. Unbalanced carrier transport is detrimental for carrier extraction in PVs, especially for OSCs due to the low carrier mobility. For OSCs, if one kind of carriers has much larger mobility compared with the other, the slower carriers cannot be fully extracted as quickly as fast carriers, which will result in space-charge limited photocurrent [23]. The space-charge limited photocurrent usually degrades the performance of PVs. However, Fig. 11.5 demonstrates that the fill factor (FF) and J_{sc} of a device with 0% SWCNTs are about 32.7% and 7.6 mA/cm² respectively while for a device with nominal 1% SWCNTs, FF is 42.4% and J_s is 9.8 mA (V_{oc} is almost the same). If carbon nanotubes work as acceptor materials, the unbalanced charge transport cannot result in the improvement of the performance; instead, the performance should decrease. It should be pointed out that the decreased performance of a nominal 3% SWCNT device is due to the carrier recombination in the metallic SWCNTs not the unbalanced charge transport.

The analysis above indicates that SWCNTs in OSCs might be donor materials to transport photoexcited holes. However, the argument so far is based only on macroscopic evidence. There is a lack of direct observation on the microscopic level. Therefore, in the following, Kelvin probe force microscopy (KPFM) will be employed to locally investigate the electrical role of SWCNTs in P3HT/PCBM BHJ solar cells. The schematic diagram for KPFM investigation is shown in Fig. 11.10. For a comprehensive review of KPFM on organic thin film, please refer to [29].

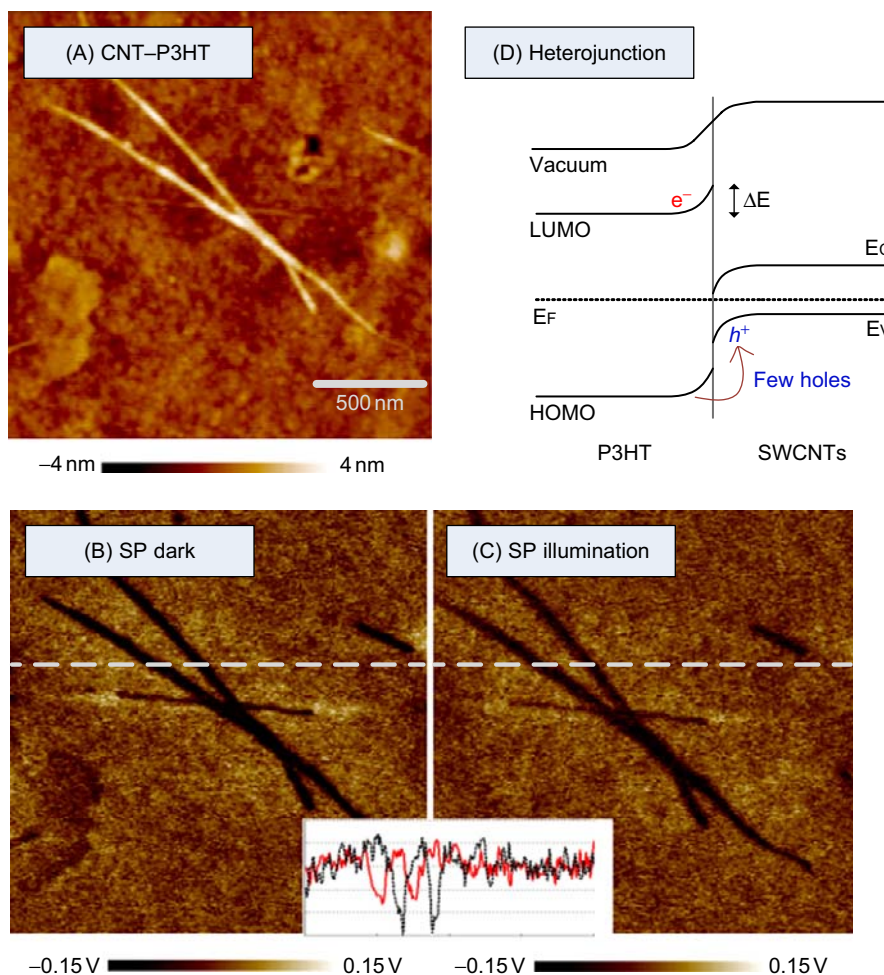
In this study, KPFM was applied to investigate SWCNTs first on top of P3HT film as shown in Fig. 11.11. The fabrication procedure followed the method in Section 11.3 except that aluminum was not coated but SWCNTs were coated on top of P3HT to expose both P3HT and SWCNTs to the AFM tip as in Fig. 11.10. The topography in the dark (Fig. 11.11A) and under illumination (not shown

**FIGURE 11.10**

Schematic of KPFM of SWCNTs on top of the active layer.

here) is almost the same except for some thermal drift. The sample was illuminated with intensity of 90 mW/cm^2 , calibrated by a thermal power meter. The surface potential (SP) images are shown in Fig. 11.11B (in the dark) and Fig. 11.11C (under illumination). The inset in Fig. 11.11B and C indicates the SP values of cross sections both in the dark and under illumination. Figure 11.11D is the band schematic diagram to show the heterojunction between P3HT and SWCNTs. Comparing Fig. 11.11B and C, SP contrast between SWCNTs and P3HT slightly decreased from 0.14 V in the dark to 0.08 V under illumination. The decreased SP contrast under illumination indicates the transport of photoexcited holes from the active layer (P3HT) to SWCNTs, which can be explained with the help of the schematic band diagram (type I heterojunction) in Fig. 11.11D. In the dark, SP of P3HT is higher than that of SWCNTs, which implies the direction of local electric field (E) is from P3HT to SWCNTs (refer to the relative vacuum level). As indicated by the arrow in Fig. 11.11D, holes can move to SWCNTs after light absorption by P3HT, which is energy favored; while electrons tend to remain in P3HT due to the energy barrier in the conduction band. The reduced SP contrast under illumination is attributed to the induced electric field by both photoexcited electrons in P3HT and holes in SWCNTs, which has a direction opposite to that of the local electric field in the dark. KPFM study of SWCNTs on top of P3HT clearly verifies that SWCNTs work as donors in P3HT/SWCNTs OSCs.

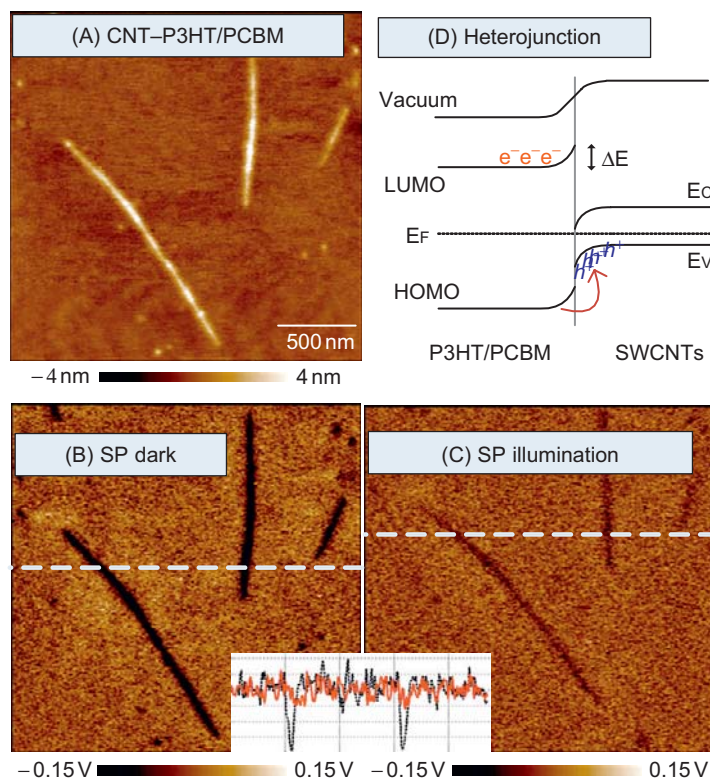
In order to explore the electrical role of SWCNTs in P3HT/PCBM/SWCNTs OSCs, KPFM was again used to study SWCNTs on top of P3HT/PCBM blended film. Figure 11.12A shows the

**FIGURE 11.11**

(A) Topography of SWCNTs on top of P3HT in the dark. (B) SP image in the dark. (C) SP image under illumination. (D) Band schematic diagram of type I heterojunction between P3HT and SWCNTs. The inset shows the SP values of the cross section indicated by the dashed line in SP images. The position of SWCNTs shifts under illumination compared with in the dark because of thermal drift.

topography of SWCNTs on top of P3HT/PCBM blended film in the dark. The SP images in the dark (Fig. 11.12B) and under illumination (Fig. 11.12C) as well as their SP values of the cross section (inset) indicate that SP contrast between SWCNTs and P3HT/PCBM under illumination almost disappeared. Specifically, SP contrast decreases from 0.19 V in the dark to 0.04 V under illumination. Similarly, we can conclude that SWCNTs work as donors in P3HT/PCBM/SWCNTs OSCs.

Compared with SWCNTs on P3HT in Fig. 11.11, the decrease of SP contrast between SWCNTs and P3HT/PCBM under illumination is more significant because more holes transport from the active

**FIGURE 11.12**

(A) Topography of SWCNTs on top of P3HT/PCBM in the dark. (B) SP image in the dark. (C) SP image under illumination. (D) SP values of the cross section. (E) Band schematic diagram of type I heterojunction between P3HT/PCBM and SWCNTs.

layer (P3HT/PCBM) to SWCNTs and as a result, the induced electric field by photoexcited electrons and holes is much stronger, making the band flatten [30]. The heterojunction band schematic diagram in Fig. 11.12D indicates photoexcited charge transport. When SWCNTs were coated on top of P3HT/PCBM blending, photoexcited excitons are effectively separated to free carriers at the interface between blended P3HT and PCBM due to BHJ configuration [13], although for SWCNTs on top of P3HT, only a small amount of excitons located at the interface between P3HT and SWCNTs can be separated to free carriers considering the exciton diffusion length is only about 10 nm. For SWCNTs on top of P3HT film, insufficient holes' transport cannot change the SP contrast between P3HT and SWCNTs (Fig. 11.11D) as much as for SWCNTs on top of P3HT/PCBM film (Fig. 11.12D), which can explain that the low efficiency of conjugate polymer/SWCNTs solar cells is attributed to insufficient exciton dissociation. The comparison between Figs 11.11 and 11.12 also demonstrates that BHJ is very important for photoexcited excitons to be separated to free electrons and holes, as discussed earlier.

The KPFM study on both P3HT/SWCNTs and P3HT/PCBM/SWCNTs demonstrates that photoexcited holes are present in SWCNTs and thus SWCNTs work as donors, which is coincident with the macroscopic observation that introducing SWCNTs in P3HT/PCBM BHJ solar cells is able to increase power conversion efficiency by increasing hole mobility.

11.6 SUMMARY

In this chapter, we discussed carbon nanotube-enhanced organic solar cells with bulk heterojunctions. It has been found that the performance of organic BHJ solar cells can be significantly increased by introducing carbon nanotubes into the active layer. The KPFM study suggests that the increased performance is due to increased hole mobility as carbon nanotubes are donor materials. However, it has also been found that excessive carbon nanotubes degrade the performance of OSCs because of the increased bimolecular recombination due to the existence of metallic CNTs. Therefore, it is critical to find new ways to fabricate pure semiconductor CNTs for enhancing the performance of OSCs with bulk heterojunctions.

References

- [1] Z. C. Wu, Z. H. Chen, X. Du, J. M. Logan, J. Sippel, M. Nikolou, K. Kamaras, J. R. Reynolds, D. B. Tanner, A. F. Hebard, and A. G. Rinzler. Transparent, conductive carbon nanotube films. *Science*, 305:1273–1276, 2004.
- [2] W. R. Michael, A. T. Mark, D. M. Michael, P. Hans-Jurgen, D. Gilles, S. Niyazi Serdar, H. Liangbing, and G. George. Organic solar cells with carbon nanotube network electrodes. *Appl. Phys. Lett.*, 88:233506, 2006.
- [3] N. M. Gabor, Z. H. Zhong, K. Bosnick, J. Park, and P. L. McEuen. Extremely efficient multiple electron-hole pair generation in carbon nanotube photodiodes. *Science*, 325:1367–1371, 2009.
- [4] E. Kymakis and G. A. J. Amaratunga. Single-wall carbon nanotube/conjugated polymer photovoltaic devices. *Appl. Phys. Lett.*, 80:112–114, 2002.
- [5] A. Du Pasquier, H. E. Unalan, A. Kanwal, S. Miller, and M. Chhowalla. Conducting and transparent single-wall carbon nanotube electrodes for polymer-fullerene solar cells. *Appl. Phys. Lett.*, 87:203511, 2005.
- [6] J. G. Xue, S. Uchida, B. P. Rand, and S. R. Forrest. 4.2 % efficient organic photovoltaic cells with low series resistances. *Appl. Phys. Lett.*, 84:3013–3015, 2004.
- [7] Y. X. Zhou, L. B. Hu, and G. Gruner. A method of printing carbon nanotube thin films. *Appl. Phys. Lett.*, 88:123109, 2006.
- [8] V. Doojin, K. Seok-Soon, J. Jang, O. Seung-Hwan, N. Seok-In, K. Juhwan, and K. Dong-Yu. Fabrication of organic bulk heterojunction solar cells by a spray deposition method for low-cost power generation. *Appl. Phys. Lett.*, 91:081102, 2007.
- [9] J. Bharathan and Y. Yang. Polymer electroluminescent devices processed by inkjet printing: I. Polymer light-emitting logo. *Appl. Phys. Lett.*, 72:2660–2662, 1998.
- [10] H. H. Lee, K. Lee, W. L. Ma, X. Gong, J. Y. Kim, S. H. Kim, and A. J. Heeger. New architecture for high-efficiency polymer photovoltaic cells using solution-based titanium oxide as an optical spacer. *Adv. Mater.*, 18:572–576, 2006.
- [11] N. S. Sariciftci, L. Smilowitz, A. J. Heeger, and F. Wudl. Photoinduced electron-transfer from a conducting polymer to buckminsterfullerene. *Science*, 258:1474–1476, 1992.

- [12] G. Yu, J. Gao, J. C. Hummelen, F. Wudl, and A. J. Heeger. Polymer photovoltaic cells: enhanced efficiencies via a network of internal donor-acceptor heterojunctions. *Science*, 270:1789–1791, 1995.
- [13] C. J. Brabec, N. S. Sariciftci, and J. C. Hummelen. Plastic solar cells. *Adv. Funct. Mater.*, 11:15–26, 2001.
- [14] C. Li, Y. H. Chen, Y. B. Wang, Z. Iqbal, M. Chhowalla, and S. Mitra. A fullerene-single wall carbon nanotube complex for polymer bulk heterojunction photovoltaic cells. *J. Mater. Chem.*, 17:2406–2411, 2007.
- [15] L. Liu, W. E. Stanchina, and G. Li. Effects of semiconducting and metallic single-walled carbon nanotubes on performance of bulk heterojunction organic solar cells. *Appl. Phys. Lett.*, 94:233309, 2009.
- [16] E. Kymakis and G. A. J. Amarunga. Carbon nanotubes as electron acceptors in polymeric photovoltaics. *Rev. Adv. Mater. Sci.*, 10:300–305, 2005.
- [17] B. Pradhan, S. K. Batabyal, and A. J. Pal. Functionalized carbon nanotubes in donor/acceptor-type photovoltaic devices. *Appl. Phys. Lett.*, 88:093106, 2006.
- [18] S. Berson, R. de Bettignies, S. Bailly, S. Guillerez, and B. Jusselme. Elaboration of P3HT/CNT/PCBM composites for organic photovoltaic cells. *Adv. Funct. Mater.*, 17:3363–3370, 2007.
- [19] E. Kymakis, N. Kornilios, and E. Koudoumas. Carbon nanotube doping of P3HT:PCBM photovoltaic devices. *J. Phys. D-Appl. Phys.*, 41:165110–165114, 2008.
- [20] L. Liu and G. Li. Investigation of recombination loss in organic solar cells by simulating intensity-dependent current–voltage measurements. *Sol. Energy Mater. Sol. Cells*, 95: 2557–2563, 2011.
- [21] M. S. Strano, C. A. Dyke, M. L. Usrey, P. W. Barone, M. J. Allen, H. Shan, C. Kittrell, R. H. Hauge, J. M. Tour, and R. E. Smalley. Electronic structure control of single-walled carbon nanotube functionalization. *Science*, 301:1519–1522, 2003.
- [22] M. G. Alvin and R. Albert. Double extraction of uniformly generated electron-hole pairs from insulators with noninjecting contacts. *J. Appl. Phys.*, 42:2823–2830, 1971.
- [23] V. D. Mihailetschi, J. Wildeman, and P. W. M. Blom. Space-charge limited photocurrent. *Phys. Rev. Lett.*, 94: 126602, 2005.
- [24] M.-C. Wu, Y.-Y. Lin, S. Chen, H.-C. Liao, Y.-J. Wu, C.-W. Chen, Y.-F. Chen, and W.-F. Su. Enhancing light absorption and carrier transport of P3HT by doping multi-wall carbon nanotubes. *Chem. Phys. Lett.*, 468: 64–68, 2009.
- [25] S. M. Sze. *Physics of Semiconductor Devices*. Wiley, London, 1981.
- [26] S. Chaudhary, H. Lu, A. M. Muller, C. J. Bardeen, and M. Ozkan. Hierarchical placement and associated optoelectronic impact of carbon nanotubes in polymer-fullerene solar cells. *Nano Lett.*, 7:1973–1979, 2007.
- [27] G. Li, V. Shrotriya, J. Huang, Y. Yao, T. Moriarty, K. Emery, and Y. Yang. High-efficiency solution processable polymer photovoltaic cells by self-organization of polymer blends. *Nat. Mater.*, 4:864–868, 2005.
- [28] V. D. Mihailetschi, H. X. Xie, B. de Boer, L. J. A. Koster, and P. W. M. Blom. Charge transport and photocurrent generation in poly(3-hexylthiophene):methanofullerene bulk-heterojunction solar cells. *Adv. Funct. Mater.*, 16(5):699–708, 2006.
- [29] V. Palermo, M. Palma, and P. Samor. Electronic characterization of organic thin films by Kelvin probe force microscopy. *Adv. Mater.*, 18:145–164, 2006.
- [30] J. Chun-Sheng, H. R. Moutinho, J. F. Geisz, D. J. Friedman, and M. M. Al-Jassim. Direct measurement of electrical potentials in GaInP2 solar cells. *Appl. Phys. Lett.*, 81:2569–2571, 2002.

Development of Optical Sensors Using Graphene

12

King Wai Chiu Lai*, Ning Xi*, Carmen Kar Man Fung†, and Hongzhi Chen*

*Department of Electrical and Computer Engineering, Michigan State University, Michigan

†Hong Kong Productivity Council, Hong Kong

CHAPTER OUTLINE

12.1 Introduction	199
12.2 Fabrication of Graphene-Based Devices	200
12.3 Dielectrophoretic Effect on Different Graphene Flakes	202
12.4 Electrical and Optical Behaviors of Various Graphene-Based Devices	203
12.5 Summary	206
References	206

12.1 INTRODUCTION

In recent years, graphene has been the subject of increasing attention because it has a great potential for use in nano-optoelectronics. Graphene is another novel nanomaterial and researchers have found a strong photoresponse near the graphene–metal interfaces [1–3]. In addition graphene-based photodetectors can potentially be used for high-speed optical communications [4, 5]. The Nobel Prize in Physics 2010 was awarded to A. Geim and K. Novoselov for their findings of exceptional properties of graphene. Graphene has a single atomic layer with carbon atoms arranged in a hexagonal honeycomb lattice. It is a fundamental building block for graphitic materials of all other dimensionalities. Graphene has excellent properties such as high charge-carrier mobility (about 100-fold compared with silicon) [6–8], unique band structure [9], and zero-bandgap [10].

Nowadays, the most common fabrication technique used for graphene-based nanostructures can be divided into two steps: first, electron beam lithography (EBL) is employed to pattern metal electrodes on a graphene [11]. Then the resulting structures are etched by an oxygen plasma [12–15]. However, plasma etching induces localization of charge carriers in graphene [9, 12] and changes its electronic properties [13]. The disadvantages of EBL include its high cost and its low throughput. EBL machines are expensive and they also require substantial maintenance. Moreover, the patterning process takes a long time to complete because the electron beam is required to scan samples pixel by pixel.

In order to develop a reliable manufacturing process, we utilize a novel approach to select and fabricate graphene-based nanodevices via dielectrophoresis (DEP) and atomic force microscopic (AFM)

nanomanipulation. We have previously discussed employing this method to manipulate and assemble carbon nanotubes (CNTs) between microelectrodes in [Chapters 2 and 4](#). In this chapter, a systematic study of the dielectrophoretic effect in graphene will be discussed.

Graphene flakes exposed to a nonuniform electric field are expected to behave differently based on the difference in conductivity of the graphene. A quantitative study is performed for optimizing the nanoassembly process of graphene flakes by controlling the frequency of the applied field. We demonstrate that DEP can be used to attract few-layer graphene (FLG) and multi-layer graphene (MLG) toward metal microelectrodes. We show that the dielectrophoretic effect in different graphene flakes is frequency-dependent. In addition, we prove that the yield of successful connection of graphene flakes between electrodes can be significantly increased after the AFM-assisted nanomanipulation process. This technique offers several advantages; that is, the AFM nanomanipulation can be integrated into local anodic oxidation to provide more robust fabrication functionality such as nanopatterning on graphene [16, 17]. Unlike plasma etching, DEP can be employed to select for different graphene flakes without modifying their properties. In addition, the graphene sample is found to be sensitive to infrared (IR) signal.

Results show that the graphene is a zero-bandgap material, which is consistent with many other studies. In addition, the infrared response of the graphene after the assembly process is investigated. We show that the graphene exhibits photocurrent to infrared light at room temperature. The experimental results agree well with the theoretical prediction. The present study offers a new method to classify graphene and opens up the possibility of developing high-fidelity practical nanodevices.

12.2 FABRICATION OF GRAPHENE-BASED DEVICES

Some of the previous fabrication techniques were employed to fabricate graphene-based devices. Initially, graphene was produced by repeatedly peeling highly oriented pyrolytic graphite (HOPG) (SPI-1, Structure Probe, Inc) off. This process is called mechanical exfoliation [11]. The graphene sample was then dispersed and suspended in alcohol medium after ultrasonic treatment for 5 minutes. Afterward, the graphene flakes were brought into contact with prefabricated microelectrodes by DEP and AFM nanomanipulation as illustrated in [Fig. 12.1](#). These processes are similar to the methods discussed in [Chapters 2 and 4](#). The graphene suspension was transferred to the microelectrodes by our DEP deposition system [18]. When an AC voltage was applied across the microelectrodes, an electric field was generated and then a DEP force was induced on the graphene flakes. It was found that the DEP force depends on the frequency of the applied field and the conductivity of the graphene flakes. Detailed theoretical analysis and experimental results will be discussed in the next section. AFM was then used to move the graphene to connect between the microelectrodes. The interlayer distance of bulk graphite is estimated to be 0.335 nm [11] and so single-layer graphene is rarely found. The thickness of the few-layer graphene flake was estimated from the AFM image as shown in [Fig. 12.2](#). Based on the AFM height information, Raman spectroscopy was used to determine the number of layers of graphene [19, 20]. By using this method, few-layer graphene (FLG) (3-layers or less and with thickness of less than 2 nm) and multi-layer graphene (4-layers or more) were identified as shown in [Fig. 12.3](#).

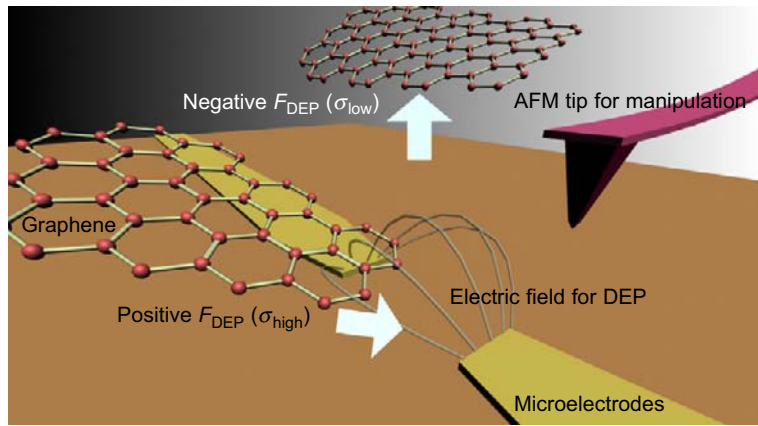
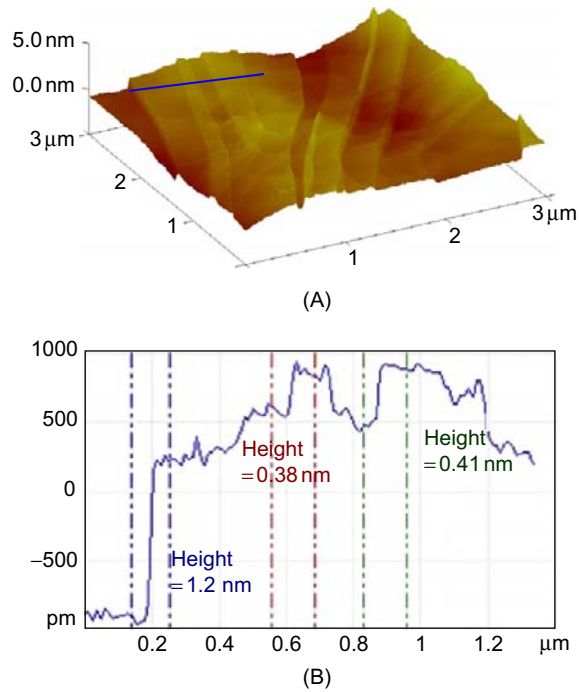
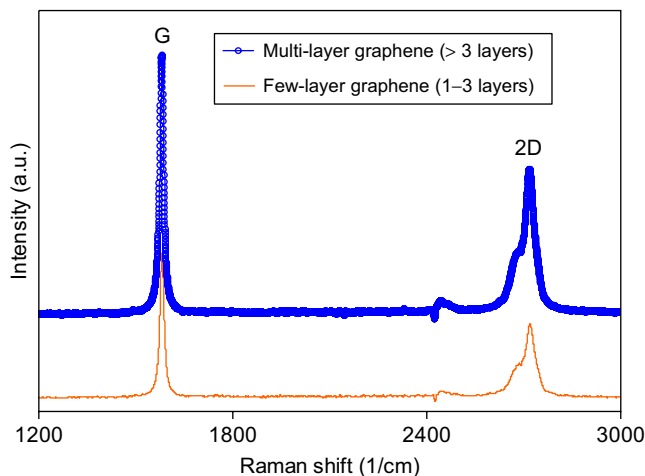
**FIGURE 12.1**

Illustration of nanomanipulation for graphene-based devices.

**FIGURE 12.2**

(A) Atomic force microscopic image of few-layer graphene. (B) Cross-section height data for the line in (A).

**FIGURE 12.3**

Raman spectra (532-nm laser wavelength, Kaiser Optical Systems HoloProbe Raman Spectrograph) measured from few-layer graphene and multi-layer graphene. The number of layers is estimated based on the peak intensities, peak positions and ratio of the G-band and 2D-band peaks. ([21], © [2010] IEEE)

12.3 DIELECTROPHORETIC EFFECT ON DIFFERENT GRAPHENE FLAKES

As stated in Chapter 2, DEP is a phenomenon in which a force is induced to move an object when it is under a nonuniform electric field [22]. An object is polarized when it is subjected to an electric field. The movement of the object depends on its polarizability with respect to the surrounding medium. When the permittivity of the object is greater than that of the medium, a net dipole is induced parallel to the electric field in the object and therefore the object is attracted to regions of stronger electric field.

To provide a better understanding of the DEP manipulation on graphene flakes, we performed theoretical analysis of the DEP force on graphene flakes with different electrical conductivity values. The conductivity of the graphene flake varies with the size and structure. For the analysis presented here, three different conductivity values ($\sigma_{\text{low}} = 10 \mu\text{S/m}$, $\sigma_{\text{mid}} = 500 \mu\text{S/m}$, and $\sigma_{\text{high}} = 10000 \mu\text{S/m}$) were chosen. The conductivity was estimated based on the resistivity measurement [11, 23]. Let $\varepsilon_p = 2.4\varepsilon_o$ denote the permittivity of the graphene flake [24], where the permittivity of free space $\varepsilon_o = 8.854188 \times 10^{-12} \text{ F/m}$. The permittivity ε_m and electrical conductivity σ_m of the alcohol medium is $20 \varepsilon_o$ and $0.13 \mu\text{S/m}$, respectively. By putting these parameters into Eq. (2.4), the Clausius–Mossotti factor (CM factor K) can be found as shown in Fig. 12.4. When the DEP force is positive ($\text{Re}(K) > 0$), the object moves toward the regions of stronger electric field. When the DEP force is negative ($\text{Re}(K) < 0$), the object moves away from regions of stronger electric field. In Fig. 12.4, a transition from positive to negative DEP occurs at a frequency set point. The frequency set point depends on the conductivity of the graphene flake. The graphene flake with low conductivity σ_{low} exhibits negative DEP at a lower frequency. DEP force can be employed to select high electrical conductivity of graphene flakes by applying AC voltage in a high-frequency range ($> 1 \text{ MHz}$) because graphene flakes with low electrical conductivity undergo negative DEP forces at the same range.

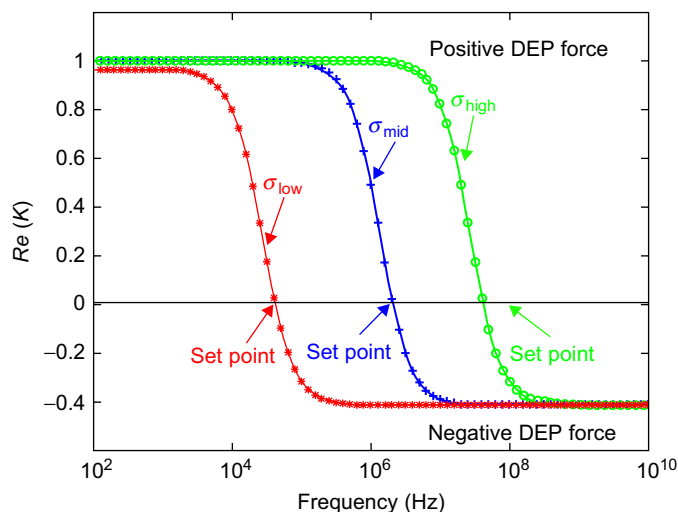


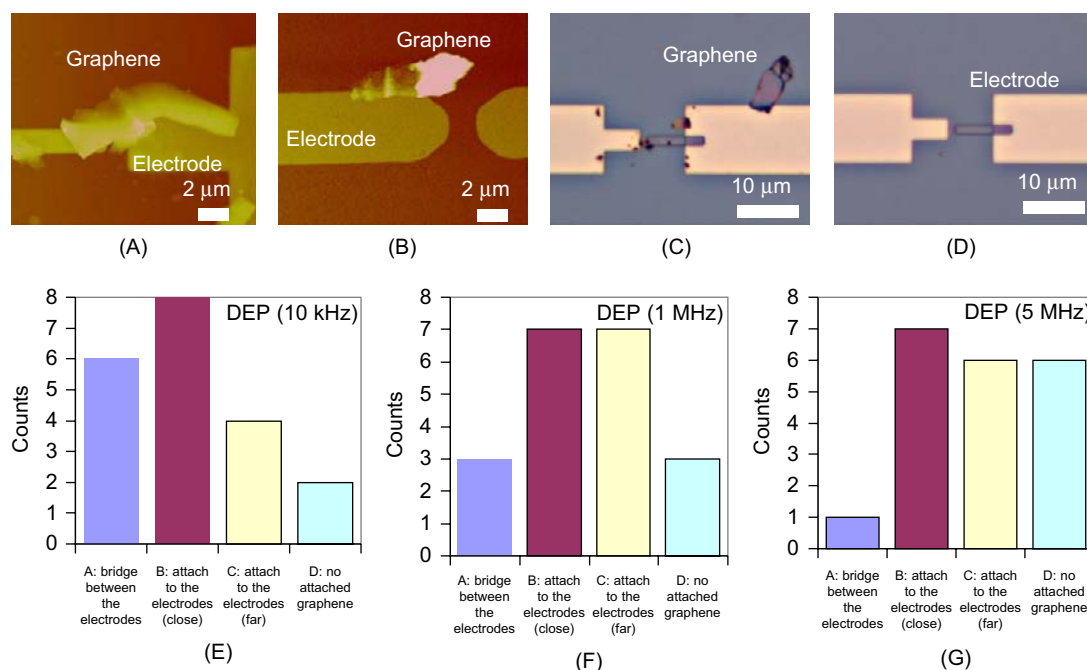
FIGURE 12.4

Plot of $Re(K)$ indicated positive and negative DEP forces on different graphene flakes.

Dielectrophoretic experiments on graphene flake formation were performed. During the experiment, an AC voltage was applied and a droplet (1 μ l) of the graphene suspension was deposited onto the metal microelectrodes. As shown in Fig. 12.5, the connection of the graphene flake between the microelectrodes can be classified into the following four cases: (1) the flakes bridged between microelectrode gaps (Fig. 12.5A); (2) the flakes were attracted to the end of one microelectrode but not connected to the other electrode ($<10\mu\text{m}$ from the center of each electrode) (Fig. 12.5B). In this case, the AFM nanorobotic system was then used to move the graphene flake such that the flake can completely bridge between electrodes; (3) the flake was placed $>10\mu\text{m}$ away from the center of each electrode (Fig. 12.5C); and (4) no flake was attracted to the microelectrodes (Fig. 12.5D). We carried out statistical analysis of DEP manipulation experiments of graphene flakes as a function of three different frequencies of the applied electric field. Histograms of these data are shown in Fig. 12.5E–G and the results show that the number of graphene flakes connecting the gaps between electrodes (Fig. 12.5A and B) depends on the applied frequency. A large number of electrode pairs are bridged by graphene flakes at low frequency (10 kHz) (Fig. 12.5E) while the number decreases as the frequency value is increased to 5 MHz (Fig. 12.5G). As predicted in the theoretical study, the DEP force depends on the applied frequency. The positive DEP occurs and most of the graphene flakes are attracted to the electrode at low frequency (10 kHz). This implies that the experimental results are in good agreement with our calculations.

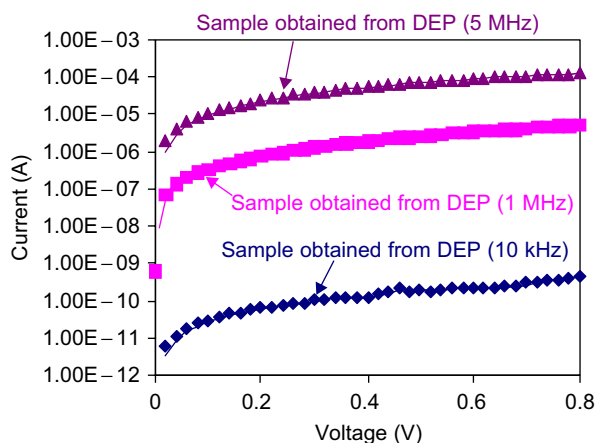
12.4 ELECTRICAL AND OPTICAL BEHAVIORS OF VARIOUS GRAPHENE-BASED DEVICES

To confirm the connection of the graphene flake between the microelectrodes, we conducted the current–voltage (I–V) measurement for each graphene sample that was seen to be bridged between

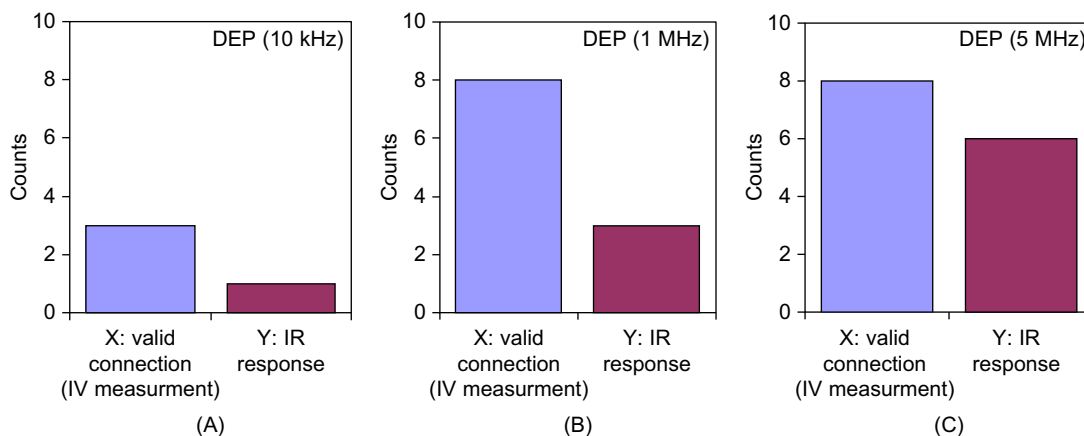
**FIGURE 12.5**

Four possible cases can be observed after DEP manipulation. (A) A flake is attracted and bridges the microelectrodes directly. (B) A flake is attracted to the microelectrodes with less than $10\ \mu\text{m}$ apart from the center of the microelectrodes. (C) A flake is attracted to the end of one microelectrode but not connected to the other electrode ($>10\ \mu\text{m}$ from the center of each electrode). (D) No flake is attracted to the microelectrodes. (E–G) Histograms of DEP manipulation result on graphene flakes for different frequencies of the applied electric field.

the electrodes (Fig. 12.5A and B). The I–V curves were obtained for each applied frequency (10 kHz, 1 MHz and 5 MHz) as shown in Fig. 12.6. The connection of the graphene between the microelectrodes is considered to be successful if the I–V curve can be obtained. The conductivity of the graphene flake after connecting between the electrodes can also be found from the I–V curve. The distribution of successful connections for three different frequency values is shown in Fig. 12.7A–C. As the high-conductivity graphene flake can be attracted to the electrodes by choosing the high-frequency electric field, our data show that the highest yield is obtained at high-frequency values (1 and 5 MHz). After studying the frequency dependence of the DEP of graphene flakes, we next investigated the IR sensing capability of graphene flakes. The graphene flake was irradiated periodically by an incident IR laser source (UH5-30G-830-PV, World Star Tech; optical power: 30 mW; wavelength: $830\ \mu\text{m}$) as illustrated in Fig. 12.8A. The experiment was conducted at room temperature and the photocurrent was measured as shown in Fig. 12.8B. The device exhibits fast response to IR and the photocurrent is proportional to the input voltage of the laser source (Fig. 12.8C). The IR experiment was conducted for

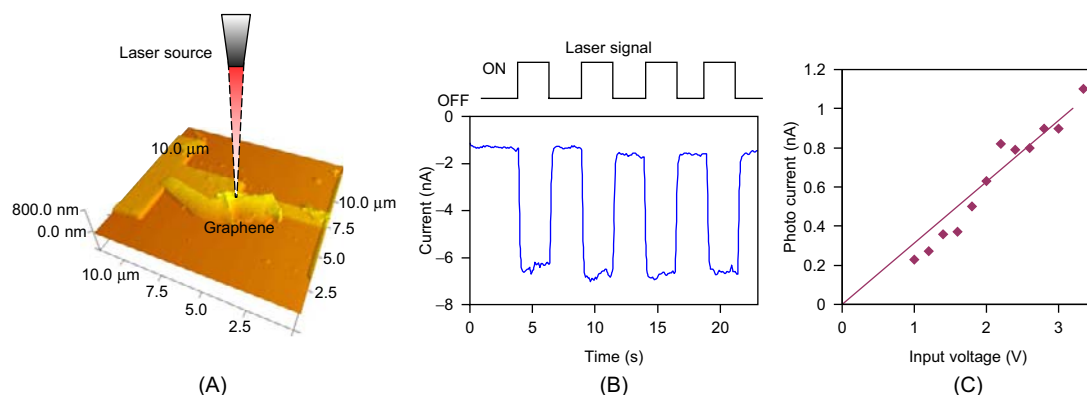
**FIGURE 12.6**

I-V characteristics of the graphene flakes which were obtained by using different frequencies of the applied electric field.

**FIGURE 12.7**

Histograms of valid electrical connection and IR response of the graphene samples prepared by corresponding DEP frequencies.

each sample after the graphene flake bridged the microelectrodes at three different frequency values. The data for each applied frequency are summarized in Fig. 12.7A–C. When the graphene flake was bridged between the microelectrodes at the high-frequency value (5 MHz) after the DEP manipulation, a large number of samples exhibited response to IR. This implies that the sensing capability of the graphene strongly depends on the conductivity of the graphene.

**FIGURE 12.8**

(A) AFM image of a graphene flake with an illustration of a laser source. (B) Temporal photoresponses of the graphene sample. (C) The relationship between the generated photocurrent from the graphene sample and the input voltage of the laser source.

12.5 SUMMARY

In conclusion, we have demonstrated a new approach to manipulate and classify the graphene flake by choosing an optimal frequency of the applied electric field. We correlated the conductivity of the graphene flake with the frequency of the applied electric field. The theoretical prediction agrees well with the experimental results. With the ability to select high-conductivity graphene, the experimental result shows that graphene is a promising candidate for IR detection. The present study provides a systematic and reproducible method of selecting and separating high-conductivity graphene, which can also be used to manufacture novel IR nano sensors.

References

- [1] E. J. H. Lee, K. Balasubramania, R. T. Weitz, M. Burghard, and K. Kern. Contact and edge effects in graphene devices. *Nat. Nanotechnol.*, 3:486–490, 2008.
- [2] F. Xia, Th. Mueller, R. Golizadeh-Mojarad, M. Freitag, Y.-M. Lin, J. Tsang, V. Perebeinos, and P. Avouris. Photocurrent imaging and efficient photon detection in a graphene transistor. *Nano Lett.*, 9(3):1039–1044, 2009.
- [3] J. Park, Y. H. Ahn, and C. Ruiz-Vargas. Imaging of photocurrent generation and collection in single-layer graphene. *Nano Lett.*, 9(5):1742–1746, 2009. PMID: 19326919.
- [4] T. Mueller, F. Xia, and P. Avouris. Photocurrent imaging and efficient photon detection in a graphene transistor. *Nat. Photonics*, 9:1039–1044, 2009.
- [5] F. Xia, T. Mueller, Y. Lin, A. Valdes-Garcia, and P. Avouris. Ultrafast graphene photodetector. *Nat. Nanotechnol.*, 4:839–843, 2009.
- [6] K. S. Novoselov, A. K. Geim, S. V. Morozov, D. Jiang, M. I. Katsnelson, I. V. Grigorieva, S. V. Dubonos, and A. A. Firsov. Two-dimensional gas of massless Dirac fermions in graphene. *Nature*, 438:197–201, 2005.

- [7] Y. Zhang, Y.-W. Tan, H. L. Stormer, and P. Kim. Experimental observation of the quantum Hall effect and Berry's phase in graphene. *Nature*, 201-205:438, 2005.
- [8] K. I. Bolotin, K. J. Sikes, Z. Jiang, M. Klima, G. Fudenberg, J. Hone, P. Kim, and H. L. Stormer. Ultrahigh electron mobility in suspended graphene. *Solid State Commun.*, 146(9-10):351-355, 2008.
- [9] S. V. Morozov, K. S. Novoselov, M. I. Katsnelson, F. Schedin, D. C. Elias, J. A. Jaszczak, and A. K. Geim. Giant intrinsic carrier mobilities in graphene and its bilayer. *Phys. Rev. Lett.*, 100(1):016602, 2008.
- [10] I. Meric, M. Y. Han, A. F. Young, B. Ozyilmaz, P. Kim, and K. L. Shepard. Current saturation in zero-bandgap, topgated graphene field-effect transistors. *Nat. Nanotechnol.*, 3:654-659, 2008.
- [11] K. S. Novoselov, A. K. Geim, S. V. Morozov, D. Jiang, Y. Zhang, S. V. Dubonos, I. V. Grigorieva, and A. A. Firsov. Electric field effect in atomically thin carbon films. *Science*, 306(5696):666-669, 2004.
- [12] S. Russo, J. B. Oostinga, D. Wehenkel, H. B. Heersche, S. S. Sobhani, L. M. K. Vandersypen, and A. F. Morpurgo. Observation of Aharonov-Bohm conductance oscillations in a graphene ring. *Phys. Rev. B*, 77(8):085413, 2008.
- [13] M. Y. Han, B. Ozyilmaz, Y. Zhang, and P. Kim. Energy band gap engineering of graphene nanoribbons. *Phys. Rev. Lett.*, 98:206805, 2007.
- [14] J. S. Bunch, Y. Yaish, M. Brink, K. Bolotin, and P. L. McEuen. Coulomb oscillations and Hall effect in quasi-2D graphite quantum dots. *Nano Lett.*, 5(2):287-290, 2005.
- [15] C. Stampfer, J. Güttinger, F. Molitor, D. Graf, T. Ihn, and K. Ensslin. Tunable Coulomb blockade in nanostructured graphene. *Appl. Phys. Lett.*, 92:012102, 2008.
- [16] L. Weng, L. Zhang, Y. P. Chen, and L. P. Rokhinson. Atomic force microscope local oxidation nanolithography of graphene. *Appl. Phys. Lett.*, 93:093107, 2008.
- [17] S. Masubuchi, M. Ono, K. Yoshida, K. Hirakawa, and T. Machida. Fabrication of graphene nanoribbon by local anodic oxidation lithography using atomic force microscope. *Appl. Phys. Lett.*, 94:82107, 2009.
- [18] K. W. C. Lai, N. Xi, C. K. M. Fung, J. Zhang, H. Chen, Y. Luo, and U. C. Wejinya. Automated nanomanufacturing system to assemble carbon nanotube based devices. *Int. J. Rob. Res.*, 28(4):523-536, 2009.
- [19] K. S. Kim, Y. Zhao, H. Jang, S. Y. Lee, J. M. Kim, K. S. Kim, J. Ahn, P. Kim, J. Choi, and B. H. Hong. Large-scale pattern growth of graphene films for stretchable transparent electrodes. *Nature*, 457:706-710, 2009.
- [20] Y. Wang, X. Chen, Y. Zhong, F. Zhu, and K. P. Loh. Large area, continuous, few-layered graphene as anodes in organic photovoltaic devices. *Appl. Phys. Lett.*, 95:63302, 2009.
- [21] K. W. C. Lai, C. K. M. Fung, H. Chen, R. Yang, B. Song, and N. Xi. Manipulation and assembly methods for graphene based nano devices. In *10th IEEE Conference on Nanotechnology IEEE-NANO 2010*, pages 623-626, Aug. 2010.
- [22] H. Morgan and N. G. Green. *AC Electrokinetics: Colloids and Nanoparticles*. Research Studies Press Ltd, Hertfordshire, UK, 2003.
- [23] Y.-W. Tan, Y. Zhang, K. Bolotin, Y. Zhao, S. Adam, E. H. Hwang, S. Das Sarma, H. L. Stormer, and P. Kim. Measurement of scattering rate and minimum conductivity in graphene. *Phys. Rev. Lett.*, 99(24):246803, 2007.
- [24] M. C. Lemme, T. J. Echtermeyer, M. Baus, and H. Kurz. A graphene field-effect device. *IEEE Electron Device Lett.*, 28(4):282-284, 2007.

Indium Antimonide (InSb) Nanowire-Based Photodetectors

13

Hongzhi Chen*, King Wai Chiu Lai*, Xuhui Sun†, Ning Xi*, and Meyya Meyyappan**

*Department of Electrical and Computer Engineering, Michigan State University, Michigan

†Institute of Functional Nano and Soft Materials (FUNSOM), Soochow University, P.R. China

**Center for Nanotechnology, NASA Ames Research Center, California

CHAPTER OUTLINE

13.1 Introduction	209
13.2 Growth of InSb Nanowires	214
13.3 Photodetectors Using Single InSb Nanowires	216
13.3.1 Symmetric InSb Nanowire Photodetectors	216
13.3.2 Asymmetric InSb Nanowire Photodetectors	218
13.4 Summary	223
References	223

13.1 INTRODUCTION

Indium antimonide (InSb) is a direct band gap semiconductor compound with a band gap energy of 0.17 eV at room temperature, making it widely used in middle-wave infrared (MWIR) cameras to acquire IR images up to wavelength of 5.5 μm . However, there are some limitations of the detectors using bulk InSb, such as high dark current and working at cryogenic temperature. These problems may be overcome by using InSb nanowires, because quantum confinement in one-dimensional (1D) nanowires imparts on their unique optoelectronic properties. Dark current of nanowire-based photodetectors will be reduced significantly due to the size shrinkage [1] and phonon scattering suppression in nanostructures [2], resulting in a higher operating temperature. A high signal-to-noise ratio can be obtained with prolonged photocarrier lifetime and shortened carrier transit time in InSb nanowire-based photodetectors due to the high surface-to-volume ratio of nanowires [3]. Considering these particular properties and the history of bulk InSb detectors, it is of interest to investigate the photoresponses of InSb nanowires-based photodetectors. Successful demonstration will find applications in medicine, defense, fire detection, communication, and astronomy.

In recent years, elemental and compound semiconductors, metals, oxides, nitrides, and a variety of other inorganic materials have been grown in the form of nanowires [4]. This is motivated by the ability to carry out band gap engineering by varying the wire diameter [5], applying quantum confinement effects for wire sizes below the Bohr radius, use of high quality single crystalline wires with

superior surfaces compared with etched structures of similar dimensions, and the possibility of realizing bottom-up integration of devices. Variation in band gap energy can be obtained by choosing a range of diameters, depending on the desired wavelength regime. The Bohr radius of InSb is 65 nm [6], and, thus, its band gap energy can be easily tailored with diameters smaller than that. Because of the unique optoelectronic properties of the 1D materials, photodetectors using 1D semiconductors have been intensively explored. High-density vertical zinc oxide (ZnO) nanowire array has been demonstrated as a high performance photoconductor due to the high surface-to-volume ratio of the nanowires [3]. A carbon nanotube (CNT) thin film-based photodetector has been reported, and its photoconductivity intensely changed under IR illumination [7]. However, photodetectors using thin films of 1D materials as functional elements lose their particular properties and advantages due to the interaction between nanowires. In addition, most thin film photodetectors were working in photoconductive mode, which introduced more noise by the bias. Therefore, using photovoltaic detectors with an individual 1D semiconductor is desirable. A 1D photovoltaic detector, consisting of a p–n junction inside a CNT, can efficiently separate the photo-generated electron and hole pairs by fabricating two gates underneath two contacts [8]. Operation of another type of photovoltaic detector depends on the Schottky barriers between a nanowire and metals, which contributes to the photo-generated carriers separation and photocurrent generation [9].

Indium antimonide nanowires have two promising properties over other materials to be utilized in an IR imaging system. First, bulk InSb has an extremely small band gap with a value of 0.17 eV (Table 13.1), which is optimal for detecting MWIR signal; the other materials shown in Table 13.1 can only sense the light from near IR (NIR) or ultraviolet (UV). In addition, the exciton Bohr radius of InSb nanowire is large compared with other semiconductors with a value of around 65 nm, which is more than 10 times larger of that of silicon, as shown in Table 13.1. This property provides more flexibility for the synthesis of nanowires with different band gap energies.

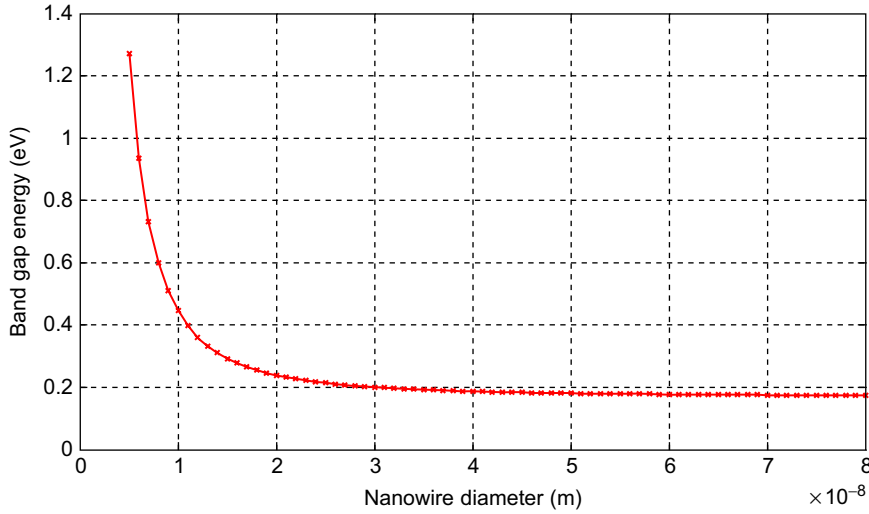
When an electron approaches a hole, it may form a Wannier exciton, approximately described by a hydrogenic Hamiltonian [10]:

$$H = -\frac{\hbar^2}{4\pi m_h^*} \nabla_h^2 - \frac{\hbar^2}{4\pi m_e^*} \nabla_e^2 - \frac{q^2}{\varepsilon |r_e - r_h|} \quad (13.1)$$

where \hbar is the Planck constant; m_h^* and m_e^* are the effective masses of hole and electron, respectively; and ε is the dielectric constant. By solving the equation using this model, the relation of the diameter

Table 13.1 Band Gap Energies and Bohr Radii of Different Materials

Materials	Band Gap Energy (eV)	Bohr Radius (nm)
CuCl	3.39	0.7
Si	1.12	4.3
GaAs	1.52	12.5
InSb	0.17	65

**FIGURE 13.1**

Relation between the diameters of InSb nanowire and corresponding band gap energies. ([33], © [2009] IEEE)

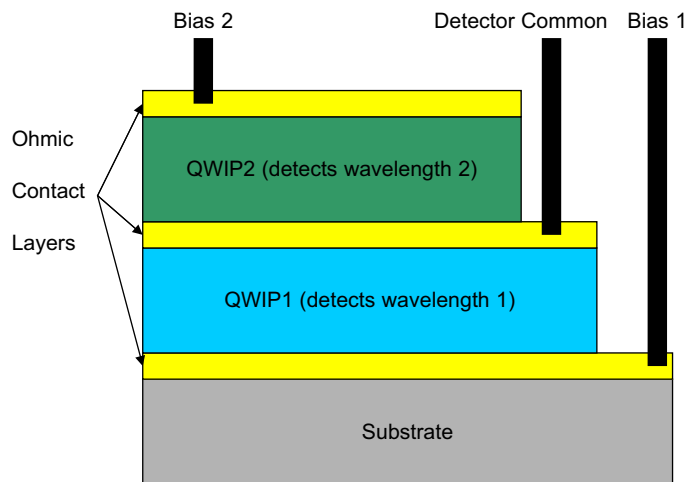
of the nanowire and band gap can be expressed as [11]:

$$E_{gn} = E_{gb} + \frac{\hbar^2 \pi^2}{8d^2} \left(\frac{1}{m_h^*} - \frac{1}{m_e^*} \right) - \frac{1.8q^2}{\epsilon d} \quad (13.2)$$

where E_{gb} is the band gap energy of bulk materials; E_{gn} is the band gap energy of the quantum confined materials; and d is the nanowire diameter.

Figure 13.1 shows the relationship between the diameters of InSb nanowires and their corresponding band gap energies. When the diameter of the nanowire is larger than 65 nm, the band gap energy stays the same as for bulk material (0.17 eV) because of no quantum confinement. When the diameter of the nanowire decreases from 65 to 30 nm, the band gap energy increases slightly from 0.17 to 0.20 eV. Band gap energy increases dramatically from 0.20 to 1.2 eV when the diameter further decreases from 30 to 5 nm. Therefore, the band gap energy covers the MWIR spectrum when the diameter of InSb nanowire is larger than 10 nm and spreads to the NIR spectrum when the diameter becomes smaller than 10 nm. In other words, a photodetector using InSb nanowire with diameters ranging from 70 to 5 nm as the functional elemental can sense IR signal from MWIR to NIR. This multispectrum detection has great potential in various fields. Two devices that improve their performance by using multispectrum detection will now be introduced.

The first device is a dual-band photodetector, which can detect signals at two different wavelengths by stacking one detector on the other. Figure 13.2 shows the structure of a dual-band quantum well infrared photodetector (QWIP) [12]. QWIP1 was grown on top of a substrate using molecular beam epitaxy (MBE), while QWIP2 was stacked on top of QWIP1. The middle contact is used as a detector common, and the top and bottom contacts are used to apply biases to two QWIPs independently. Two stacking QWIPs have different detection spectra to achieve dual-band detection. The fabrication

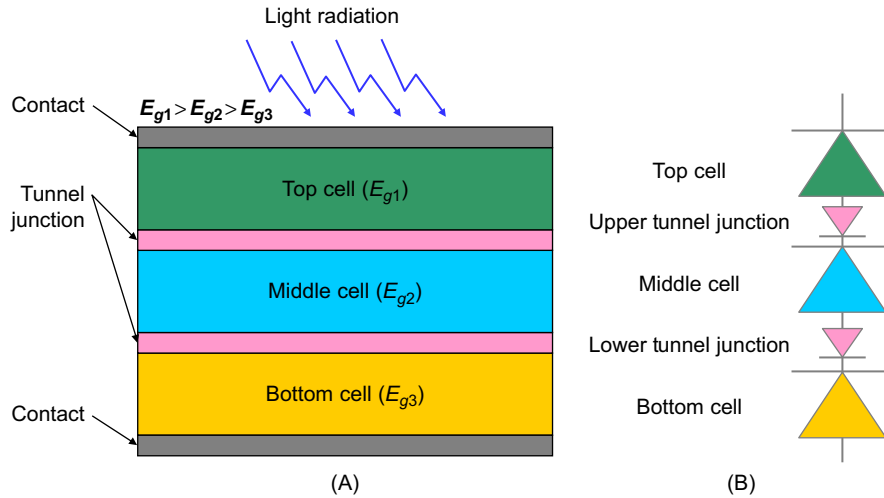
**FIGURE 13.2**

The structure of a dual-band QWIP.

of dual-band photodetectors is motivated by enhancing detection of targets in clutter and distinguishing between targets and decoys. In addition, compared with single-band photodetectors, dual-band photodetectors can operate in a wider range of ambient conditions and can be more effective in eliminating IR countermeasures such as smoke, camouflage, and flares [12]. Several types of dual-band photodetectors have been reported with different detection spectra: a dual-band photodetector can detect two wavelengths in the MWIR (3–5 μm) [13]; another photodetector detected two wavelengths in the long-wave infrared (LWIR) (8–12 μm) [14]; and one other photodetector can be operated in both the LWIR and the MWIR spectral regions [15].

The multijunction solar cell (also called tandem solar cell) is another device that improves its performance by using multispectrum detection. Single-junction solar cells have a maximum theoretical efficiency of around 30%, called the Shockley Queisser limit, which means that only 30% of sunlight irradiating the solar cell can be absorbed [16]. The reason for this limit is that semiconductors have only one band gap energy value in single-junction solar cell. Photons with lower energies than the band gap energy cannot be absorbed, because electrons cannot be excited from the valence band to conduction band, whereas photons with higher energies than the band gap energy lose excess energies through hot electron thermalization, because only one electron and hole pair can be generated by these photons. To enhance the efficiency of solar cells, a multijunction structure was proposed by constructing more than one junction in a solar cell, each junction having a different band gap energy [17].

The structure of a triple-junction solar cell is shown in Fig. 13.3A, which comprises three p–n junctions made from GaInP, GaInAs, and Ge stacked on top of each other, and each layer has a band gap energy (E_g) lower than that of the layer on top of it [18]. Low resistive tunnel junctions are sandwiched between each pair of junctions, acting as small resistance barriers for photo-generated carriers. The equivalent electrical circuit diagram is illustrated in Fig. 13.3B, showing top, middle, and bottom junction diodes and interconnecting upper and lower tunnel junctions. It was reported that double-junction

**FIGURE 13.3**

(A) The structure of a triple-junction solar cell. (B) The electrical circuit equivalent diagram of the triple-junction solar cell.

solar cells have 42% efficiency; triple-junction solar cells have 49% efficiency; and infinite-junction solar cell can reach 68% efficiency [17]. The most essential reason for the improvement is that multijunction solar cells cover wider-spectrum absorption.

Most of the dual-band photodetectors and multijunction solar cells were fabricated by epitaxially growing one layer upon another monolithically. There are certain challenges to fabricate these monolithic devices. First, the entire device must be fabricated on the same substrate layer by layer, and, thus, the lattice constant and growth conditions of these layers must be similar. Second, high-quality is required for all layers, because defects will severely affect the collection of minority carriers in these stacking structures. The third challenge is that the range of doping levels and dopants must be controllable, because the monolithic device used needs to avoid the doping of one layer affecting the other layers.

These challenges may be overcome by replacing the traditional materials with InSb nanowires. The lattice constant similarity problem does not exist in the nanowire platform, because they are not epitaxially grown. In addition, there are many different methods to fabricate InSb nanowires on the substrate, such as direct growth [19], contact printing [20], and roll transfer printing [21]. Moreover, the band gap energy of InSb can be easily controlled by the growth of nanowires with different diameters rather than using different materials. Therefore, InSb nanowires have great potential in devices requiring wide-spectrum detection.

This chapter will start by introducing the growth technique of synthesizing high-quality InSb nanowires. Indium antimonide nanowires have been synthesized using a vapor-liquid-solid (VLS) approach with the aid of Au nanoparticles as catalyst. The synthesized InSb nanowires have diameters ranging from 10 to 35 nm and are up to 10 μm in length. Thereafter, both symmetric and asymmetric photodetectors are investigated and discussed. The detectors show low dark current and high quantum efficiency under IR illumination and can be operated at room temperature.

13.2 GROWTH OF InSb NANOWIRES

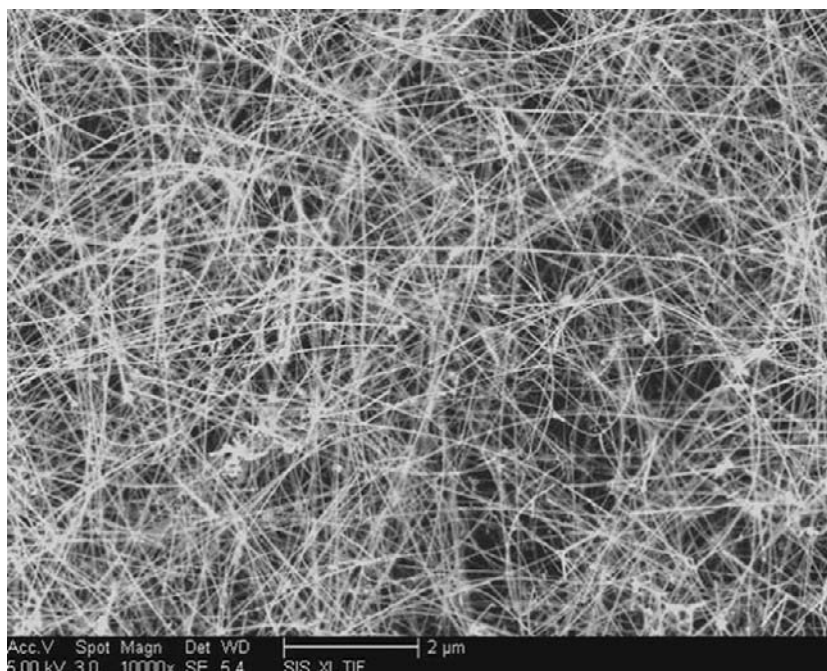
Synthesis techniques for nanowires have recently become highly sophisticated. Diameter, length, doping level, composition, and uniformity are more controllable. Among various nanowire materials under investigation, antimonide (Sb) is an interesting candidate for many optoelectronics applications. The electron effective mass in Ga and InSb is low, 0.042 and 0.0135 m_0 , respectively, with corresponding room temperature band gap energies of 0.72 and 0.17 eV, respectively. Ternary alloy nanowires, $\text{Ga}_x\text{In}_{1-x}\text{Sb}$, can provide continuous variation in band gap energy between 0.17 and 0.72 eV. Instead, variation in band gap energy can be obtained by choosing a range of diameters of either material, depending on the desired wavelength regime. The Bohr radius for InSb is 65 nm, and its band gap energy increases from 0.17 to 0.4 eV for nanowires of 10 nm diameter, thus allowing coverage of 3.1–7.3 μm . The band gap energy covers the NIR and UV region when the diameter becomes smaller than 10 nm.

Work to date on Sb has been limited when compared with Si, Ge, and other III-V semiconductors [4]. Vaddiraju et al. [22] reported direct antimonidization of Ga and In droplets by exposing them to Sb vapor, resulting in nanowire formation. Chin et al. [23] reported the first NIR nanowire-based lasers at wavelength of 1550 nm using GaSb nanowires. InSb nanowires can also be readily prepared using anodized alumina templates [24–27], which allow variation of nanowire diameter by changing the pore size. IR absorption studies have indeed showed that the optical absorption edge moves to the short wavelength region when the diameter is decreased below the Bohr radius [27], and the large exciton Bohr radius provides more flexibility for synthesis and fabrication of quantum devices.

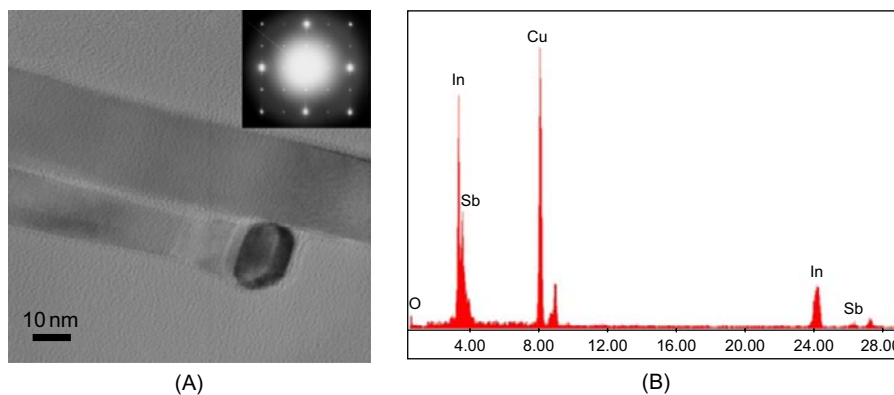
Indium antimonide nanowires were synthesized using a vapor-liquid-solid (VLS) approach with the aid of Au nanoparticles as a catalyst. The nanowire synthesis was carried out in a tube furnace system under reduced pressures and a hydrogen environment to avoid oxide wire formation. An Al crucible containing high-purity InSb powder (99.999%, Aldrich) was placed in the middle of a quartz tube inserted into the furnace. Gold nanoparticles (20 nm) were dispersed as a catalyst on a Si (111) substrate for the growth of nanowires. The substrate was placed on top of the crucible covering the InSb powder. The reactor tube was evacuated to a base pressure of 10^{-2} Torr before the experiment. The carrier gas, hydrogen (99.999%), was introduced at a flow rate of 100 sccm (standard cubic centimeters per minute) and at a pressure of approximately 300 Torr. The furnace temperature was increased to 515°C and maintained for 3 hours. At the end of the growth period, the reactor was slowly cooled to room temperature before removal of the substrate. The morphology and structure of the synthesized products were characterized by scanning electron microscopy (SEM, FEI XL30 Sirion) and transmission electron microscopy (TEM Philips CM20, operated at 200 kV) equipped with energy dispersive X-ray spectroscopy (EDS) for single nanowire chemical composition analysis.

Figure 13.4 shows a SEM image of the as-synthesized InSb nanowires on the Si (111) substrate, showing high-yield nanowire growth. The nanowires have diameters in the range of 10–35 nm and are up to tens of micrometers in length.

Au catalyst beads are visible at the tips of the nanowires as seen in the TEM image of Fig. 13.5A, providing evidence for the VLS growth mechanism. No growth of InSb nanowire was observed on Si substrate without the Au catalyst in a controlled experiment, further confirming the metal-catalyzed VLS growth. Figure 13.5A shows a TEM image of two single InSb nanowires with uniform diameter along their entire length. The selected area electron diffraction (SAED) pattern taken from the nanowire

**FIGURE 13.4**

SEM image of as-synthesized InSb nanowires on a Si substrate using 20-nm Au nanoparticles as catalyst.

**FIGURE 13.5**

(A) TEM image of two InSb nanowires. The inset shows the SAED pattern of a cubic lattice structure of InSb nanowire. (B) EDS analysis of the nanowire revealing the InSb stoichiometry. ([33], © [2009] IEEE)

(shown in the inset) reveals that the latter is a single crystal with cubic (zincblende) lattice structure. The EDS analysis of an individual nanowire with locally focused beam spot confirms that it is composed of only In and Sb with an atomic ratio close to 1:1, as shown in Fig. 13.5B. The trace O peak is from the outer oxide layer.

13.3 PHOTODETECTORS USING SINGLE InSb NANOWIRES

Indium antimonide nanowire photodetectors with symmetric and asymmetric metal structures were fabricated and investigated so as to better understand their working principles.

13.3.1 Symmetric InSb Nanowire Photodetectors

The configuration of a symmetric InSb nanowire photodetector is illustrated in Fig. 13.6A. A nanowire contacts two Au electrodes on a quartz substrate. Figure 13.6B shows the AFM image of an InSb nanowire with a diameter of 30 nm bridging the electrodes. The inset shows the height data for the InSb from the AFM.

The fabrication process starts with making two Au electrodes with a gap of 500 nm using photolithography, thermal evaporation, and lift-off on top of a quartz substrate. Thereafter, a Si/SiO₂ substrate with synthesis nanowires was immersed in alcohol for 1–2 days. Some nanowires will peel off into the solution for DEP deposition. A single InSb nanowire can be deposited between two electrodes by the DEP deposition system as well as the AFM manipulation system. The DEP force can attract nanowire close to the prefabricated electrodes, and the nanowire will be pushed into the desired position via the AFM manipulation system if it is not connected properly.

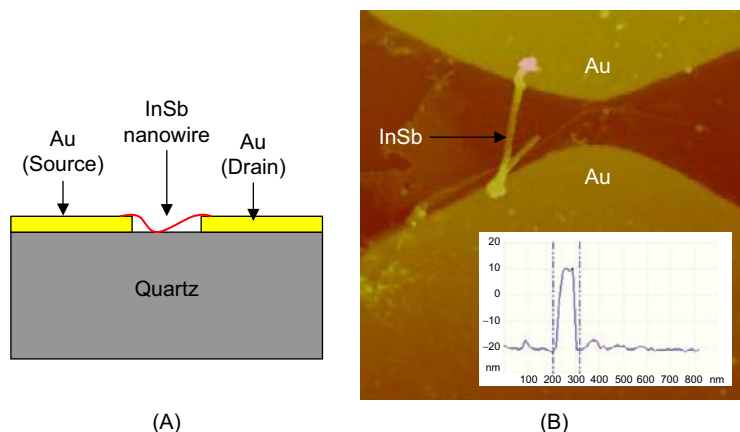
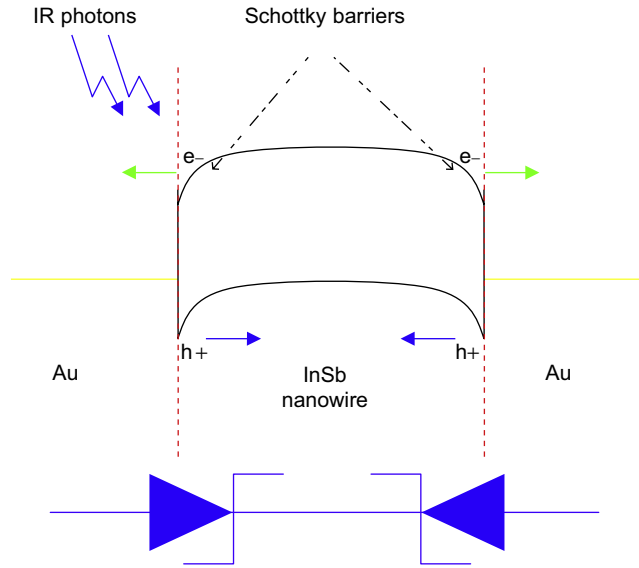


FIGURE 13.6

(A) Structure of the symmetric InSb IR detector. (B) AFM image of an InSb nanowire bridging two Au electrodes; the inset shows the height data for the InSb nanowire with a diameter of 30 nm.

**FIGURE 13.7**

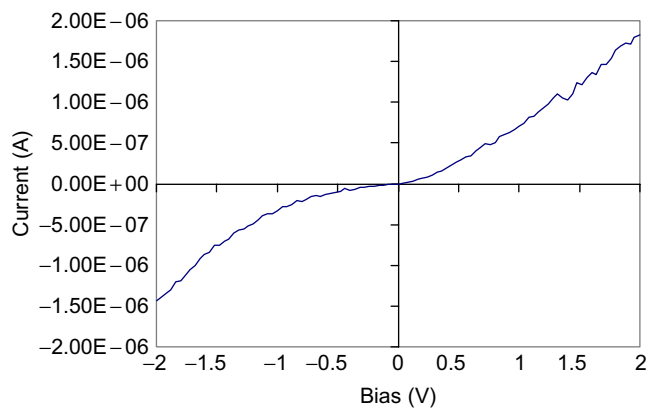
Band diagram of the symmetric InSb nanowire photodetector.

Electron and hole pairs can be generated in the InSb nanowire if photons with energy higher than its band gap energy are irradiated onto it, but they may recombine afterward, resulting in no photocurrent generation. External force is required to separate the electron and hole pairs. The external force can be provided by the electrical field of the depletion region from a Schottky barrier between a metal and InSb nanowire. The structure of the symmetric InSb nanowire detector in Fig. 13.6 will generate two symmetric Schottky barriers reversely connected to each other, as shown in the band diagram of Fig. 13.7.

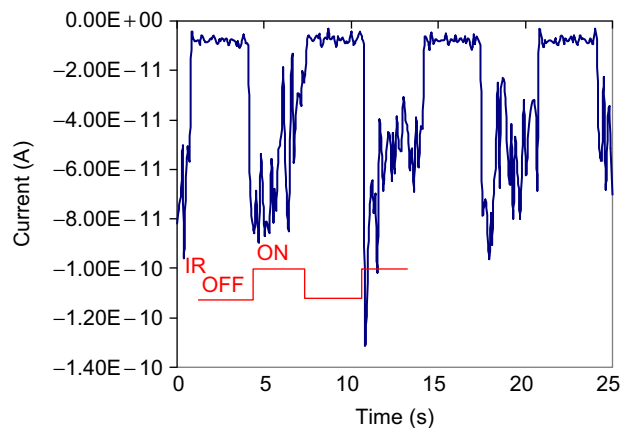
When an IR source with photon energy greater than the band gap energy of the nanowire illuminates the device, electrons and holes will transport in opposite directions at each Schottky barrier, as indicated in Fig. 13.7. As a result, photocurrent will be generated, and the value of the photocurrent is the current difference between these two barriers.

By applying biases between two Au electrodes, the current response was measured, as shown in Fig 13.8. Weak parabolic I-V characteristics are observed: a small threshold voltage is needed to turn the device on, rapidly increasing the current. The threshold voltages are symmetric at positive and negative biases. This indicates that the Schottky barriers are formed between the Au and the InSb nanowire.

The photoresponse of the symmetric InSb nanowire detector was measured with an NIR laser of wavelength 830 nm and power 50 mW. The IR source was mainly focused onto one of the Schottky barriers of the nanowire photodetector. The current signal was measured by switching the IR source ON and OFF periodically, as shown in Fig. 13.9. Zero bias was applied between the two electrodes during measurement. The dark current at the OFF state was around -8×10^{-12} A; when the IR source was turned ON, the current was fluctuating around -8×10^{-11} A. Thus, the ON/OFF (photocurrent-to-dark current ratio) ratio was around 10. However, the photoresponse was very unstable, fluctuating at the

**FIGURE 13.8**

I-V characteristics of the symmetric InSb photodetector.

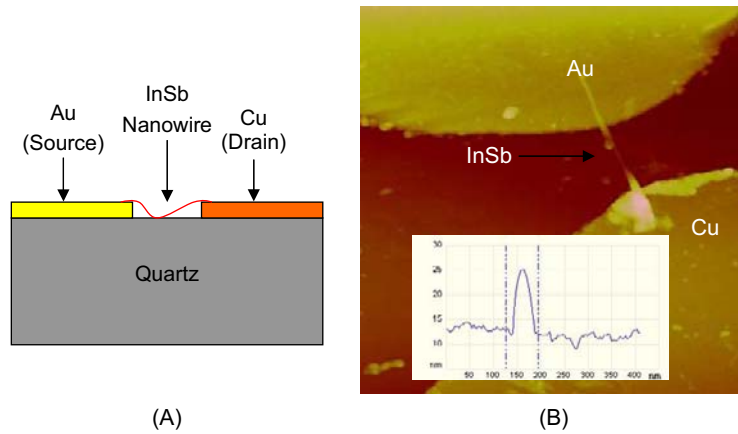
**FIGURE 13.9**

Photoresponse of the symmetric InSb nanowire photodetector.

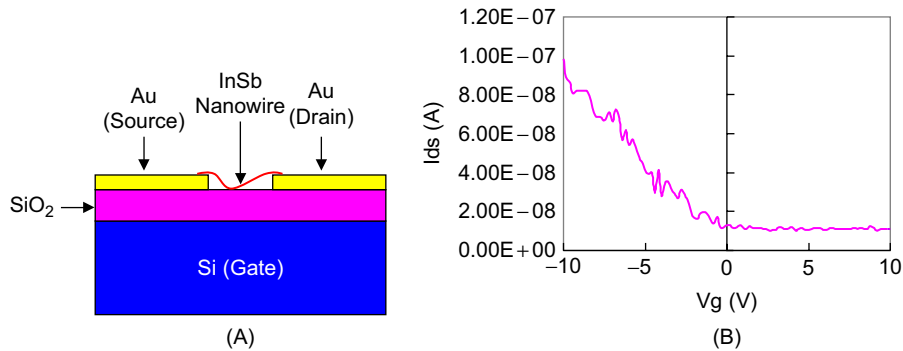
ON state. This may be caused by the material itself, because the IR characteristics of bulk InSb are very unstable, drifting over time.

13.3.2 Asymmetric InSb Nanowire Photodetectors

However, the symmetric metal structure cannot deliver optimal performance, because its photocurrent is the current difference of two symmetric barriers, and also the photo-generated carriers need to tunnel through another barrier before contributing to the photocurrent. The asymmetric photodetector can improve performance by using metals with high/low workfunctions to contact two ends of the InSb

**FIGURE 13.10**

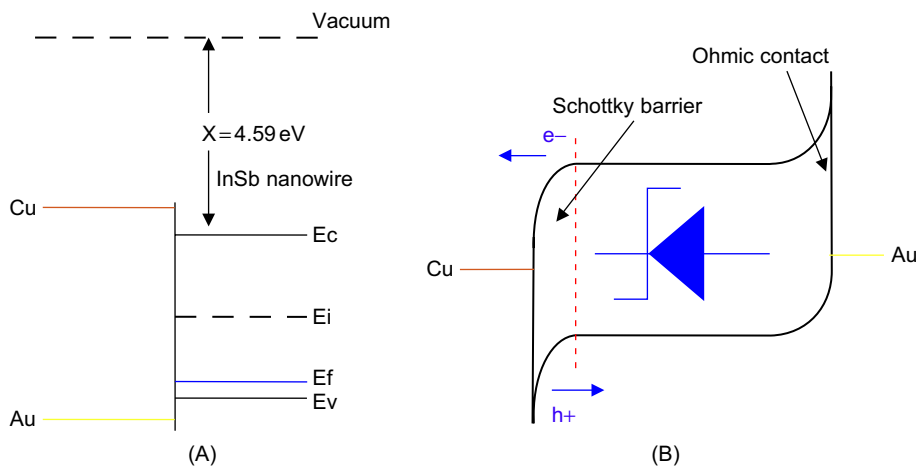
(A) Schematic of the asymmetric InSb nanowire photodetector. (B) An AFM image of the device, the inset showing the height information of the InSb with a diameter of 10 nm. ([33], © [2009] IEEE)

**FIGURE 13.11**

(A) Structure of the InSb nanowire transistor. (B) The transfer characteristics of the InSb nanowire transistor with 0.2V bias.

nanowire. The configuration and an AFM image of the asymmetric InSb photodetector are shown in Fig. 13.10. A single InSb nanowire (diameter of 10 nm and 1 μ m long) makes contact with Au and Cu electrodes on a quartz substrate.

The selection of Au and Cu electrodes is based on the results from a back-gate InSb nanowire transistor, as shown in Fig. 13.11A: an InSb nanowire connecting to two Au electrodes on top of a Si/SiO₂ substrate, which serves as back-gate. It exhibits p-type transistor characteristics: increasing conductance with negative gate voltage (V_g) and vice versa with positive V_g (Fig. 13.11B). The p-type doping may come from the charge transfer from the oxygen in the atmosphere to the InSb nanowire

**FIGURE 13.12**

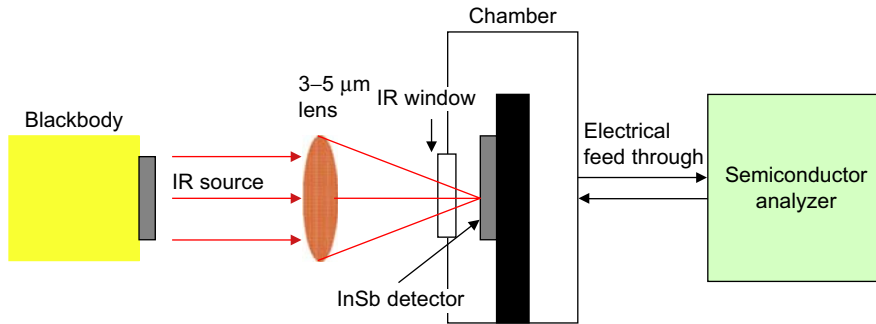
(A) Energy alignment of Au, Cu, and InSb nanowire. (B) Band diagram of the asymmetric photodetector.

[28]. For a p-type InSb nanowire, Au with a work function that is higher than its Fermi energy will form an Ohmic contact, and another metal with a work function smaller than its Fermi energy is required to form a Schottky barrier; Cu (4.5 eV) meets this need. Therefore, the photocurrent of the asymmetric InSb nanowire detector is mainly generated from the separated electron and hole pairs at the InSb-Cu interface.

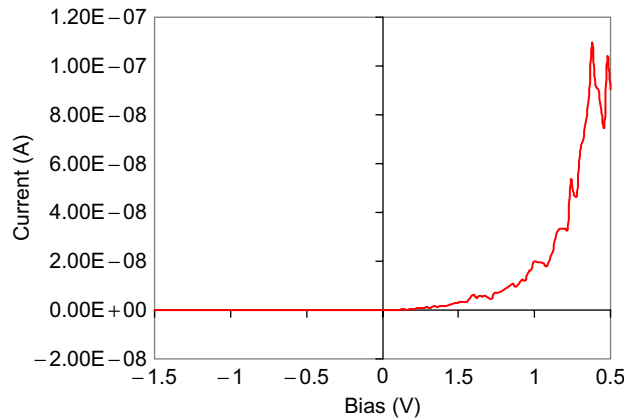
The band diagram of Au and Cu contact with an InSb nanowire is illustrated in Fig. 13.12A. The electron affinity of the InSb is 4.59 eV. The InSb nanowire transistor results indicate that the InSb nanowire is a p-type material; thus, its Fermi energy (E_f) is lower than its mid-gap energy (E_i). The workfunctions of Cu and Au are approximately 4.5 and 5.1 eV, respectively. The Cu can guarantee Schottky contact and high barrier height, while Ohmic contact or a very weak Schottky barrier will be formed between the InSb nanowire and Au. Figure 13.12B shows the band diagram of the asymmetric InSb nanowire photodetector. The photocurrent will be determined by only one Schottky barrier between Cu and the nanowire in this structure, and the separated electrons and holes do not need to transport another depletion region as in the symmetric design and as a result, higher photocurrent will be produced.

The fabrication of the asymmetric photodetector starts with making an Au electrode on a quartz substrate by photolithography, thermal evaporation, and lift off. The quartz substrate prevents the photogating effect, which was reported using Si/SiO₂ as a substrate [29]. Thereafter, a Cu electrode was fabricated using the same process, and the insulating gap between the electrodes is controlled to be around 500 nm. A single nanowire is deposited between the electrodes using a dielectrophoretic (DEP) deposition system assisted by AFM manipulation.

The testing system (Fig. 13.13) consists of a blackbody source, which is focused through a lens with a 3–5 μm antireflection coating layer, a detection chamber with an IR window housing the InSb detector, and a semiconductor analyzer.

**FIGURE 13.13**

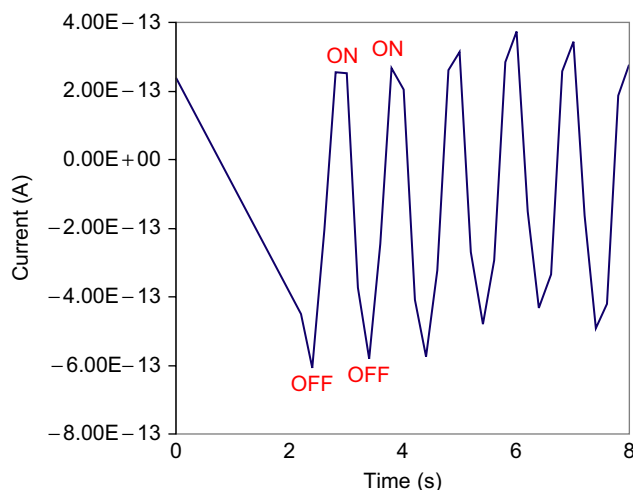
Testing system for the asymmetric InSb nanowire photodetector.

**FIGURE 13.14**

I-V characteristics of the asymmetric InSb nanowire photodetector.

The I-V characteristics of the asymmetric nanowire photodetector (Fig. 13.14) are found to be those of a Schottky diode with rectifying behavior, because the carrier transport is dominated by one Schottky barrier. The current increases dramatically with forward drain voltage (0–1.5 V) by diminishing the barrier, with a maximum drain current of 1×10^{-7} A. However, the barrier width increases when a reverse bias is applied, and, hence, the current is close to zero.

Figure 13.15 shows the photoresponse measured at room temperature with 1000°C blackbody radiation by switching the chopper ON and OFF at 1 Hz. The corresponding peak signals were 0.3 and -0.4 pA at zero bias. The dark current is -0.4 pA, and 0.3 pA is the current during IR illumination on the detector, indicating a measured photocurrent of 0.7 pA. The lens (with a 3–5 μm antireflection coating layer) focused the blackbody radiation onto the detector. Electron and hole pairs are generated in the InSb nanowire when photons with energy higher than 0.4 eV (band gap energy of a 10-nm

**FIGURE 13.15**

Photoresponse of the InSb nanowire photodetector at a chopper frequency of 1 Hz.

nanowire) illuminate it. An external force is needed to separate the electron and hole pairs and to avoid recombination, which is supplied by the electric field of the Schottky barrier depletion region.

Quantum efficiency is the percentage of incident photons converting into electron and hole pairs. High quantum efficiencies of 95% at 87 K were obtained in bulk InSb photodetectors due to the wide spectral response with its narrow band gap energy [30]. Absorption depth cannot be neglected to accurately estimate the quantum efficiency of this 1D photodetector, because photodetectors typically require three times their absorption depth to absorb 95% of the incident photons [31]. The absorption depth varies widely with different wavelengths, increasing from 1 to 100 μm when the wavelength increases from 2.5 to 5.4 μm [32]. The radiation from the blackbody was 1000°C with emission peak at around 2.3 μm according to Wien's displacement law. Thus 1 μm is taken as the absorption depth for our detector. The ratio of the photons absorbed by the nanowire to the whole incident photon flux is $10\text{ nm}/(3 \times 1\text{ }\mu\text{m}) = 0.33\%$, as we assume uniform absorption through the whole absorption length. Based on its photo-response (Fig. 13.15), the quantum efficiency of the InSb nanowire photodetector is approximately 60%. In other words, this InSb nanowire photodetector maintains a high quantum efficiency with shrunk size and can operate at room temperature.

Traditional InSb photodetectors require cryogenic cooling owing to the high dark current at room temperature. Suppressing dark current in a photodetector will improve the detection performance as less cooling or no cooling is needed, and a higher signal-to-noise ratio can be obtained. In the InSb nanowire photodetector, the physical volume reduction into the nanoscale and phonon scattering suppression in the 1D system result in a $-4 \times 10^{-13}\text{ A}$ dark current, which is seven orders of magnitude smaller than that of a high speed InSb photodetector ($6.4 \times 10^{-6}\text{ A}$) [32]. The dark current of the nanowire photodetector mainly comes from the tunneling at the interface between Cu and InSb. It can be further suppressed with a higher barrier by selecting a metal with proper work function or controlling the doping of the InSb.

13.4 SUMMARY

In this chapter, a photodetector using a single InSb nanowire has been shown to effectively detect IR signals at room temperature. Indium antimonide nanowires with diameters of 10–35 nm and tens of microns long were grown by the VLS approach using an InSb powder source and Au catalyst. The quantum confinement can modify the band gap energy when the diameter of the nanowires is smaller than the Bohr radius, making the fabrication of InSb photodetectors covering both NIR and MIR feasible. Both symmetric and asymmetric InSb nanowire photodetectors were fabricated and investigated under NIR and MIR irradiation. High quantum efficiency was observed for a 10-nm InSb nanowire photodetector at room temperature. The dark current of the nanowire detector was significantly reduced due to the nanoscale diameter of the wire and suppression of phonon scattering.

References

- [1] D. M. Kuo, A. Fang, and Y. C. Chang. Theoretical modeling of dark current and photo-response for quantum well and quantum dot infrared detectors. *Infrared Phys. Technol.*, 42:422–433, 2001.
- [2] U. Bockelmann and G. Bastard. Phonon scattering and energy relaxation in two-, one-, and zero-dimensional electron gases. *Phys. Rev. B*, 42(14):8947–8951, 1990.
- [3] C. Soci, A. Zhang, B. Xiang, S. A. Dayeh, D. P. R. Aplin, J. Park, X. Y. Bao, Y. H. Lo, and D. Y. Wang. ZnO nanowire UV photodetectors with high internal gain. *Nano Lett.*, 7:1003–1009, 2007.
- [4] M. Meyyappan and M. K. Sunkara. *Inorganic Nanowires: Applications, Properties, and Characterization*. CRC Press, Boca Raton, FL, 2009.
- [5] D. D. D. Ma, C. S. Lee, F. C. K. Au, S. Y. Tong, and S. T. Lee. Small-diameter silicon nanowire surfaces. *Science*, 299(5614):1874–1877, 2003.
- [6] K. Zhu, J. Shi, and L. Zhang. Preparation and optical absorption of InSb microcrystallites embedded in SiO₂ thin films. *Solid State Commun.*, 107(2):79–84, 1998.
- [7] S. Lu and B. Panchapakesan. Photoconductivity in single wall carbon nanotube sheets. *Nanotechnology*, 17:1843–1850, 2006.
- [8] J. U. Lee. Photovoltaic effect in ideal carbon nanotube diodes. *Appl. Phys. Lett.*, 87:073101, 2005.
- [9] J. Zhang, N. Xi, H. Chen, K. W. C. Lai, G. Li, and U. Wejinya. Photovoltaic effect in single carbon nanotube-based Schottky diodes. *Int. J. Nanoparticles*, 1(2):108–118, 2008.
- [10] L. Brus. Electron-electron and electron-hole interactions in small semiconductor crystallites: the size dependence of the lowest excited electronic state. *J. Chem. Phys.*, 80(9):4403–4409, 1984.
- [11] R. Reisfeld. Nanosized semiconductor particles in glasses prepared by the sol-gel method: their optical properties and potential uses. *J. Alloys Compd.*, 341(1–2):56–61, 2002.
- [12] A. C. Goldberg, T. Fischer, S. W. Kennerly, S. C. H. Wang, M. Sundaram, P. N. Uppal, M. L. Winn, G. L. Milne, and M. A. Stevens. Dual-band QWIP MWIR/LWIR focal plane array test results. In *Proc. SPIE*, vol. 4028, page 276, 2000.
- [13] J. Caufield. Simultaneous integrating staring two color IRFPAs. In *Proc. 1997 IRIS Detector Specialty Group Meeting on Detectors*, ERIM, page 351, 1998.
- [14] M. Sundaram. Advances in QWIP FPA (2-color and 1-color) technology. In *Proc. 1998 IRIS Specialty Group Meeting on Detectors*, ERIM, page 219, 1999.
- [15] P. Warren, M. Satyshur, M. Kruer, D. Scribner, and J. Schuler. Dual-band QWIP MWIR/LWIR focal plane array test results. In *Proc. SPIE*, Munich, Germany, vol. 4029, page 276, 2000.

- [16] W. Shockley and H. J. Queisser. Detailed balance limit of efficiency of p-n junction solar cells. *J. Appl. Phys.*, 32(3):510–519, 1961.
- [17] A. De Vos. Detailed balance limit of the efficiency of tandem solar cells. *Physics*, 13(5):839–846, 1980.
- [18] H. Cotal, C. Fetzer, J. Boisvert, G. Kinsey, R. King, P. Hebert, H. Yoon, and N. Karam. III–V multijunction solar cells for concentrating photovoltaics. *Energy Environ. Sci.*, 2:174–192, 2009.
- [19] Y. Wu and P. Yang. Direct observation of vapor-liquid-solid nanowire growth. *J. Am. Chem. Soc.*, 123(13):3165–3166, 2001.
- [20] Z. Fan, J. C. Ho, Z. A. Jacobson, R. Yerushalmi, R. L. Alley, H. Razavi, and A. Javey. Wafer-scale assembly of highly ordered semiconductor nanowire arrays by contact printing. *Nano Lett.*, 8(1):20–25, 2008.
- [21] Y.-K. Chang and F. C.-N. Hong. The fabrication of ZnO nanowire field-effect transistors by roll-transfer printing. *Nanotechnology*, 20(19):253112, 2009.
- [22] S. Vaddiraju, M. K. Sunkara, A. H. Chin, C. Z. Ning, G. R. Dholakia, and M. Meyyappan. Synthesis of group III antimonide nanowires. *J. Phys. Chem. C*, 111(20):7339–7347, 2007.
- [23] A. H. Chin, S. Vaddiraju, A. V. Maslov, C. Z. Ning, M. K. Sunkara, and M. Meyyappan. Near-infrared semiconductor subwavelength-wire lasers. *Appl. Phys. Lett.*, 88(16):163115, 2006.
- [24] X. Zhang, Y. Hao, G. Meng, and L. Zhang. Fabrication of highly ordered InSb nanowire arrays by electro-deposition in porous anodic alumina membranes. *J. Electrochem. Soc.*, 152(10):C664–C668, 2005.
- [25] Y. W. Yang, L. Li, X. H. Huang, M. Ye, Y. C. Wu, and G. H. Li. Transport properties of InSb nanowire arrays. *Appl. Phys. A*, 84:7–9, 2006.
- [26] Y. Yang, L. Li, X. Huang, G. Li, and L. Zhang. Fabrication and optical property of single-crystalline InSb nanowire arrays. *J. Mater. Sci.*, 42:2753–2757, 2007.
- [27] H. D. Park, S. M. Prokes, M. E. Twigg, Y. Ding, and Z. L. Wang. Growth of high quality, epitaxial InSb nanowires. *J. Cryst. Growth*, 304(2):399–401, 2007.
- [28] P. G. Collins, K. Bradley, M. Ishigami, and A. Zettl. Extreme oxygen sensitivity of electronic properties of carbon nanotubes. *Science*, 287:1801–1803, 2000.
- [29] M. S. Marcus, J. M. Simmons, O. M. Castellini, R. J. Hamers, and M. A. Eriksson. Photogating carbon nanotube transistors. *J. Appl. Phys.*, 100(8):084306, 2006.
- [30] J. Varesi, R. Bornfreund, A. Childs, W. Radford, K. Maranowski, J. Peterson, S. Johnson, L. Giegerich, T. de Lyon, and J. Jensen. Fabrication of high-performance large-format MWIR focal plane arrays from MBE-grown HgCdTe on 4" silicon substrates. *J. Electron. Mater.*, 30:566–573, 2001.
- [31] F. C. Foy and R. Foy. *Optics in Astrophysics*. Springer, London, 2005.
- [32] I. Kimukin, N. Biyikli, T. Kartaloglu, O. Aytur, and E. Ozbay. High-speed InSb photodetectors on GaAs for mid-IR applications. *IEEE J. Sel. Top. Quantum Electron.*, 10(4):766–770, 2004.
- [33] H. Chen, X. Sun, K. W. C. Lai, M. Meyyappan, and N. Xi. Infrared detection using an InSb nanowire. In *Nanotechnology Materials and Devices Conference*, pages 212–216, 2009.

Carbon Nanotube-Based Infrared Camera Using Compressive Sensing

14

Bo Song, Ning Xi, Hongzhi Chen, King Wai Chiu Lai, and Liangliang Chen

Department of Electrical and Computer Engineering, Michigan State University, Michigan

CHAPTER OUTLINE

14.1 Introduction	225
14.2 Theoretical Foundation of Compressive Sensing	228
14.2.1 General Idea	229
14.2.2 Sparsity	229
14.2.3 Restricted Isometry Property	230
14.2.4 Random Matrix	231
14.2.5 Compressive Sensing Applications	231
14.3 Compressive Sensing for Single-Pixel Photodetectors	231
14.3.1 System Architecture	231
14.3.2 Measurement Matrix	233
14.3.3 Data Sampling and Image Reconstruction Algorithm	234
14.4 Experimental Setup and Results	236
14.4.1 Static Measurement	236
14.4.2 Dynamic Observation	237
14.4.3 Performance Analysis	237
14.5 Summary and Perspectives	240
References	241

14.1 INTRODUCTION

In addition to single-pixel photodetectors, infrared (IR) imaging plays an important role in industrial, medical, and military applications, but traditional IR imaging still has limited functions. Advances in IR cameras using nanomaterials has become an interesting topic. After the discussion of a number of nanomaterial-based photodetectors in previous chapters, we will now introduce an IR imaging system using the carbon nanotube (CNT) [1]. Instead of a large-scale CNT detector array, the system requires only one pixel (or very few pixels) because of the use of compressive sensing. Initially, compressive sensing had fewer measurements than Nyquist–Shannon sampling rate but kept the main data on the observed signal [2, 3]. The Nyquist–Shannon sampling theorem has been seen as the basic foundation of information theory for many years. According to this theory, the data sampling rate should be at

least twice the maximum frequency (Nyquist rate) of the observed signal. It demands the sampling device to have higher bandwidth to catch the original signal. However, the problem is that there is increasing demand for faster data sampling technology to deal with the current deluge in data sensing and processing [4, 5]. Compressive sensing has solved this problem. It provides a better solution for using fewer measurements but can still get the same measurement results for signals. Moreover, if the sensor itself has limitations on power or sensing cell size which means it can only deliver a few measurements, compressive sensing can instead be used. Compressive sensing has realized the dream for using only one optical detector to sample data and reconstruct the observed images.

In a traditional data sensing and processing device such as a digital camera, compressed processing happens in the step after sensing, as shown in Fig. 14.1. Under this working principle, the data sensing component must have a powerful data sampling ability to deal with large area sensing, such as the charge-coupled device (CCD). The number of CCD arrays must be large enough to sense a high-resolution image. In some case, if the sensing device has the constraints of space or power consumption, a better solution is not just improving the sensing cell but to find a way to use fewer measurements in the sensing process and reconstruct the signal [6]. Compressive sensing provides a way to solve this problem.

If a signal (with dimension = N) is compressible, there must be some method to directly sense the compressed data (take $K = M$ measurement) instead of plentiful but less useful information as shown in Fig. 14.2. The original signal should then be exactly reconstructed. Candes et al. gave the mathematical proof that the signal could be fully recovered under Fourier transfer. This is the foundation of compressive sensing [7]. Candes et al. and Donoho proposed the term compressive sensing in 2006 [7, 8].

Compressive sensing undertakes compressive processing in the sampling step as shown in Fig. 14.3, each time compressive sensing senses a sum of linear projections from the original signal to the measurement matrix [9]. After a few measurements, the original signal can be recovered by use of

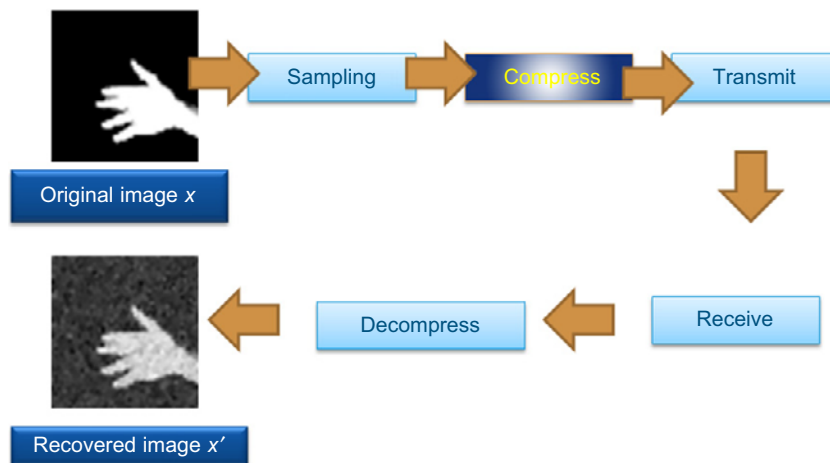
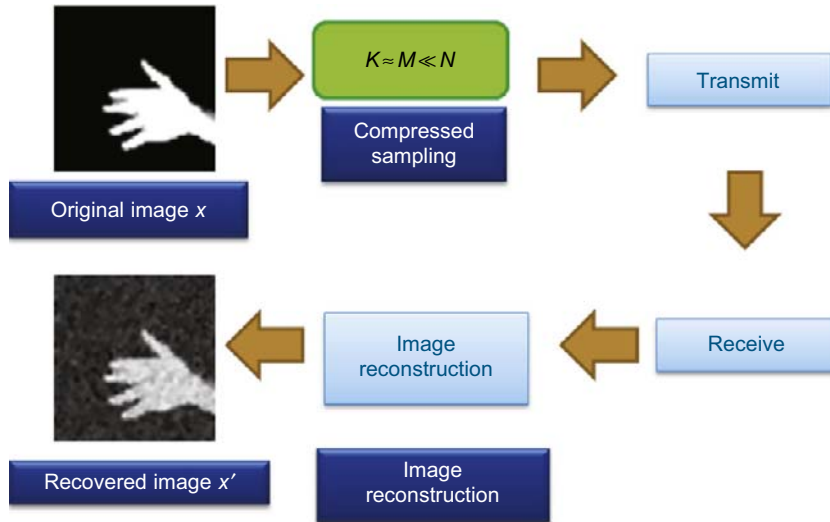
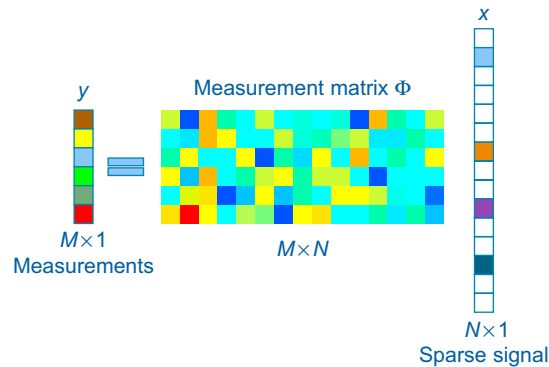


FIGURE 14.1

Data sensing in the traditional sensing device.

**FIGURE 14.2**

Data sensing in the compressive sensing process.

**FIGURE 14.3**

General idea.

a reconstruction algorithm. Because the measurement times are smaller than those corresponding to the dimensions of the original signal, compressive sensing can break through the restriction of Nyquist–Shannon sampling theory if the signal is sparse.

Thanks to this high-powered technique of compressive sensing, it provides a highly effective method to decrease sensor size, reducing expenditure markedly on the fabrication of larger sensing arrays. Compressive sensing makes this a reality in imaging using single-pixel photodetection. Instead of millions of sensing cells and millions of measurements for imaging mega pixels, compressive sensing

can use only one detector to sense the data, during which fewer measurements are taken than with the traditional camera, using the image reconstruction algorithm to recover the image. In this chapter, a single-pixel camera based on a special photodetector for IR detection is introduced. The IR detector has a wide use in monitoring and security areas due to its unique characteristics. The electromagnetic radiation emitted from the human body and other heated objects is in the IR spectrum, particularly in the middle-wave IR (MWIR) range. Two types of traditional IR detectors, thermal detectors and photodetectors, have been used for IR detection for years. Although they work well in certain respects, their drawbacks are obvious: slow response and low sensitivity for thermal detectors, and a cooling system needed for photodetectors. Therefore, there is increasing demand for fast response, high sensitivity, and cooling-free operation of IR detectors. A CNT-based IR detector is used as a photon signal sensor for the compressive sensing-based imaging system because of its outstanding performance and ability to work at room temperature.

As a one-dimensional (1D) material, CNT has very special physical, electrical, and mechanical properties. Therefore, it works as building blocks for various sensors, such as pressure and gas sensors [10–13]. Moreover, the 1D-structured CNT is promising for fabricating photodetectors [14], and photoemitters [15] due to its unique optical properties. CNT can be metallic or semiconductor depending on its chirality angles, as stated in Chapter 2 [16]. In Chapter 5, we also mentioned semiconductor CNT as a direct bandgap material with tunable bandgap energy by varying its diameter, which determines the bandgap energy of quantum-confined materials [17]. As a result, multispectrum detection can be achieved by using CNTs with different diameters. Multiple electron-hole pair generation was observed in a CNT photodetector, which shows the potential applications of using CNTs to build photodetectors with enhanced performance [18]. In addition, the 1D structure of CNT has high surface-to-volume ratio, which can improve the signal-to-noise ratio of CNT detectors by prolonging photocarrier lifetime and shortening carrier transit time [19].

There are two typical kinds of photovoltaic CNT photodetectors: p-n junction and Schottky barrier-based photodetectors. An IR photodiode using a p-n junction inside a SWCNT was reported by applying opposite gate voltages to the gates underneath the source and drain [20]. The other kind of photovoltaic photodetector depends on the Schottky barrier between metal and CNT. This detector was demonstrated as a sensitive IR detector [21], which has a much simpler fabrication process than p-n junction-based photodetectors, and is thus used in our imaging system.

14.2 THEORETICAL FOUNDATION OF COMPRESSIVE SENSING

The main features for compressive sensing are signal sparse representation, measurement matrix design, and reconstruction algorithm. Most natural signals are not sparse, and therefore one has to find the efficient sparse representation methods. Actually, wavelet and Fourier transforms can transfer signals from the time domain to the frequency domain. Almost all the signals in nature have a certain sparse in the frequency domain. Moreover, the ridgelet [22], bandelet [23], and contourlet [24] methods are also used for signal sparsity representations. The main idea behind these methods is to find a proper basis where signals can be decomposed into sparse elements. Each of these techniques deals with a characteristic signal, but it is very difficult to find a general or universal basis to make all signals well sparsed. Redundant diction is another way to find signal sparse representation. In this

method, instead of choosing a basis, the goal is to find or create a dictionary in which the most sparse coefficients can be found. This is much harder than choosing a suitable basis but redundant dictionary suits nearly all signal sparsity. Possibly then, strategies such as Matching Pursuit (MP) [25] algorithms might be a good way to achieve the local optimization of signal sparse.

To choose a stable and efficient measurement matrix, Candès, Romberg, and Tao provided a very important theory – Restricted Isometry Property (RIP) [26, 30]. Their work shows that if a matrix satisfied RIP, this matrix could be used as a measurement matrix and with it the original signal could be well reconstructed. The RIP is a sufficient condition for the measurement matrix. Moreover, random Gaussian, Bernoulli, and Fourier matrices [27, 28] which satisfy the RIP have been shown to be a good preferential and stable measurement matrices.

Although the RIP guarantees that the sparse signal can be recovered with a properly designed measurement matrix, the recovery time is a problem for compressive sensing. The signal reconstruction in compressive sensing might seem to be a l_0 norm minimization problem. However, the algorithms for solving l_0 norm are NP-hard [29], so one usually uses l_1 norm to approximate l_0 norm [7, 30]. Basis Pursuit [31] is one of these algorithms. The main idea is to convert the problem into a linear one and solve with the complexity $O(N^3)$. Other methods such as Matching Pursuit could also be used in compressive sensing signal recovery. Of the MP methods, Orthogonal Matching Pursuit (OMP) [32], Gradient Pursuits (GP) [33], and Tree-Based Orthogonal Matching Pursuit (TOMP) [34, 35] are good-performance and efficient algorithms.

14.2.1 General Idea

Consider an unknown signal x in \mathcal{R}^N ; we want to make M linear measurements to sense the original signal x , such as in Eq. (14.1). In the case of $M = N$, the original signal x can be reconstructed perfectly by solving the linear equation. However, we are more interested in the situation $M \ll N$, which means we can make fewer measurements but still reconstruct the original signal.

$$y = \Phi x \quad (14.1)$$

Here, Φ is used as a measurement matrix, and each measurement might seem to be a linear projection from the original signal x to the measurement matrix Φ . y is the measurement result in which $y \in \mathcal{R}^M$. From Eq. (14.1), there are obvious infinite solutions for the original signal x . It is an underdetermined equation. However, if the original signal is sparse and measurement matrix is properly designed, the original signal x could be reconstructed [7] by solving to minimize the 0-norm optimization problem

$$\hat{x} = \arg \min \|x\|_0 \quad \text{s.t.} \quad \Phi x = y \quad (14.2)$$

Because solving 0-norm minimization problem is a NP-hard problem [36], it would be better to use 1-norm minimization instead of 0-norm. Therefore, Eq. (14.2) solves

$$\hat{x} = \arg \min \|x\|_1 \quad \text{s.t.} \quad \Phi x = y \quad (14.3)$$

14.2.2 Sparsity

Compressive sensing involves compressed sampling and reconstructing the signal with the solving of optimal equations. This theory is based on the assumption that the observed signal is sparse, which

means only a small amount of the observed signal has significant value and all the remainder is equal to zero or could be seemed to be zero [37, 38]. Actually, most natural signals such as sound and image do not satisfy this assumption. Therefore, a method must be found to convert these unparsed signals into the sparse form under some transform [39–41]. In other words, if we have a vector f , then $f \in \mathbb{R}^N$. In an orthonormal basis $\Psi = [\psi_1, \psi_2, \dots, \psi_n]$, the vector f could decompose into

$$f(t) = \sum_{i=1}^n x_i \psi_i(t) \quad (14.4)$$

where x is the coefficient of vector f . On a different basis, x is a different coefficient. For example, on the wavelet basis, x could seem to be wavelet coefficients that are sparse. Make $f = \Psi x$ where Ψ is a $n \times n$ matrix. For the example discussed previously, x is the observed signal, so that

$$x = \Psi s \quad (14.5)$$

where s is the sparse representation of signal x in basis Ψ . Actually, many transforms have the ability to make a signal sparse. They could transfer signal from the time domain to the frequency domain such as wavelet, curvelet, and fourier transforms. Now the expression for compressive sensing changes to

$$y = \Phi \Psi s \quad (14.6)$$

The measurement matrix turns to $\Phi \Psi$, and here we use $\tilde{\Phi} = \Phi \Psi$ to denote the new measurement matrix. If the original signal is already sparse, the transform basis $\Psi = I$.

14.2.3 Restricted Isometry Property

In order to guarantee the original signal x can be exactly reconstructed, the measurement matrix $\tilde{\Phi}$ must have some restriction. The Restricted Isometry Property (RIP) provides a sufficient condition to ensure compressive sensing functions properly [7]. Let δ_k be the smallest number such that

$$(1 - \delta_K) \|x\|_2^2 \leq \|\tilde{\Phi} x\|_2^2 \leq (1 + \delta_K) \|x\|_2^2 \quad \forall x \in \mathbb{R}^{l^T} \quad (14.7)$$

and if $\delta_k \in (0, 1)$, the original signal x sensed by measurement matrix $\tilde{\Phi}$ can be exactly reconstructed. The RIP is the sufficient condition for whether a measurement matrix has a superior performance to sense data and reconstruct signal. Until recently, there has not been any research that shows the necessary condition for the measurement matrix. It has been shown that the random Gaussian matrix [42], Bernoulli Matrices [26], Random Partial Fourier Matrices [43], etc. work well and stably as measurement matrixes. How to define whether a reconstruction method is optimal is another issue for the compressive sensing. Candès and Tao [26] gave the definition of optimal recovery as follows:

$$\|f - f'\|_{l_2} \leq C \cdot R \cdot (M/\log N)^{-r}, \quad r = 1/p - 1/2 \quad (14.8)$$

where f and f' are the original and recovery signals respectively; C is the constant, only depending on p . R is the smallest value of $\|f\|_{l_1}$. M and N are the measurement times and total length of original signal. p is the power-law decay parameter of original signal. In words, the parameter p controls the decay speed of the original signal. The smaller is p , the faster is the decay.

With this optimal recovery theorem, it is obvious that the error range of signal recovery has been constrained by the measurement times and the property of the original signal [44]. Also, the larger the measurement times the better the recovery signal.

14.2.4 Random Matrix

RIP provides a guide for finding the measurement matrix for compressive sensing. The challenge is whether we can design some measurement matrix that needs fewer measurements but with high probability of recovering the original signal [45]. However, it is difficult to build a matrix to satisfy this condition, and moreover RIP only tells whether a matrix could serve as a measurement matrix, but does not mention how to build it up. Fortunately, some random matrices such as the random Gaussian matrix, random binary matrix, and Fourier matrix have been tested and found to be measurement matrices with superior performance. All of these three matrices satisfy RIP, and measurements obey

$$m \geq C \cdot S \log(n/S) \quad (14.9)$$

where S is the number of the largest significant elements or coefficients in signal x , and C is a constant but varies according to different measurement matrices.

14.2.5 Compressive Sensing Applications

Compressive sensing could minimize the measurements required in the hardware of the sensing component, so it has many practical applications. Richard Baraniuk and Kevin Kelly of Rice University developed an interesting implantation for compressive sensing [46, 47]. They use only one photodiode to sense and acquire images and then successfully perform reconstruction by compressive sensing. A digital micromirror device (DMD) was used in their “single-pixel camera” as a measurement matrix generator, and with the help of lens, the original image would be reflected and focused onto the signal photodiode. Thus what the photodiode measured is the linear projection from the original image into the measurement matrix generated by the DMD, not the entirety pixels in the original image. The measurement times are far the lower than the length of original signal (the number of pixels in the original image).

Another application for compressive sensing is the fast radar imaging system [48]. Because of the presence of a compressive sensing implant in the radar imaging system, the bandwidth of the sensing device is decreased. Also, instead of a complicated signal receiver device, a compressive sensing signal recovery system could obtain as a good performance as with the expensive hardware in a radar system. Compressive sensing can also be used in biology and medical areas such as DNA chips [49], fast imaging magnetic resonance system [50], and so forth. One of the significant advantages of compressive sensing is that it can decrease the hardware and power requirements in sensing devices, so a very popular research area is using compressive sensing to built up distribute sensor network. Researchers from Rice University successfully use the joint sparsity recovery method to decrease the noise and error level in sensor networks [51].

14.3 COMPRESSIVE SENSING FOR SINGLE-PIXEL PHOTODETECTORS

14.3.1 System Architecture

In this section, we are interested in the integration of compressive sensing with our CNT-based photodetectors to form a single-pixel IR imaging system. In compressive sensing, the measurement matrix is an essential feature, which realizes the linear projection from the original signal (image) to the

measurement results. For this application, the measurement matrix must be represented by a hardware device that can let partial IR light pass through and focus IR light into CNT-based IR detectors. A digital micromirror device (DMD) from Texas Instruments (TI) is most suitable for this work.

The architecture of this IR imaging system is shown in Fig. 14.4. First, an IR source, such as an IR laser or a blackbody, is needed to generate IR light. Because the light path from the light source is not a parallel beam, a lens is also used here to focus the light. Thereafter, an IR spot is directly projected onto the DMD surface. There are 1064×768 micromirrors in the DMD array, and each mirror can rotate over two different angles: ± 12 degrees, which represent the “On” and “Off” status of each mirror. The main idea of this experimental setup is using the DMD to generate the measurement matrix and reflect the IR light to the CNT-based detector. Therefore, a proper and accurate alignment of the DMD and the CNT detector is needed here to make the light reflect onto the detector when the mirrors are at the state of “On”. By means of a well-aligned DMD, the IR signal can be reflected to the CNT detector. However, the sensing area for the CNT detector is not large enough to sense all the IR light that is reflected from the DMD. Another lens should be added in the middle of the CNT detector and the DMD. Then, each measurement of the CNT detector is the linear projection from the original signal x to the measurement matrix Φ_i .

The detector detects all light signals reflected by the DMD, and it generates photocurrent. To enable subsequent signal processing, a current monitoring circuit is needed here. For CNT-based IR detectors [52, 53], photocurrent is generated in the range of nanoamperes. The readout circuits must work at zero input impedance, because the photocurrent of the CNT-based IR detector is highly dependent on

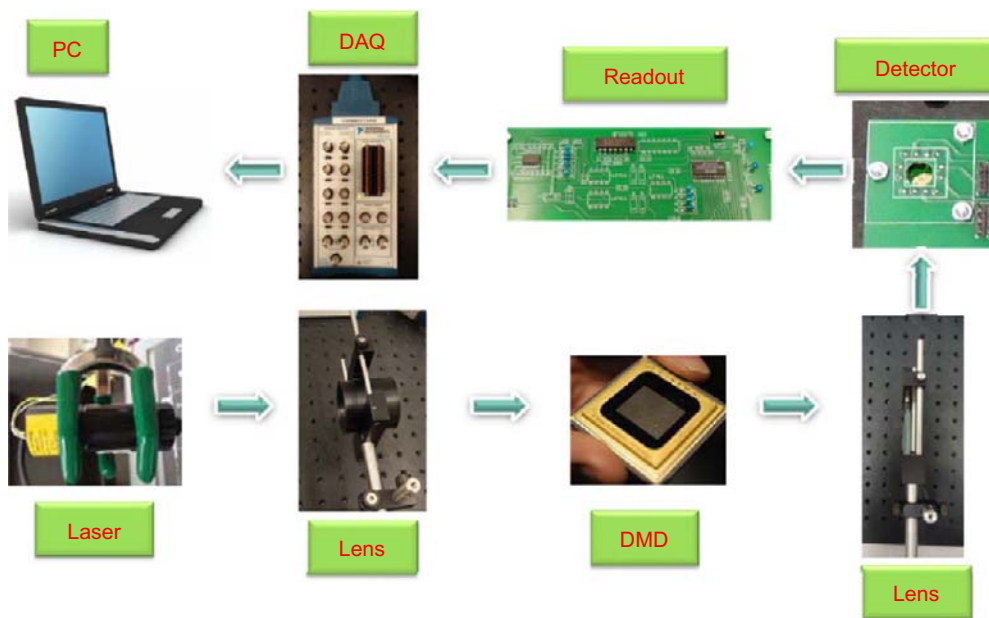
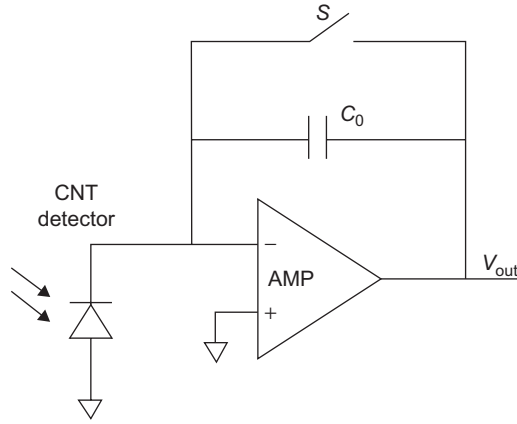


FIGURE 14.4

Architecture of compressive sensing-based single-pixel CNT detector imaging system.

**FIGURE 14.5**

Schematic of capacitor type I-V converter.

the applied bias voltage [53]. In such a low-current sampling system, a high-performance current-to-voltage amplifier (also named trans-impedance amplifier) becomes the most important module. Compared with a resistor-based amplifier [54], capacitive trans-impedance amplifier (CTIA) also works as a current-to-voltage converter (I-V converter), and it also can be designed to have high current-to-voltage conversion ratios and low noise. Fig. 14.5 shows the basic circuit of a CTIA using a switch capacitor to reset.

The amplifier works in deep negative feedback control, which imparts on CNT-based IR detectors zero bias. The circuits have two working statuses as shown in Fig. 14.5. When the switch S is on, the capacitor C_0 is reset to discharge, while in phase 2, the switch S is off in T_{off} seconds, and the photocurrent (I_p) charges the left plate of the capacitor C_0 . V_{out} can be calculated by using Eq. (14.11). This circuit can detect low current based on the input noise.

$$Q = I_p \times T_{\text{off}} \quad (14.10)$$

$$V_{\text{out}} = Q/C_0 \quad (14.11)$$

Since noise dominates the readout characteristics in low-current sensing, a low-pass filter (LPF) is used to limit the bandwidth and optimize the thermal noise contribution relating to the CTIA. Meanwhile, the LPF can reduce all high-frequency noise and the power frequency noise. In Fig. 14.6, the readout system also includes ADC circuits, which convert values of the current from analog to digital, which are sent to a PC/Data processor via a DAQ card.

14.3.2 Measurement Matrix

The measurement matrix is one of most essential parts in compressive sensing. For this application, the measurement matrix decides each time which part of the IR light will be reflected and finally reach the CNT detector. Correctly selected measurements will lead to fewer measurements and a clear reconstructed image. In this application, the measurement matrix is represented by DMD through controlling

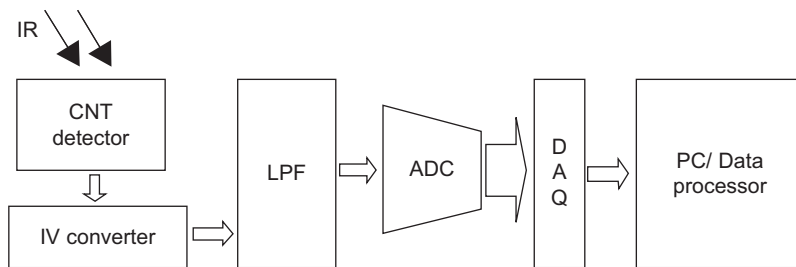
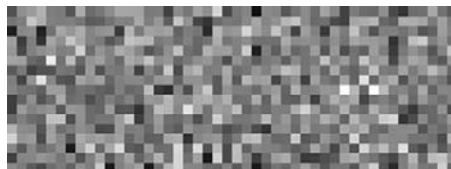
**FIGURE 14.6**

Diagram of readout system.

**FIGURE 14.7**

Random Gaussian measurement matrix.

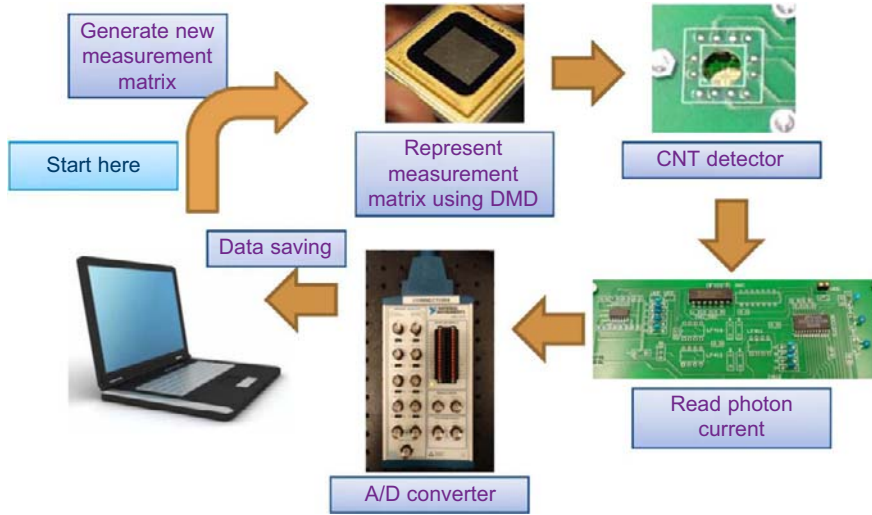
**FIGURE 14.8**

Random Bernoulli measurement matrix.

the “On” and “Off” status of each mirror. This means a simple and convenient measurement matrix for DMD: a binary matrix which only consist of “0” and “1”. “1” represents “On” while “0” represents “Off”. Although using random Gaussian distribution (Fig. 14.7) is also a good idea for the compressive sensing measurement matrix, considering the working principle of DMD, generating gray scale value will mean it takes longer to rotate the mirror several times, which in turn will increase the time required for data sampling. Therefore, a better measurement matrix to use is the random Bernoulli matrix, which only contains “1” and “0” in the distribution shown in Fig. 14.8.

14.3.3 Data Sampling and Image Reconstruction Algorithm

With the help of DMD and the readout device designed for this experiment, data are sampled continuously as shown in Fig. 14.9. During each cycle, a computer first generates a measurement matrix ϕ_i and

**FIGURE 14.9**

Data sampling process.

sends it to the DMD. Then, the DMD presents this measurement matrix by turning each mirror “On” or “Off”. Simultaneously, the data sampling system (CNT detector, readout device, and DAQ card) will save the photon current and transform into digital data and send it to the computer. Once the data has been collected, the computer will generate a new measurement matrix ϕ_{i+1} and repeat the sampling cycle. Because the working frequency is about 5 kHz, the total measurement only takes seconds.

Once all the data has been received, an image reconstruction algorithm will run for image recovery. Besides the widely used 1-norm minimization compressive sensing recovery algorithm, $\hat{x} = \arg \min \|x\|_1$ s.t. $\Phi x = y$, the minimization total variation method as per Eq. (14.12) also could be used for signal reconstruction in compressive sensing. Minimization total variation norm reflects the consistency of an image. Therefore, the reconstruction image under this constraint would be more continuous and smooth.

$$\hat{x} = \arg \min TV(x) \quad \text{s.t.} \quad \Phi x = y \quad (14.12)$$

where $TV(x) = \sum_{i,j} \sqrt{(x_{i+1,j} - x_{i,j})^2 + (x_{i,j+1} - x_{i,j})^2}$.

Another major and essential factor for image reconstruction is sparse basis choice. Most natural images are not sparse at all, and therefore compressive sensing cannot be directly used in this case. A well-considered sparse basis is needed and under which the image will convert into the sparsified form. Here we choose the Haar Wavelet basis Ψ_w to carry out the signal decomposition and transform. Under the wavelet basis domain, the signal (image) x can be transformed as

$$x = \Psi_w s \quad (14.13)$$

where s is the sparse representation of signal x . The compressive sensing equation then changes to

$$y = \Phi \Psi_w s \quad (14.14)$$

and the constraint and solution for that equation can be written as

$$\hat{x} = \arg \min TV(s) \quad \text{s.t.} \quad \Phi \Psi_w s = y \quad (14.15)$$

where $TV(x) = \sum_{i,j} \sqrt{(x_{i+1,j} - x_{i,j})^2 + (x_{i,j+1} - x_{i,j})^2}$.

14.4 EXPERIMENTAL SETUP AND RESULTS

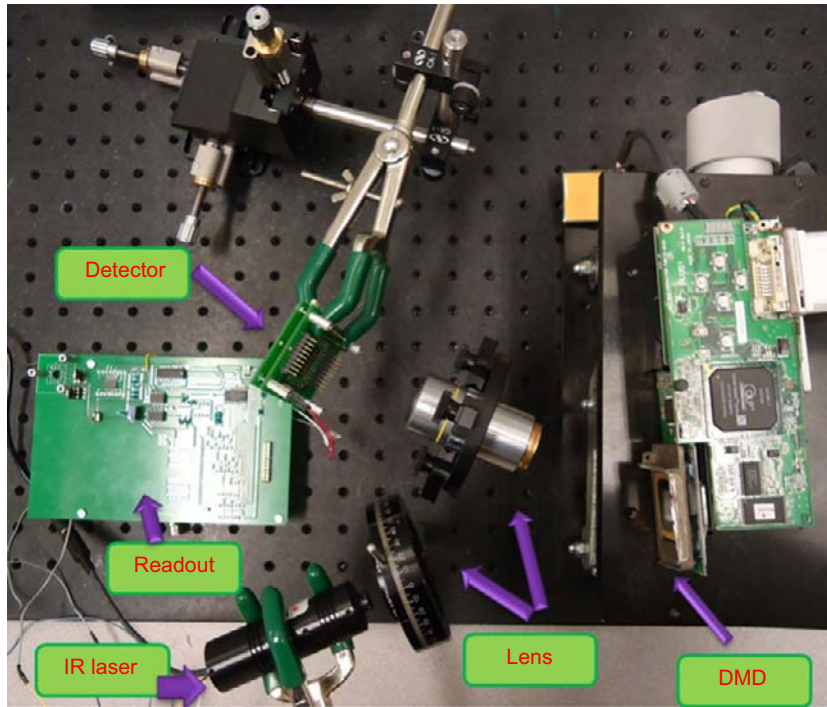
To test the performance of this CNT detector and compressive sensing application, a couple of experiments were set up. The test platform consisted of four parts: laser source, DMD, readout device, and lenses. To generate IR light for the detector to detect, a laser with wavelength of 1064 nm was used here as an IR source. The maximum output power of this laser source was 100 mW and in this experiment, the output power is usually set as 50 mW. After choosing and setting up the IR source, the alignment of laser source, lenses, DMD, device, and CNT detector was ensured. The aim is to make sure all the IR light coming from the laser will be reflected by the DMD device and after focusing by the lens will finally reach the surface of sensing area of the CNT detector (Fig. 14.10).

For the measurement matrix, here Φ selects a random Bernoulli matrix with dimensions 1000×2500 . Each cycle measurement Φ_i will be represented by the DMD after reshaping, which means converting the vector into the matrix. For instance, during this test, the dimensions of Φ_i are 1×2500 and after reshaping, Φ_i converts into 50×50 , which will be presented on the DMD. Each time data are collected by the readout system, the DMD will change into another pattern of Φ_{i+1} (Fig. 14.11). This cycle will remain until reaching Φ_{1000} , the last measurement. Once the measurement process has finished, a compressive sensing image reconstruction program will run to recover the image.

14.4.1 Static Measurement

In this experiment, a fixed 1064 nm laser was equipped for generating a static IR light spot. For our purposes, $N = 2500$, and for M we selected $M_1 = 1000$ and $M_2 = 500$. Therefore, the compressed ratios are $N/M_1 = 2.5$ and $N/M_2 = 5$. After measurement 1000 times and 500 times, a minimization total variation reconstruction algorithm was used for recovering the IR images as shown in Fig. 14.12. The only difference in these two images is the contrast. Although the $\times 1000$ measurement led to better contrast than the $\times 500$ measurement, this difference is not significant.

The light spot in these two images is the IR laser spot with the wavelength of 1064 nm. The diameter of the laser spot is around $100 \mu\text{m}$. In addition, in the 50×50 pixel recovery images, each pixel covers about 0.036 mm^2 . Therefore, usually the laser spot only covers one or two pixels in the recovery image and that is the reason for the presence of only one spot. Comparing these two images, the measurement time has some effect on the recovered images but not a very significant one.

**FIGURE 14.10**

Experiment setup layout.

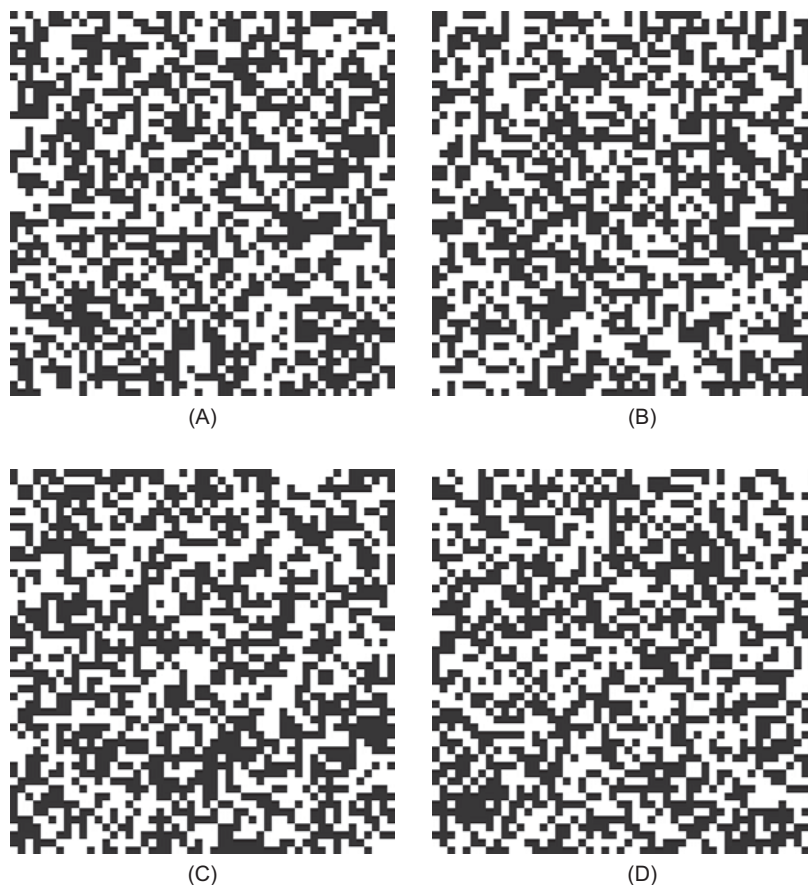
14.4.2 Dynamic Observation

Previous experimental results have shown the imaging ability of this compressive sensing-based CNT photodetector. To further investigate the performance of this imaging system, a dynamic observation experiment was designed. In this experiment, the laser source, an IR laser with 1064-nm wavelength, was not fixed, but moving in the vertical direction. A movable stage was fixed on the test platform for mounting and carrying the laser and supporting its motion. After careful design, the stage traveled at a low speed to guarantee that the compressive sampling speed was not compromised. After several measurement steps, the IR images were recovered by use of a compressive sensing image reconstruction algorithm as shown in Fig. 14.13 on p. 239.

Each image from Fig. 14.13A to E shows the laser spot movement process step by step. Every recovered image is 50×50 pixels and uses a minimization total variation algorithm for image reconstruction.

14.4.3 Performance Analysis

This compressive sensing-based single-pixel photodetector imaging system has shown good performance during previous testing. It can compress the sample data by using only one CNT photodetector

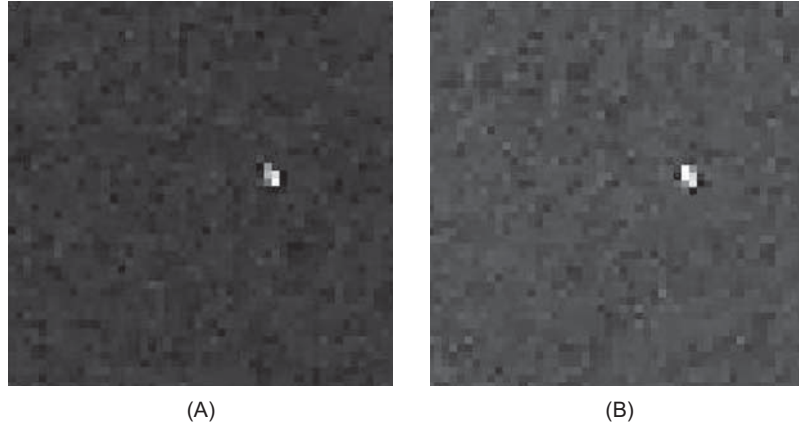
**FIGURE 14.11**

Random Bernoulli measurement matrices using in a compressive sensing-based IR imaging system. (A)–(D): four different measurement matrix patterns (ϕ_1 – ϕ_4).

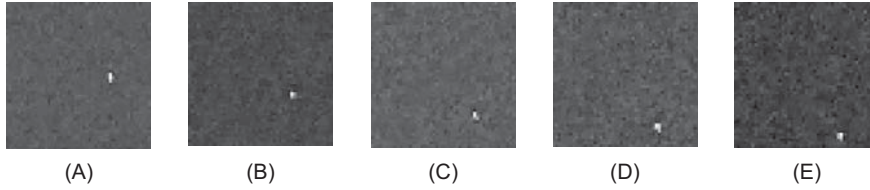
to measure the IR light intensity changes during testing. Through the compressive sensing image reconstruction algorithm, this system enabled recovery of the IR images inside which the IR laser spot looks clear and obvious. However, there are still a couple of potential problems that may affect the photodetector performance.

Non-Noise Free System

Previous discussions on compressive sensing have been based on a noise-free working environment [55]. Actually, this will never happen in nature. If the CNT photodetector could achieve high signal-to-noise ratios, compared with the eventual signal, this kind of noise would be negligible. Unfortunately, if the signal-to-noise ratio is not large enough, the situation worsens. The valuable signal might

**FIGURE 14.12**

Experimental results of IR images reconstruction. (A) and (B) are recovery images from two sets of measurements ($\times 1000$ and $\times 500$ respectively) (resolution: 50×50 pixels).

**FIGURE 14.13**

Reconstructed images for the IR spot moving from top to bottom.

become merged with the noise during testing. The compressive sensing equation then changes into

$$y = \Phi x + e \quad (14.16)$$

where e can be a noise or error with the bound of $\epsilon \geq \|e\|_{l_2}$ and ϵ is a positive number. If we consider the noise element, measurement would always be inaccurate. Therefore, the solution of Eq. (14.16) has to change into

$$\hat{x} = \arg \min TV(\tilde{x}) \quad \text{s.t.} \quad \|\Phi \tilde{x} - y\|_{l_2} \leq \epsilon \quad (14.17)$$

where $TV(x) = \sum_{i,j} \sqrt{(x_{i+1,j} - x_{i,j})^2 + (x_{i,j+1} - x_{i,j})^2}$.

In practice, the compressive sensing image reconstruction algorithm needs to be reconsidered to enable the necessary adjustment that is based on a good understanding of noise.

Dynamic Range and Analog-to-Digital (A/D) Converter

Dynamic range and resolution are essential characteristics of a sensor. For common sensing arrays such as CCD or CMOS, if each sensing cell has the same dynamic range D , the entire sensing array has the dynamic range of D . However, the condition changes when applied to the compressive sensing-based single-pixel CNT photodetector. For compressive sensing, the dynamic range has a relationship with the measurement matrix Φ if Φ has a dimension of $M \times N$, in other words, if the original image has N elements and each element has a dynamic range of D , the sensor under compressive sensing must have the dynamic range of $ND/2$ so that it can correctly measure the entire data. Item “1/2” means, in the random Bernoulli matrix, that always half of all elements are “1” while the other half are “0.” From the above analysis, a sensor with high dynamic range would enjoy compressive sensing and could attain a clear reconstructed image. The same issue applies to the A/D converter. Because of the demand on the high dynamic range as well as resolution, the A/D converter used in compressive sensing must have more bits than in the traditional sampling method to enrich the gray scale or color scale in recovered images.

14.5 SUMMARY AND PERSPECTIVES

In this chapter, we introduced an IR imaging system using a CNT-based single-pixel IR camera. IR detection is very popular in community and homeland security. The traditional IR detector has drawbacks such as the need for a cooling system or low resolution. CNT is a natural 1D material for serving as the sensing cell of IR detectors. With the help of this special type of CNT-based photodetector, a single-pixel IR imaging system has been developed. In this system, the data sampling process is quite different from that for traditional detectors or cameras. Compressive sensing is used here for compressed data sampling and reconstruction of images. It has realized the dream of a camera with only one photodetector. Theoretical analysis shows this CNT-based single-pixel IR camera can sense the data and reconstruct the observed IR image. In addition, a couple of experiments were set up, with the results wholly supporting the compressive sensing theory. Although this CNT-based IR camera has many advantages such as cooling-free working environment, high resolution, and less-measurement demand, there are still some restrictions for the further development. First, the dynamic range is not sufficiently large to support high-resolution imaging. The higher the resolution, the bigger the dynamic range that is needed, as well as a longer time for image reconstruction. Moreover, a high performance A/D converter is also needed for providing increased gray or color scale of recovered images.

Rather than capturing an IR light spot, we are concerned about the capability of capturing more complicated IR patterns using compressive sensing. A high performance IR camera must have the ability to capture and recover more complicated images. Therefore, for further testing the potential performance of this compressive sensing-based IR imaging system, we used a normal projector for generating light patterns. The visible light is filtered by an IR filter and only IR patterns were projected to the other optical parts including the DMD. The experimental setup was similar to the setup we discussed in [Section 14.4](#), but we used a silicon photodiode for optical sensing because the intensity of the IR light generated by the traditional projector was very small, in other words, the weak IR light was hard to sense by the CNT-based IR detector directly. In the experiment, we took 800 measurements to get a reconstructed image with 50×50 pixels as shown in [Fig. 14.14](#). The results demonstrated that clear infrared images can be reconstructed using the compressive sensing-based IR system. In

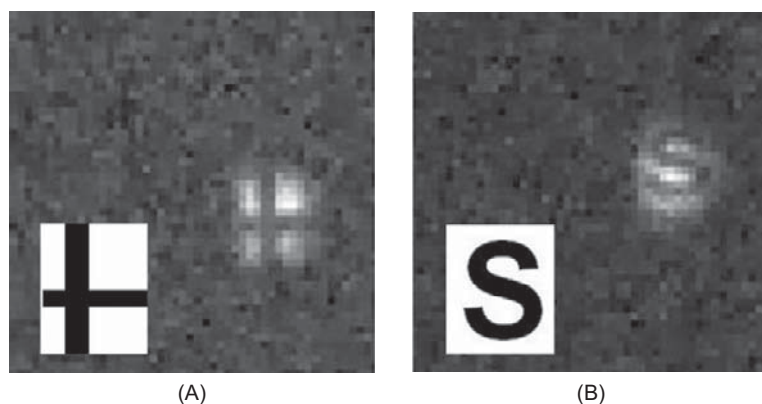


FIGURE 14.14

Experimental results of IR image reconstruction. Insets show the original patterns generated by the projector.

the future, we would like to conduct further research into increasing both the sensing range and the resolution of our CNT-based IR sensors. This will be helpful for the compressive sensing-based IR camera to achieve better performance.

References

- [1] H. Chen, N. Xi, S. Bo, L. Chen, K. W. C. Lai, and J. Lou. Infrared imaging using carbon nanotube-based detector. *Proc. SPIE*, 8058, 80580N, 2011.
- [2] E. J. Candès and M. Wakin. An introduction to compressive sampling. *IEEE Signal Process. Mag.*, 52(2): 21–30, 2008.
- [3] J. Romberg. Imaging via compressive sampling. *IEEE Signal Process. Mag.*, 25(2):14–20, 2008.
- [4] R. Baraniuk. More is less: signal processing and the data deluge. *Science*, 331(6018):717–719, 2011.
- [5] M. Fornasier and H. Rauhut. *Handbook of Mathematical Methods in Imaging*. Springer, New York, 2011.
- [6] M. A. Davenport, P. T. Boufounos, M. B. Wakin, and R. G. Baraniuk. Signal processing with compressive measurements. *IEEE J. Sel. Top. Signal Process.*, 4(2):445–460, 2010.
- [7] E. J. Candès, J. Romberg, and T. Tao. Robust uncertainty principles: exact signal reconstruction from highly incomplete frequency information. *IEEE Trans. Inf. Theory*, 52(2):489–509, 2006.
- [8] D. L. Donoho. Compressed sensing. *IEEE Trans. Inf. Theory*, 52(4):1289–1306, 2006.
- [9] D. Donoho and Y. Tsaig. Extensions of compressed sensing. *Signal Process.*, 86(3):533–548, 2006.
- [10] J. R. Wood and H. D. Wagner. Single-wall carbon nanotubes as molecular pressure sensors. *Appl. Phys. Lett.*, 76(20):2883–2885, 2000.
- [11] C. Y. Li and T. W. Chou. Strain and pressure sensing using singlewalled carbon nanotubes. *Nanotechnology*, 15(11):1493–1496, 2004.
- [12] L. Valentini, I. Armentano, J. M. Kenny, C. Cantalini, L. Lozzi, and S. Santucci. Sensors for sub-ppm no 2 gas detection based on carbon nanotube thin films. *Appl. Phys. Lett.*, 82:961–963, 2003.
- [13] J. Li, Y. Lu, Q. Ye, M. Cinke, J. Han, and M. Meyyappan. Carbon nanotube sensors for gas and organic vapor detection. *Nano Lett.*, 3:929–933, 2003.

- [14] C. K. M. Fung, N. Xi, B. Shanker, and K. W. C. Lai. Nanoresonant signal boosters for carbon nanotube based infrared detectors. *Nanotechnology*, 20(18):185–201, 2009.
- [15] J. A. Misewich, R. Martel, P. Avouris, J. C. Tsang, S. Heinze, and J. Tersoff. Electrically induced optical emission from a carbon nanotube FET. *Science*, 300(5620):783–786, 2003.
- [16] A. Phaedon. Carbon nanotube electronics. *Chem. Phys.*, 281:429–445, 2002.
- [17] K. W. C. Lai, N. Xi, C. K. M. Fung, H. Chen, and T.-J. Tarn. Engineering the band gap of carbon nanotube for infrared sensors. *Appl. Phys. Lett.*, 95(22):221108, 2009.
- [18] N. M. Gabor, Z. Zhong, J. Park, K. Bosnick, and P. L. McEuen. Extremely efficient multiple electron-hole pair generation in carbon nanotube photodiodes. *Science*, 325(5946):1367–1371, 2009.
- [19] C. A. Soci, A. A. Zhang, B. A. Xiang, S. A. A. Dayeh, D. P. R. A. Aplin, J. A. Park, X. Y. A. Bao, Y. H. A. Lo, and D. Y. Wang. ZnO nanowire UV photodetectors with high internal gain. *Nano Lett.*, 7:1003–1009, 2007.
- [20] J. U. Lee. Photovoltaic effect in ideal carbon nanotube diodes. *Appl. Phys. Lett.*, 87:073101, 2005.
- [21] J. Zhang, N. Xi, H. Chen, K. W. C. Lai, G. Li, and U. Wejinya. Photovoltaic effect in single carbon nanotube-based Schottky diodes. *Int. J. Nanoparticles*, 1(2):108–118, 2008.
- [22] M. N. Do and M. Vetterli. The finite ridgelet transform for image representation. *IEEE Trans. Inf. Theory*, 12(1):16–28, 2003.
- [23] E. Le. Pennec and S. Mallat. Sparse geometric image representation with bandelets. *IEEE Trans. Image Process.*, 14(4):423–438, 2005.
- [24] M. N. Do and M. Vetterli. Compressed sensing. *IEEE Trans. Image Process.*, 14(12):2091–2106, 2005.
- [25] S. G. Mallat and Z. Zhang. Matching pursuits with time-frequency dictionaries. *IEEE Trans. Signal Process.*, 41(12):3397–3415, 1993.
- [26] E. J. Candès and T. Tao. Near optimal signal recovery from random projections: universal encoding strategies? *IEEE Trans. Inf. Theory*, 52(12):5406–5425, 2006.
- [27] H. Rauhut. Stability results for random sampling of sparse trigonometric polynomials. *IEEE Trans. Inf. Theory*, 54(12):5661–5670, 2008.
- [28] M. Rudelson and R. Vershynin. On sparse reconstruction from Fourier and Gaussian measurements. *Commun. Pure Appl. Math.*, 61(8):1025–1045, 2008.
- [29] M. A. T. Figueiredo, R. D. Nowak, and S. J. Wright. Gradient projection for sparse reconstruction: application to compressed sensing and other inverse problems. *IEEE J. Sel. Top. Signal Process. Spec. Issue Convex Optim. Methods Signal Process.*, 1(4):586–598, 2007.
- [30] E. J. Candès, J. Romberg, and T. Tao. Stable signal recovery from incomplete and inaccurate measurements. *Commun. Pure Appl. Math.*, 59(8):1207–1223, 2006.
- [31] S. B. Chen, D. L. Donoho, and M. A. Saunders. Atomic decomposition by basis pursuit. *SIAM J. Sci. Comput.*, 43(1):129–159, 1998.
- [32] J. A. Tropp. Greed is good: algorithmic results for sparse approximation. *IEEE Trans. Inf. Theory*, 50(10):2231–2242, 2004.
- [33] G. Peyre. Gradient pursuits. *IEEE Trans. on Signal Process.*, 56(6):2370–2382, 2008.
- [34] C. La and M. N. Do. Tree-based orthogonal matching pursuit algorithm for signal reconstruction image processing. In *IEEE International Conference on Image Processing*, Atlanta, Georgia, pages 1277–1280, 2006.
- [35] J. Tropp and A. Gilbert. Signal recovery from random measurements via orthogonal matching pursuit. *IEEE Trans. Inf. Theory*, 53(12):4655–4666, 2007.
- [36] D. L. Donoho. For most large underdetermined systems of linear equations, the minimal ℓ_1 -norm solution is also the sparsest solution. *Commun. Pure Appl. Math.*, 59(6):797–829, 2006.
- [37] E. J. Candès and J. Romberg. Sparsity and incoherence in compressive sampling. *Inverse Probl.*, 23(3):969–985, 2007.
- [38] C. Dossal, G. Peyre, and J. Fadili. A numerical exploration of compressed sampling recovery. *Linear Algebra Appl.*, 432(7):1663–1679, 2010.

- [39] G. Peyr. Best basis compressed sensing. *IEEE Trans. Signal Process.*, 58(5):2613–2622, 2010.
- [40] S. Jokara and V. Mehrmann. Sparse solutions to underdetermined Kronecker product systems. *Linear Algebra Appl.*, 432(12):2437–2447, 2009.
- [41] G. Kutyniok. *Compressed Sensing: Theory and Applications*. Cambridge University Press, UK, 2011.
- [42] E. J. Candès and T. Tao. Decoding by linear programming. *IEEE Trans. Inf. Theory*, 51(12):4203–4215, 2005.
- [43] A. C. Gilbert, S. Guha, and P. Indyk. Near-optimal sparse Fourier representations via sampling. *ACM Symposium on Theoretical Computer Science*, 152–161, 2006.
- [44] R. Baraniuk, M. Davenport, R. DeVore, and M. Wakin. A simple proof of the restricted isometry property for random matrices. *Constr. Approx.*, 28(3):53–263, 2008.
- [45] R. A. DeVore. Deterministic constructions of compressed sensing matrices. *J. Complex.*, 23:918–925, 2007.
- [46] M. F. Duarte, M. A. Davenport, D. Takhar, J. N. Laska, T. Sun, K. F. Kelly, and R. G. Baraniuk. Single-pixel imaging via compressive sampling. *IEEE Signal Process. Mag.*, 25(2):83–91, 2008.
- [47] M. Wakin, J. Laska, M. Duarte, D. Baron, S. Sarvotham, D. Takhar, K. Kelly, and R. Baraniuk. An architecture for compressive imaging. In *International Conference on Image Processing (ICIP)*, Atlanta, Georgia, pages 1273–1276, 2006.
- [48] R. Baraniuk and P. Steeghs. *Proceedings of 2007 IEEE Radar Conference*, Boston MA, pages 128–133, Waltham, MA, 2007.
- [49] M. Sheikh, O. Milenkovic, and R. Baraniuk. Designing compressive sensing DNA microarrays. *IEEE International Workshop on Computational Advances in Multi-Sensor Adaptive Processing (CAMSAP)*, St Thomas, Virgin Islands, pages 141–144, 2006.
- [50] M. Lustig, D. L. Donoho, and I. M. Pauly. The application of compressed sensing for rapid MR imaging. *Magn. Reson. Med.*, 58(6):1182–1195, 2007.
- [51] M. F. Duarte, S. Sarvotham, D. Baron, M. B. Wakin, and R. G. Baraniuk. Performance limits for jointly sparse signals via graphical models. *Proceedings of the Sensor, Signal and Information Processing (SenSIP) Workshop*, Sedona, Arizona, 2008.
- [52] J. Zhang, N. Xi, H. Chen, K. W. C. Lai, G. Li, and U. C. Wejinya. Design, manufacturing and testing of single carbon nanotube based infrared sensors. *IEEE Trans. Nanotechnol.*, 8(8):245–251, 2009.
- [53] H. Chen, N. Xi, K. W. C. Lai, C. K. M. Fung, and R. Yang. Development of infrared detectors using single carbon nanotubes based field effect transistors. *IEEE Trans. Nanotechnol.*, 5(9):582–589, 2010.
- [54] L. Chen, N. Xi, H. Chen, and K. W. C. Lai. Development of readout system for carbon nanotube based infrared detector. In *IEEE Nanotechnology Materials and Devices Conference, Monterey, CA*, pages 230–234, 2010.
- [55] J. Haupt and R. Nowak. Signal reconstruction from noisy random projections. *IEEE Trans. Inf. Theory*, 52(9):4036–4048, 2006.

INDEX

Page numbers followed by “*f*” indicates figures and “*t*” indicates tables.

<u>Index Terms</u>	<u>Links</u>			
3D manipulation forces	58			
3D nanoforce feedback	56			
A				
AAO, <i>see</i> Anodic aluminum oxide				
AFM, <i>see</i> Atomic force microscopy				
Analog-to-digital (A/D) converter	240			
Anodic aluminum oxide (AAO)	109			
Armchair CNT	13			
Asymmetric photodetectors	112			
Atomic force microscopy (AFM)	6	95	96 <i>f</i>	113
based augmented reality system				
limitations of	60			
nanomanipulation with	60			
real-time visual feedback generation	59	59 <i>f</i>		
3D nanoforce feedback	56			
based nanomanipulation	55			
CNT manipulation	136			
image	146	147 <i>f</i>	200	201 <i>f</i>
of fabrication process	141 <i>f</i>			
mode	53			
principle	52			
scanning mechanism	52			
Au–CNT–Au Schottky photodiode	115	115 <i>f</i>		

Index Terms

Links

Augmented reality system

AFM based

limitations of	60			
nanomanipulation with	60			
real-time visual feedback generation	59	59f		
3D nanoforce feedback	56			

local enhanced, nanomanipulation

nanoparticles	66	66f	67f	
nanorods	67	70f		

local scan mechanism

for nanoparticle	62			
for nanorod	64			

B

Back-gate Ag–CNT–Ag transistors	130			
structure of	133f			
Back-gate Au–CNT–Ag transistors	132			
Back-gate Au–CNT–Au transistors	127			
Barrier injection transit time (BARITT) diodes	126			
Bimolecular recombination	188	189f	190	
Bohr radius	209			
Bulk heterojunction (BHJ)	184			

C

CAD, *see* Computer-aided design

Capacitive trans-impedance amplifier (CTIA)	233				
Carbon nanotube (CNT)	2	5	81	151	154
application of	37	184			
armchair	13				
automated manipulation of	74				
band gap of	14	82	89	91	

Index Terms

Links

Carbon nanotube (CNT) (*Cont.*)

breakdown, effects of	87 <i>f</i>	88 <i>f</i>		
current-voltage characteristics	87	89 <i>f</i>		
IR responses	89	90 <i>f</i>		
chiral vector	13	13 <i>f</i>		
current-voltage characteristics	87	89 <i>f</i>		
detectors				
in Au–CNT–Au structure	130			
behavior	126			
design	140			
devices				
electrical and optical stability of	101	102 <i>f</i>	103 <i>f</i>	104 <i>f</i>
manufacturing method	35			
dielectrophoretic phenomenon on	16	17	17 <i>f</i>	
dynamic modeling of rotational motion of	35			
electric field design for	37			
electrical breakdown controller of	85	86 <i>f</i>		
electrokinetic force	12			
energy levels of	132			
fabrication and treatment	11	12 <i>f</i>	185	
Fermi energy of	140			
Fermi level of	127			
IR detector	125	155	158 <i>f</i>	159 <i>f</i>
AFM images of fabricated	157 <i>f</i>			
configuration of	152 <i>f</i>			
structure of	156 <i>f</i>			
IR sensors				
photocurrent mapping of	180	180 <i>f</i>	181 <i>f</i>	
photoresponses of	179	179 <i>f</i>		
laser polarization and	143			
metallic	14			

Index Terms

Links

Carbon nanotube (CNT) (*Cont.*)

typical I-V curves	20	20f		
by microrobotic workstation, deposition of	21	22f	23f	
MWCNT	14			
nanomanufacturing process for	3f			
1D structure of	228			
optoelectronic devices	11			
particles	32			
polyethylene thin film packaging	100	100f	101f	102f
electrical and optical stability of	101	102f	103f	104f
photodetector	134	228		
photodiodes	108	108f	109f	110f
rotation angle and velocity of	48f			
semiconducting	14	19	20f	21f
separation process	19	19f		
simulation results				
dielectrophoretic force	40			
electrorotation	45			
rotational motion of carbon nanotubes	45			
suspensions	20	21f	22	
SWCNT	13			
thermal annealing	94	95f	96f	97f
electrical and optical responses of	96	98f	99f	
using microfluidics	14			
Carbon nanotube field-effect transistors (CNTFETs)	110	125		
asymmetric multigate				
with simplified gate structure	146			
structure of	16f			
IR detectors	126			
structure of	126f			
using Ag electrodes	129			

<u>Index Terms</u>	<u>Links</u>					
Charge-coupled device (CCD)	226					
Chiral vector	13	13 <i>f</i>				
Clausius–Mossotti (CM) factor	17	18 <i>f</i>	31	33	40	41 <i>f</i>
	202					
CNT, <i>see</i> Carbon nanotube						
CNTFETs, <i>see</i> Carbon nanotube field-effect transistors						
Compressive sensing	226					
A/D converter used in	240					
applications	231					
dynamic range	240					
for single-pixel photodetectors	231					
theoretical foundation of	228					
random matrix	231					
sparsity	229					
Compressive sensing-based CNT photodetector						
dynamic observation	237					
performance analysis	237					
static measurement	236					
Computer-aided design (CAD)	74					
guided automated nanoassembly	71					
two-dimensional	73 <i>f</i>					
Contact mode	54					
D						
Data sampling	234	235 <i>f</i>				
Data sensing						
in compressive sensing process	227 <i>f</i>					
in traditional sensing device	226	226 <i>f</i>				
DEP, <i>see</i> Dielectrophoresis						

Index Terms

Links

Deposition	4				
of CNTs	6	12	19		
by microrobotic workstation	21	22 <i>f</i>	23 <i>f</i>		
Detector array, CNT-based transistors	146				
Dielectric constants, effect of	167	167 <i>f</i>	174		
Dielectric mode	170				
Dielectric particles	30	31 <i>f</i>			
Dielectrophoresis (DEP)	6	14	29	30 <i>f</i>	200
fluidic medium on CNTs particles by	36				
forces	15	16	202	203 <i>f</i>	
derivation of	34				
manipulation	17	94	95		
Dielectrophoretic force model	30				
electrorotation modeling for nanomanipulation	34				
rotational motion of CNTs	35				
simulation results for	40				
Digital micromirror device (DMD)	231	235			

E

EBL, <i>see</i> Electron beam lithography					
Effective area	152 <i>f</i>				
EKF, <i>see</i> Extended Kalman filter					
Electric field design	39				
for CNTs applications	37				
Electrokinetic force	12				
Electron beam lithography (EBL)	6	156	199		
Electrorotation					
modeling for nanomanipulation	34				
simulation results	45				
Electrostatic doping	132				
Energy concentration mode	170				

<u>Index Terms</u>	<u>Links</u>				
Etching	4	4 <i>t</i>			
Extended Kalman filter (EKF)	82				
for fault detection	85	86 <i>f</i>			
F					
Fabrication					
of graphene devices	200	201 <i>f</i>	202 <i>f</i>		
of nano sensor	154	156 <i>f</i>	157 <i>f</i>		
Fermi energy	130	141	143	144	220
Finite Difference Time Domain technique	153				
Force analysis model	57	57 <i>f</i>			
G					
Graphene	13	13 <i>f</i>	199		
devices					
electrical and optical behaviors	203	206 <i>f</i>			
fabrication of	200	201 <i>f</i>	202 <i>f</i>		
flakes	200				
dielectrophoretic effect on	202				
Green's function	153				
Raman spectra of	202 <i>f</i>				
H					
Hamiltonian matrix	83				
Hermitian operator	4				
High-pressure carbon monoxide (HiPco)					
synthesis process	5	12	14		
I					
Image reconstruction algorithm	234				

<u>Index Terms</u>	<u>Links</u>				
Indium antimonide (InSb) nanowires	209				
diameters of	211	211 <i>f</i>			
growth of	214	215 <i>f</i>	216		
photodetectors					
asymmetric	218	219 <i>f</i>	220 <i>f</i>	221 <i>f</i>	222 <i>f</i>
symmetric	216	216 <i>f</i>	217 <i>f</i>	218 <i>f</i>	
Infrared (IR) detector	228				
bias-dependent measurement with	136 <i>f</i>				
CNT-based	125	155	158 <i>f</i>	159 <i>f</i>	
AFM images of fabricated	157 <i>f</i>				
configuration of	152 <i>f</i>				
structure of	156 <i>f</i>				
CNTFET-based	126				
photoresponse of	94				
Infrared imaging					
architecture of	232 <i>f</i>				
reconstruction	239 <i>f</i>	241 <i>f</i>			
Infrared responses	89	90 <i>f</i>			
Infrared sensors					
CNT-based					
photocurrent mapping of	180	180 <i>f</i>	181 <i>f</i>		
photoresponses of	179	179 <i>f</i>			
nanoantenna design for	152	152 <i>f</i>			
InSb nanowires, <i>see</i> Indium antimonide nanowires					
Interatomic force	53	53 <i>f</i>			
IR, <i>see</i> Infrared					
J					
Jacobeian matrix	86				

Index Terms

Links

K

Kelvin probe force microscopy (KPFM) 193 194 194^f

L

Lattice

arrangement 165 167 167^f 168 171 177^f
dielectric 164
number 177
structures of photonic crystal 176^f
unity 170^f

Local enhanced augmented reality system

nanomanipulation

nanoparticles 66 66^f 67^f

nanorods 67 70^f

Local Scan After Manipulation (LSAM) 62 64

for nanoparticles 67^f

for nanorods 69^f

Local scan algorism 62

Local Scan Before Manipulation (LSBM) 62 64 66

Long-wave infrared (LWIR) 212

Low-pass filter (LPF) 233

LSAM, *see* Local Scan After Manipulation

LSBM, *see* Local Scan Before Manipulation

LWIR, *see* Long-wave infrared

M

Maximum a posteriori probability (MAP) 85

Maxwell's equation 166

MBE, *see* Molecular beam epitaxy

Measurement matrix, for compressive sensing 233 234^f

Mechanical exfoliation 200

<u>Index Terms</u>	<u>Links</u>					
Metal-induced gap states (MIGS)	111					
Metal-oxide-semiconductor field effect transistor (MOSFET)	125					
Metallic CNT	14	18	20	20 ^f		
Microchamber	14	19				
Microchannel	14	19				
Microelectrodes	15	16 ^f	19	22	23	101
design	37					
for carbon nanotube implementation	38 ^f					
theory for	38					
Microfluidics						
classification of CNT using	14					
role of	5					
Micronanofluidic manipulation	16					
Middle-gate transistors	136					
Middle-wave infrared (MWIR)	209					
MIGS, <i>see</i> Metal-induced gap states						
Molecular beam epitaxy (MBE)	211					
Multigate transistors						
asymmetric multigate CNTFET	140					
temporal photoresponses	144					
Multiple electron-hole pair generation	228					
Multiple exciton generation (MEG)	184					
Multi-walled carbon nanotube (MWCNT)	14	20	82	94	98	
MWIR, <i>see</i> Middle-wave infrared						
N						
Nano particles, dynamic effect of fluid medium on	36					
Nano sensor						
fabrication of	154	156 ^f	157 ^f			
photocurrent measurement on	157	158 ^f	159 ^f			

Index Terms

Links

Nanoantenna design, for IR sensors	152			
Nanoantenna near-field effect	153	155	<i>f</i>	
Nanoassembly				
CAD guided automated	71			
robotic	6			
Nanodevices, manufacturing	4	5	<i>f</i>	
Nanoenvironments, modeling of	72			
Nanomanufacturing	2			
Nanomaterials	1			
based devices, manufacturing	4			
impact of	2			
Nano-objects	71	72	72	<i>f</i> 73
Nanoparticles	66	66	<i>f</i>	67
local scan mechanism for	62			
Nanorobotic system, mechanism of	56			
Nanorods	60			
local scan mechanism for	64			
manipulation of	67	70	<i>f</i>	
Nano-sized quantum optical sensor	81			
Nanotubes, sorting of	15	16	<i>f</i>	
Negative dielectrophoresis	30			
NEGF, <i>see</i> Nonequilibrium Green's functions				
NEP, <i>see</i> Noise equivalent power				
NETD, <i>see</i> Noise equivalent temperature difference				
Noise equivalent power (NEP)	119			
Noise equivalent temperature difference (NETD)	119			
Noncontact mode	54			
Nonequilibrium Green's functions (NEGF)	82	83	<i>f</i>	
Non-noise free system	238			
Nyquist–Shannon sampling theorem	225	227		

Index Terms

Links

O

Open circuit voltage (Voc)	143	143 <i>f</i>	186
Optical nanoantennas	152	152 <i>f</i>	
Optical waveguide	164		
Optoelectronics	1	11	
fabrication process of	4		
Organic photovoltaic (OPV) cells	184		
Organic solar cells (OSC)	184		
J-V characteristics of	188 <i>f</i>		
dark	191 <i>f</i>		
performance analysis of	185		
SWCNT-enhanced, J-V of	190		
Orthogonal Matching Pursuit (OMP)	229		

P

Packaging process	93			
Parylene photonic crystal	168	180		
of TE-like mode	170 <i>f</i>			
Parylene thin film packaging	100	100 <i>f</i>	102 <i>f</i>	
Patterning	4			
Phantom TM	55			
Photocurrent	125	130		
mapping of CNT-based IR sensors	180			
measurement on nano sensor	157	158 <i>f</i>	159 <i>f</i>	
Photodetectors	134			
asymmetric	218	219 <i>f</i>		
p-n junction-based	228			
symmetric	216	216 <i>f</i>	217 <i>f</i>	218 <i>f</i>
Photodiodes				
p-n junction	110 <i>f</i>			
review of	108			

Index Terms

Links

Photodiodes (*Cont.*)

Schottky photodiodes, *see* Schottky
photodiodes

Photonic band gap

diagram of photonic crystal 167*f* 169*f* 171*f*
energies 210 210*t*
of photonic crystal 166
width for photonic crystal 172*f*

Photonic crystal

164 165*f*
photonic band gap diagram of 167*f* 169*f* 171*f*
photonic band gap width for 172*f*
CNT-based IR sensor with 178*f*
defect
design of 173 173*f*
effect from dielectric constants 167 167*f*
effect from different structures 168 169*f* 170*f* 171*f* 172*f*
photonic band gap of 166
principle for 165
silicon dioxide 174 174*f* 175*f* 176*f*
for TM-like and TE-like mode 171*f*

Photonic crystal cavity

173
AFM images of 179*f*
CNT-based IR sensors with
photocurrent mapping of 180 180*f* 181*f*
photoresponses of 179 179*f*
defect from dielectric constants 174 175*f*
defect from dielectric size 176 176*f* 177*f*
design of 178 178*f*
effect from lattice number 177 177*f*

Photovoltaic photoresponse

134

PMMA, *see* Polymethylmethacrylate

Index Terms

Links

Poisson's equation	84	85 <i>f</i>	
Polarizability, of dielectric particles	30	31 <i>f</i>	
Poly(3-octylthiophene) (P3OT)	184		
Poly 3-hexylthiophene (P3HT)	185	186 <i>f</i>	194
Polymethylmethacrylate (PMMA)	14	15 <i>f</i>	156
Positive dielectrophoresis	30		
Potential theory	37		
Pseudo normal force	58		
Pythagorean theorem	32		

Q

Quad photodiode detector	57 <i>f</i>		
Quantum electron transport model			
NEGF	82	83 <i>f</i>	
Poisson's equation	84	85 <i>f</i>	
self-consistent algorithm	84	85 <i>f</i>	
Quantum well infrared photodetector (QWIP)	211		
structure of dual-band	212 <i>f</i>		
QWIP, <i>see</i> Quantum well infrared photodetector			

R

Raman spectroscopy	200	202 <i>f</i>	
Random Bernoulli measurement matrix	234 <i>f</i>	238 <i>f</i>	
Random drift	61		
Random Gaussian measurement matrix	234 <i>f</i>		
Real-time force feedback	56		
Real-time visual feedback generation	59	59 <i>f</i>	
Reliable manufacturing process	199		
Restricted Isometry Property (RIP)	229	230	

Index Terms

Links

Robotic nanoassembly	6				
Rotational motion of CNT					
dynamic modeling	35				
simulation results	45				
S					
SAED, <i>see</i> Selected area electron diffraction					
Scanning electron microscopy (SEM)	214	215 <i>f</i>			
Schottky barriers	94	130	134	141	144
Schottky photodiodes					
asymmetric	117				
design of	111				
structure of single CNT-based	110				
symmetric	112				
Selected area electron diffraction (SAED)	214	216			
Self-consistent algorithm	84	85 <i>f</i>			
Semi-conducting CNT	5	14	19 <i>f</i>	20 <i>f</i>	21 <i>f</i>
SEM, <i>see</i> Scanning electron microscopy					
Shockley Queisser limit	212				
Signal-to-noise ratio	117				
Silicon dioxide photonic crystal	174	174 <i>f</i>	175 <i>f</i>	176 <i>f</i>	
Silicon slab	168	171 <i>f</i>	172	172 <i>f</i>	
Silicon–CNT heterojunction photodetector	109 <i>f</i>				
Single-junction solar cell	212				
Single-pixel photodetectors					
compressive sensing for					
measurement matrix	233				
system architecture	231				
Single-walled carbon nanotube (SWCNT)	13	19	93	154	190
electrical role of, OSC	193				

Index Terms

Links

Single-walled carbon nanotube (SWCNT) (*Cont.*)

metallic	18	
semiconducting effect	189	
topography of	195	195 <i>f</i>
Split photodiode	57 <i>f</i>	
Surface potential (SP) images	194	
SWCNT, <i>see</i> Single-walled carbon nanotube		

T

Tandem solar cell	212	
Tapping mode	54	
TEM, <i>see</i> Transmission electron microscopy		
Thermal annealing, CNTs	94	
electrical and optical responses of	96	98 <i>f</i> 99 <i>f</i>
Thermal detectors	228	
Thermal drift	62	
Thin-film photodetector	108	108 <i>f</i>
Tip scanning	52	
Transformation matrix	78	
Transmission electron microscopy (TEM)	214	215 <i>f</i>
Triple-junction solar cell	212	213 <i>f</i>

V

van der Waals force	53	
Vapor-liquid-solid (VLS)	213	214
VLS, <i>see</i> Vapor-liquid-solid		

W

Waveguide		
crystal	164	165

Index Terms**Links**Waveguide (*Cont.*)

optical

164

Wood–Ashcroft theory

153

Z

Zigzag carbon nanotubes

13